UNIVERSITY OF ADELAIDE LIBRARY
5·9·73

CORONAL BROADENING OF THE CRAB NEBULA AND ASPECTS OF INTERPLANETARY SCINTILLATION AND IONOSPHERIC REFRACTION

by

R. G. Blesing, B.Sc. (Hons)

A Dissertation
presented for the degree of

DOCTOR OF PHILOSOPHY

at the
UNIVERSITY OF ADELAIDE
(Department of Physics)

April 1972

CONTENTS

SUMMARY (i)

PREFACE (iv)

ACKNOWLEDGEMENTS (v)

CHAPTER 1. RELEVANT THEORY AND REVIEW 1

- 1.1 Introduction 1
- 1.2 Scattering in the Interplanetary Medium 2
- 1.3 Coronal Broadening 7
- 1.4 Interplanetary Scintillation 16
- 1.5 Ionospheric Refraction in Radio Astronomy 25

CHAPTER 2. METHODS OF OBSERVATION 28

- 2.1 Introduction 28
- 2.2 Coronal Broadening of the Crab Nebula - Two-dimensional Images 28
- 2.3 Coronal Broadening of the Crab Nebula - Drift Scans 35
- 2.4 Interplanetary Scintillation Observations at Culgoora 36
- 2.5 Ionospheric Refraction 39
- 2.6 Interplanetary Scintillation Observations at Parkes 40

CHAPTER 3. ANALYSIS AND RESULTS OF THE CORONAL BROADENING MEASUREMENTS 42

- 3.1 Introduction 42
- 3.2 Analysis of the Magnetic Tape Data 43
- 3.3 Analysis of the Chart Data 53
- 3.4 Results of the Tape and Chart Data 57

3.5 Model of the Brightness Distribution 64
3.6 Unusual Events 71
3.7 Summary 84

CHAPTER 4. IONOSPHERIC REFRACTION 86
4.1 Analysis and Results 87
4.2 Travelling Ionospheric Disturbances 100
4.3 Comparison with Results 104
4.4 Conclusion 107

CHAPTER 5. SOME ASPECTS OF INTERPLANETARY SCINTILLATION 110
5.1 Introduction 110
5.2 Digital Spectral Analysis 113
5.3 Interplanetary scintillation at 80 MHz 128
5.4 Observations at Parkes 135
5.5 Bessellian Power Spectral Analysis 140

CHAPTER 6. THE ADELAIDE PROJECT 151
6.1 Introduction 151
6.2 Specification 152
6.3 The Antenna Design 157
6.4 The Receivers 161
6.5 Progress and Future Development 164

CHAPTER 7. SUMMARY 166

BIBLIOGRAPHY 174

APPENDIX I Some examples of two-dimensional source movements. 180

APPENDIX II Circuit diagrams of the receiver used on the Adelaide project. 181

APPENDIX III Reprint: "80 MHz Observations of the
Coronal Broadening of the Crab Nebula"
by J. R. Harries, R. G. Blesing and
P. A. Dennison.

SUMMARY

This dissertation is concerned with observations of extraterrestrial radio sources insofar as they are affected by the intervening interplanetary medium and Earth's ionosphere. In traversing these media, which constitute irregular plasmas, radio waves may be scattered by irregularities in electron density and may also be refracted in the presence of significant density gradients.

In the case of the interplanetary medium, the scattering effects normally give rise to a diffraction pattern on the Earth which is observed as interplanetary scintillation. However, when the scattering becomes very strong, as occurs for example on a source observed close to the sun, the source may appear to increase in angular size and such coronal broadening is a most useful technique for studying the inner regions of the interplanetary medium. In this latter case, where sources are observed through the denser regions of the solar corona, refraction may also play a role in defining the shape of the observed image.

Before signals can be recorded by the observer they must pass through the Earth's ionosphere where both scintillation and refraction may affect the approaching radio waves. Scintillation due to ionospheric irregularities might be observed but with much slower periods

than interplanetary scintillation, and ionospheric refraction may affect the apparent positions of the sources of radiation.

Three major sections are presented in this dissertation. Most of the data for each of these were recorded at 80 MHz using the C.S.I.R.O. radioheliograph at Culgoora, N.S.W. The first part concerns direct observations of two-dimensional images of the Crab Nebula when broadened by the solar corona. These observations constitute the first of their type and allow positive estimates of the size, shape and orientation of the broadened image. The second topic is devoted to refraction in the ionosphere. Spherical and steady wedge components are considered, but most importantly irregular wedge refraction is shown to be caused by Travelling Ionospheric Disturbances (TID's). Two-dimensional plots of source movements are seen to agree well with expected movements based on the current knowledge of the properties of TID's. The final major section deals with several aspects of interplanetary scintillation. Determinations of the angular structure of radio sources are attempted, three frequency information (from Parkes, N.S.W.) is considered and the possibility of obtaining two-dimensional power spectra of scintillation via Bessel transforms is investigated.

In addition to the above work the author was involved with the initial stages of construction of aerials and receivers for three receiving sites in South Australia. This project was aimed at recording interplanetary scintillation on two frequencies simultaneously from three spaced sites. Initially, intensity information is to be recorded but it is hoped that the recording of phase information will be possible as a future development. The specifications of the aerials and receivers for the project are described.

PREFACE

This dissertation contains no material which has been submitted to any other University and to the best of the author's knowledge no material previously published by other persons, except where due reference is made.

R. G. Blesing

University of Adelaide
28/4/72

ACKNOWLEDGEMENTS

The work described in this thesis was carried out in the Department of Physics at the University of Adelaide under the supervision of Dr P. A. Dennison. The author is grateful to him for many helpful discussions and his encouragement throughout the course of the work.

The data were recorded using the radioheliograph at Culgoora and the 210 ft radiotelescope at Parkes, N.S.W. and the author wishes to express his gratitude to the C.S.I.R.O. Division of Radiophysics for making these facilities available. In particular the author would like to thank Dr J. P. Wild and other members of the Division for their assistance in operating the equipment.

The recording of the initial observations of the coronal broadening of the Crab Nebula and also the preliminary analysis of this data were carried out jointly with Dr J. R. Harries. Recording and computer analysis of the interplanetary scintillation information was carried out in conjunction with the author's colleague, Mr M. Wiseman. Some assistance with the power spectral analysis was provided by Dr R. Buckley and the work concerning the Bessellian power spectral analysis was undertaken in collaboration with Mr B. D. Ward. Considerable assistance in the data reduction was provided by

Mrs McLean and Mrs Lomax.

The author is indebted to Mr R. E. Lomax for his technical assistance in the construction of the antennas and receivers for the Adelaide project.

Finance for the projects was supplied by the Australian Research Grants Committee and the University of Adelaide. The author was a holder of a Commonwealth Postgraduate Award and later a University Research Grant.

UNIVERSITY OF ADELAIDE LIBRARY

CHAPTER 1

RELEVANT THEORY AND REVIEW

1.1 Introduction

Since the first observations of radio wave scattering in the interplanetary medium (Machin and Smith, 1952), rapid developments in the study of coronal broadening and interplanetary scintillation of extra-terrestrial radio sources have established many parameters of the expanding solar corona (the solar wind). Such techniques have provided data on the solar wind from regions close to the sun out to regions beyond the orbit of the earth, and over a wide range of heliocentric latitude. More recently, direct sampling of the interplanetary plasma by spacecraft has provided information about the magnetic field structure and proton and electron densities. The spatial scale of these observations (determined by the sampling rate at the spacecraft) is, however, several orders of magnitude greater than the scale of the irregularities studied by the radio-scattering techniques. In addition spacecraft are presently confined to the ecliptic plane and to heliocentric distances of about 1 A.U., a restriction which does not apply to the radio techniques. Spacecraft observations differ in another way in that they essentially sample the solar wind at points in space, whereas the radio-scattering measurements yield information about the interplanetary medium integrated along a line of sight.

In this chapter we present the fundamentals of scattering in the interplanetary medium and introduce formulae relevant to later sections. Brief summaries of previous work in the fields of coronal broadening and interplanetary scintillation are then given with a final section devoted to refraction within the ionosphere, mentioning the difficulties which this effect has caused during position measurements of radio sources.

1.2 Scattering in the Interplanetary Medium

The existence of electron density irregularities within the solar wind is now well established. To introduce the phenomena of coronal broadening and interplanetary scintillation we shall refer to Figure 1.1. The solar wind, containing irregularities of scale a, and electron density deviation ΔN_e, relative to the ambient density N_e, is convected outward from the sun with a velocity u. The plasma irregularities impose random phase deviations across the wavefront of incident radio waves of wavelength λ, and the rms value of these phase deviations is denoted by ϕ_o. We shall assume that most of the scattering is imposed within a slab of irregularities having a thickness L. In addition we shall assume that the effect on the original radio wave is purely a phase variation and that amplitude changes are negligible. This breaks down when $\phi_o > 1$ radian, but we shall see later that theories based on this assumption have adequately predicted many of the observations. The scattering region can therefore be described as a phase changing screen situated at the distance at which the wave emerges from the region.

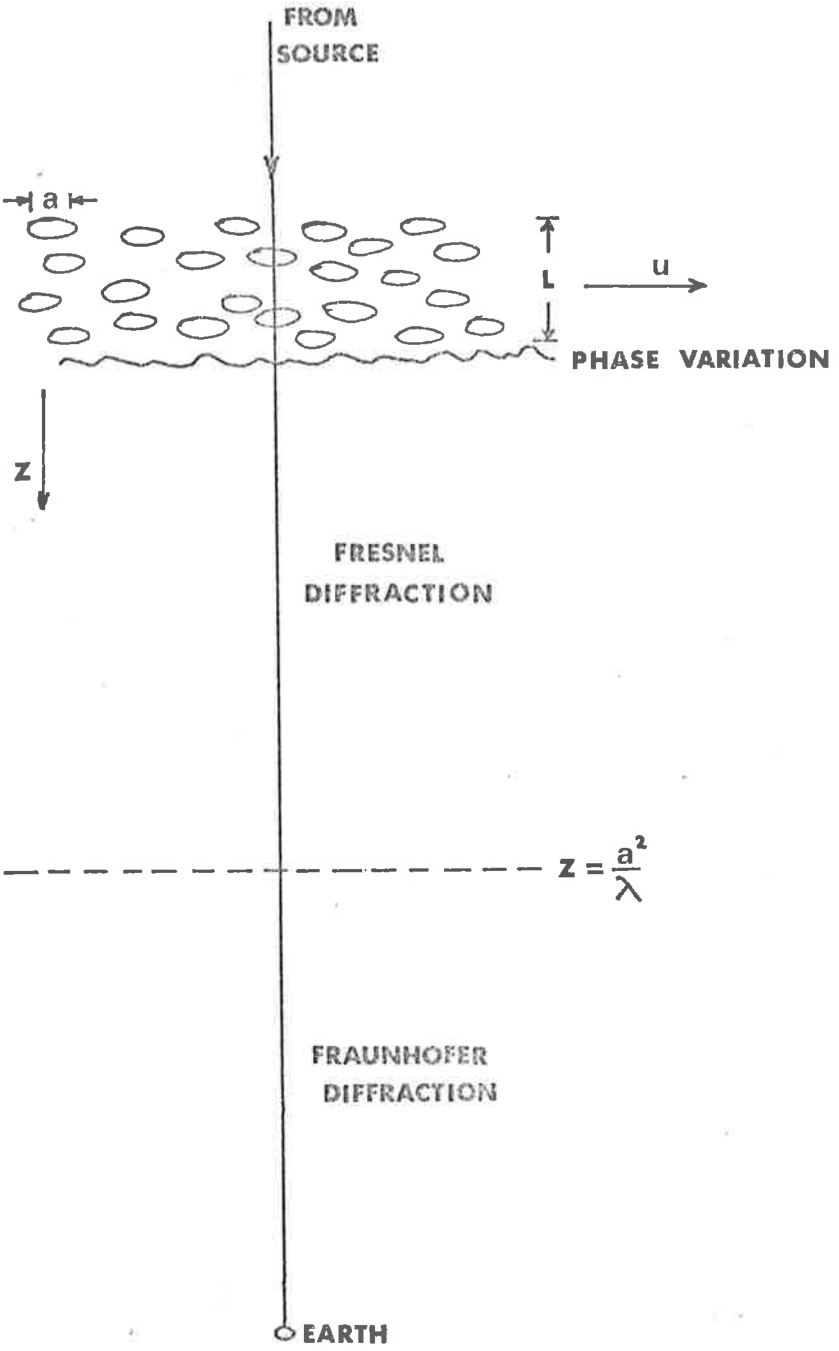
FROM
SOURCE
a
L
u
PHASE VARIATION
Z
FRESNEL
DIFFRACTION
$Z = \frac{a^2}{\lambda}$
FRAUNHOFER
DIFFRACTION
EARTH

Figure 1.1 Parameters associated with scattering and diffraction in the interplanetary medium

The value of ϕ_o, the rms phase deviation is given by (Bramley, 1954, 1955)

$$\pi^{\frac{1}{4}} r_e (aL)^{\frac{1}{2}} \lambda \Delta N_e,$$

where r_e is the classical radius of the electron. If $\phi_o < 1$ and L is not too large so that multiple scattering can be neglected, the emergent wave can be considered as consisting of an unscattered component plus an angular spectrum of scattered radiation occupying a cone of angle $\theta_o = \frac{\lambda}{a}$. If L is large or $\phi_o > 1$ then we have strong scattering and all the radiation is scattered into a cone whose angle is given by $\theta_o \simeq \frac{\lambda}{a} \sqrt{2}\, \phi_o$. Coronal broadening is the observation of this angular spectrum of the scattered radiation usually with an interferometer, and in most cases when $\phi_o > 1$ so that $\theta_o \propto a^{\frac{1}{2}} \Delta N_e$. The visibility of the interferometer fringes is reduced by the apparent increase in angular size of the source.

Interplanetary scintillation is observed as the interference pattern of this scattered radiation. Because of the random nature of the imposed phase variations the interference pattern will also be random. Usually the intensity of the pattern is recorded as it is swept across a receiving site by the motion of the solar wind. Since interplanetary scintillation is a diffraction phenomenon both the parameters of the medium or screen and the position of the observer with respect to this screen govern the nature of the observed scintillation. In addition the intrinsic structure of the source emitting the radiation also has an effect on the received signal.

Indicated in Figure 1.1 are the two main regions of diffraction. Just beyond the screen is the Fresnel zone ending when the distance from the screen $Z \doteq Z_F$ $(= \frac{a^2}{\lambda})$, the Fresnel distance for irregularities of scale a and observing wavelength λ. Beyond Z_F lies the Fraunhofer zone.

On emerging from the screen or scattering layer the variations across the wavefront are purely phase variations. However, at increasing distances from the screen the scattered components progressively lose their phase relationship with the main (unscattered) component of radiation, gradually building up amplitude variations until, at the Fresnel distance Z_F, approximately equal power is contained in both the phase and amplitude components. Beyond Z_F the amplitude fluctuations are saturated.

It can be seen that the most widely scattered components will lose their phase relationship first and produce amplitude fluctuations of a much smaller scale than the electron density irregularities. However, at greater distances from the screen larger components will be introduced until in the Fraunhofer region, provided the scattering is weak the scale of the intensity fluctuations reaches a constant value equal to the scale of the irregularities. It follows that power spectra of scintillation within the Fresnel region under conditions of weak scattering must exhibit a lack of power at low spatial frequencies. In other words the fact that interplanetary scintillation is a diffraction phenomenon means that irregularities of scale greater than $\sim\sqrt{Z\lambda}$ do not contribute to the intensity pattern observed at a distance Z. This is the radius of the first Fresnel zone for the given distance.

When interplanetary scintillation is observed simultaneously at two frequencies there may be some correlation between the two signals depending on various parameters. Budden (1965) has studied the case for a weakly scattering thin screen and Bakhareva (1959) has investigated the case when the observer is immersed in the screen. The two treatments give essentially the same results. Salpeter (1967) has discussed the strong scattering case. For weak scattering the cross-correlation ρ is always high (and $\lesssim 1$) in the Fresnel region whereas in the Fraunhofer region it is high provided the following condition holds,

$$\frac{\Delta f}{f} \lesssim \frac{2\pi a^2}{Z\lambda}$$

where f and f + Δf are the two observing frequencies. For a thick region L >> a and ρ approaches some value less than unity.

In the case of strong scattering when $\phi_o > 1$, the cross-correlation is high in the Fresnel region for

$$\frac{\Delta f}{f} < \phi_o^{-\frac{1}{3}},$$

and high in the Fraunhofer region if

$$\frac{\Delta f}{f} < \frac{2\pi a^2}{\phi_o{}^2 Z\lambda}.$$

The above considerations are also important for correlation of signals across a receiver bandwidth. Theoretical investigations on this aspect have been carried out by Little (1968) and Budden and Uscinski (1970, 1971).

The discussion so far has been concerned with radiation emitted from a point source. If, however, the source has finite dimensions it can be considered as a group of point sources and the resulting diffraction pattern the sum of the diffraction patterns from each of these points. Each pattern is of course slightly displaced from the other patterns and their addition results in the blurring of the scintillation. If the angular dimensions of the source are large (>> 1") no scintillation is observed at all. Little and Hewish (1966) derived the following results for a source of finite size. If a' is the pattern scale from an ideal point source, then the scale of the scintillation from a circular Gaussian source of diameter ψ is given by $a' \left[1 + 2 \left(\frac{Z\psi}{a'}\right)^2\right]^{\frac{1}{2}}$. Other parameters such as the scintillation index m, the width of the angular spectrum θ_o and the frequency cross-correlation are also affected. It can be seen that the smearing increases with distance from the screen. Therefore for a source of finite angular dimensions the intensity fluctuations build up until the Fraunhofer region is reached and then gradually disappear as the waves

	Weak Scattering $\phi_o << 1$		Strong Scattering $\phi_o >> 1$	
	Fresnel	Fraunhofer	Fresnel	Fraunhofer
Scale of pattern a'	$< a$	a	$\propto \lambda^{-n}$	$\frac{a}{\sqrt{2}\,\phi_o}$
Width of angular spectrum Θ_o	$\frac{\lambda}{a}$	$\frac{\lambda}{a}$	$\sqrt{2}\,\phi_o\,\frac{\lambda}{a}$	$\sqrt{2}\,\phi_o\,\frac{\lambda}{a}$
Scintillation index m	$\propto \lambda^2$	$\sqrt{2}\,\phi_o$	$\gtrsim 1$	~ 1
Intensity probability distribution	Gaussian	Gaussian	Skewed	Exponential
Upper limit of $\frac{\Delta f}{f}$ for good cross-correlation	~ 1	$2\pi\,\frac{a^2}{\lambda z}$	$\phi_o^{-\frac{1}{3}}$	$\frac{2\pi}{\phi_o^2}\,\frac{a^2}{\lambda z}$

Table 1.1

propagate further towards the observer.

A summary of the basic properties of interplanetary scintillation observed with a point source under different scattering conditions is presented in Table 1.1. This summary is based on previous references.

1.3 Coronal Broadening

A paper published in 1951 by Machin and Smith suggested that the radiation from an extra-terrestrial radio source might be completely cut off by refraction within the outer corona of the sun. To test this hypothesis the Crab Nebula which, during June, passes within 4.6 $R_\odot$ of the sun was chosen for observation. Initial attempts to obtain an interferometric record of the source were hampered by solar activity, but during the following year (Machin and Smith, 1952), successful recordings were obtained at 38 and 81.5 MHz. The visibility of the interferometer fringes at both frequencies was found to gradually decrease within about 10 $R_\odot$ from the sun. Link (1952) had theoretically derived the expected change in source intensity basing his calculations purely on refraction within the solar corona. The observations, however, did not agree entirely with this simple model, in particular with its strong dependence on the observing wavelength. Machin and Smith concluded that their observed decrease in fringe visibility was due to either a genuine reduction of the flux reaching the earth or an increase in the apparent angular size of the image resulting from scattering of the radiation on passing through the solar corona. Hewish (1955) further investigated the phenomenon by observations of the Crab Nebula during the following year at the same frequencies but on more than one interferometer baseline. Hewish discounted absorption and refraction as single causes of the effect and showed that a theory of Fejer (1954) on weak ($\phi_o < 1$) isotropic scattering of radio waves by an irregular plasma was able to account for the observations. Actually the theory depends on whether the total phase deviation after traversing the scattering region is less than or greater than 1 radian. In the former case the observed radiation would consist of a specular (unscattered) component plus a scattered component giving the source image a halo appearance. The other case in which all the radiation becomes scattered gives the appearance of a completely broadened source. Calculations by Hewish revealed that this second case fitted the observations, and a lower limit was placed on the size and density fluctuation of the irregularities responsible for the scattering. Under conditions when the phase deviation produced by a single irregularity is greater than 1 radian, Frejer's theory is no longer valid and Chandrasekhar's (1952) ray theory may be used. Hewish was therefore able to tabulate, for distances 5 - 15 $R_\odot$ from the sun, a range of electron densities and irregularity sizes to an upper limit of 10^5 km which were based on the extrapolation of visible coronal rays. Vitkevitch (1955) also came to similar conclusions that the coronal broadening was a strong scattering effect.

In a later paper Hewish (1958) examined interferometer measurements at different frequencies taken over a number of years and found that the angle of scattering scaled as the square of the wavelength. Vitkevitch (1955) had also concluded this and Erickson (1964) by combining the observations of different authors confirmed the relation over the frequency range 26 MHz to 170 MHz, indicating that strong scattering was still predominant at the higher frequencies.

Anisotropy in the shape of the image became apparent with Hewish's (1958) data obtained from interferometers at different position angles. By using three baselines the elongation and orientation of the image were estimated, assuming a simple elliptical Gaussian model for the image distribution. There was a tendency for the image to be elongated and oriented tangentially to the radial direction from the sun. Vitkevitch (1958) had also noted this. Slee (1959) using fan beam and pencil beam antenna systems as well as an interferometer, found that the broadened image was skewed towards the sun and in some cases a secondary peak appeared on the side of the image nearest the sun. He interpreted this as evidence for the presence of a large refracted component. Hewish (1958) also suggested that refraction was necessary to explain the intensity variation of some of his results. This was based on an isotropic scattering model but later Högbom (1960) showed that scattering in an anistropic medium explained the observations without invoking refraction. In the light of all subsequent observations it would appear that the secondary response observed by Slee might have been a spurious effect, rather than evidence for refraction, possibly related to solar activity.

The variation of the scattering with radial distance from the sun has been one of the main topics of discussion in the literature on coronal broadening. In the earlier papers (e.g. Slee, 1961; Hewish and Wyndham, 1963; Erickson, 1964), attempts were made to fit the observed scattering angles to power law variations with distance from the sun. However, discrepancies arose between the results of different authors. One cause of this was the solar cycle variation which affects the scattering at all heliocentric distances. In fact plots of the scattering angle at a given distance correlate well with the smoothed sunspot number (Hewish, 1958; Vitkevitch, 1960; Okoye and Hewish, 1967; Matheson and Little, 1971). An error common to earlier papers was to combine different phases of the solar cycle into a single plot and to estimate the power law variation of this, giving misleading results. Also the scattering anisotropy mentioned earlier is an important consideration when only one interferometer was used since different cross-sections of the elongated image would be measured as the source moved past the sun. For instance, Slee (1966) found agreement between his results and those of other observers when these effects were taken into account. One remaining effect which has been investigated in detail by Okoye and Hewish (1967) is the tendency for the power law index to vary with distance from the sun. These authors observed various sources including the Crab Nebula and 3C123 over a wide range of heliocentric distance (10 - 100 $R_{\odot}$). The observed scattering angles (in the radial direction to the sun) combined with values from previous years revealed a gradual decrease in the power law index with increasing distance from the sun. The effect of different phases of the solar cycle was merely to shift the complete scattering curve up or down leaving its general shape the same. Therefore, over large distances the simple power law model broke down. Now an extrapolation of Blackwell and Petford's (1966) optical data ($N_e \propto R^{-2.3}$) to spacecraft data at the Earth shows good agreement, and assuming $N_e \propto R^{-2.3}$ at all distances from the sun and using Högbom's (1960) conclusion that the scattering follows variations in the electron density, the scattering should also vary as $\sim R^{-2}$. This was not the case and Okoye and Hewish (1967) suggested that plasma instabilities might be responsible for producing extra irregularities away from the sun causing a reduction in the power law index. The possibility of plasma instabilities had in fact been pointed out in the early theoretical models of the solar wind by Parker (1958). Hewish and Wyndham (1963) had previously attempted to solve the problem by suggesting that the solar wind converged towards the solar equator. However, the instability proposal was far more attractive since interplanetary scintillation revealed structure on a very small scale, $\sim$100 km, close to the ion gyro-radius in the medium (Hewish, Dennison and Pilkington, 1966), thus supporting the instability model. The concept of instabilities in the solar wind brings us to the discussion of the actual size and nature of the scattering irregularities. Hewish (1955) placed an upper limit of 10^5 km on the size of the irregularities, as well as, from scattering theory, a very small lower limit. Later Hewish and Wyndham (1963) improved the estimate to give an upper limit of 5000 km at 60 $R_\odot$, and suggested the irregularities might originate from the granular structure in the photosphere. This was the best that could be established from coronal broadening measurements.

A major difficulty which was never completely resolved with interferometric measurements was the restriction mentioned earlier in which only cross-sections of the brightness distribution could be measured. As early as 1958 Hewish found evidence that the scattering irregularities might be filamentary and aligned along the solar magnetic field lines. Further evidence has been given by Högbom (1960), Gorgolewski and Hewish (1960) and Hewish and Wyndham (1963). Results of this nature, however, have been rather marginal as to the true orientation of the irregularities or the 'frozen in' field lines. In fact Erickson (1964) concluded that the field lines were rather randomly orientated with only a slight radial preference. On the other hand spacecraft data have indicated a filamentary structure for the magnetic field (Ness, Scearce and Cantaro, 1966), with an orientation conforming to the spiral pattern predicted by Parker (1958). The anisotropy or filamentary nature of the scattering irregularities appeared to be reduced during sunspot minimum (Slee, 1966; Okoye and Hewish, 1967). In addition Slee found that his observations between 20 and 80 $R_{\odot}$ during 1960 and 1962 (near solar minimum) indicated that the scattering tangential to the solar magnetic field decreased with the decline in the solar cycle while the radial component remained approximately constant.

At this point it is appropriate to discuss the actual shape of the scattering corona, that is the shape of the contours of constant scattering. Okoye and Hewish (1967) observed a decrease in scattering with increasing heliocentric latitude. Other authors (Vitkevitch, 1958, 1960; Slee, 1961, and Hewish and Wyndham, 1963) have found that surfaces of constant average scattering were approximately ellipsoidal with major axes coincident with the solar equator. Erickson (1964), observing the Crab Nebula from 1959 to 1961, found no difference between approach and recession and assumed an almost spherical corona. However, Slee (1966) estimated an axial ratio of 1.7 for much the same period, indicating both the uncertainty of the data, in particular the difference between the radial and tangential scattering, and that no significant change in the shape of the scattering corona occurred between 1960 and 1962 despite a considerable reduction in the level of solar activity.

As mentioned previously refraction was at first thought to be a significant component (Hewish, 1958) to account for the observed variation in intensity of the Crab Nebula as it passed close to the sun. This was overcome by Högbom (1960) by taking into account scattering anisotropy. Erickson (1964) also calculated the variation in integrated intensity (at 26 MHz) for isotropic, tangential and radial scattering. In addition the brightness distributions were calculated in each case. Since actual two-dimensional brightness distributions were unattainable little was gained from estimating these at the time but the integrated intensities were of interest. They all showed an increase in intensity before the decrease at closest approach, an effect which has never been observed, indicating that the simple model does not completely explain the true variation in intensity. A recent paper by Bliokh, Sinitsyn and Fuks (1969) has predicted, using a more complex approach, the same form of intensity variation. The actual scattering and refraction processes at these lower frequencies and close to the sun might be more complicated than these authors have assumed.

Erickson (1964) remarked on the difference he observed between the variation in total flux during approach and recession of the source and the results of other authors (Slee, 1961; Vitkevitch, 1960) which showed opposite differences. Erickson supposed that another large scale component of scattering might exist to explain the results. However, Erickson observed during 1960-1962 while Slee and Vitkevitch observed prior to this nearer the previous sunspot maximum. This could account for the differences.

Recently, theoretical work by Hollweg and Harrington (1968) and Hollweg (1970) has sought to obtain a better understanding of the variations of the parameters of the interplanetary medium by developing a model and fitting it to the coronal broadening observations. The latter paper deals with a modified power law structure for the electron density variations to agree with spacecraft observations of the magnetic field. In both papers several interpretations of the solar wind parameters are possible, and new information on the solar wind properties can only be derived when simultaneous observations of the changes in frequency or phase of a coherent signal are available.

Since the initial observations of the angular broadening of the Crab Nebula, work continued in the field mainly using interferometers but occasionally fan beams and pencil beams. The true shape and orientation of the image had not been recorded until 1969 when Harries, Blesing and Dennison (1970) published the results of two-dimensional observations of the broadened image of the Crab Nebula. This has opened a new avenue in the study of coronal broadening and should bring back renewed interest in this field.

1.4 Interplanetary Scintillation

During a 178 MHz survey of radio sources conducted at Cambridge, U.K., it was noticed that certain sources exhibited random fluctuations in intensity similar to ionospheric scintillation but of a much smaller (1-2 sec) period (Hewish, Scott and Wills, 1964). The fluctuations were peculiar to sources of very small angular diameter < 1" arc (mainly quasars) and it was concluded that they were not of ionospheric origin but resulted from scattering by irregularities in electron density in the solar wind. The phenomenon was therefore called interplanetary scintillation. More extensive observations of several of these sources, in particular 3C48 which was known to have small angular dimensions (Allen et al., 1962), immediately revealed a strong heliocentric dependence of the scintillation as well as suggesting a dependence on source dimensions. The scintillation index of 3C48 was observed to increase as the source moved closer to the sun. Simultaneously, the signal was observed to fluctuate more rapidly at greater heliocentric latitudes. The observations suggested that a much smaller irregularity scale might exist in the interplanetary medium compared to the upper limit of 5000 km previously suggested by angular broadening measurements. The usefulness of interplanetary scintillation as a tool for estimating parameters of the medium and of the radio sources was at first in doubt since angular broadening measurements had indicated that the rms phase deviation might be too large. However, Little, Hewish and Dennison (1966) showed that there was good correlation between scintillation at 81.5 and 178 MHz at a distance of 0.5 A.U. from the sun, and concluded that the medium constituted a weak scattering region. This conclusion arose because the ratio of indices was approximately equal to the ratio of recording wavelengths and the cross-correlation between the signals was good (∿0.6) implying similar pattern scales. The authors discussed the cross-correlation expected from different scattering models and concluded that a pattern scale of 300-400 km was required. This estimate was somewhat larger than other estimates of the scale (∿150 km) by Hewish, Scott and Wills (1964), Hewish, Dennison and Pilkington (1966) and Dennison and Hewish (1967), using one, two and three receiving sites respectively. Little, Hewish and Dennison also pointed out that the irregularity size ∿100 km was close to the proton gyro-radius under typical conditions in the interplanetary medium and that irregularities of this size might be expected as a result of plasma instability.

A systematic method of estimating the angular structure of radio sources was developed by Little and Hewish (1966), and the results of a survey were presented in a following paper, Little and Hewish (1968). These authors derived factors representing the effect of different source shapes on the observed parameters of the medium compared with the point source values. The formula was introduced in Section 1.2 for a circular Gaussian source. Other forms such as an elliptical Gaussian source, a double point source and a core halo source were also treated and the corresponding factors derived. To use this method, values of the scintillation index (m) and the diffraction pattern scale (a') for a point source must be known. For this purpose some very strongly scintillating sources were chosen (3C138, 3C237, 3C119 and 3C147). From their observations, over a sufficiently long period, a series of contours of m and a' were constructed around the sun assuming m increased to unity near the sun. By comparing the values of m and a' from other sources, estimates of their angular structure were deduced. A large number of the sources observed in their survey showed similar variations of m with distance from the sun compared to a point source but with an overall reduced magnitude. This was interpreted as indicating two components, one small and scintillating and the other large and non-scintillating. The ratio of m to the index for a single point source is equivalent to the ratio of the fluxes of the two components.

The construction of three receiving sites at Cambridge, U.K. enabled more detail to be deduced about the diffraction pattern and hence about the medium itself (Hewish and Dennison, 1967; Dennison and Hewish, 1967; Dennison, 1969). The source 3C48 was observed and the speed and direction of motion of the pattern was determined from full correlation analysis (Briggs, 1968a, 1968b). During the period of observation the source covered a reasonably wide range of heliocentric distance and latitude, and the velocity of the diffraction pattern was estimated to be 300 km sec^{-1} near the ecliptic increasing to 450 km sec^{-1} over the north solar pole. Since the observations were within the Fraunhofer region it was possible to directly relate the observed parameters of the diffraction pattern to the electron density irregularities in the solar wind. The irregularity scale was found to vary with heliocentric distance from 160 km at 0.9 A.U. to 100 km at 0.35 A.U. The observed anisotropy of the diffraction pattern indicated that the plasma irregularities were elongated by a factor of about 2:1 along the direction of motion, which was always closely radial to the sun. Large day to day variations in the scintillation index were noted and on one occasion a very large change in index was believed to be related to a stream of plasma ejected from an active region on the sun.

Cohen (1965) began investigations at Cornell but was confined to a single receiving site in using the Arecibo 1000 ft reflector and he therefore concentrated more on the statistics of scintillation such as the power spectra and intensity probability distributions. Preliminary angular diameter estimations at a single site were described in another paper (Cohen et al., 1966). Just as the scale of the pattern increases for an extended source, the power spectrum width f_2 $(\simeq \frac{u}{2\pi a'})$ decreases. This method relies on the velocity u being constant.

Cohen, Gundermann, Hardebeck and Sharp (1967) have discussed in detail some of the Arecibo results at 195, 430 and 611 MHz in terms of different diffraction regimes as shown in Figure 1.2. It is possible, by examining the scintillation index, power spectrum and intensity probability distribution, to place the observations in a particular position on the regime diagram, although there is a certain amount of unavoidable uncertainty inherent in results of observations from a single site. The irregularity scale was estimated to be about 100 km (assuming a velocity of 350 km sec^{-1}) at 0.5 A.U. in agreement with the Cambridge observations. The phase deviation ϕ_o was estimated from the variation of the scintillation indices with solar elongation. These authors deduced weak scattering beyond 0.5 A.U. and estimated the electron density variation to be about 2-3% of the ambient density over the range 0.2 to 0.9 A.U. from the sun.

In the weak scattering, Fresnel regime low frequency dips in the power spectra of the scintillation are expected. These were not seen at first and it was suggested that the general variability of the velocity and its varying projection along the line of sight would fill in the dips. However, dips have since been observed by Dennison and Wiseman (1968) and by Cohen and Gundermann (1969) although under very special conditions. Further Arecibo observations were reported by Sharp and Harris (1967) who found large increases in scintillation index and spectral widths on March 27th and 31st, 1966. They associated these with the ejection of plasma from a solar active region on which strong flare activity was reported. In concluding they suggested that careful

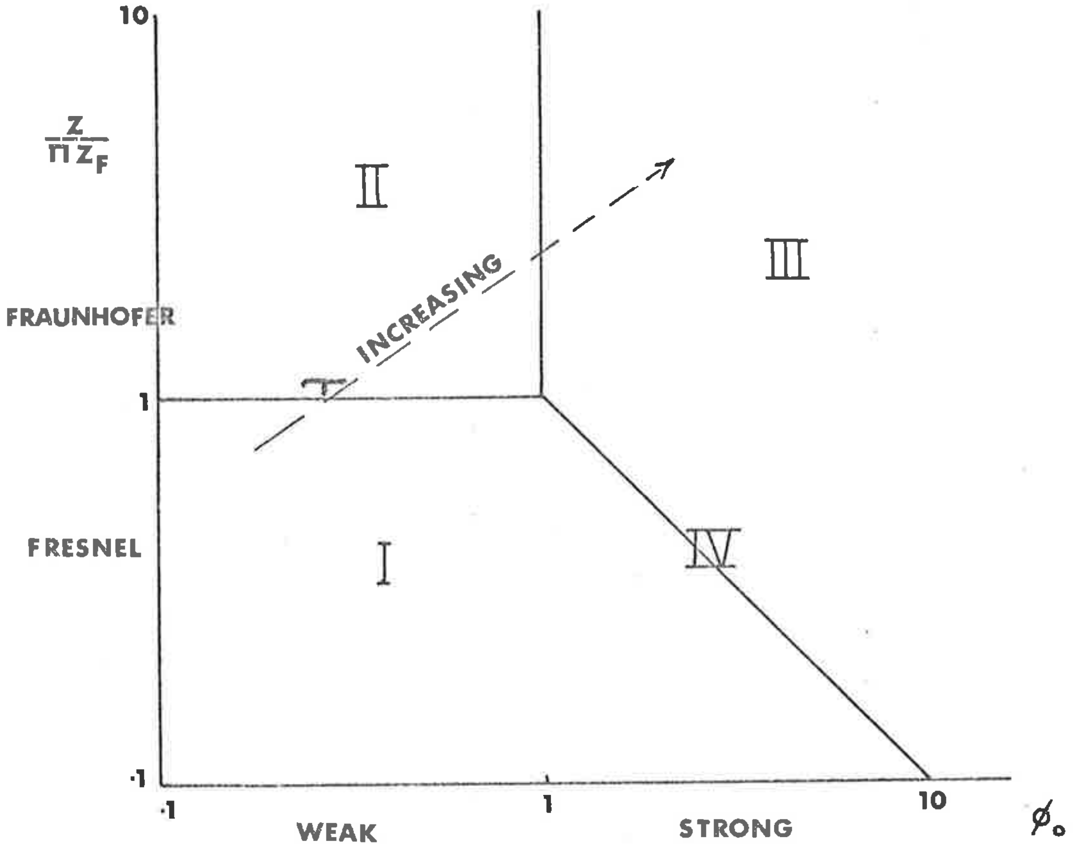
10
$\frac{z}{\pi z_F}$
II
INCREASING
III
FRAUNHOFER
λ
1
FRESNEL
I
IV
·1
·1
1
10
ϕ_o
WEAK
STRONG

Figure 1.2 Scattering regime diagram. The broken line represents observations at different wavelengths but under the same scattering conditions

monitoring of a grid of sources could provide a useful tool for investigating the effects of solar activity on the interplanetary medium.

An extensive angular diameter survey described by Cohen, Gundermann and Harris (1967) was in fair agreement with the results of the survey by Little and Hewish (1968) although, as mentioned earlier, different methods were employed. Cohen et al. also found sources which fitted the model of a small diameter scintillating component associated with a larger diameter, non-scintillating component. Another survey was carried out by Harris and Hardebeck (1969) who examined a large number of sources north of the ecliptic and obtained statistical information on the structure and degree of scintillation of these sources.

To investigate scintillation near the sun, but to avoid diameter blurring, Cohen and Gundermann (1967) observed the source 3C279, which passes within 1 $R_\odot$ of the sun at wavelengths of 21 and 11 cm. Recordings were characterised by short term bursts of scintillation. On the 9th of October when 3C279 was 2.6 $R_\odot$ from the sun, the 11 cm signal was analysed to reveal a power spectrum width of about 6.1 Hz while the 21 cm signal showed only very weak scintillation. This implied an angular diameter $\sim$0.02" arc assuming a velocity $u = 350$ km $\sec^{-1}$. However, the presence of an extended tail out to 25 Hz on the spectrum indicated a component of the source with a diameter $\sim$0.005" arc. The extended tail was believed to be caused by short bursts of scintillation but might also have been related to an enhanced background of solar noise which they noted was prevalent during the observations. A much more detailed description of short wavelength measurements between 4 and 35 $R_\odot$ is given by Cohen and Gundermann (1969). The scintillation indices were found to peak at about 8-10 $R_\odot$ and the spectral widths increased until about the same distance from the sun. Occasionally the power spectra exhibited a definite dip at low frequencies but these were not commented on although in all cases the results were interpreted as being in the Fraunhofer zone. Using the Parker model of the solar wind, in which the velocity increases from 50 km sec^{-1} at 3.5 $R_\odot$ to 300 km sec^{-1} 30 $R_\odot$ to 490 km sec^{-1} at 1 A.U., they derived the scale of the electron density irregularities (for weak scattering at distances > 10 $R_\odot$). The calculated scale increased from 10 km at 10 $R_\odot$ to 120 km at 1 A.U. From the scintillation index curve for 3C279 against distance from the sun, a component diameter of ∿0.002" was inferred. The spikes observed close to the sun were explained as focussing spikes produced by filamentary structures ∿400 km acting as individual lenses and travelling faster than the background solar wind. Golley and Dennison (1970) have also found evidence for velocity dispersion but at distances greater than 0.3 A.U., deduced from observations of 3C48 at 81.5 MHz. Recently Ekers and Little (1971) have, at 2296 MHz, found turbulence in the corona out to 30 $R_\odot$ which could also account for the high frequency tail on the observed power spectra.

The focussing spikes are consistent with observations in region IV on the regime diagram illustrated in Figure 1.2. Theoretical treatment of scintillation under these conditions has been carried out by Mercier (1962), Bramley and Young (1967) and Buckley (1970, 1971). However, the measurements by Cohen and Gundermann were thought to lie in regimes II and III (Fraunhofer region), so that larger and faster irregularity 'lenses' than actually required by the observations were postulated.

The relation between solar activity and scintillation has been further clarified by observations at Culgoora, N.S.W. (Dennison and Wiseman, 1968; Wiseman and Dennison, 1972). These authors have traced the movement of corotating plasma streams and 'blasts' from individual strong flares through the medium, by monitoring their effects on the scintillation of a 'grid' of radio sources. Other effects of solar activity which appear to be related to scintillation have been noted by Burnell (1969) and Houminer (1971). These types of observation provide detailed information about the large scale structure of the interplanetary medium over a much wider range of heliocentric coordinates than at present available to space probes.

Some different information was supplied by Slee and Higgins (1968) when they observed interplanetary scintillation of radio emission from Jupiter at 19.7 MHz. They deduced a solar wind speed of about 600 km sec^{-1} with an irregularity scale of 150 km sec^{-1}. Also, for the first

?

time, phase measurements of the diffraction pattern were obtained.

Recently attempts have been made to explain interplanetary scintillation in terms of the observed modified power law spectra of the magnetic field irregularities detected by spacecraft. Papers concerning this aspect have been published by Jokipii and Hollweg (1970), Buckley (1971), Hewish (1971), Hollweg and Jokipii (1971) and Little (1971). Although the situation is still not fully resolved the concensus appears to be towards regarding scintillation as caused by a small scale plasma structure, not much larger than the ion gyro-radius, quite distinct from the much larger scales detected by spacecraft in the form of a turbulence spectrum for the magnetic field fluctuations. Cronyn (1970) has proposed a theory in which he begins with a modified power law structure for the irregularities and results in a power law spectrum for the interplanetary scintillations. He adcpts this approach on the grounds that many power spectra which have been referred to as Gaussian in shape could be fitted just as well to a power law. In fact some observers (Lovelace, Salpeter, Sharp and Harris, 1970) noticed that the high frequency part of their spectra often conformed to a power law variation with frequency suggesting that Cronyn's approach may be an important step in understanding the detailed shape of scintillation power spectra. The final clarification of the relation between the spectra of magnetic field fluctuations and the spectrum of the electron density fluctuations which cause scintillation, must however await direct measurements by spacecraft of the electron density spectra out to the high spatial frequencies which correspond to the observed scintillations. This in turn requires a considerable increase in the sampling rates currently available in the plasma probes carried by spacecraft.

1.5 Ionospheric Refraction in Radio Astronomy

The effects of ionospheric refraction on radio source positions are of interest to all persons concerned with accurate position measurements of radio sources at metre wavelengths, and accurate methods to correct for this are clearly desirable. Large ionospheric gradients may be determined approximately from spaced ionospheric sounders, but there exist rapidly varying components which cannot be allowed for in this way. Ionosondes, however, only provide information up to the point of reflection in the ionosphere. Swept frequency sounders therefore provide information up to the F2 peak and the shape of the ionosphere above this point must be assumed. An attempt to gain information about the complete ionospheric profile was made by Kerr, Shain and Higgins (1949) in Australia, by reflecting 17.84 MHz signals from the moon. The most interesting characteristic of the reflections was a wide variation in amplitude with periods of 5 - 20 min.

Smith (1952a) discussed the various techniques in use at the time for determining positions of radio sources. In an appendix he considered the effects of the ionosphere classifying them under steady refraction, due to the approximately spherical shape of the ionosphere, and wedge components due to local gradients in the electron density causing departures from spherical symmetry. In a following paper, Smith (1952b) discussed exclusively refraction of 81.5 MHz radiation from radio stars. The apparent regular movement of the source positions was ascribed to regular wedge refraction and the results were compared with the knowledge of the ionosphere from pulsed soundings. Some of the observations exhibited short term position fluctuations with periods ∿20 min and magnitudes equivalent to steady wedge components which varied during the day. These records were discarded and the remainder were compared with expected source displacements calculated from the ionosonde data. Some agreement was observed between the theoretical and the observed displacements. Komesaroff and Shain (1959), and Komesaroff (1960), developed improved formulae for both spherical refraction and steady wedge refraction, although their work is, strictly, applicable only to source positions at transit. Examples of corrections to some position measurements at 19.7 MHz were given. Although the scatter of positions was considerably reduced, there still remained a significant component of refraction which could not be removed in this way - the irregular wedge refraction. Clarke (1964) attempted to correct source positions from some surveys conducted in the U.K. She developed a more general (but slightly less accurate) formula than Komesaroff, allowing reasonable corrections for observations at any declination or hour-angle. These corrections were based on ionosonde data and certain assumptions about the ionosphere, and allowed an estimate of the expected steady wedge refraction to be made. An example of the irregular refraction observed at 81.5 MHz was shown and it appeared to have a pseudo-period of $\sim$20 min and a maximum value $\lesssim$ 1' arc. Travelling Ionospheric Disturbances (Munro and Heisler, 1956) were suggested as a possible cause of this effect. Clarke's corrections for the steady ionospheric gradients during the different surveys at 178 MHz proved partially successful, leaving a smaller random fluctuation due mainly to the irregular refraction.

Lawrence, Little and Chivers (1964) have reviewed ionospheric refraction and note that irregular wedge refraction has been reported by Vitkevitch (1958), Vitkevitch and Kokurin (1958) and Wild, Sheridan and Neylan (1959), in addition to the authors we have already mentioned. It is clear that this type of refraction, with a period $\sim$20 min, constitutes a major problem for position measurements of extra-terrestrial radio sources and we shall refer to it again in Chapter 4.

CHAPTER 2

METHODS OF OBSERVATION

2.1 Introduction

In the previous chapter we saw how the scattering properties of the interplanetary medium have provided information not only about the medium itself but also about the structure of radio sources. Also we saw how refraction in the ionosphere has a major effect on the apparent positions of the sources.

The aim of this present work has been to provide further information in these fields of study. However, before embarking on discussions of the analysis of the data accumulated over the past four years, the different observing and recording techniques will be described. Most of the data were recorded with the radioheliograph (Wild et al., 1967) located at the C.S.I.R.O. Solar Observatory, Culgoora, N.S.W. during six observing sessions from May, 1968 to June, 1971. The remainder were obtained in January, 1968 using the 210 ft radiotelescope (Bowen and Minnett, 1963), also operated by the C.S.I.R.O., at Parkes, N.S.W. The observations may be divided into several groups but basically they fall under the main headings of coronal broadening, ionospheric refraction and interplanetary scintillation.

2.2 Coronal Broadening of the Crab Nebula - Two-Dimensional Images

Primarily the radioheliograph was built to obtain two-dimensional images of the sun at 80 MHz, although since it began operating in 1967 it has been used for many other purposes. The receiving section of the radioheliograph consists of 96 steerable, equatorially mounted, paraboloid reflectors with crossed dipole feeds, spaced evenly around a circle of 3 km diameter. Each aerial has a half-power beam-width of 20° and a range of roughly $\pm 30^\circ$ in declination and ± 2.5 hour in hour-angle.

Connecting the aerials in phase results in the formation of a beam with a power polar diagram represented by the squared Bessel function J_o^2. Introducing phase increments $\frac{2\pi k}{96}$ between adjacent aerials produces other beams represented by higher order Bessel functions, J_k^2, where k is an integer. The undesirable feature associated with the J_o^2 beam is the relatively large sidelobes, the first of which is about 15% of the main lobe. However, by adding and subtracting beams of different orders, a process known as J^2 synthesis (Wild, 1965), a polar diagram may be formed with sidelobes reduced to less than 2% of the main lobe, as shown in Figure 2.1.

By using a branching network 48 such beams are formed independently. These are aligned in a N-S direction and at zenith have a separation of 2.1' arc and a half-power beam-width of 3.75' arc. The complete process of beam forming and positioning in declination and hour-angle is achieved by electronically switching the appropriate

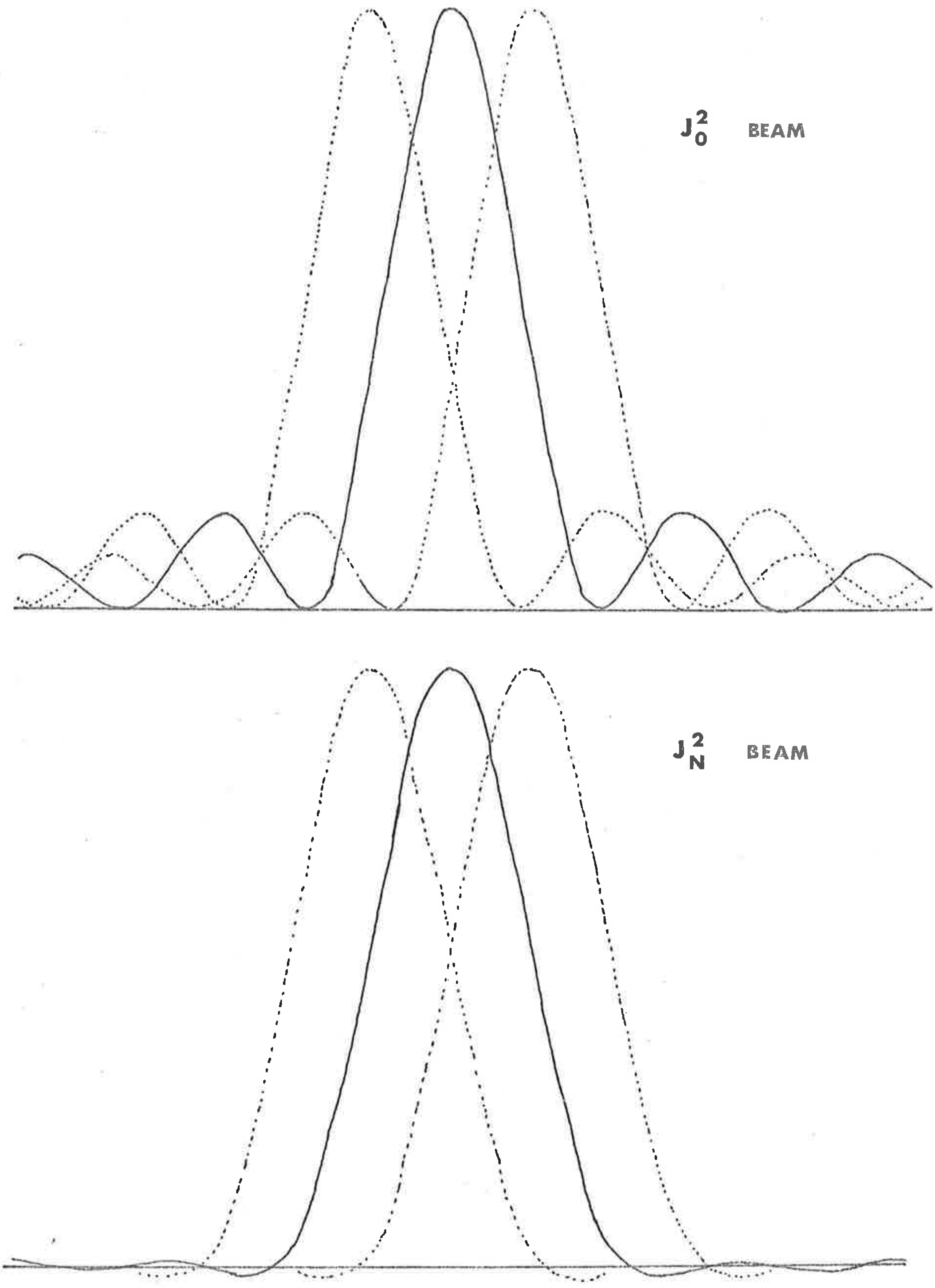

Figure 2.1 The radioheliograph beams

phase increments into the aerial feeds. In the normal mode of operation the beams are simultaneously swept from East to West across a 2° square of sky, taking up 60 positions in the time required to complete a single scan. The 48 outputs of the branching network are fed into individual intermediate frequency amplifiers with bandwidths of 1 MHz. The signals then pass to square-law detectors and integrators which perform the beam synthesis. An input to a final integrator consists of a series of signal levels from each independent beam shape required to form the synthesized beam and the output, apart from an adjustable offset corresponds to the total power received by the integrated or J_N^2 beam.

From these integrators the signals pass through a multiplexer and are recorded digitally on magnetic tape as well as being displayed on cathode ray tubes as two 48 x 60 arrays of intensity modulated points. Usually two polarisations are displayed, one on each tube, and during the recording of the Crab Nebula left and right hand circular polarisations were chosen. The integration time associated with each picture point is 8 ms, with the process of beam formation and integration taking place during this time. The picture repetition rate is normally 1 $\sec^{-1}$ but by selecting one half of the scan width a repetition rate of 2 $\sec^{-1}$ may be obtained.

Since the 96 aerials effectively constitute a ring of discrete receiving points rather than a continuous annulus, grating responses occur at specific angular distances from the central beam, In fact, the spacing of the aerials around the circle was chosen to place the first order response just outside the field of view. The height of this response is about 5% of the main lobe possibly causing confusion between nearby radio sources. Thus, in the case of the Crab Nebula data, when the sun was situated on this response, a method was used during analysis to reduce the effect on the shape of the image.

Finally, it is important to appreciate that the method of beam steering employed by the radioheliograph has an effect on the shape of the sampled section of sky as well as on the shape and widths of the beams. To bring the picture back to a right ascension (or hour-angle) - declination coordinate system the array of points must be skewed and elongated depending on the declination and hour-angle settings. The coefficients associated with this transformation, which is approximately linear over the 2° field, are called distortion coefficients.

The radioheliograph was therefore a suitable instrument for studying the increase in the image size of the Crab Nebula as it neared the sun. The angular broadening was expected to reach about 30' arc or greater, compared to the few minutes of arc resolution of the radioheliograph and so detailed measurements of the shape, size and orientation could be obtained. In addition the picture repetition rate offered an opportunity for studying short term fluctuations in the solar corona as have been reported by other authors (e.g. Slee, 1959).

Records of the angular broadening of the Crab Nebula were obtained during June, 1969, 1970 and 1971. At this time each year the line of sight to the Crab Nebula approaches the sun and reaches its closest approach on the 15th as shown in Figure 2.2. The following sub-sections describe in detail the methods adopted for each year's observations.

2.2.1 1969 Observations

During this year observations extended from the 30th May to the 24th June, and an attempt was made to record the image of the Crab Nebula at least twice a day. On those days when angular broadening was evident the number of observations was, when possible, increased to three because when nearing closest approach the image increased in size rapidly and differences were expected between separate observations on the same day. All observations on a given day were spaced as far apart as possible and the duration of each was from 5 to 10 min. A picture repetition rate of 2 sec^{-1} was normally used except when the angular extent of the image approached the edge of the picture when the full scan was used. To enable corrections to be made to the levels of the integrator outputs, 10 sec of data were recorded with a resistive load replacing each aerial. The data then consisted of a record of the DC offsets of the integrators and during analysis the pictures were

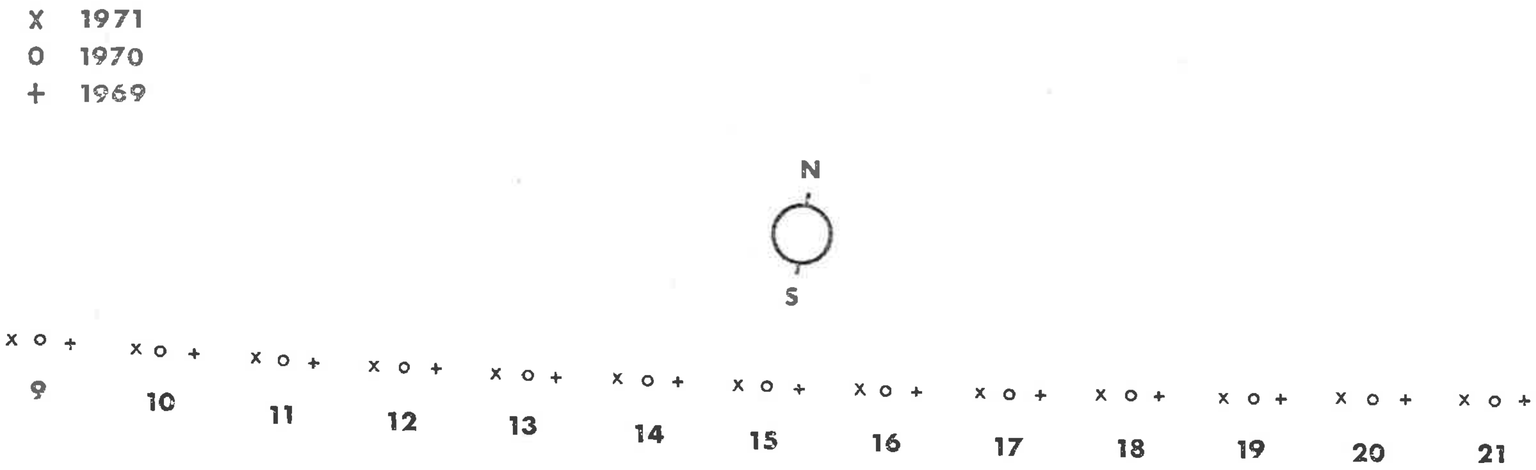
X 1971
O 1970
+ 1969
N
S
9
10
11
12
13
14
15
16
17
18
19
20
21

Figure 2.2 Positions of the Crab Nebula in relation to the sun during June

normalised by adjusting the levels of the signals from each beam according to the calculated offset differences. In addition to the Crab Nebula and resistive load data, about one minute of data were recorded from the radio source 3C123 which was nearby yet far enough from the sun to be considered unbroadened within the limitations of the instrument. Comparison of the observations of the two sources provided a means of estimating the total flux contained in the image of the Crab Nebula.

Solar bursts on occasions affected the observations by enhancing the signals received through the sidelobe structure around the actual source image and these effects were naturally more troublesome during the days of closest approach to the sun. The most reliable broadened images were recorded on the 13th, 17th and 18th June. The days leading up to and away from this period showed little or no signs of angular broadening, except on the 9th when a sporadic increase occurred, believed related to an active region on the sun. On the central days 14th, 15th and 16th June the source could not be observed probably because the broadening was so great that the signal received by each beam fell below the background noise level.

Initially all the information was recorded on large 7200 ft reels of magnetic tape and those sections required for further analysis were transferred to smaller 2400 ft tapes written in a form compatible with the computer. This editing procedure enabled the 'cleanest' data to be selected from each observation. The maximum amount of data able to be stored on a 2400 ft reel was approximately 15 min and since a limited number of reels were available, only about 10 min of data were retained for each of the days during which the image was broadened and 4 min for the remaining days. Recordings of data from the source 3C123 and using resistive loads were also transferred for each day. Finally, records were obtained in the form of photographs of the cathode ray tube display for either single frames, or series of frames integrated photographically over periods of 8 and 16 seconds.

2.2.2 1970 Observations

This observing session was conducted along similar lines to that of 1969, except that each observation of the Crab Nebula was extended over a longer period with the specific aim of detecting short term fluctuations in the solar corona. Again activity on the sun hampered observations and prevented records being obtained on every day. The session began on the 30th May and continued until the 20th June.

All the data free from effects of major solar activity were first recorded on film integrated over 8 seconds. This film was processed and carefully examined for unusual events and also for the purpose of selecting the best sections of data to transfer from the large magnetic tapes to the smaller tapes for computer analysis. As in the previous year the bulk of the data were recordings of observations when the image was broadened.

2.2.3 1971 Observations

Except for one minor radio burst the sun remained very quiet during the 1971 observations. In fact it had been exceptionally inactive over a number of rotations before June and the degree of broadening showed a definite reduction compared to the previous two years which indicated approximately equal degrees of broadening. Data were recorded from the 10th to the 19th June using the same procedures of the 1969 observations. That is, only short samples of data (∿10 min) were initially recorded at each observation of the source instead of the much longer samples recorded during 1970.

2.3 Coronal Broadening of the Crab Nebula - Drift Scans

During 1969 and 1970, as well as observing the Crab Nebula displayed as a two-dimensional picture, the method of drift scans was used to obtain a measure of the size and orientation of the image. In this method the 48 beams are fixed ahead of the source and the scanning mechanism inhibited. After the source had drifted through and had traced out the scans on paper charts the process was repeated. Pen-recorders with time constants of 2 sec were used for this purpose, simultaneously tracing the cross-sections of the image with between 3 and 9 adjacent beams depending on the degree of broadening, as illustrated in Figure 2.3. From 10 to 20 scans were recorded each day,

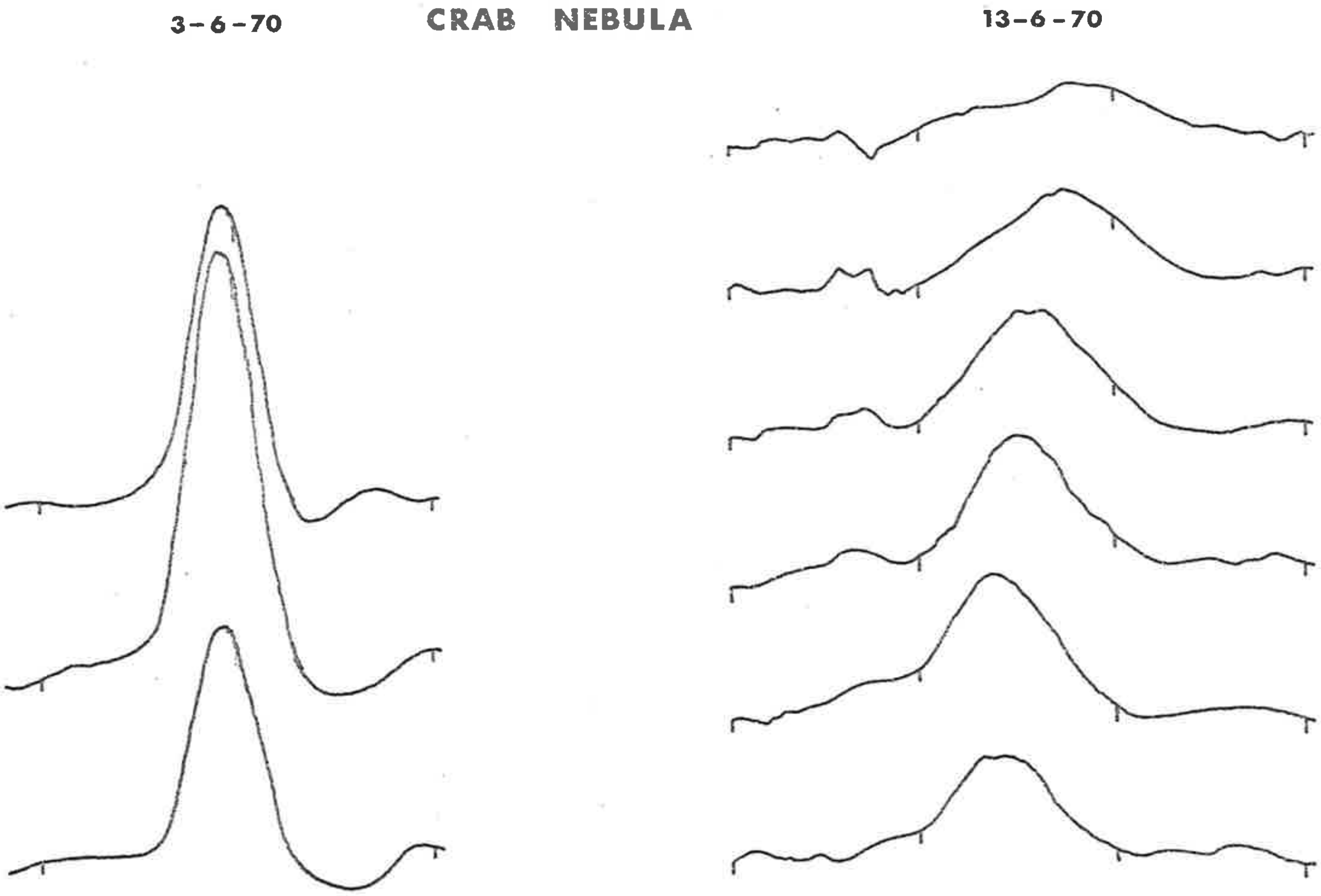

Figure 2.3 Recordings of the signals from adjacent beams from two scans of the Crab Nebula. The image was unbroadened on the 3rd and broadened on the 13th

except from the 14th to the 17th during both years when the signal to noise ratio was not great enough to allow reliable results to be obtained. This effect was due to the sun increasing the background noise. Drift scans of 3C123 were also recorded and an event during which this source showed an exceptional increase in its angular diameter occurred on the 31st May, 1969 and will be discussed in Chapter 3. A feature of the drift scans was the variability in height and width from one scan to the next. This was attributed to ionospheric scintillation.

2.4 Interplanetary Scintillation Observations at Culgoora

The observations of interplanetary scintillation were carried out as a joint project with M. Wiseman, whose part was to investigate the large scale structure of the interplanetary medium by observing a grid of about 30 radio sources known to scintillate and positioned as widely as possible over the celestial sphere. From the day to day variations in the degree of scintillation of each source, movements of large-scale structure within the solar wind could be mapped out over the period of observation. Features such as corotating streams, blast waves and sector boundaries have been detected in this manner (Wiseman, 1972; Wiseman and Dennison, 1972). The characteristics of each feature were deduced by correlating the scintillation evidence with spacecraft observations and geophysical events. It is important to note that the three-dimensional characteristics of the structure within the medium may be determined in this way whereas spacecraft data are confined to the ecliptic plane.

The second part of the project which concerned the author was to investigate the possibility of obtaining other information from the scintillation data. One aspect was the effect of the intrinsic source size and the determination of such sizes from the scintillation data. Another was to investigate the shape of the power spectra of the scintillations to obtain additional information about the nature of the scattering medium. These aspects will be discussed in Chapter 5.

We will now discuss the technique for recording interplanetary scintillation with the radioheliograph. Because the signal to noise ratio associated with the J_o^2 beam was greater than that of the synthesized J_N^2 beam, the former was used. The large sidelobes associated with this beam did not affect the observations. The only confusion that could have arisen was from the grating response, but the observed sources were well separated from other scintillating sources and this caused no problem.

Each source was examined in turn for scintillation by setting the radioheliograph beams ahead and allowing the source to drift through. The outputs of the three central beams were traced using a pen-recorder with a time constant of 0.1 sec. When no scintillation was evident on two or three scans another source was observed. If ionospheric effects were prevalent causing the apparent position of the source to move with respect to the beam positions, the outputs of six adjacent beams were recorded simultaneously and the source could then be followed from one beam to another.

When a source did scintillate during a drift scan the beams were set into a tracking mode as the source passed into the beam on the next scan. In the absence of ionospheric refraction the pen-recorder traced the intensity of the recorded signal as the diffraction pattern moved across the aerial array. An example of a drift scan and some scintillation is shown in Figure 2.4. As well as chart recordings the data were also recorded digitally on magnetic tape. Since the beams overlap, as seen in Figure 2.1, the signal appeared on two or three beams depending on the position of the source with respect to the beams. The strongest signal was selected for recording on tape and fed from the square-law detector into a differential amplifier with a time constant of 0.05 sec. It was then passed into an analogue to digital converter, which sampled the signal 32 times per second and wrote the values onto the magnetic tape.

During all observing sessions, except those in June, 1971, unwanted 50 Hz hum contaminated the digitally recorded signal. The trouble arose from the relatively long distance between the recording equipment and

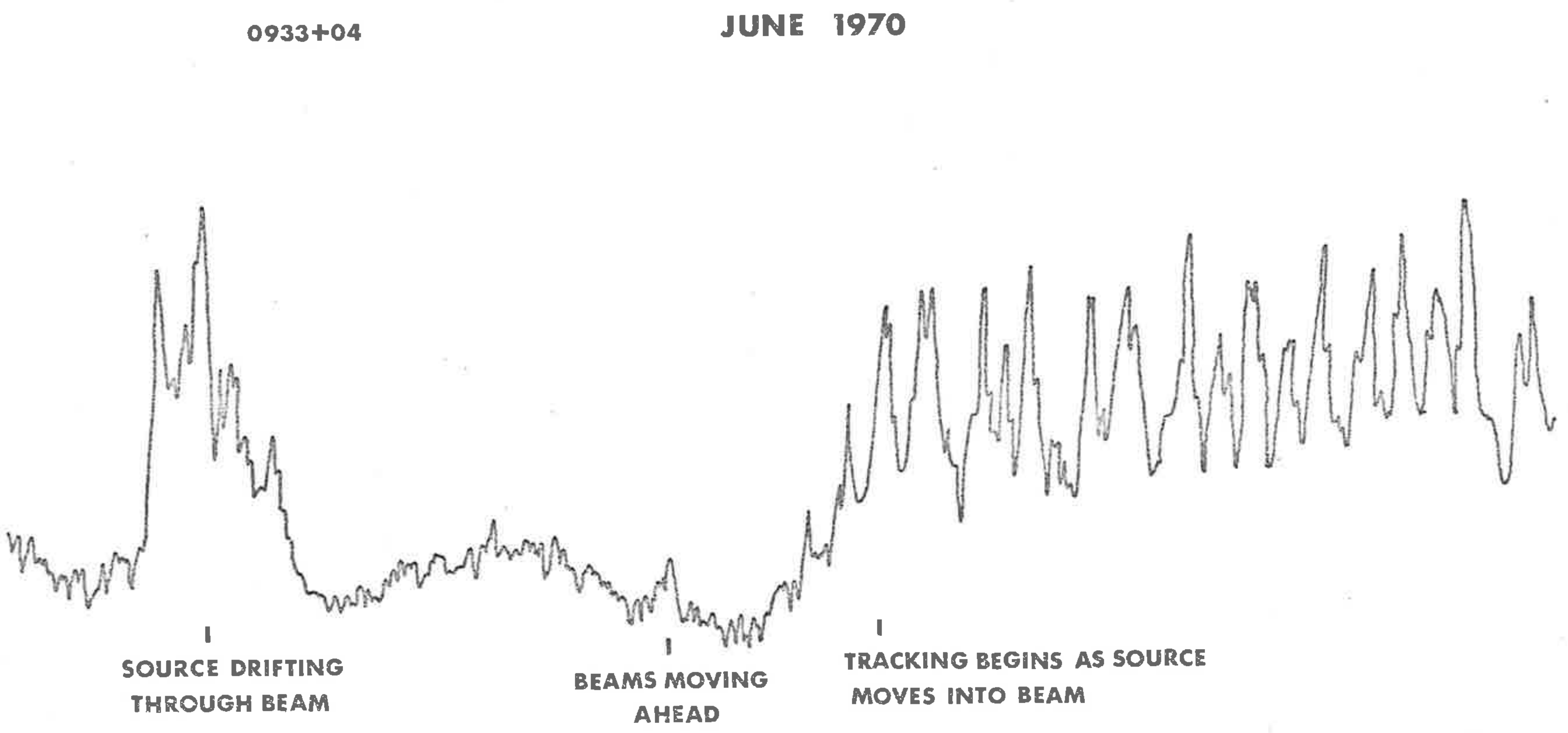

Figure 2.4 An example of a drift scan followed by a section of scintillation after the beams were set into the tracking mode partly through the second scan

the detectors of the radioheliograph and was eventually corrected. The hum degraded the signal inasmuch as a large aliasing peak occurred in the power spectra of the signals. This component was filtered from the data during analysis.

At the above sampling rate one block of data on the magnetic tape contained about 90 seconds of information, which included about 30 to 45 independent scintillation peaks. The number of blocks recorded consecutively from one radio source varied from about three up to several tens of blocks, depending on the behaviour of the ionosphere. From time to time, as a result of ionospheric refraction, the scintillation gradually decreased in amplitude as the source moved away from the setting of the beam. On some occasions, rapid movements of the apparent source position made recording impossible.

As well as recording scintillation or 'on-source' signals, a sample of the background noise or 'off-source' signal was also recorded by allowing the source to pass out of the beam until clear of the sidelobes and then resuming tracking. Comparison of the two signals gave a measure of the scintillation index.

2.5 Ionospheric Refraction

As mentioned in Section 2.3, series of drift scans of the Crab Nebula and 3C123 were obtained for estimating angular broadening. Also during other observing sessions long series of drift scans were obtained of a number of different sources. These data have provided information for a study of regular and irregular refraction effects within the ionosphere. By knowing the time of arrival of a source and the hour-angle and declination of the beams it was possible to determine the accurate position of the source for each scan. Thus the rate, extent and predominant direction of refraction could be studied by tracing the two-dimensional movements of the source over a number of scans.

In addition to the above long series of scans further information on refraction was obtained from the scintillation observations which required one or more scans of each source in order to detect scintillation and estimate the source height. Here again the positions of the sources could be found and could therefore be used to study ionospheric refraction. Because the sources covered a wide range of declination and hour-angle, data collected from all observing sessions provided a useful statistical coverage of ionospheric refraction. It was therefore possible to study the variation of refraction with parameters such as declination, hour-angle and local time.

2.6 Interplanetary Scintillation Observations at Parkes

Although the description of observations of interplanetary scintillation obtained with the Parkes 210 ft radiotelescope has been left until last, it was actually the first recorded data in this study and was obtained from the 19th to the 21st of January, 1968. A number of sources which were possible scintillators were observed on the frequencies 150, 600 and 1410 MHz. The radiotelescope was driven to the expected position of a source chosen for observation. When the beam moved on to this source, identified by an increase in the recorded intensity, the radiotelescope was set to track at the sidereal rate. The signals from the source at the three frequencies were recorded on charts with a time constant of 0.1 sec. On the few occasions during which scintillation was present, digital records on paper tape were also obtained at a sampling rate of 6 $\sec^{-1}$. The length of the sampled data varied from 4 to 8 minutes. In addition, a few minutes of background noise were recorded by moving the aerial about 1° N or S of the source. Scintillation was usually observed only on the centre frequency. The signal to noise ratio at 1410 MHz was too low to distinguish any slight scintillation which may have been present at this frequency and much of the 150 MHz signal was contaminated by solar activity. One unusual event was observed, however, occurring on the Parkes catalogue source 1938-15, when scintillation appeared on the 150 MHz signal during the 20th whereas the 600 MHz signal remained constant over the three days.

CHAPTER 3

ANALYSIS AND RESULTS OF THE CORONAL BROADENING MEASUREMENTS

3.1 Introduction

In the previous chapter we described in detail the three forms in which the angular broadening of the Crab Nebula was recorded, namely on film, digitally on magnetic tape and (during 1969 and 1970) as a series of drift scans on paper charts.

The films provided a visual record of all the data stored on tape but were generally unsuitable for detailed quantitative analysis due to various factors, particularly their limited dynamic range and the difficulty in specifying their response characteristics. However, the film records were examined closely as a check on the results of the magnetic tape analysis, especially when the broadened image did not have the shape, size or orientation expected. Several such occurrences were found and will be described separately in Section 3.6.

The films were also used to produce a composite picture of the broadening as a summary of the three years of observation. Daily photographs of the Crab Nebula were selected and placed in their correct position relative to the sun as shown in Figure 3.1. The upper sequence, from 1971, includes the observed solar disk at 80 MHz; for 1970 and 1969 the visible disk is outlined. This composite figure shows

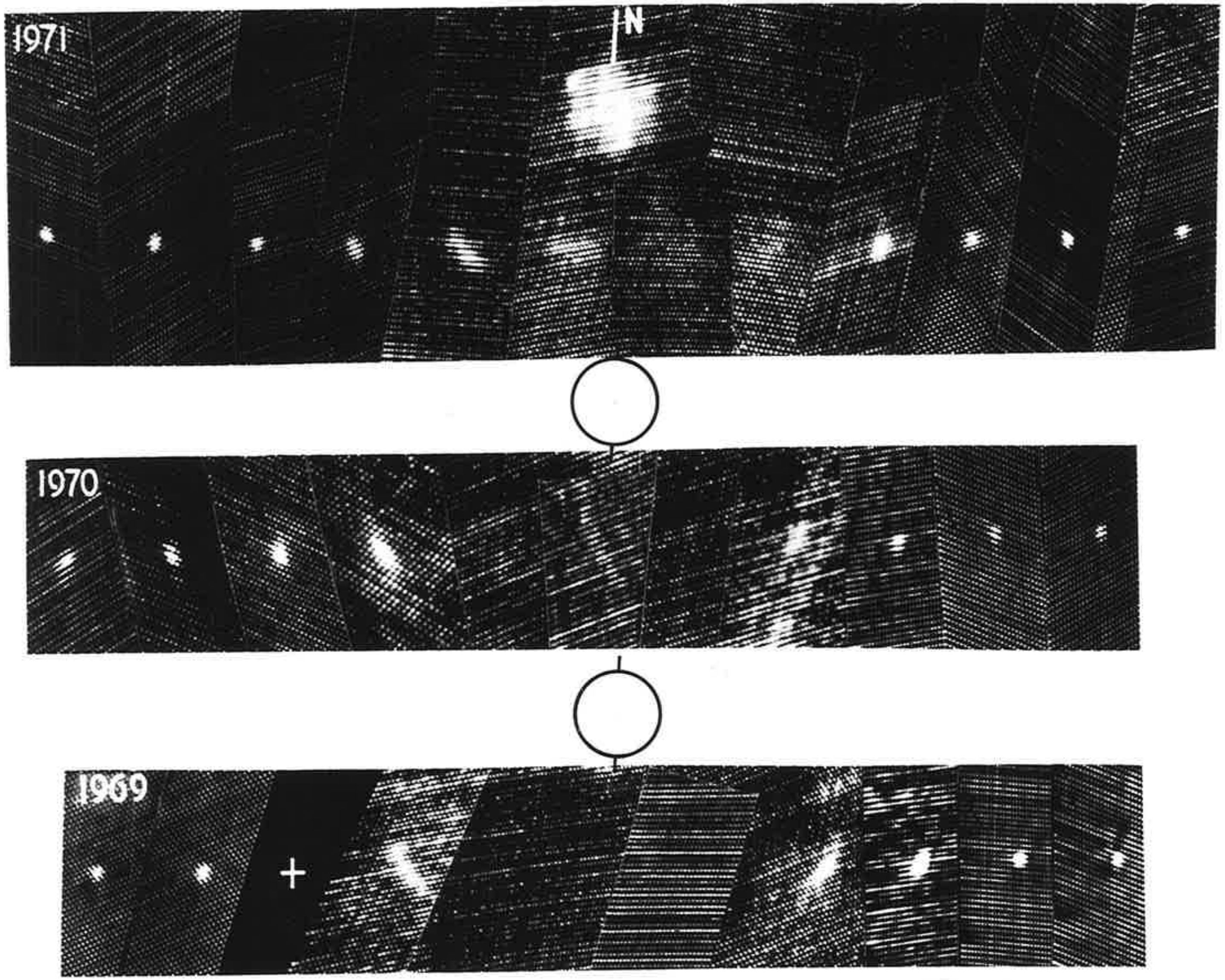
1971
N
1970
1969
+

Figure 3.1 The coronal broadening of the Crab Nebula 1969-71

many of the more obvious features of the scattering process, for example, the decline in scattering with the solar cycle over the three years and the elongation of the broadened image tangentially to the sun. However, these and other features of the scattering will be described in more detail as the results of the magnetic tape analysis are presented.

In the remainder of this chapter we shall describe in detail the techniques involved in the reduction and analysis of the tape and chart data and discuss the results in relation to previous work by other authors. In addition new findings are presented and a model representing the properties of the scattering medium is proposed. Finally unusual events observed on both the Crab Nebula and 3C123 will be discussed together with their possible causes. These include short term changes in angular diameter which have been observed by other authors (e.g. Slee, 1959; Erickson, 1964).

3.2 Analysis of the Magnetic Tape Data

One of the major problems in analysing the Crab Nebula observations was concerned with obtaining a satisfactory signal to noise ratio. Since the Crab Nebula is one of the strongest radio sources in the sky, and the radioheliograph an instrument of high sensitivity, this appears surprising at first sight and is worth explaining in some detail.

As explained in the previous chapter, the recording of a single full-frame picture on the radioheliograph took 1 sec, with an integration time, τ, of $\frac{1}{120}$ sec for each of the 60 E-W picture points. Assuming a system noise temperature $\sim 700^\circ$K and a bandwidth B $\sim$1 MHz, the minimum detectable temperature of the instrument was $\Delta T = \frac{700}{\sqrt{B\tau}} = 8^\circ$K. The antenna temperature expected from a point radio source of flux S $Wm^{-2}Hz^{-1}$, observed using an antenna of collecting area A m^2, is $T_A = \frac{SA}{2k}$, where k is Boltzmann's constant. For the Crab Nebula, $S \simeq 2.4 \times 10^{-23}$ $Wm^{-2}Hz^{-1}$, and for the radioheliograph (assuming 50% efficiency) A $\sim$ 6000 m^2, so that $T_A \sim 4000^\circ$K.

The above figures suggest an overall signal to noise ratio of about 500 : 1, but since the Crab Nebula was resolved by the radioheliograph, being spread over about 4 beams when unbroadened by the solar corona, a more realistic figure would be about 125 : 1. However, this value was not attained in practice. The observed rms fluctuation of the intensity of each beam was typically $\sim$ 8% of the recorded height of the unbroadened Crab Nebula for single frame observations even at distances out to 40 $R_\odot$ from the sun. This implied an observed signal to noise ratio roughly a factor of 10 worse than the theoretical value.

Near the sun the background noise was made up of not only galactic and receiver noise but also a contribution due to leakage of solar noise through the sidelobe structure of the radioheliograph beams. On many occasions this was the dominant contribution to the background. The sidelobe leakage diminished in proportion to the distance of the source from the sun but the observed signal to noise ratio was found to remain constant, implying that the solar contribution was in general a minor effect. Two instrumental effects were known to be the main cause of the decreased signal to noise ratio. Switching frequencies in the system contaminated the signal with non-random noise because of insufficient shielding of the signal paths and also 50 Hz hum was present in the multiplexer and later stages of the radioheliograph introducing a modulation of the offset levels of the signals from each beam. Sometimes the hum tended to beat with the picture scan causing one or more offset levels to change significantly across the picture. During analysis of the magnetic tape data this was noticed on several occasions, Work by the C.S.I.R.O. staff on integrating images of the quiet sun has revealed the same phenomenon.

In addition to these effects, when the source was observed within 20 $R_\odot$ of the sun and became broadened by coronal scattering, its image was spread over a larger number of beams. The corresponding reduction in peak intensity of the source also contributed to a reduction in the signal to noise ratio for each of the recorded beams.

It was therefore necessary to improve the signal to noise ratio and to this end records of the Crab Nebula, 3C123 and resistive load values were integrated by computer over a number of frames. During this process all frames containing parity errors or illegal data points were discarded. The two recorded senses of circular polarisation were analysed separately since one method of sidelobe minimisation, to be described later, relied on the fact that some solar radio bursts appeared stronger on one polarisation than on the other. The integration was normally carried out over 30 frames which ideally would have reduced the rms fluctuation by $\sqrt{30}$, to about 1-2% of the unbroadened source height. Depending on whether full or half-width scans were recorded this integration period corresponded to observation over 30 or 15 seconds respectively. At the same time longer integrations were performed, typically over 120 frames.

Obviously the best signal to noise ratio could have been achieved simply by integrating all the data from a single observation However, ionospheric refraction was always present to some degree and images produced by an integration over several minutes would have been unreliable. Nevertheless, when the image was broadened to such an extent that it was lost or barely visible amongst the background noise, even after integrating 120 frames, no choice was left but to integrate the total available data, despite the effects of refraction, in an attempt to make the image more clearly visible. Actually, on most occasions, refraction was only ~1-2' arc during the integration period and would not have affected the shape of the image when broadened to a full width of 30' arc or more. The exceptions were a few occasions when the source was observed to be rapidly refracted by 5-10' arc. Ionospheric refraction and its relation to Travelling Ionospheric Disturbances believed to be responsible for such effects will be described in the next chapter. The long integrations failed to reveal any images unseen on the photographs and unfortunately did not improve the images which were just visible, by the expected amount. These latter occasions corresponded to the effect of the non-random contributions to the background noise already discussed which, because of their nature, prevented the attainment of the improved signal to noise ratio expected on statistical grounds.

Before proceeding with the analysis the film records corresponding to the data which had been integrated were carefully examined for several reasons. Firstly, any ionospheric refraction was noted as this would have increased the apparent size of the integrated image, secondly the effects of solar radio bursts and the grating response of the radioheliograph were noted, and thirdly records containing extraneous noise, for example from motor vehicle ignition systems, were also noted and excluded from subsequent analysis.

To eliminate the difference between the offsets of each beam, or in other words to level the picture background, a set of 48 normalising values were computed for each observing period on each day, utilising the integrated resistive load records. By averaging the picture point values across the array, absolute offset values were calculated and subtracted from the corresponding Crab Nebula or 3C123 data before processing was continued.

During the June, 1970 recording period the radioheliograph integration offsets varied markedly within a few hours. They were adjusted at the beginning of each day but drifted so much that in most cases the resistive load values bore no relation to the offsets of the real data. An alternative method was therefore used to derive the normalising values. This entailed a similar process of averaging the picture point values of each beam across the picture; however, instead of the resistive load records the actual Crab Nebula or 3C123 data were used, omitting a N-S strip of the array containing the image of the source.

Another trouble occurring with all normalisations, and which was corrected by a trial and error process, was due to the variation of the beam offsets across the picture as mentioned previously. This naturally caused some difficulty when the peak height of the image was of the same order as the offset correction values.

After the picture background had been normalised, a reduction of the effects of the sun and solar activity was attempted. The solar noise appeared in the data through the grating response and minor sidelobes of the beam. Although these were small compared with the power gain of the beam, the radiation emitted by active regions on the sun could be thousands of times more intense than the Crab Nebula and hence, on occasions, dominated the picture. When observing at 8 $R_{\odot}$ the grating response fell on the sun and its effect on the pictures was noticeable even when the sun was quiet.

Sidelobe suppression was attempted by one of two different methods, or both in some cases, depending on whether the effects were due to the grating response of the system or to a polarised radio burst from the sun. Firstly, consider the sidelobe reduction when the data were contaminated by a polarised radio burst. The effects of such a burst were stronger on one of the recorded senses of circular polarisation, say array A, than on the other, array B, whereas the Crab Nebula was of similar strength on both. The procedure consisted in fitting one array to the other by the method of least squares, the variable parameter being the amplitude of array B. After achieving the best fit by multiplying array B by this parameter, array A was then subtracted from the modified array B to obtain a final picture which was considerably 'cleaner' than either of the originals. The method relied on the similar sidelobe structure of the two arrays and became more effective as the degree of polarisation of the solar burst increased. If the two arrays were initially equally affected by the sun the adoption of the above procedure produced an array with an increased variance compared with the original arrays, and a reduced or eliminated image of the Crab Nebula.

The second procedure was necessary only when the source was observed at about 8 $R_\odot$ from the sun, which was then overlapped by the grating response. The 1970 photographs of Figure 3.1 show good examples of this response appearing on the 13th and especially the 17th. Although difficult to remove completely, particularly when the sun contained one or more active regions, considerable improvement could nevertheless be achieved. Essentially an arc shaped enhancement representing the grating response and centred on the sun was subtracted from the data. The cross-section of the arc was an average cross-section of the observed grating response estimated from the data and excluding a section of the array containing the image of the Crab Nebula. If most of the radiation was emitted from an active region which was not at the centre of the solar disk, only a partial reduction of the grating response was possible because the method relied on a knowledge of the exact distance of the sun or active region from the line of sight to the source. The way in which the remnant of the grating response affected the source image after this correction process, depended on the relative positions and widths of both. Either an increase or a decrease in the image width could have resulted but in all cases the error introduced was believed to be negligible.

A minor effect which could not be removed was due to small phasing errors in the radioheliograph. These enhanced the sidelobes of the main beam allowing the sun to contaminate the picture in a somewhat irregular fashion. Also at times, one or more aerials were switched out of the system leaving gaps in the ring, and this too had a minor degrading effect.

At this stage we have described the initial integration of the tape data, the calculation of the normalisation values and the sidelobe removal techniques, and are now in a position to describe the actual analysis of the magnetic tape data. The two end products of this analysis were a series of computed contour plots of the broadened source, and the results of fitting a model to the image of the Crab Nebula by the method of least squares.

Contour plots were produced for all the integrated data containing 120 frames, except when the source was unbroadened when only one or two representative plots were drawn. They provided an easy means of detecting unusual shapes of the image and were also used for comparison with the theoretical model to be discussed later in Section 3.5. As mentioned earlier, integrations were carried out over longer periods when the source was observed close to the sun in an attempt to resolve the very broadened images. Also, in cases where ionospheric refraction was clearly not present, such long integrations were carried out irrespective of the degree of broadening to achieve the greatest signal to noise ratio. The results of such long integrations were again displayed in the form of contour plots, thus gaining the maximum amount of reliable information from the data.

The numerical results of the analysis were derived by fitting an elliptical Gaussian model to the observed image, by the method of least squares. To avoid ionospheric refraction the records containing only $\sim$30 integrated frames were used for this purpose. The model, of the form $A\exp(-Bx^2-Cy^2)$, was fitted to a section of the array containing the image of the Crab Nebula. Strictly, this model should have taken into account the slight curvature of the image and also the radial decrease of scattering power with solar distance. However, tests proved that the errors introduced were small in using the far simpler elliptical Gaussian model, and that they decreased at greater distances from the sun. Before the model was fitted to each section of integrated data, the array was skewed according to the calculated distortion coefficients explained in Section 2.2, to transform it back to a right ascension - declination coordinate system. The coefficients were also applied to the arrays before they were plotted as series of contours.

The parameters derived from the least squares fit were the background height and the peak intensity, radial and tangential widths, and the orientation of the image. After fitting the model to each of the sections of integrated data from a particular observing session, the parameters were averaged giving their mean values together with errors estimated from the least squares fit. Where the sidelobes were not completely removed an additional uncertainty arose in the parameters since in some cases the image lay on a depression in the background and in others on a sidelobe enhancement. No definite degree of error could be estimated for these cases and such data were treated with caution. When the radio source was only slightly broadened, or when it was extended to such a degree that its height was less than a few standard deviations above the background noise, the least squares fit often failed to converge and not all of the data from observations in these situations yielded values of the parameters. However, a check with a rough estimate of the size of the image from contour plots showed that the computed values, when the least squares fit did converge, were correct within the limits of their specified errors.

From the ellipse representing the image, and designated by major and minor axes and an orientation or position angle, the elliptical beam shape and inherent source size were deconvolved leaving the scattering ellipse. The beam shape depended on the hour-angle at which the source was observed, and the Crab Nebula was assumed to be a circular Gaussian source with a full width at half power of 3' arc.

3.3 Analysis of the Chart Data

Drift scans of the Crab Nebula and also 3C123 were obtained using pen recorders during 1969 and 1970. The initial step in their analysis was the reading from the charts of the height, width and time of arrival of each scan on each of the beams, and also the corresponding hour-angles of the radioheliograph beams. Normally, when unbroadened, the Crab Nebula appeared on two or three adjacent beams depending on its displacement from its true position due to ionospheric refraction. However, during the days when it was broadened by the solar corona up to 9 adjacent beams were recorded to cover the whole image, each beam tracing out a cross-section of the source in hour-angle.

To determine the E-W, or hour-angle widths it was a simple matter to convert the measured widths to minutes of arc rather than seconds of time by applying a factor proportional to the cosine of the source declination. For the unbroadened Crab Nebula, and all 3C123 recordings, the method used to determine the N-S or declination widths of the source was to assume the beams and source were Gaussian in shape and to insert the measured beam heights into a formula. This formula is simply derived with reference to Figure 3.2. The values of a, b and c represent the heights of three adjacent beams which are assumed to lie on a Gaussian curve centred about the line of sight to the source as shown. The displacement of the source from the central beam is denoted by α. Taking the distances between beams as unity we can write

$$a = A \exp\left(-\frac{(1+\alpha)^2}{\sigma^2}\right)$$

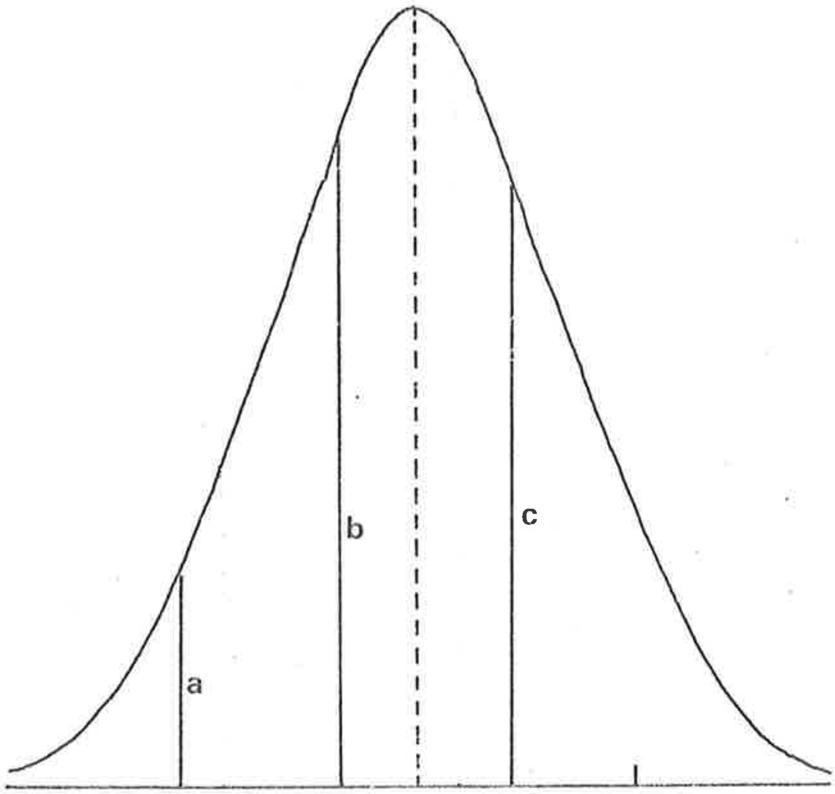

Figure 3.2 The geometry associated with the declination width determination

$$b = A \exp\left(-\frac{\alpha^2}{\sigma^2}\right)$$

$$c = A \exp\left(-\frac{(1-\alpha)^2}{\sigma^2}\right)$$

where A is the height of the image and σ is the half width (at e^{-1}) of the Gaussian envelope. Eliminating A and α leaves an expression relating σ, the half width of the image, to the measured beam heights

$$\sigma = \left\{\ln\left(\frac{b^2}{ac}\right)\right\}^{-\frac{1}{2}},$$

where σ is expressed in terms of the beam spacing. The widths were converted to minutes of arc by multiplying by the actual beam spacing which depended on the hour-angle and declination of the observations. Using the appropriate formulae the N-S and E-W widths of the radioheliograph beams were computed, and the squares of these values were subtracted from the squares of the image widths. The inherent source size was similarly removed to give a measure of the broadening in the two directions. Up to 15 or 20 useful scans were recorded each day and average values of the broadening were calculated in each case. Some scans could not be analysed when the source lay between two beams giving only two height measurements from which the declination widths could not be reliably calculated. When the image of the Crab Nebula covered four or more beams the formula used above was discarded in preference to fitting a Gaussian curve to the beam heights by the method of least squares. The half width of the Gaussian was equivalent to the parameter σ in the previous method.

Although the positions of the beam cross-sections taken from a single scan were not useful when the source was unbroadened, it was hoped that some information about the shape and orientation of the image could be determined as the broadening increased. In fact the orientation of the image did agree with the corresponding results from the digital analysis.

Useful Crab Nebula data recorded as drift scans were limited by the poor signal to noise ratio when the image peak intensity was small, and also by activity on the sun. On the other hand when the source was unbroadened, and in the case of all 3C123 data, inaccuracies in the chart reading produced relatively large errors in the angular broadening estimates. This was particularly noticeable with the N-S values. Probably the main error arose from the uncertainty in the baseline estimates for each scan because the actual shape of the beam was slightly asymmetric. A simple calculation indicated that an error of $\sim$7% in the height measurements could introduce errors of up to 50% in the calculated N-S widths, and $\sim$17% in the E-W widths of the unbroadened image.

During recording, a noticeable feature at times was the variability in height of the peaks from one scan to the next. This was attributed to ionospheric scintillation which, having a similar time scale to the width of the scan, would have introduced a variability in the height to width ratio of successive scans. Since the 3 km diameter of the aerial array was larger than the average scale of the diffraction pattern of ionospheric irregularities, the magnitude of this effect was generally not troublesome. Ionospheric refraction was also present to some degree in most cases but the rate at which the source was refracted was slow compared to the time taken to complete a scan of the source and would not have introduced significant errors.

The total useful data, bearing in mind all the above considerations, finally amounted to records on the 13th during 1969 and the 12th and 13th during 1970. Assuming the scattering was elliptical, the major and minor axes were estimated and agreed very well with the values calculated from the tape data.

3.4 Results of the Tape and Chart Data

Figure 3.1 as mentioned before is a composite picture made from typical images of the Crab Nebula recorded during the three years of observations. The images have been placed in their correct position with respect to the sun and in each case the first image was recorded on the 10th June. The different alignments of the background grid are due to the application of the distortion coefficients to bring the particular images back into the right ascension - declination coordinate system. All images are integrated by 16, that is over a duration of either 8 or 16 sec depending on the scan width.

The increase in size of the image as the source was observed closer to the sun is clearly evident, and the tangential elongation suggests the presence of filamentary irregularities in the solar corona. One exception is clearly the 12th, 1970 where the image was oriented in almost a N-S direction; this event will be mentioned later in Section 3.6. The degree of broadening appeared symmetrical about the sun apart from the anomalous increase during the 16th and 17th, 1971. Also apparent is the decrease in the degree of scattering during 1971 compared to the earlier years 1969 and 1970, which were approximately similar. This was a reflection of the decline in the solar cycle. In fact the scattering was so strong during 1969 and 1970 that the image could not be resolved within about 8 $R_\odot$ of the sun. From a knowledge of the rms deviation of each picture point a lower limit of about 40' arc was calculated for the scattering on these occasions. Although the photographs provided a summary of the observations they were not suitable for a detailed study, which was provided by the least squares fit of the elliptical Gaussian model and the contour plots.

The results of the analysis of the magnetic tape and chart data are shown in Figure 3.3 where the major and minor axes of the scattering ellipse (measured at e^{-1}) are plotted separately against radial distance from the sun. The values for 1971 are seen to be generally lower than the 1969 and 1970 values. Lines of best fit were calculated for the 1971 tangential scattering values and for the combined 1969-70 values, both

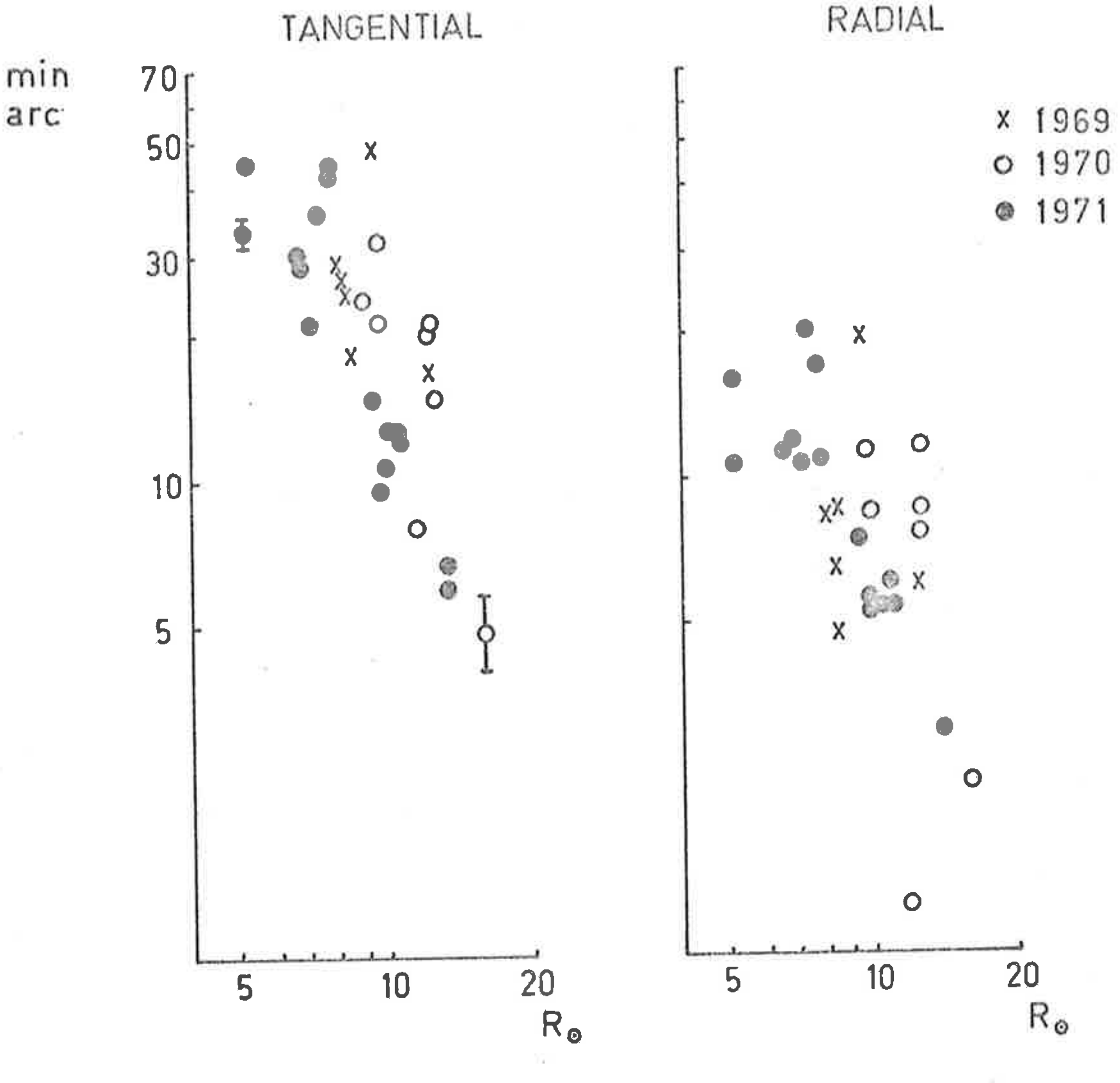

Figure 3.3 Values of the tangential and radial broadening (full width, e^{-1}) during 1969-71 at 80 MHz

of which followed closely a power law variation with distance. After scaling the values from 80 MHz to 38 MHz, assuming a λ^2 dependence on wavelength as predicted for strong scattering, these lines are shown in Figure 3.4 together with results of other authors (Okoye and Hewish, 1967) at different parts of the solar cycle. Note that in this figure we have represented the semi-major axis of the scattering ellipse. Good agreement is apparent both for the degree of scattering at the relevant part of the solar cycle and for the slope of the lines. A comparison of the radial scattering at 12 $R_\odot$ with smoothed sunspot numbers over nearly two solar cycles is shown in Figure 3.5 (Matheson and Little, 1971), with our 1970 and 1971 values from Culgoora added to the diagram. The values have been scaled to 80 MHz and the scattering is seen to follow the degree of activity of the sun. A line of best fit was calculated for the radial scattering values and was found to have a slope of -1.6 compared with the tangential scattering slopes of -2 and -3 for 1969-70 and 1971 respectively. This suggests an increase in the axial ratio of the irregularities close to the sun. The only previous reference to a variation of the axial ratio was made by Slee (1966), who suggested that the overall anisotropy of the irregularities decreased with the decline of the solar cycle. His results, however, were based on observations between 20-80 $R_\odot$, whereas in our case we are concerned with a variation within 20 $R_\odot$ of the sun. A plot of the axial ratio against solar elongation is presented in Figure 3.6 and it would appear that beyond 10 $R_\odot$ the axial ratio remained constant at $\sim$2:1, a value similar to that

distance?

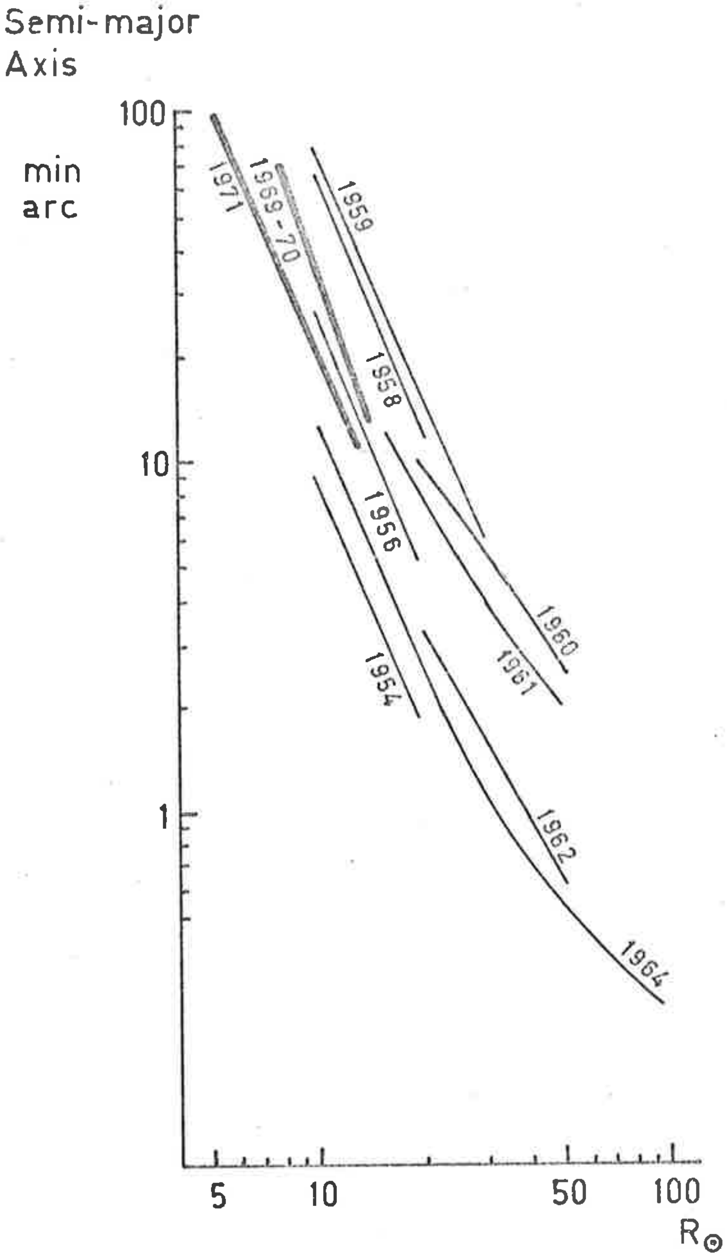

Figure 3.4 Values of the tangential broadening (heavy line) scaled to 38 MHz for comparison with earlier work at various phases of the solar cycle. (NOTE all values are half-widths to e^{-1})

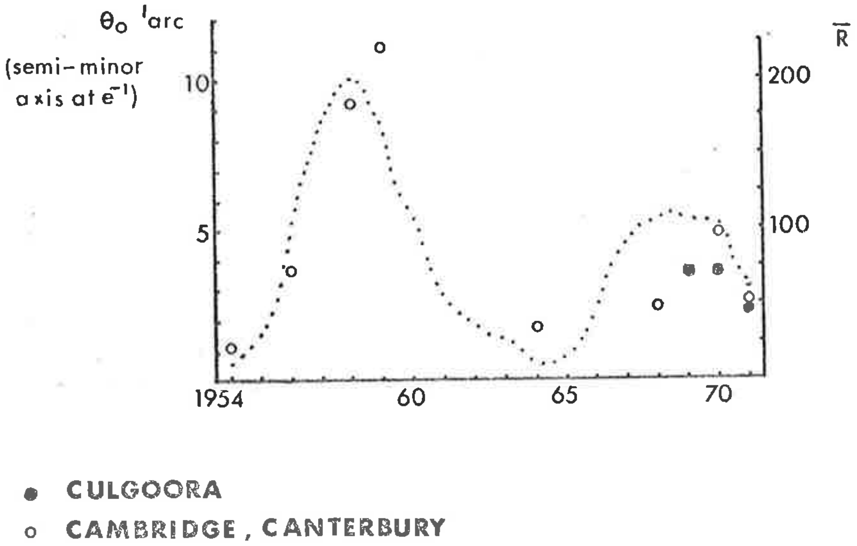

Figure 3.5 Comparison of radial scattering at $12R_\odot$ with the smoothed sunspot number. All values are scaled to 80 MHz.

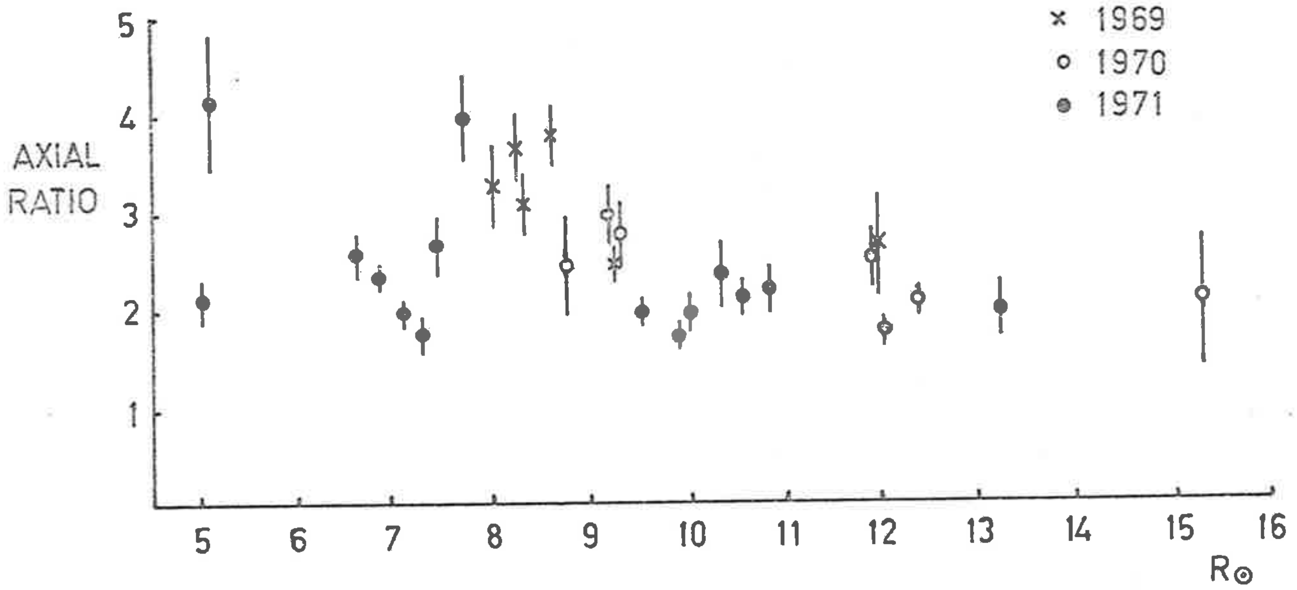

Figure 3.6 Values of the axial ratio of the scattered distribution as a function of radial distance from the sun

found by Dennison (1969) from spaced receiver observations of interplanetary scintillation in the region 70-200 $R_\odot$. However, for distances less than 10 $R_\odot$ there was a tendency for the elongation to increase to $\sim$3 or 4:1 at 5 $R_\odot$. It is generally assumed that elongation of the scattering irregularities is caused by a reduction in plasma diffusion across the magnetic field lines, and it is of interest to note that within 10 $R_\odot$, where we observe enhanced elongation, the magnetic pressure is expected to dominate the kinetic gas pressure (Pneuman, 1966). It seems possible that the enhanced elongation we have observed might be related to the increasingly important role of the magnetic field within this region.

We have assumed in the above discussion that the axial ratio of the irregularities in the solar corona was directly related to the axial ratio of the scattered distribution. An additional effect contributing to the elongation of the image might occur close to the sun when the scattering becomes so large that regions of the solar corona of varying scattering power become involved. Although this effect would result in an elongation of the image towards the sun due to greater scattering power of those regions, it would still need to be allowed for in interpreting our results. However, the effect was in fact negligible for the conditions of the present observations as shown in Figure 3.7, where the image at 5 $R_\odot$ has been plotted (for isotropic scattering irregularities) as a function of the degree of scattering with the

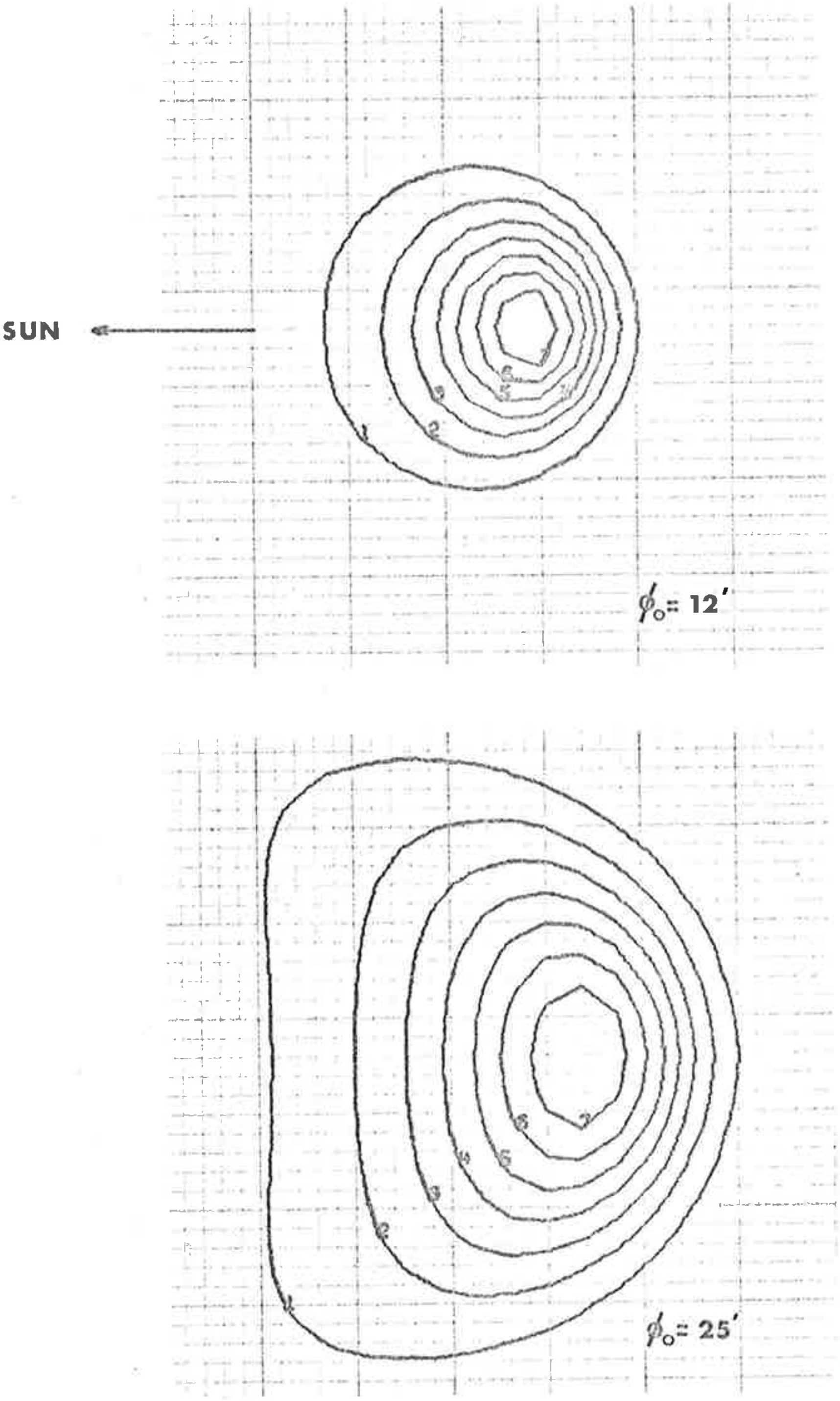

Figure 3.7 Theoretical images for isotropic scattering at $5R_\odot$ showing the curvature introduced when the scattering is large

parameter ϕ_o representing the half-width of the angular spectrum of 5 $R_\odot$. These results were computed on the basis of a model described in detail in Section 3.5. Not until the degree of scattering becomes double the observed radial value does the image show significant elongation. We therefore conclude that the geometry of the scattering was not reflected in any way into our results. Also the possibility of refraction by the solar corona was investigated as another possible influence on the results. However, at our observing frequency of 80 MHz such refraction was calculated to be < 1' arc at 5 $R_\odot$ and was therefore negligible (Jaeger and Westfold, 1950).

So far we have been using major and minor axes and tangential and radial scattering interchangeably without proof that they are equivalent. Their uses are justified since apart from the special case of the 12th, 1970, the minor axis varied randomly from the radial direction with an rms deviation $\sim 5^o$, as shown in Figure 3.8(a). This is also apparent in Figures 3.9(a), (b) and (c) where the major and minor axes representing the scattering to e^{-1} are drawn at each position of the image. It appears, then, that within the experimental accuracy the scattering irregularities, and hence the magnetic field, are aligned radially to within 5 $R_\odot$ of the sun. Pneuman (1966) has investigated the magnetic field configuration close to the sun assuming an inner dipolar field which is eventually drawn out, and frozen into, the radially expanding solar wind. An interesting conclusion of his work is that

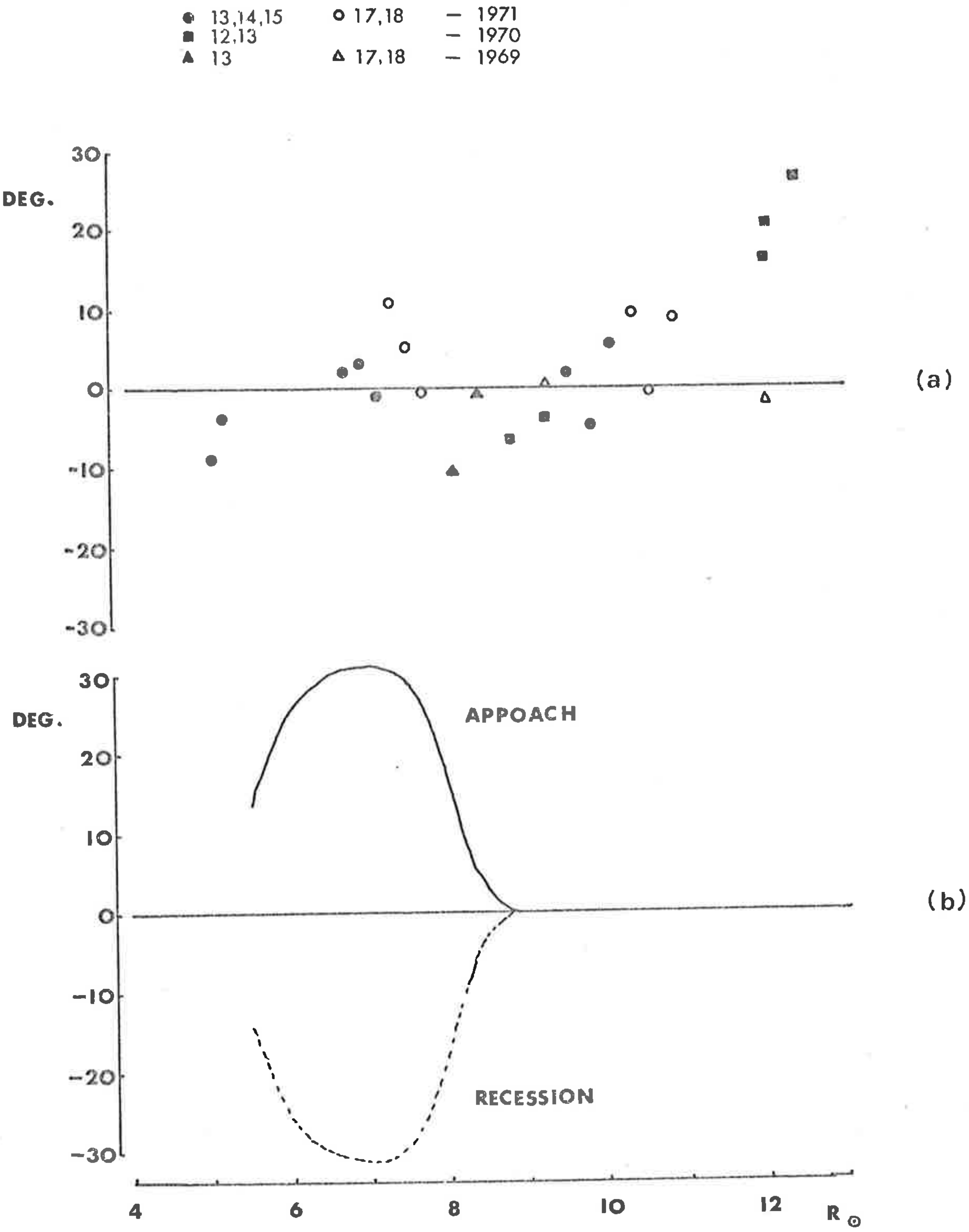

Figure 3.8 (a) The observed (clockwise) deviation of the minor axis from the radial direction.
(b) Theoretical deviations based on a solar magnetic field model developed by Pneuman.

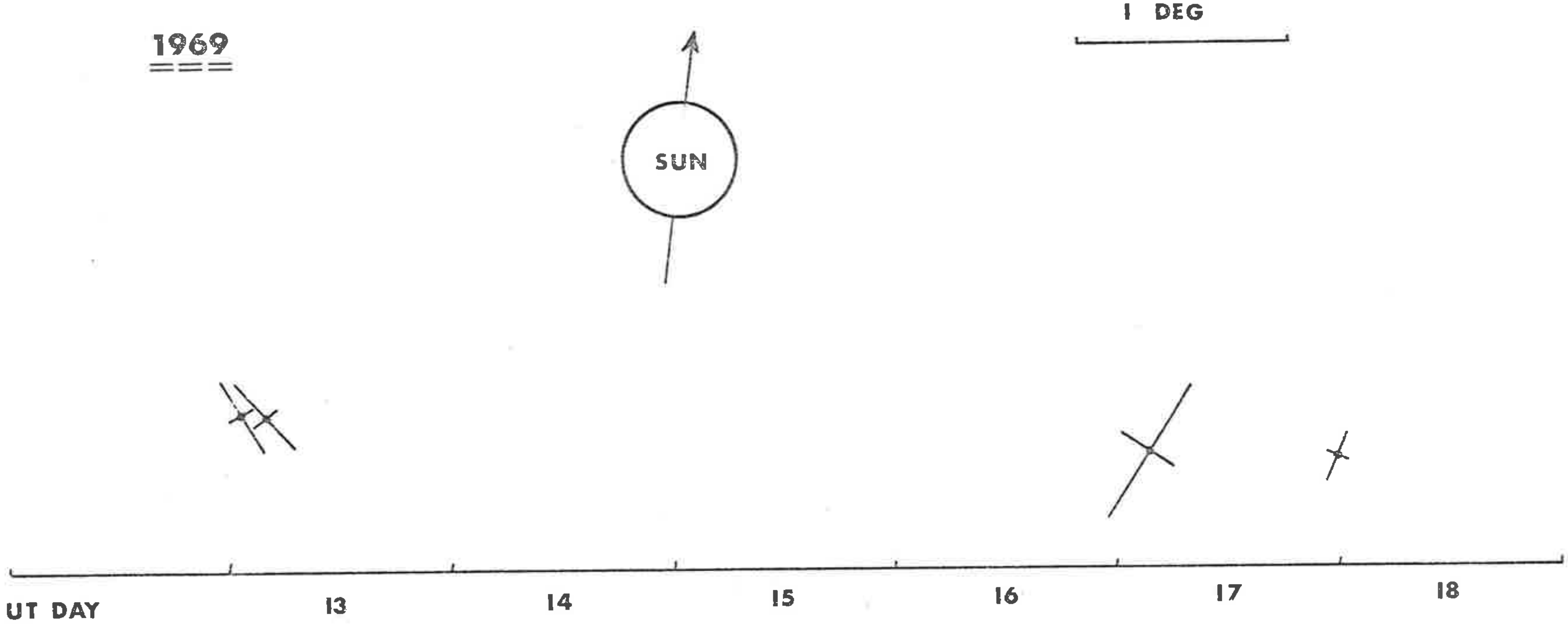

Figure 3.9 (a) Axes of the scattering ellipses during 1969.

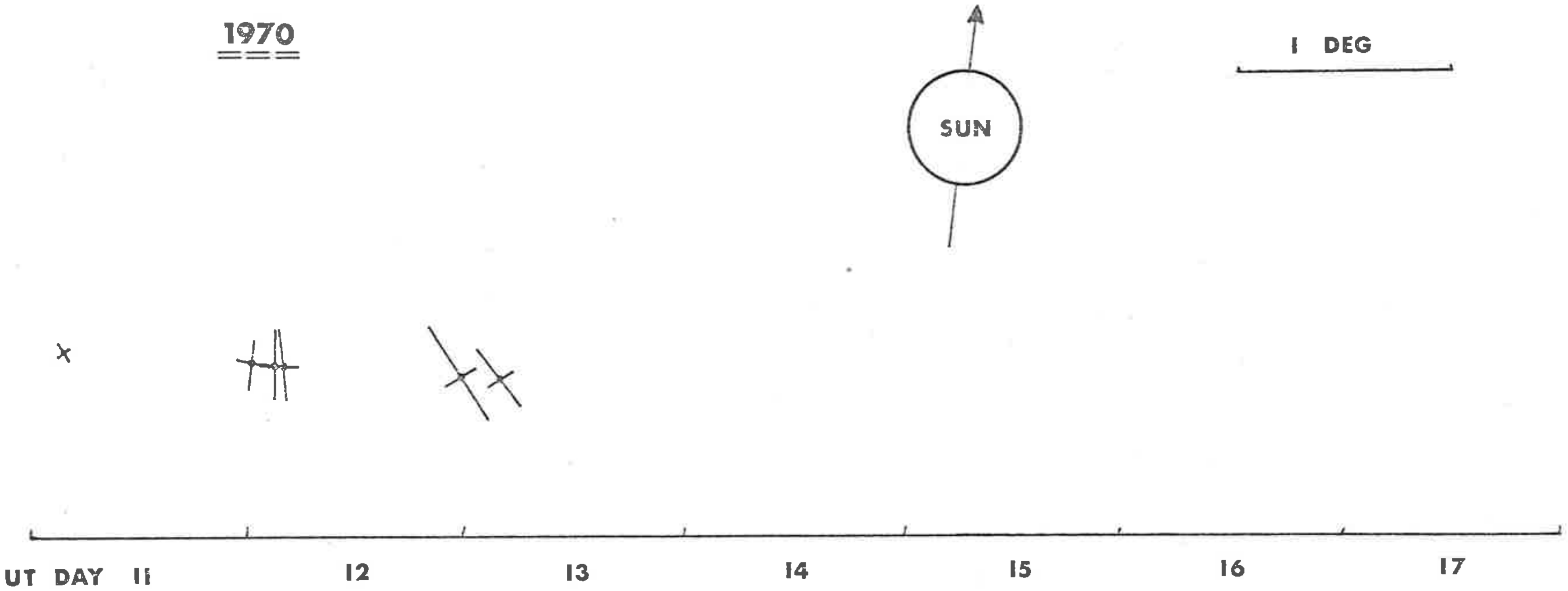

Figure 3.9 (b) Axes of the scattering ellipses during 1970.

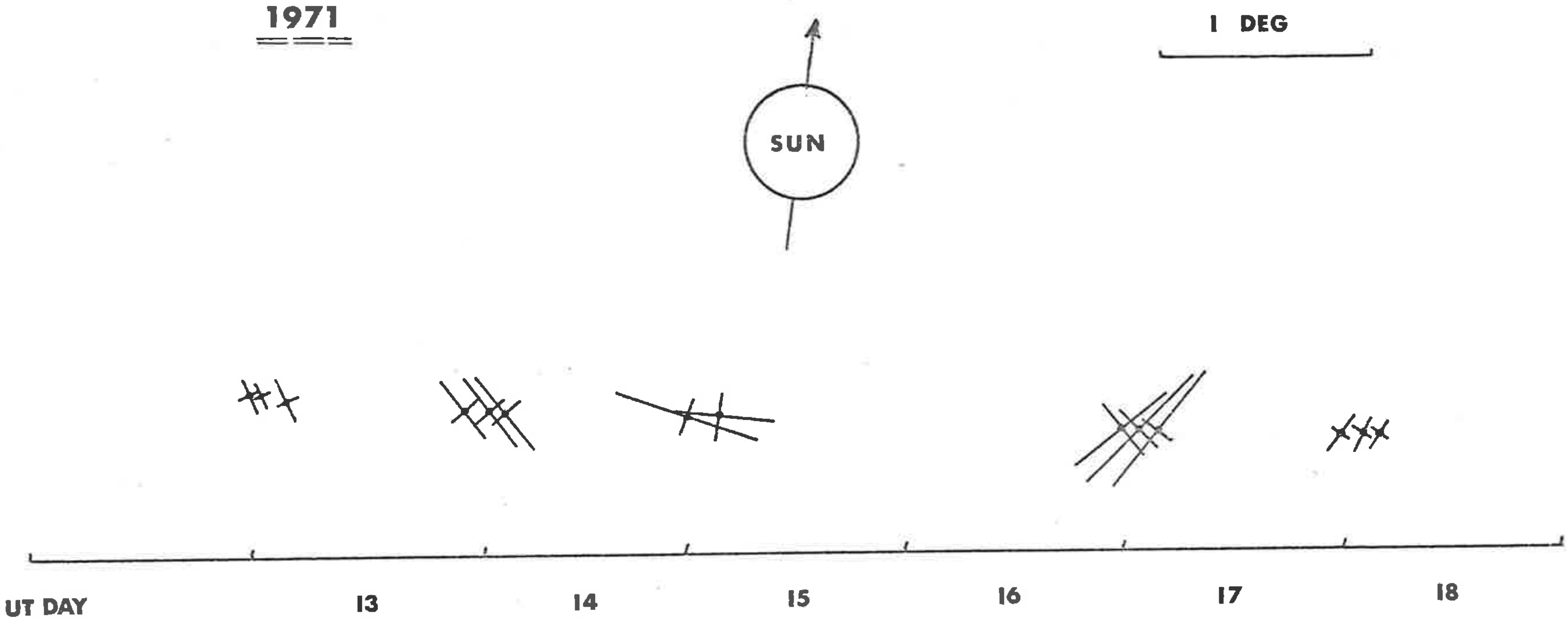

Figure 3.9 (c) Axes of the scattering ellipses during 1971.

although the field would be almost radial under solar maximum conditions, it would tend to dominate the kinetic gas pressure within 9 $R_\odot$ when the sun was quiet. Inside this boundary he suggests a configuration intermediate between the radial and dipolar forms. A dipolar field or some intermediate configuration suggested by Pneuman would have produced a definite trend in the variation of the minor axis of the scattering ellipse from the radial direction. This effect is shown in Figure 3.8(b) based on Pneuman's results. Although we find no evidence of a non-radial field configuration we have, as mentioned earlier, observed an increase in elongation within about 10 $R_\odot$ which may be the first indication of the changing role of the magnetic field. The fact that we have observed such a variation in the axial ratio suggests that only slight differences between the magnetic and kinetic gas pressures are able to produce detectable changes in the elongation of the irregularities.

Continuing with other conclusions derived from our observations, it was found that in general there was not a large change between observations recorded on the same day except in one case, the 17th, 1969, when the image was not visible at the beginning of the day but appeared in the final observation. Other less rapid changes occurred, for instance, the first observation on the 17th, 1971 showed a broader image compared with the second observation. However, on most occasions large scale structure was known to have been present in the medium from interplanetary scintillation observations (Wiseman and Dennison, 1972; Wiseman, 1972) and could account for the relatively sudden changes. Also no general asymmetry was observed between the approach and recession of the Crab Nebula. One possible cause of asymmetry would be the 7° tilt of the solar axis in the presence of an equatorially extended corona. However, Figure 3.10 which shows an idealized (minimum) corona of elongation 2:1 and the relative positions of the Crab Nebula, indicates this 'tilting' effect to be small, particularly at frequencies $\gtrsim$ 80 MHz.

Since both coronal broadening and interplanetary scintillation arise from the same basic scattering process, it was considered of interest to look for any variations in the brightness distribution of the broadened Crab Nebula on the rapid ($\sim$1 sec) time scale characteristics of scintillation. For this purpose several sections of very clean data were chosen, and the elliptical Gaussian model was fitted to single consecutive frames by the method of least squares. The averages and standard deviations of the parameters were determined for each section, and compared with the average deviations calculated directly from the least squares fit of the single frames. In all cases they differed by factors of 2-5 suggesting that genuine fluctuations might be present. Some typical results of the least squares fit are shown in Table 3.1. This, however, cannot be considered conclusive since only a fraction of the data was treated in this way because of the large computing expense involved and further analysis might reveal that the above deviations of

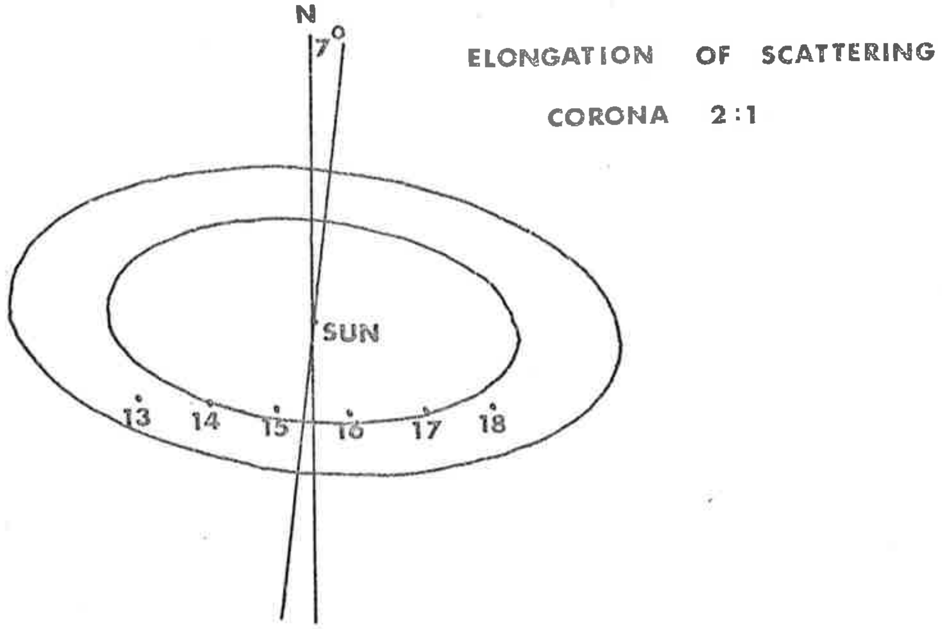
N
7°
ELONGATION OF SCATTERING
CORONA 2:1
SUN
13
14
15
16
17
18

Figure 3.10 The relation between contours of constant scattering and the positions of the Crab Nebula during June 1971 for an elongated scattering corona

	Average rms deviations	
	Separate calculation from 82 samples	Average of deviations derived from least squares fit
Height	11.0	7.4 ± 0.7
Width (radial)	1.81	0.29 ± 0.03
Width (tangential)	1.17	0.5 ± 0.09
Orientation	7.6°	4.87 ± 3.0

Table 3.1 Least squares fit results of 82 consecutive single frames of the Crab Nebula recorded on 12th June, 1970.

the parameters were not indicative of real variations in the observed brightness distributions.

An attempt was also made to determine the absolute flux contained within the image of the Crab Nebula by using 3C123 as a calibrating source. However, the results were outweighed by detrimental effects such as ionospheric scintillation and the asymmetry of the beam shape making total flux estimates, particularly from 3C123, extremely unreliable.

3.5 Model of the Brightness Distribution

The derivation of a model to describe the observed brightness distribution of the Crab Nebula is of considerable interest because we have for the first time the complete two-dimensional image of the broadened source. The simplest case to treat is that of an angular spectrum which has Gaussian cross-sections. The relation between the spatial power spectrum of the irregularities and the observed angular spectrum of the radiation after passing through the irregularities is well known (Ratcliffe, 1956); the Gaussian angular spectrum we consider here is equivalent to a Gaussian spatial power spectrum for the irregularities.

Shown in Figure 3.11 are the sun and source seen projected on to the celestial sphere. The value of the brightness B (r, α) at all points around the source was calculated assuming that the scattering gave rise

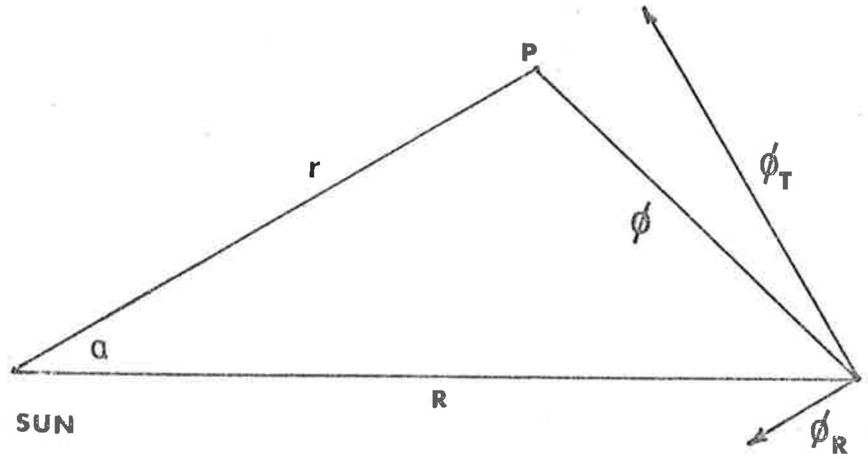
P
r
ϕ_T
ϕ
a
R
SUN
ϕ_R

Figure 3.11 The scattering geometry

to an angular spectrum of the form exp $(-\frac{\phi^2}{\phi_o^2})$, where ϕ_o is the scattering angle and is a function of the radial distance r. Also, ϕ_o was assumed to possess an elliptical distribution with semi-axes ϕ_R and ϕ_T in the radial and tangential directions respectively. From observational evidence it was seen that ϕ_R and ϕ_T could be represented by power laws

$$\phi_R = \frac{1}{A_R} r^{-S_R} \text{ and } \phi_T = \frac{1}{A_T} r^{-S_T}.$$

Following the procedure of Erickson (1964), who calculated B(r, α) for isotropic scattering, we express ϕ_R and ϕ_T in radians and r and R as radians subtended at the earth. Since the scattering angles were small, ϕ, the scattering angle at P expressed in radians, was approximately equal to the angular distance between P and the source. From Figure 3.11 we see that the scattering angle may be divided into radial and tangential components (R cos α - r) and (R sin α) respectively. Using the above components of ϕ_o and ϕ the exponent of the angular spectrum may be written in component form and the angular spectrum is then represented by

$$\exp\left[-\frac{(R\cos\alpha - r)^2}{A_R^{-2}\, r^{-2S_R}} - \frac{(R\sin\alpha)^2}{A_T^{-2}\, r^{-2S_T}}\right] \quad \text{--------} \ (1)$$

We require the integrated flux to remain constant at all distances R, of the source from the sun and the angular spectrum then becomes

$$\frac{c}{(A_R^{-2}\, r^{-2S_R}\, A_T^{-2}\, r^{-2S_T})^{\frac{1}{2}}} \exp\left[-\frac{(R\cos\alpha - r)^2}{A_R^{-2}\, r^{-2S_R}} - \frac{(R\sin\alpha)^2}{A_T^{-2}\, r^{-2S_T}}\right].$$

This expression, evaluated at all points P around the source, becomes the brightness distribution, $B(r, \alpha)$. Taking into account the inherent source size, θ, by convolving equation (1) with $\exp\left(-\frac{\phi^2}{\theta^2}\right)$ before normalising for constant flux, the brightness distribution can then be represented by

$$\frac{c}{\left[(A_R^{-2}\ r^{-2S_R} + \theta^2)(A_T^{-2}\ r^{-2S_T} + \theta^2)\right]} \times$$

$$\exp\left[-\frac{(R\cos\alpha - r)^2}{(A_R^{-2}\ r^{-2S_R} + \theta^2)} - \frac{(R\sin\alpha)^2}{(A_T^{-2}\ r^{-2S_T} + \theta^2)}\right]$$

For comparison with observed brightness distributions, $B(r, \alpha)$ has been computed as a function of distance R from the sun and the axial ratio of the scattering irregularities defined by $\frac{\phi_R}{\phi_T} \equiv \frac{A_T}{A_R}$. Some examples of these are shown in Figures 3.12(a), (b) and (c) where the values of the parameters were typical of the observed values for 1969-70.

$S_R \simeq S_T \simeq 2$

$A_R \simeq 5.3 \times 10^5$

θ (Crab Nebula) = 5.25×10^{-4} radians

$A_T = 5.3 \times 10^5$ (axial ratio 1:1) Figure 3.12(a)

2.65×10^5 (axial ratio 1:2) Figure 3.12(b)

1.32×10^5 (axial ratio 1:3) Figure 3.12(c)

In comparing such distributions with our observational data we found closest agreement using values of 2-3 for the elongation of the irregularities.

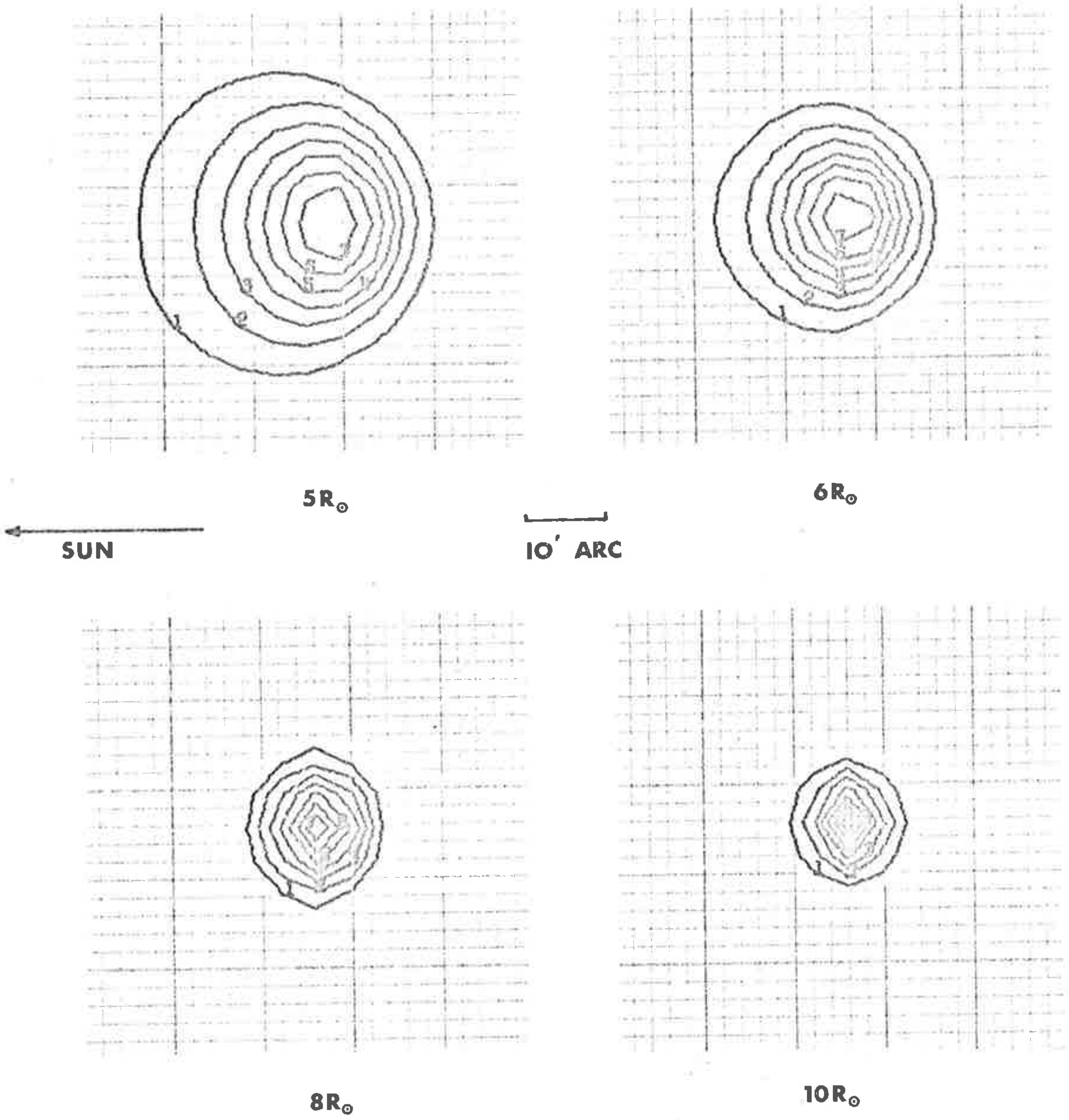

Figure 3.12 (a) Theoretical brightness distributions for isotropic scattering (12' x 12' arc at $5R_\odot$).

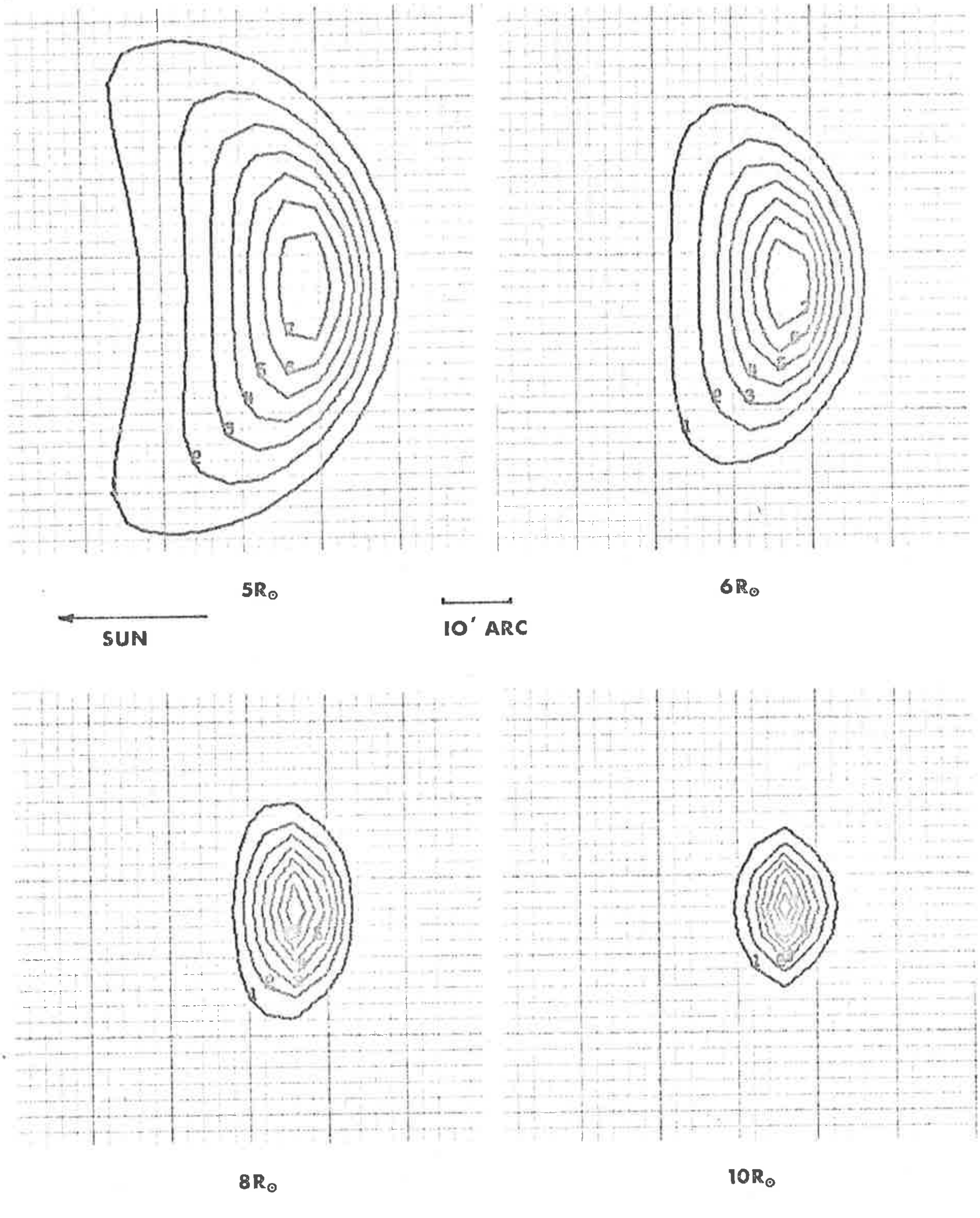

Figure 3.12 (b) Theoretical brightness distribution for 1:2 scattering (12' x 24' arc at $5R_\odot$).

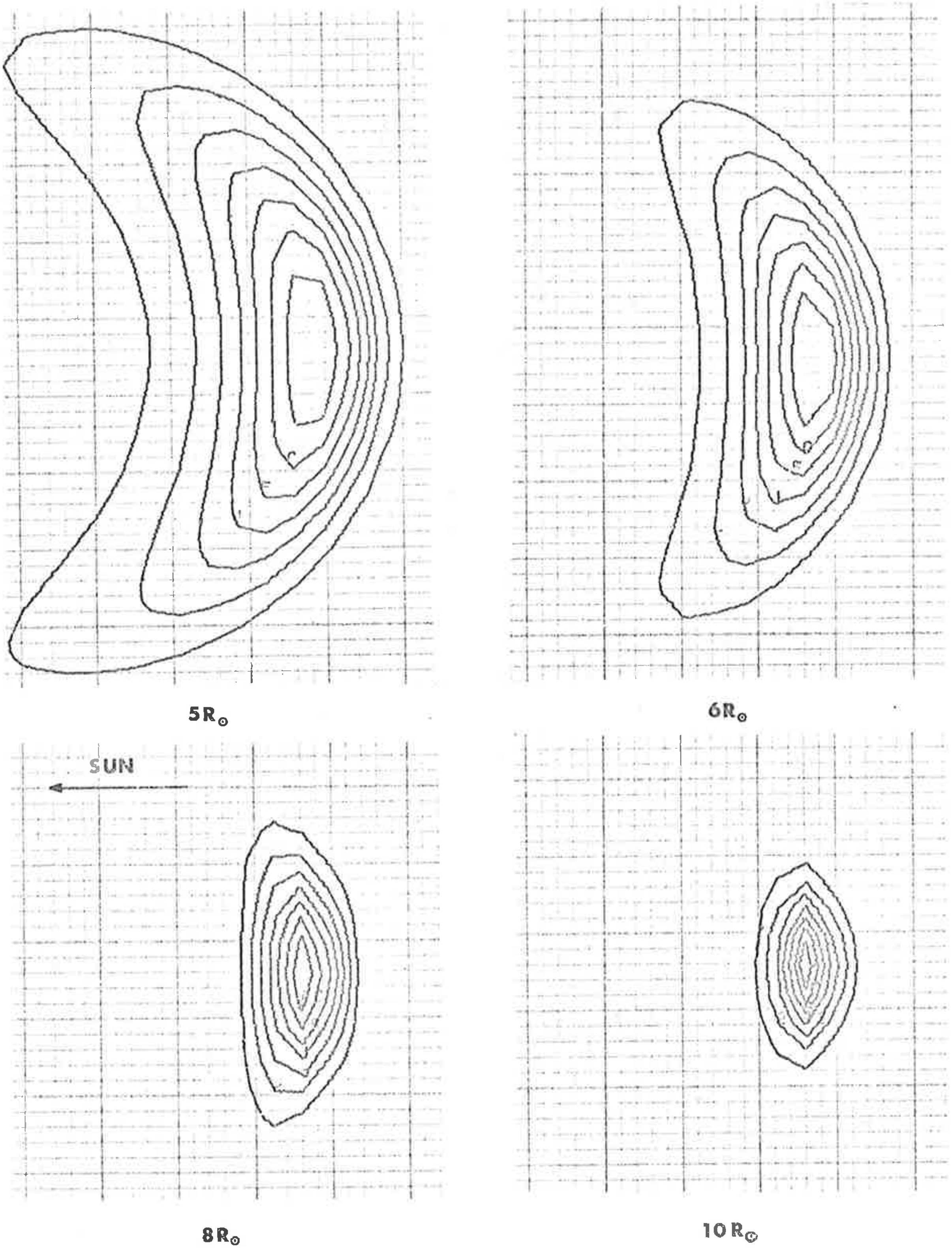

Figure 3.12 (c) Theoretical brightness distributions for 1:3 scattering (12' x 36' arc at $5R_{\odot}$).

Theoretical distributions were also calculated for direct comparison with selected observations. Some examples of these are presented in Figure 3.13 in the form of contour plots. There is a linear relationship in power between successive contour levels, and the levels on the model correspond to those of the observed image. To estimate the parameters required for the theoretical distribution, images were selected in which the elongation of the radioheliograph beam was approximately parallel or perpendicular to the radial direction. This enabled the semi-axes of the elliptical beam to be convolved with the theoretical scattering function in the same manner in which the effect of the inherent source size was introduced. The radio cross-section of the image was plotted, a baseline estimated and the half-power width and contour level positions for the model were then determined. Also the tangential width at the corresponding half-power point was found. From the two widths the effects of the source and beam were subtracted leaving values for ϕ_R and ϕ_T, after adjusting to e^{-1}. The distance of the source from the sun was known allowing A_R and A_T to be calculated with $S_R = S_T = 2$. The striking feature of the theoretical distributions in Figure 3.13 is their excellent agreement with the observed images. We therefore conclude that the Gaussian form for the angular spectrum is in remarkedly close agreement with the observations. However, it is still possible that other models might also lead to satisfactory agreement with the observations. One possibility would be a modified power low spectrum P(q) of the scattering irregularities, as

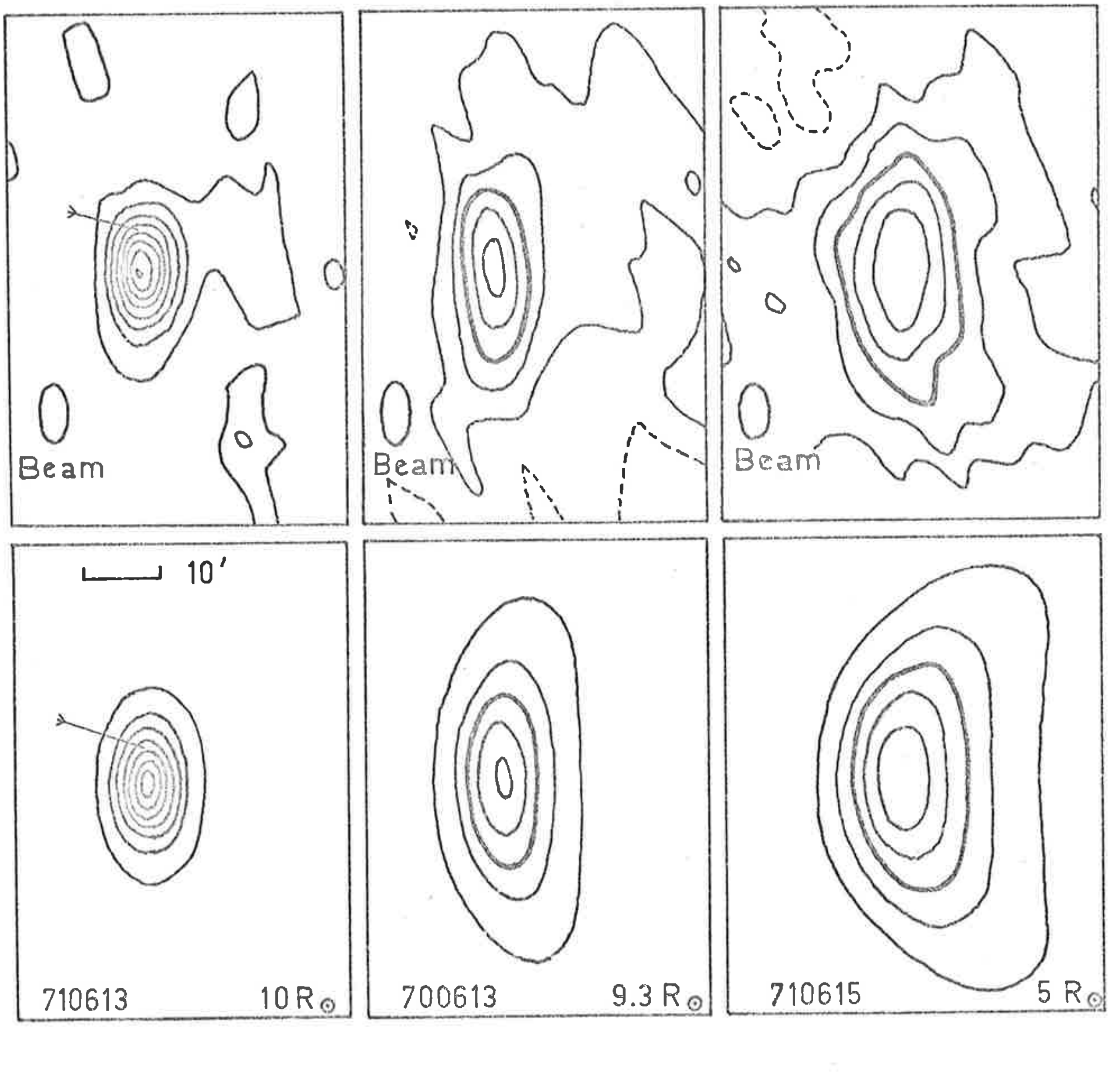
Beam
Beam
Beam
10′
710613
10 R⊙
700613
9.3 R⊙
710615
5 R⊙

Figure 3.13 Observed brightness distributions compared to theoretical distributions for the same radial distance from the sun. Heavy lines or arrows indicate the half-power contours

shown in Figure 3.14(a). This is an important model for consideration because the interplanetary magnetic field observed by spacecraft near 1 A.U. (Jokipii and Coleman, 1968), has a spectrum similar to Figure 3.14(a). The only difference is that we have scaled the spatial frequency axis to give values relevant to 10 $R_\odot$ assuming the irregularity scale varies linearly with r, the distance from the sun. Such a form for the spatial power spectrum of the irregularities is similar to the well known Kolmogorov turbulence spectrum and implies a wide range of scale sizes extending from the so-called outer scale or correlation length (suggested to be $\sim 10^6$ km for the interplanetary magnetic field) down to the inner, or dissipation scale ($\sim 10^2 - 10^3$ km). Because of the difficulty of finding an analytical solution to the problem it was treated numerically, and restricted to only one dimension. The initial aim was to investigate the form of the angular spectrum arising from such a power law model for the scattering irregularities, and to see whether it differed significantly from the Gaussian form which we have shown was able to predict brightness distributions similar to those observed. The auto-correlation function $\rho_{\Delta N}(r)$, of the irregularities was established from the Fourier transform of P(q), the spatial power spectrum. The auto-correlation function $\rho_f(r)$, of the radiation received by the observer was found using a result of Bramley (1955), $\rho_f(r) = \exp\left\{-\phi_o^2\left[1 - \rho_{\Delta N}(r)\right]\right\}$, where ϕ_o is the standard deviation of the phase variation across the diffracting medium. Another Fourier transform gave the required result, the angular spectrum F(Θ),

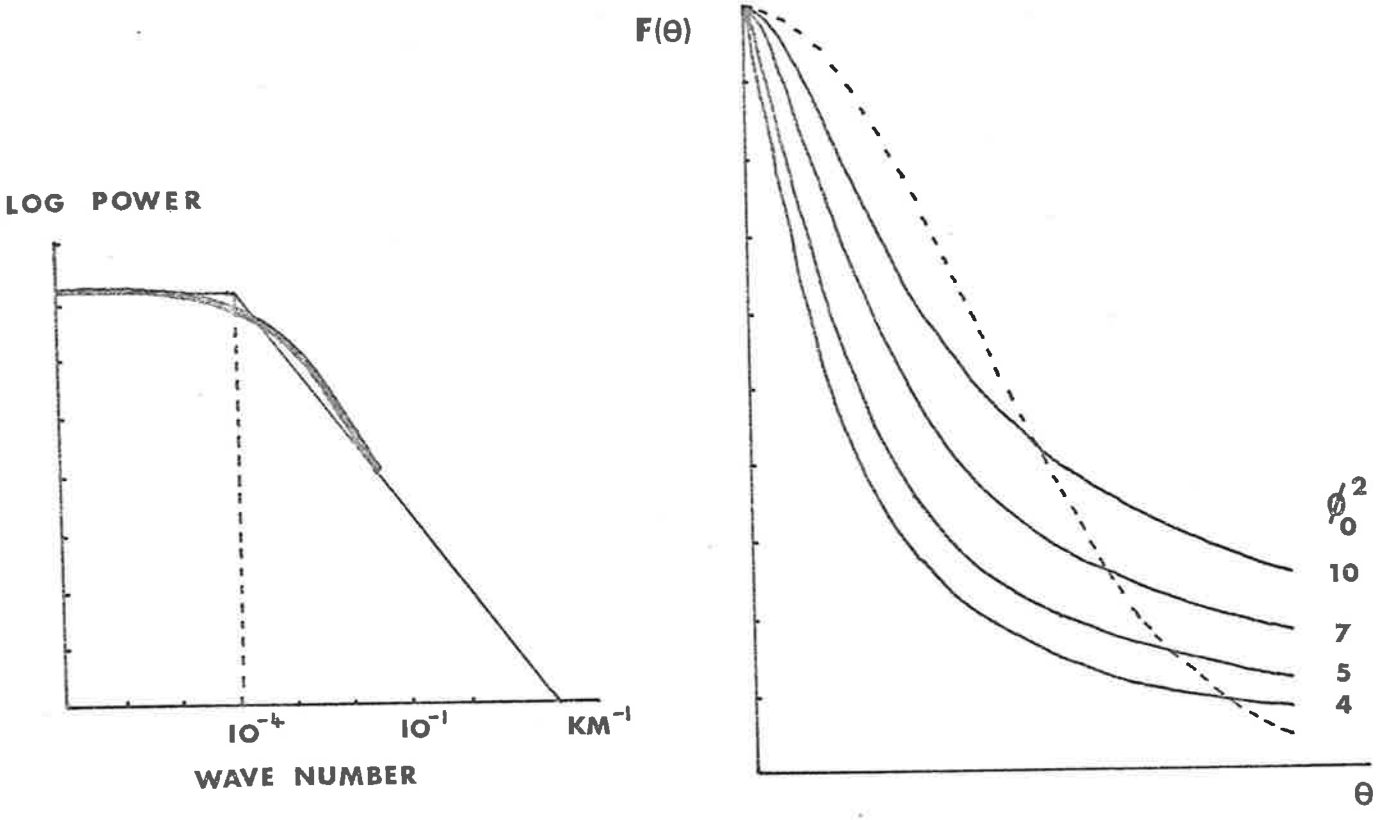

(a)

(b)

Figure 3.14 (a) Power spectrum of magnetic field irregularities in the interplanetary medium (thick line) and the approximation for calculating the theoretical angular spectra

(b) Theoretical angular spectra for different values of the phase variation ϕ_0 compared with a Gaussian curve from the relation $\rho_f(r) \overset{FT}{\leftrightarrow} |F(\Theta)|^2$. Computed curves of $F(\Theta)$ for different values of ϕ_o^2 are shown in Figure 3.14(b) compared with a Gaussian curve. The axes are drawn to arbitrary scales since the main interest is a comparison of the shapes of the spectra. There is obviously a large difference between the angular spectra of the two models, the power law model falling off more rapidly for small Θ but having an extended tail. It should be noted that the curves in Figure 3.14(b) have been normalised to the same height at the origin, whereas physically the total area under each curve must remain constant to conserve energy. Thus, for larger values of the phase deviation ϕ_o, proportionally more power is scattered out to large angles. The radial cross-section of the brightness distribution produced by irregularities represented by a modified power law spatial power spectrum would therefore have a shape similar to $F(\Theta)$, but extended somewhat towards the sun. None of the observed images had cross-sections of such a form. An assumption we have made however, is that the region producing the greatest scattering was confined to a relatively thin layer. In view of the rapid decrease in the phase deviation ϕ_o, with radial distance from the sun, the majority of the scattering can be assumed to take place in a layer of thickness equal to the distance of the source from the sun. Close to the sun we would therefore expect a thin layer to be a good approximation. A crude evaluation of the effects of a thick layer can be achieved by dividing the region into a number of thin layers, computing the brightness distribution of each and adding the results.

This obviously will produce an angular spectrum with a less prominent tail but it still would be non-Gaussian for large values of ϕ_o. The result of this approximation is valid only for a limited number of layers because statistically the angular distribution would approach a Gaussian form as the number of layers was increased. It would appear then, that a power law spectrum of the scattering irregularities would produce brightness distributions noticeably different to those predicted by a Gaussian model. The latter model implies a single well-defined scale structure in the interplanetary medium responsible for the scattering, rather than a range of scales which would be admitted by a power law model. We stress again the remarkably close agreement between the predictions of the Gaussian model and the observed distributions. To make this point even clearer, and to stress the sensitivity of the observations to the form of the angular spectrum, we have considered a power law form of the angular spectrum but modified in such a way as to give the closest possible agreement with the observed brightness distribution. The modification consisted in restricting the scattered power to a constant value within a scattering angle Θ_m, and in selecting a power law index for the remainder of the spectrum to give the closest fit to the observed brightness distribution. The parameters of the model are illustrated in Figure 3.14(c), and an example of such a computed distribution is shown in Figure 3.14(d) compared to the observed distribution and to a distribution computed using the Gaussian model. Even though the parameters of the model were chosen to give the

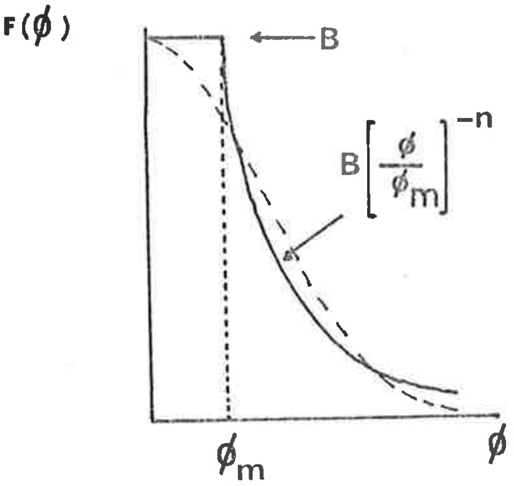

Figure 3.14 (c) A power law model for the angular spectrum with a Gaussian curve shown for comparison

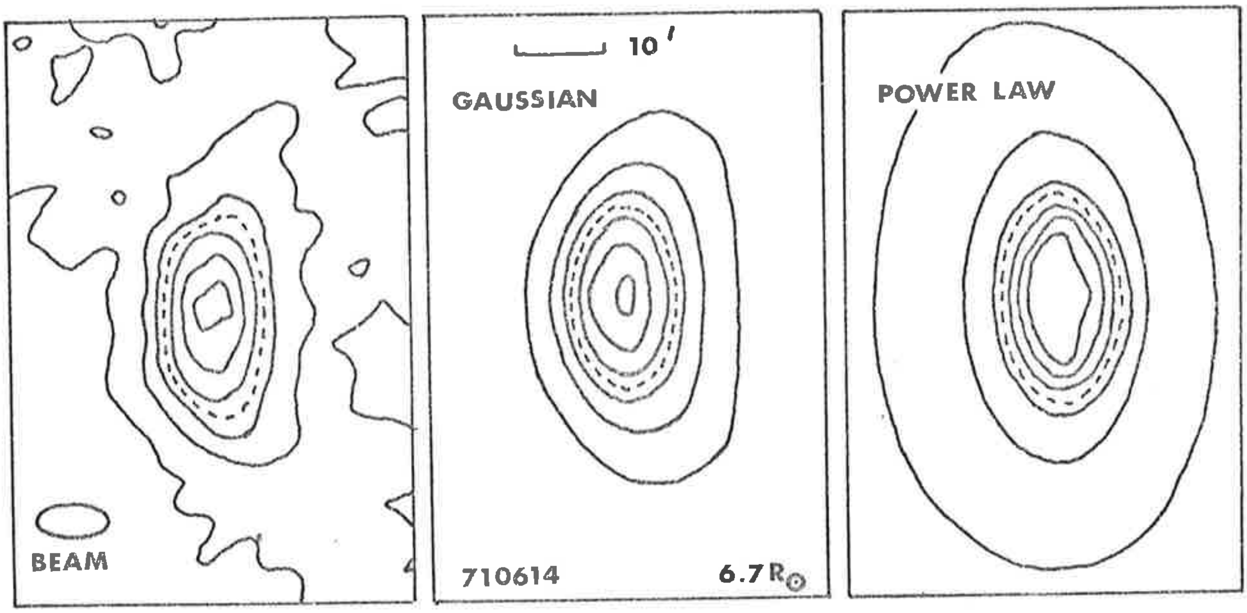
BEAM
10′
GAUSSIAN
710614
6.7 $R_\odot$
POWER LAW

Figure 3.14 (d) Two theoretical brightness distributions of the Crab Nebula compared with an observed distribution closest fit to the observations, it is clear that significant differences still remain in the form of a 'flat top' and extended tail to the power law prediction.

From the work that has been described it is clear that the Gaussian model shows the best agreement with the observational data. We conclude that the spatial power spectrum of the irregularities causing the scattering is also of a Gaussian form, implying that these irregularities possess a single dominant scale structure.

3.6 Unusual Events

Throughout this chapter we have mentioned the occurrence of unusual events or formations of the observed image. We shall now discuss these and other features in more detail and propose explanations for them. One event concerns the angular broadening of 3C123 while the others all relate to the Crab Nebula.

3.6.1 Angular Broadening of 3C123

The only observed angular broadening of 3C123 occurred on May 31st 1969 and was recorded as a series of drift scans on paper chart. Analysis revealed an increase in angular size of about 7' arc in both the N-S and E-W directions of the image. The position of 3C123 in relation to the sun is shown in Figure 3.15(a) and during the observation the line of sight to the source passed the sun at a distance

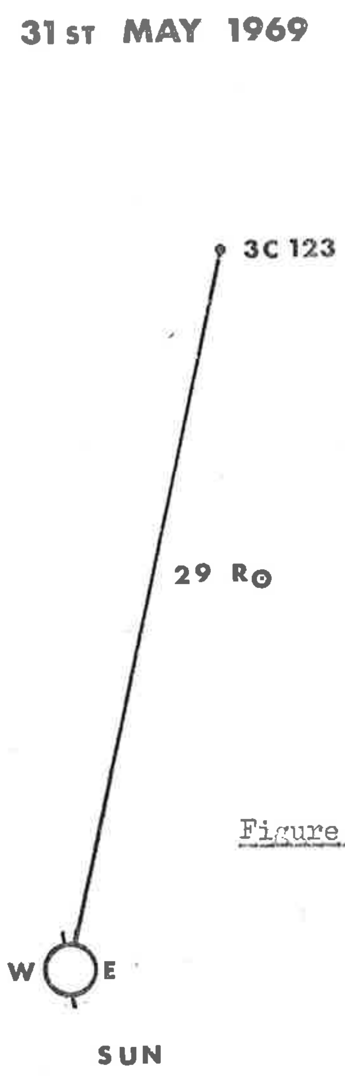
31 ST MAY 1969
3C 123
29 R⊙
W
E
SUN

Figure 3.15 (a) Position of 3C123 in relation to the sun on the 31st May, 1969.

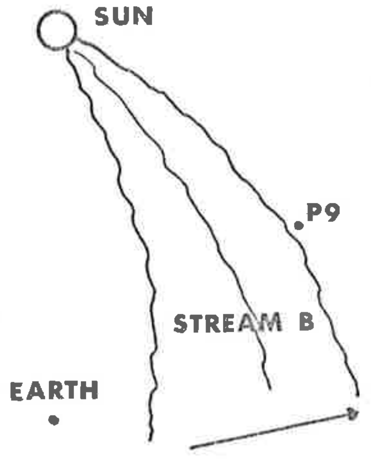
SUN
P9
STREAM B
EARTH

Figure 3.15 (b) Position of a corotating stream during 31st May, 1969.

of 29 $R_\odot$. On the basis of the Crab Nebula observations described earlier in this chapter we would expect, under normal conditions, a broadening of only 1.3' arc at this distance from the sun, a value undetectable by the radioheliograph. It was seen earlier (Section 1.2) that the broadening of a source is related principally to the electron density fluctuation and the irregularity size in the medium. An increase in the former, or a decrease in the latter, could cause enhanced broadening. The increases in broadening observed here could have been caused by an increase in the rms fluctuation of the electron density by a factor of 2.3, a decrease in scale size by a factor of 5.4, or a combination of both. The former effect however, would seem to be the most likely cause.

Any disturbance close to the ecliptic such as a corotating stream with a typical cone angle of 30° would not have crossed the line of sight from the source until well into the interplanetary medium at a distance of about 70 $R_\odot$ from the sun. Therefore an exceptionally strong disturbance would have been necessary to propagate this distance and still produce the required enhancement, dominating the scattering normally confined to the regions of the line of sight closest to the sun. A corotating stream was in fact present at the time with a position shown in Figure 3.15(b), (Wiseman and Dennison, 1972). Also shown in the figure is the location of Pioneer 9 from which Croft (1971) has deduced electron densities of the interplanetary medium. There were no sudden increases observed during the period June 1-3 although the data were widely spaced and the results inconclusive.

A wide angle emission or plasma blast wave from the sun would have crossed the line of sight before travelling much further than 40-50 $R_\odot$. However, its effect would have been noticed on other sources by an increase in scintillation index as it moved outward from the sun. No significant increases were observed (Wiseman, 1972).

We therefore have no definite evidence to help explain the angular broadening of 3C123 although we do know there was an active region on the western limb of the sun at N10° to which the previously mentioned plasma stream was attached. A sudden ejection of high velocity plasma may have produced a 'kink' in the stream causing it to move across the line of sight to 3C123 at a distance closer to the sun and hence account for the broadening. The active region in question produced a class 2 flare on May 28th and was therefore moderately active.

Additional information relevant to this event comes from studies of the inner coronal magnetic field configuration by Newkirk and Altschuler (private communication). These authors have computed the theoretical field configuration out to 2.5 $R_\odot$ based on observations of the photospheric field made at Mt. Wilson. Their basic data were averaged over the solar rotation during which our observations were made and do not therefore include any short term changes in the field. The computed field configuration on May 31st is shown in Figure 3.16(a). We note again that this configuration is an average over a complete solar rotation interval. To illustrate its three-dimensional structure the same configuration as seen from the Earth 4.5 days earlier is shown in Figure 3.16(b). It is seen that the north polar region of the sun shows a most unusual arched field configuration extending out in the direction of the line of sight. The loop, whilst being rooted to two surface regions (one behind the sun) separated by $\sim 40^{\circ}$, is extremely narrow in the direction transverse to the line joining the two base regions. It is possible that such a field configuration might have restricted the outflow of plasma to a similar, narrow wedge-like stream. Such a situation would explain the absence of enhanced broadening on the days after the observation when the source had moved out of the stream. The region behind the sun to which the loop was attached was probably McMath Plage 10088. This region was relatively active, a class 3B flare being observed on June 12th.

We are therefore faced with an alternative explanation for the event in terms of an unusual polar field configuration underneath the line of sight. Whether this field configuration was related to activity on the sun is open to question since the associated regions were behind the sun at the time of our observation. Further than outline these various possibilities it seems difficult to draw any firm conclusions in

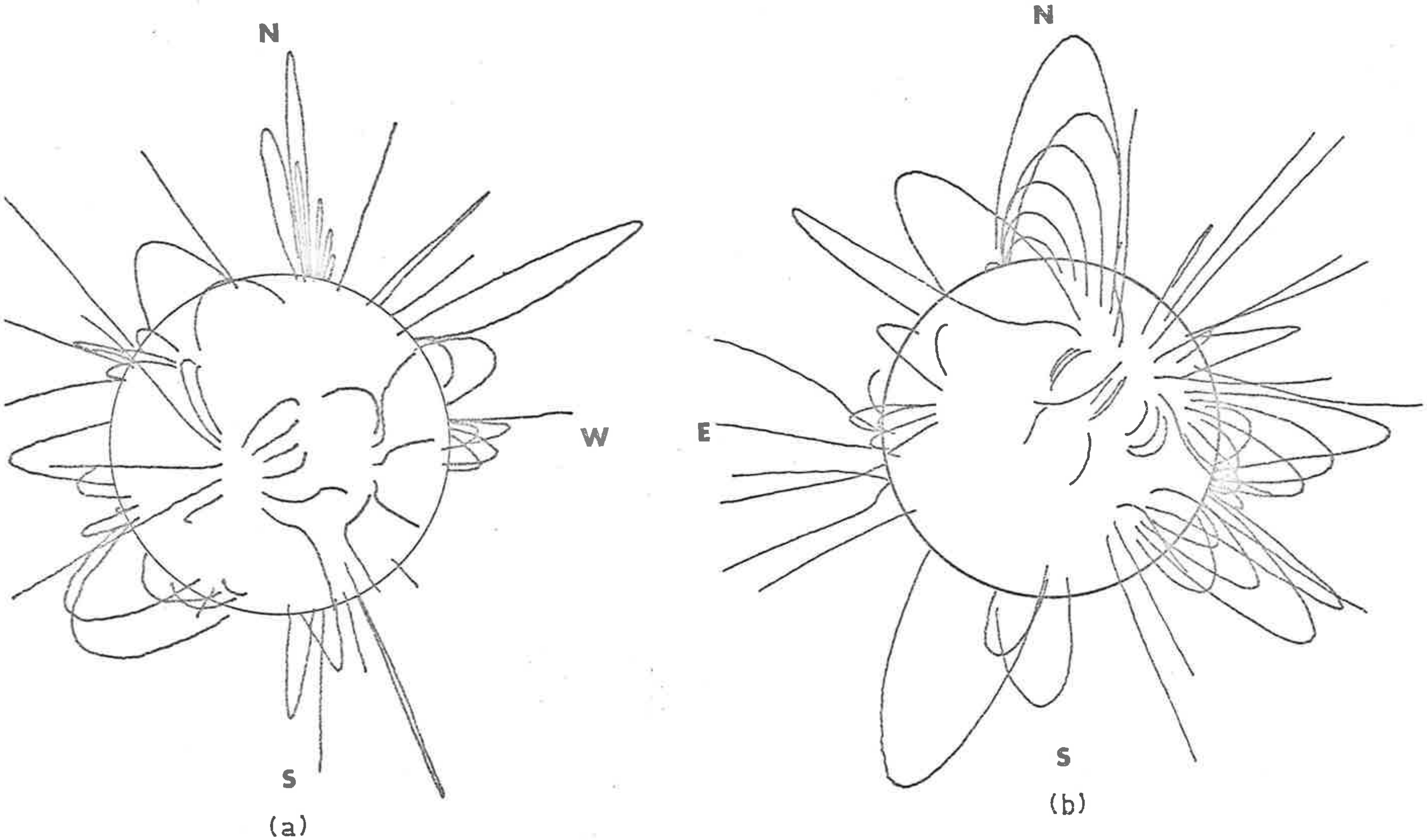

Figure 3.16 (a) Solar magnetic field configuration during 31st May, 1969.
(b) The same field configuration viewed after rotating through 220° revealing the structure of the prominent loop.

the absence of other relevant information.

3.6.2 Sporadic Angular Broadening of the Crab Nebula

During an observation of the Crab Nebula on June 9th, 1969, the source suddenly increased in size, remaining broadened for about 6 min. In addition rapid variations in the shape of the image occurred and Table 3.2, describing the sequence of changes, was compiled from photographic records and contour plots integrated over 8 and 15 sec respectively. Also, Figure 3.17 shows a series of photographs of the source taken during the event, and Figure 3.18 shows selected contour plots of the broadened source.

Because of the rapid changes involved, both ionospheric and interplanetary origins were investigated as possible causes. Three outstanding features were noticeable as seen in Figures 3.17 and 3.18. Firstly, a predominantly E-W angular broadening was apparent, lasting for about 30 sec. Secondly, a narrow extension developed on the northern edge and moved along the image towards the sun simultaneous to the image becoming broadened again in the E-W direction; and finally the symmetry of the main body of the image changed, producing on the eastern side a tapered tail which eventually disappeared leaving an unbroadened image.

From examination of Figure 3.18(a) (and 3.18(c)) the increase in E-W width was symmetrical indicating the effect to be largely due to

Sidereal Time	Shape of source image
051247*	Slight E-W broadening
051255	Broadening increased
051303	Broadening decreased
051319	Image normal size
051355*	Image normal size
051439	Image normal size
051447*	E-W broadening again. Evidence of Nth extension
051507*	Broadening increased. Extension more prominent
051515*	Broadening constant. Extension moved towards sun
051531*	Broadening constant. Extension at end of image and most prominent
051547	Broadening decreased. Extension diminished
051623*	Image developing tail. Extension diminished
051659*	Tail fully developed. Extension disappeared
051707	Tail diminishing
051743	Tail disappeared
051811*	Image normal size

*Correspond to photographs of the image in Figure 3.17.

Table 3.2

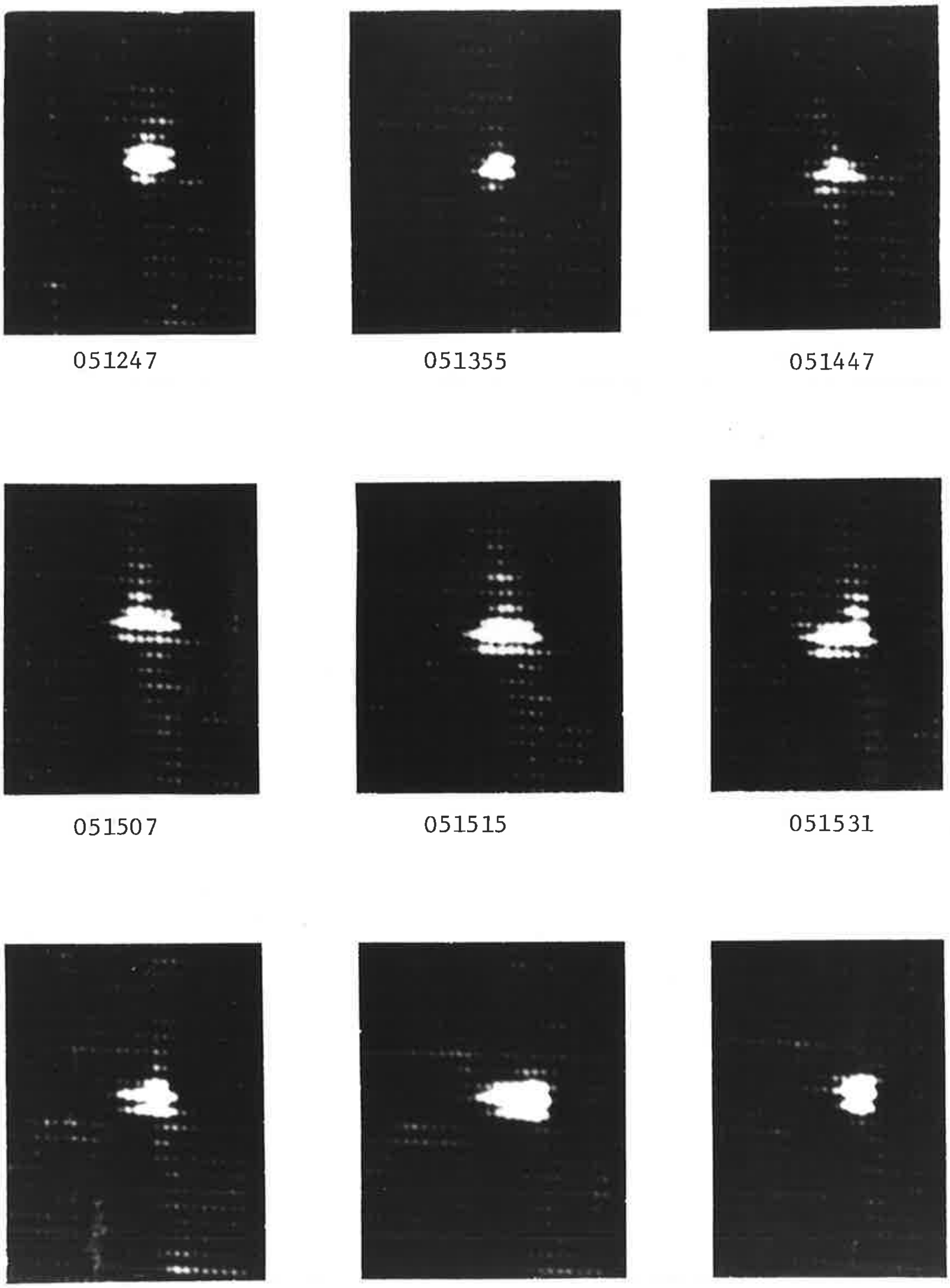

051247

051355

051447

051507

051515

051531

051623

051659

051811

Figure 3.17 Selected frames recorded during 9th June 1969

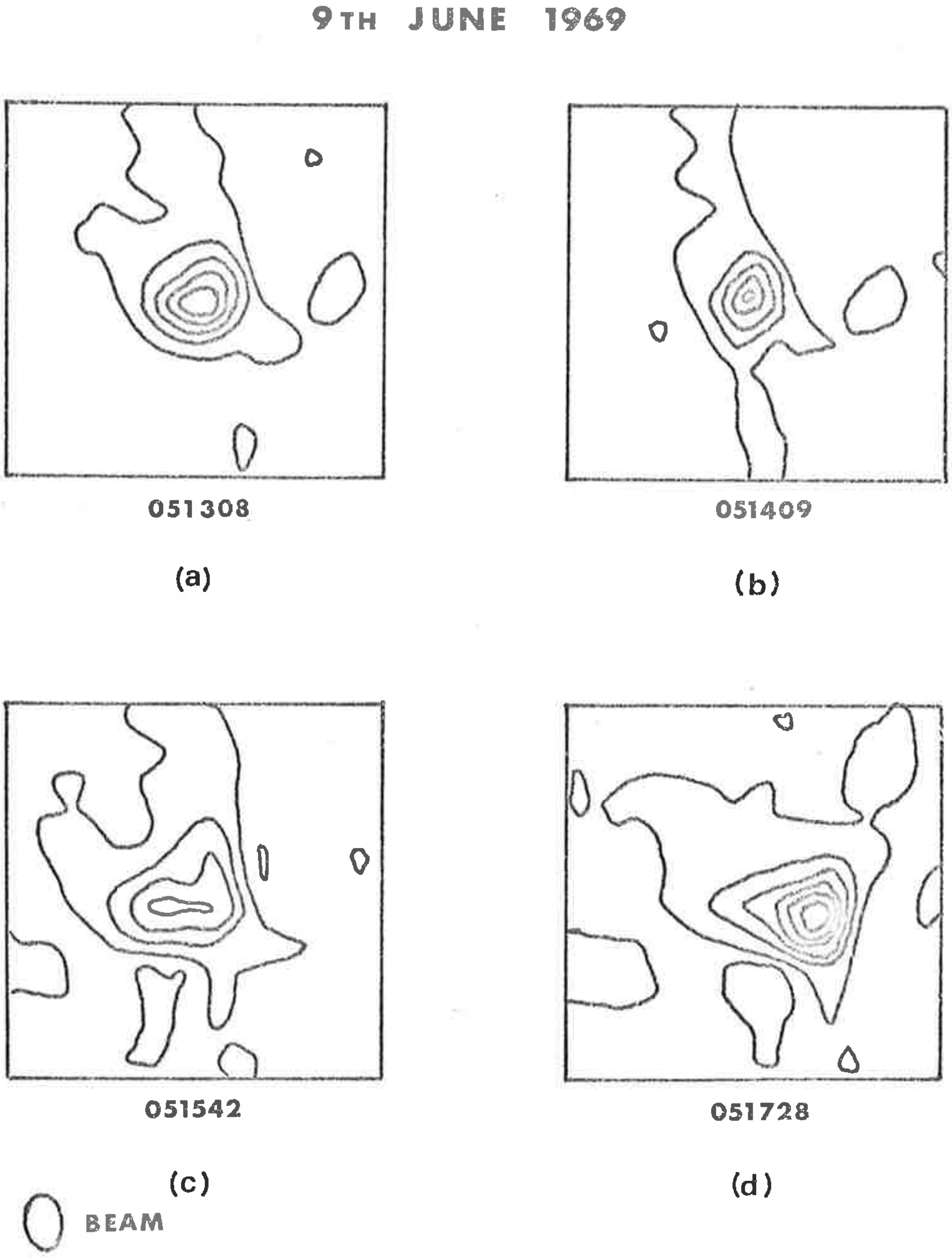

Figure 3.18 Selected contour plots at indicated sidereal times of the observed image of the Crab Nebula on the 9th June, 1969

diffraction rather than refraction. If the diffraction occurred under weak scattering conditions with ϕ_o, the rms phase deviation, less than one radian, then the angle of scattering, Θ would be dependent on the observing wavelength λ, and the scale of the irregularities a, according to the relation $\Theta \sim \frac{\lambda}{a}$. The measured angle of scattering was 6' arc, implying an irregularity scale of ∿2.1 km. Irregularities of such a small size suggest that the diffracting region may have been situated in the ionosphere. This could automatically account for the predominantly E-W nature of the angular broadening because ionospheric irregularities are elongated, approximately N-S, along the terrestrial magnetic field lines. In the case of multiple scattering when $\phi_o > 1$, $\Theta \sim \frac{\lambda\phi_o}{a}$ and the scale would be greater than 2.1 km.

Assuming the broadening was due to ionospheric irregularities situated in a layer at a typical height of 300 km, the maximum width of the region contributing to the signal received within a cone angle of 6' arc would have been only ∿1 km. We therefore have an irregularity scale of the same size as the scattering region, a situation which would not give rise to angular broadening.

In view of the E-W broadening being an unlikely ionospheric effect we shall consider an interplanetary origin of the phenomenon. Within the interplanetary medium we need the irregularities elongated N-S, in the tangential direction, which is contrary to results of other observations. However, at the time of observation, two corotating plasma streams intersected the line of sight to the Crab Nebula as shown in Figure 3.19(a). The leading edge of the stream moving behind the sun may have been responsible for the enhancement as it met and overlapped the line of sight. The irregularity alignment would have been almost parallel to the line of sight. However, in a plane perpendicular to the line of sight as seen by an observer, it is feasible that the irregularities may have had a cross-section elongated perpendicular to the ecliptic and this could have caused the observed E-W broadening of the source.

The tail protruding from the image, shown in Figure 3.18(d), may have been due to refraction by a gradient in the electron density, increasing towards the sun. Such a gradient would be found in the leading edge of a stream which would have a cross-section similar to Figure 3.19(b), derived from spacecraft data (Carovillano and Siscoe, 1969). The diagram actually refers to the boundary of a sector but a similar structure might be expected at the edge of a stream, with perhaps greater variations in electron density. The initial increase in electron density would have provided the necessary gradient for the observed refraction. To determine the feasibility of this postulate we will calculate the electron density gradient required to produce the extended tail. The geometry of the stream structure in the interplanetary medium at the time of observation is shown in Figure

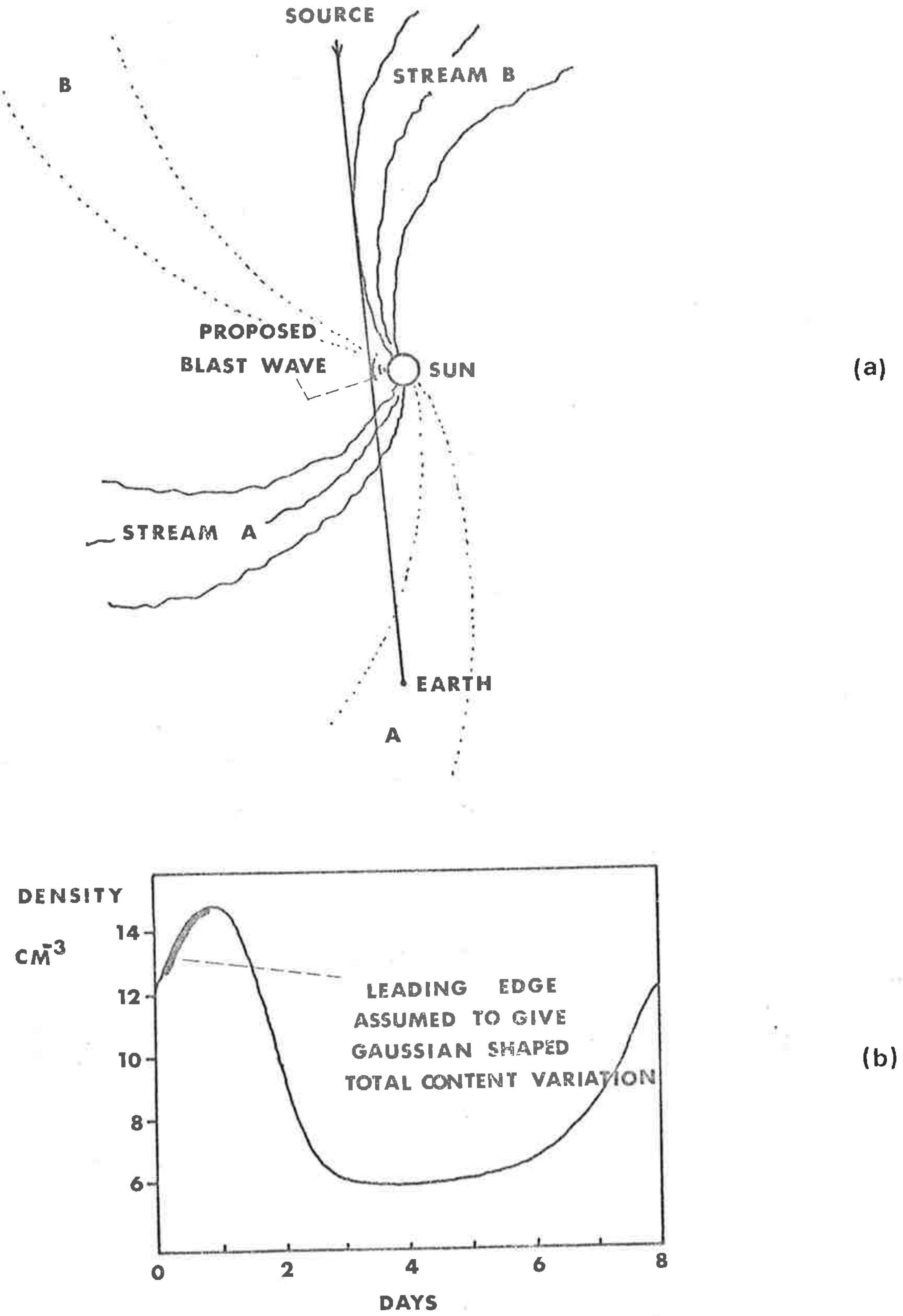
SOURCE
STREAM B
B
PROPOSED
BLAST WAVE
SUN
(a)
STREAM A
EARTH
A
DENSITY
CM^{-3}
14
12
10
8
6
LEADING EDGE
ASSUMED TO GIVE
GAUSSIAN SHAPED
TOTAL CONTENT VARIATION
(b)
0
2
4
6
8
DAYS

Figure 3.19 (a) Stream geometry during 9th June, 1969 and 13th June (dotted line).

(b) Proton (or electron) density variation across a sector.

3.19(a). We shall assume the density profile of the stream varied in such a way that the cross-section of the total electron constant N, of the enhancement responsible for the refraction could be represented by part of a Gaussian, as shown in Figure 3.19(b). Therefore $N = N_o \exp\left(-\frac{x^2}{x_o^2}\right)$, where N_o is the maximum value of the total content of the enhancement and x_o the half width. The angle of refraction β, proportional to the derivative of the total content, in this case has a maximum value,

$$\beta_{max} = \frac{No}{\sqrt{2}\, x_o} \cdot \frac{e^2}{\varepsilon_o\, m\, \omega^2} = \frac{No}{\sqrt{2}\, x_o} \quad 7.95 \times 10^{-13} \text{ radians}$$

with N_o expressed in electrons m^{-2} and x_o in metres. From measurement, the maximum angle of refraction β, was roughly 6-8' arc, implying a corresponding gradient in the electron density of

$$\frac{No}{x_o} = 2.08 \times 10^9 \text{ electrons } m^{-2}/m.$$

Taking $x_o = 5 \times 10^6$ km, a value equal to $\frac{1}{10}$th of the width of a typical stream measured at 0.5 A.U. from the sun, the total content becomes $N_o \simeq 10^{19}$ electrons $m^{-2} \equiv 10^{15}$ electrons cm^{-2}. If the enhancement was spread along the line of sight for 0.1 A.U. the corresponding increase in electron density within this region would have been $\sim 6 \times 10^2$ electrons cm^{-3} which is about an order of magnitude greater than the ambient electron density at 0.5 A.U. Larger values of x_o require correspondingly larger increases in electron density over the same distance along the line of sight.

The rate at which the stream would have swept past the line of sight was ~ 500 Km $\sec^{-1}$. Since the refraction lasted for about 1-2 min the width of the enhancement within the stream boundary was only $\sim 6 \times 10^4$ km, a value small in comparison to the total width of the stream. This model therefore implies a very localised region of increased electron content at the boundary of the stream. The values we have estimated for the size of the region and the increase in electron density indicate that this refraction model could be a valid explanation for the observed shape of the image. Stream A was also crossing the line of sight to the source and although it was possibly disturbed during the 9th by strong flares occurring on the 5th (class 1B and 3B), 6th (class 2B) and 7th (class 2N and 2B), an explanation in terms of this region proved unrealistic.

To be of ionospheric origin we require a single irregularity acting as a lens. Since the tail on the image lasted for about 1 min this situation appears extremely unlikely, requiring the irregularity to remain almost stationary during the 1 min period.

The results therefore tend to indicate an interplanetary origin for the event. Another possibility along these lines, explaining both the E-W broadening and the extended tail on the image, would be a blast wave of enhanced plasma density moving outwards from the sun and intersecting the line of sight as indicated in Figure 3.19(a). We must again, however, postulate irregularities elongated in a N-S direction to explain the predominantly E-W scattering. Within the boundary of the blast wave we would expect electron density gradients to account for the refraction in a way similar to that of the corotating stream model. The velocity of a blast wave at 21 $R_\odot$ from the sun may be 1000 km sec^{-1} or greater and we might expect the existence of steeper gradients in electron density compared to those found within a stream. We can estimate the thickness of this plasma enhancement since we know the total duration of the event, being about 6 min. At a velocity of 1000 km sec^{-1} this implies that the region responsible for the observed changes in the shape of the image was $\sim 3.6 \times 10^5$ km in width. This width is at least two orders of magnitude less than the width of a corotating stream (at 0.5 A.U.). The occurrence of the required scattering region and density gradient within a plasma blast wave seems even more feasible than their occurrence in a stream, and the blast wave alternative might appear more attractive. It should be noted, however, that the width of the blast derived above is very close to the size of the scattering region implied by the observed ($\sim$6' arc) angular spectrum. Thus the velocity, $\sim$ 1000 km sec^{-1}, used in the calculation must represent a lower limit to the velocity of a blast wave if this were the cause of the event. Also, no evidence of the blast wave was found during analysis of the scintillation data (Wiseman, 1972) suggesting that perhaps the corotating stream was responsible for the unusual event.

The feature which has not yet been mentioned is the northern extension of the source shown in Figure 3.19(c). As indicated in Table 3.1 it moved from the outermost side of the source towards the sun and remained prominant at the end of the image for about 30 sec. An explanation of this effect has proved very difficult because a thin diffracting layer would produce an extension to the south as well as the observed northern extension. The odd aspect of this feature is the movement towards the sun defying all explanation. Both interplanetary and ionospheric origins were considered but required unrealistic electron density gradients and irregularity structures. The northern extension therefore remains unexplained.

3.6.3 Increased curvature of the Image

During the second observation on June 13th, 1969 the image of the Crab Nebula was curved to an extent greater than expected as shown in Figure 3.20(a). The effect was noticed mainly on the side of the image nearest the sun.

One possible explanation involves the magnetic field lines from the sun diverging at an angle greater than the normal radial divergence. Such a situation could arise above a helmet field structure in the corona. However, the source was 8 $R_\odot$ from the sun, a distance at which the field would normally be completely dominated by the radially outflowing plasma, particularly at solar maximum.

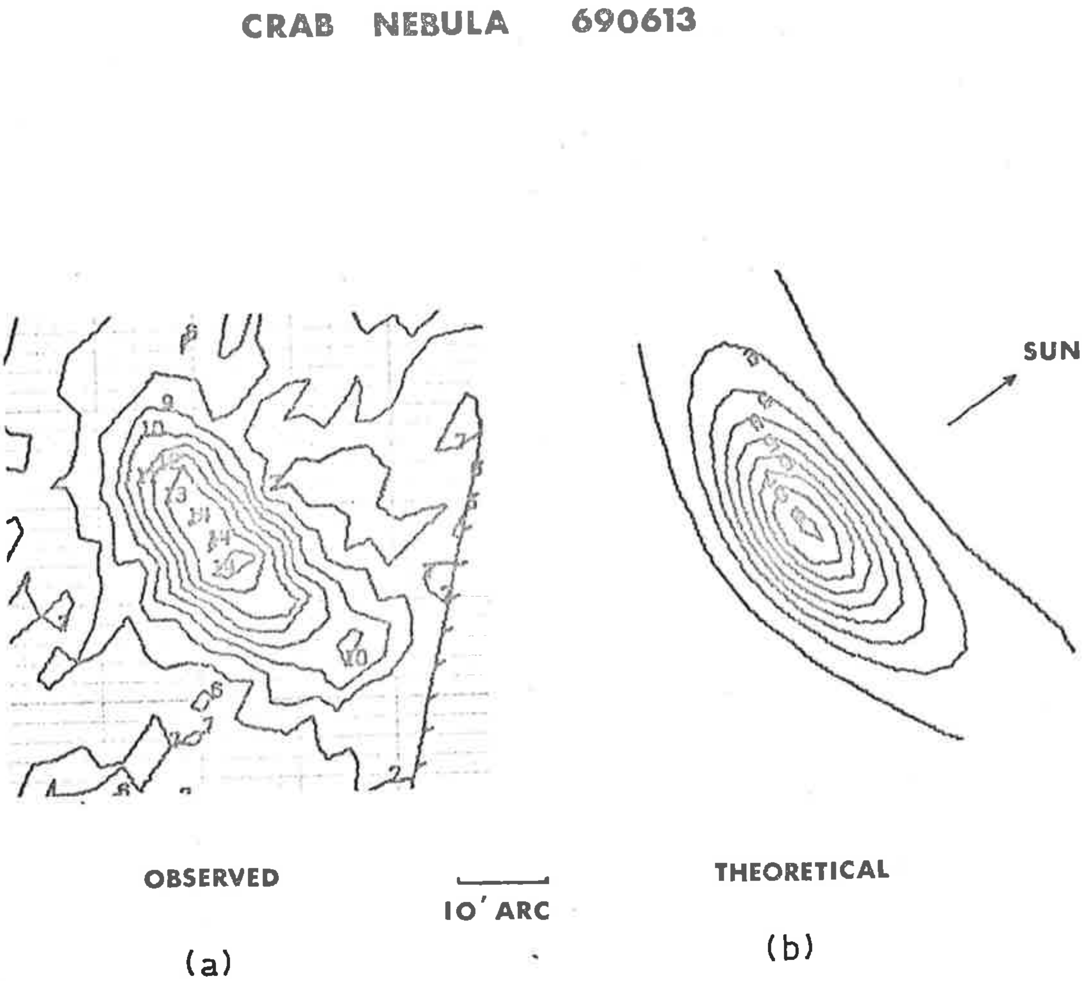

Figure 3.20 Observed brightness distribution of an unusually curved image of the Crab Nebula compared to the theoretical distribution

The second possibility involves a variation in the plasma moving outward from the sun, and we consider a decrease in the scattering power of the medium at the centre of the image. This could have arisen from an increase in scale or decrease in electron density of the irregularities related to a filamentary structure intersecting the line of sight. Using the Gaussian model described in Section 3.5 a theoretical brightness distribution was calculated assuming ϕ_R, the degree of scattering in the radial direction, decreased toward the centre of the source. The result is illustrated in Figure 3.20(b) with ϕ_R having a Gaussian dependence on α (which has the same meaning as in Section 3.5). For this model, when α varied from 30° to 0°, ϕ_R decreased by about 60%.

An analysis of interplanetary scintillation data by Wiseman and Dennison (1972) indicated the presence of two corotating streams situated, during our observation, on the same side of the sun as the Crab Nebula. These are illustrated in Figure 3.19(a). The source had an ecliptic latitude of -35° and to explain our observation we must again postulate activity in a region well away from the ecliptic if our observation is a true indication that the medium was non-uniform at the time. Either of the active regions on the sun associated with these streams may have been the cause of the curvature of the image although region A as indicated by Wiseman and Dennison (1972) was the stronger of the two. There was no obvious activity before the 13th which might have been associated with the observed phenomenon.

3.6.4 A Rapid Decrease in Angular Broadening

The three observations of the Crab Nebula during June 17th, 1969 showed a rapid decrease in the angular broadening over a period of 3 hr. During the first observation the source was not visible at all, however it appeared slightly above the background for the second observation and was fully visible for the third although the background noise was similar for each occasion. This event had no direct correlation with any solar activity, although stream A, mentioned in the previous subsection, had moved around the western limb of the sun. It was therefore near the line of sight to the source and may have produced the rapid change in angular broadening although no large flares were observed just prior to June 17th.

3.6.5 Unusual Orientation of the Image of the Crab Nebula

A N-S orientation of the image persisted on June 12th, 1970 and is clearly visible on Figure 3.1, the composite photograph of the observations. This orientation was considerably different from the more normal tangential orientation observed, being $\sim 20^{\circ}$ from the tangential direction. On this occasion the source was only 15° below the plane of the ecliptic and the line of sight was in reach of corotating structure in the interplanetary medium. At the time three streams were present in the medium (Wiseman, 1972) and from the high degree of scintillation on most sources it was concluded that the whole interplanetary medium was somewhat disturbed. However, no direct correlation between flare activity and the non-tangential alignment of the source image was found.

3.6.6 Unusually Large Broadening During 1971

On June 16th and 17th, 1971, the images were broadened to a greater extent than expected from observations at corresponding distances from the sun during the approach of the Crab Nebula. The effect is shown clearly in Figure 3.1 where the source was observed on the 15th and 16th at similar distances from the sun, but was broadened to a considerably greater extent on the latter occasion. No details were known about the medium at this time although an active region on the sun moved off the western limb on the 18th. This region may have been responsible for the increase in scattering.

3.7 Summary

In this chapter we have discussed the first two-dimensional recordings of the broadened Crab Nebula which have allowed direct observation of the size, shape and orientation of the image. Measurements of the degree of broadening were shown to agree well with the angular broadening studies of other authors during previous years.

It is significant that the observed axial ratio estimated for the irregularities within the solar corona was approximately equal to that derived from interplanetary scintillation measurements. In addition the elongation of these irregularities was ∿2-3:1 increasing towards the sun, and their orientation was radial indicating that the solar magnetic field was radial as close to the sun as 5 $R_\odot$.

Remarkable similarity was found between theoretical brightness distributions and the observed distributions, suggesting that the irregularity structure within the scattering corona may be closely Gaussian. However, further theoretical work concerning scattering in the regions close to the sun must be carried out before other forms of irregularity structures (such as the modified power law) are completely ruled out. In particular such work should investigate more thoroughly the effects of an extended scattering layer on the form of the angular spectrum.

Several unusual image formations and short term variations have been examined and are believed to have been related to activity in the interplanetary medium, either in the form of corotating streams of plasma or flare-induced blasts.

CHAPTER 4

IONOSPHERIC REFRACTION

Data in the form of usually 2 or 3 drift scans of each radio source observed during interplanetary scintillation studies, and also data consisting of up to 30 or more successive scans of the Crab Nebula, 3C123 and other sources, have provided a means for investigating the effects of the ionosphere on the apparent positions of extraterrestrial sources of radiation. The two forms of data were treated differently. The first gave a statistical coverage of refraction, since sources were observed over a wide range of declination and local times on each day. The second form allowed the apparent position of the source to be followed in two dimensions; the extent and pattern of this movement provided more detail about the irregularities in the ionosphere which might be causing the refraction.

A description of the methods by which the data were obtained was given in Section 2.5. We will now discuss the analysis and presentation of the data, following with a brief summary of the current knowledge of disturbances in the ionosphere. The results will then be explained in terms of these disturbances and finally the bearing of this study on radio-astronomical work, particularly in the metre wavelength range will be discussed.

4.1 Analysis and Results

Initially, both the statistical data and the data consisting of long series of scans were analysed in the same manner. First the heights of the scans on each beam and their times of arrival were read from the charts and listed with the corresponding hour-angles of the central beam. The declination setting of the beam was also noted for each source, and its right ascension - declination coordinates were selected by choosing the most accurate values available from a number of surveys conducted at the Royal Radar Establishment, U.K. and at Parkes, N.S.W.

From the beam heights of a given scan the apparent declination of the source was estimated utilising the formula introduced in Section 3.3. The hour-angle was calculated from the measured time of arrival of the source and the hour-angle of the beam. Subtraction of the known source coordinates from the measured values provided deviations, in declination and hour-angle, of the source from its true position.

The first major observing session at Culgoora, extending from September 24th to October 10th, 1968 was of a trial nature with the purpose of selecting a suitable grid of sources for later observations. Therefore, a large number of sources were covered and useful refraction information was extracted from about 60 of these. The number of observations of any one source ranged from 2 up to ~ 15. The statistical data from June 1969 and June 1970 consisted of daily observations of ∿35 radio sources over periods of about 20 days. During February, 1969 observations were made over 12 days but the number of useful records was reduced by 50% by electrical interference from local thunderstorms. Attempts were made to observe daily the same 35 radio sources as were recorded in the two later sessions.

Since the number of scans from one recorded observation of a source was usually two or three, the corresponding calculated deviations in declination and hour-angle were averaged over the observation to provide mean values which we shall identify by $\Delta\delta$ and Δh. The averaged values were treated as samples of ionospheric refraction at intervals of 15 - 30 min, which was roughly the average time between observations of successive sources. During all sessions we adhered to a relatively tight observing schedule, especially during June 1969 and 1970, allowing the broadening of the Crab Nebula to be recorded. Therefore, sources were observed at approximately the same sidereal times each day. In fact the rms deviation of this time was generally within $\pm \frac{3}{4}$ hr over the whole observing session. The distribution of $\Delta\delta$ and Δh for any source would be, within our error limites, unaffected by hour-angle dependencies although there would be a slight local time effect (2 hr per month) due to the different rates of the local and sidereal times. This variation also was only of $\sim\pm \frac{3}{4}$ hr and was treated as negligible. Therefore we assumed that the distributions of $\Delta\delta$ and Δh for each source were free from effects which may have been introduced by any dependencies on these parameters. The mean values, $\overline{\Delta\delta}$ and $\overline{\Delta h}$ of the distributions were calculated, and plotted against declination as shown in Figures 4.1 and 4.2. Positive values of $\overline{\Delta\delta}$ correspond to sources being observed at more northerly declinations than the catalogued values, and positive $\overline{\Delta h}$ values correspond to right ascensions less than the catalogued values. Although the average trends of the plots in Figure 4.1 appear to be in agreement over the four observing sessions, and similarly in Figure 4.2, there are large differences in the number of records of each source. During September and October 1968 the number of observations varied evenly between 2 and 10, with a few sources yielding up to ∿15 samples. However, in February 1969 we had only 2 to 6 observations per source, accounting for the increased scatter of the points compared with the September/October plot. Throughout the long observing sessions of June 1969 and 1970 the number of samples contributing to each of the points plotted was 20 - 25, and the scatter of $\overline{\Delta\delta}$, although greater than expected, appears to be slightly less than for the September/October distribution. This was not the case for the $\overline{\Delta h}$ values which showed a similar degree of scattering as in the January 1969 plot and a proposed explanation of this will be offered later in this section.

At this stage it is in order to discuss the errors involved in the recording and reading of the data. Because of the difficulty of

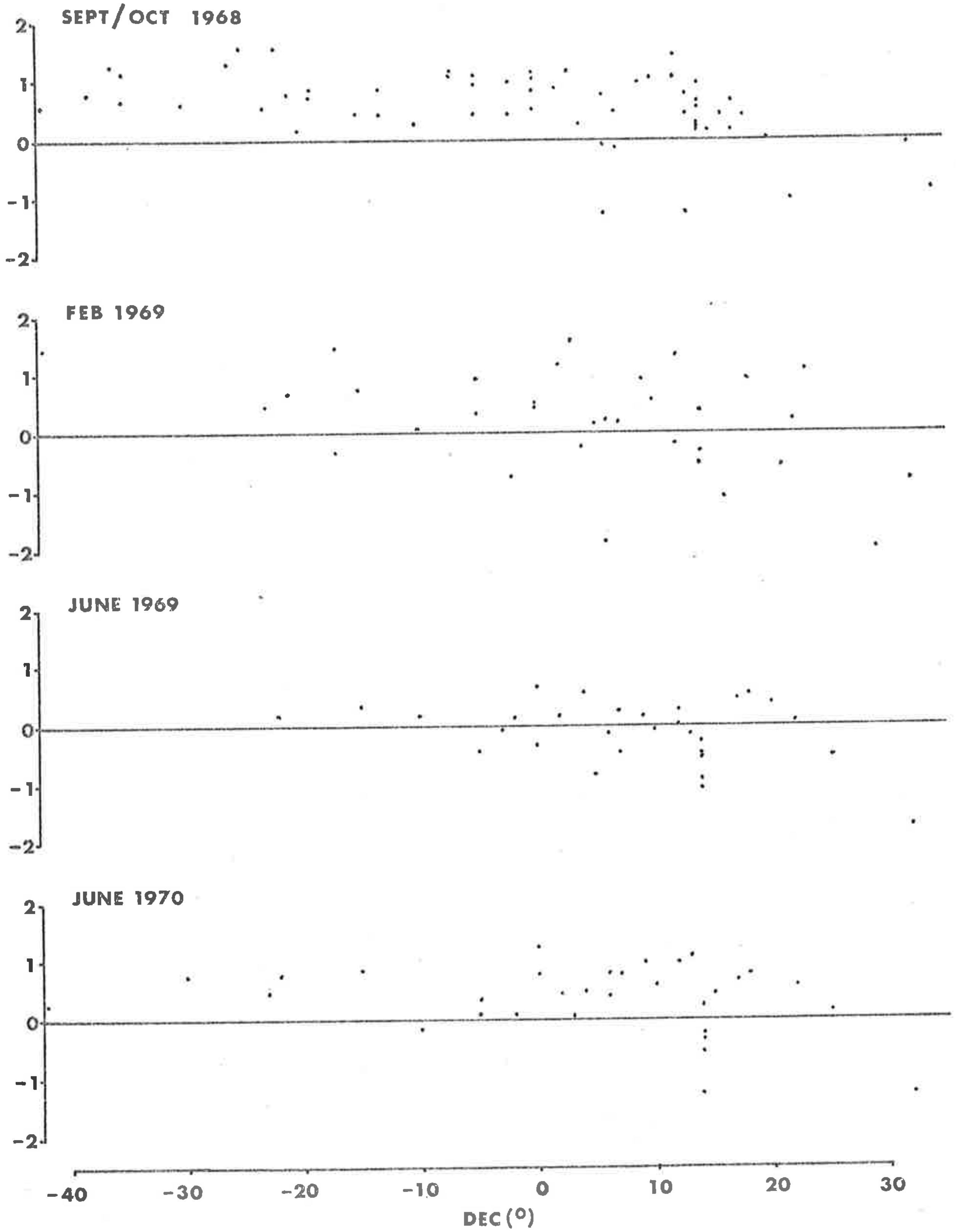

Figure 4.1 Plot of ΔS ('arc) against declination. (Each point represents an average for each source)

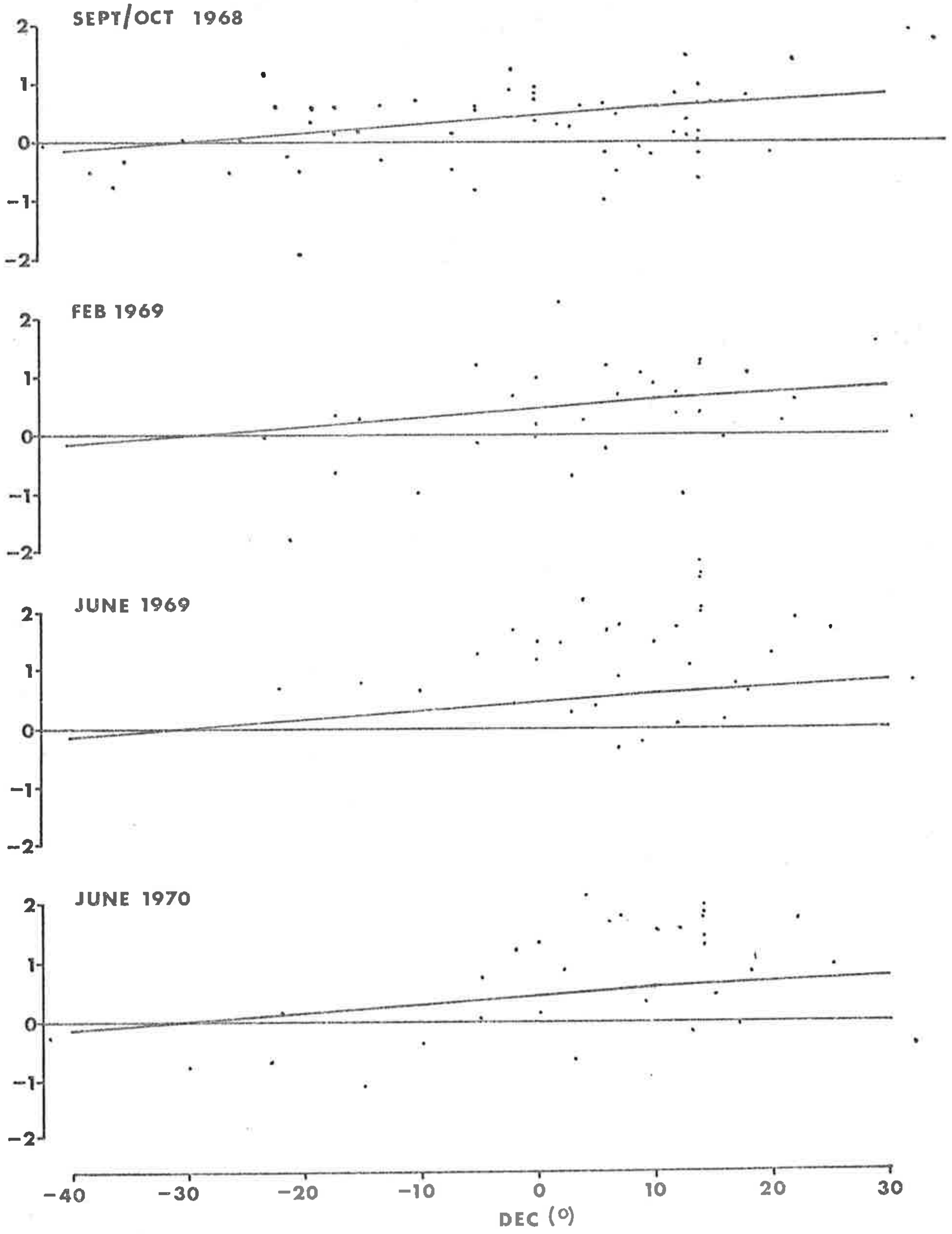

Figure 4.2 Plot of Δh ('arc) against declination. (Each point represents an average for each source). The solid line represents the known collimation error in the radioheliograph

estimating the baseline and height of a scan when the source was weak, or when it was scintillating strongly, larger errors were expected in the calculated declination values for such cases. To investigate the effect of source flux, the deviations in declination $\overline{\Delta\delta}$ from the 1969 data were plotted against source flux as shown in Figure 4.3. It would appear that no significant error was introduced in this way although the statistics are poor for strong sources. On the other hand the degree of interplanetary scintillation might well have influenced the observations, since during September/October 1968, when little scintillation was observed compared to the other three sessions, the source positions showed a significantly smaller spread.

As far as the hour-angle determinations were concerned, the errors in reading the charts were $\sim\pm 1$ sec in time, although the spread of the plots of $\overline{\Delta h}$ against declination in Figure 4.2 indicate that much larger errors were involved. These have been attributed largely to the inaccuracy of the sidereal times written on the charts. Since the last three observing sessions were primarily aimed at obtaining large amounts of interplanetary scintillation data with the study of ionospheric refraction a sideline, apparently not enough care was exercised in maintaining calibration of the sidereal clock. Also the time marker clock, which was set according to this main sidereal clock, tended to drift slowly out of phase causing the markers on the chart to appear at progressively different times within the minute. This effect, amounting

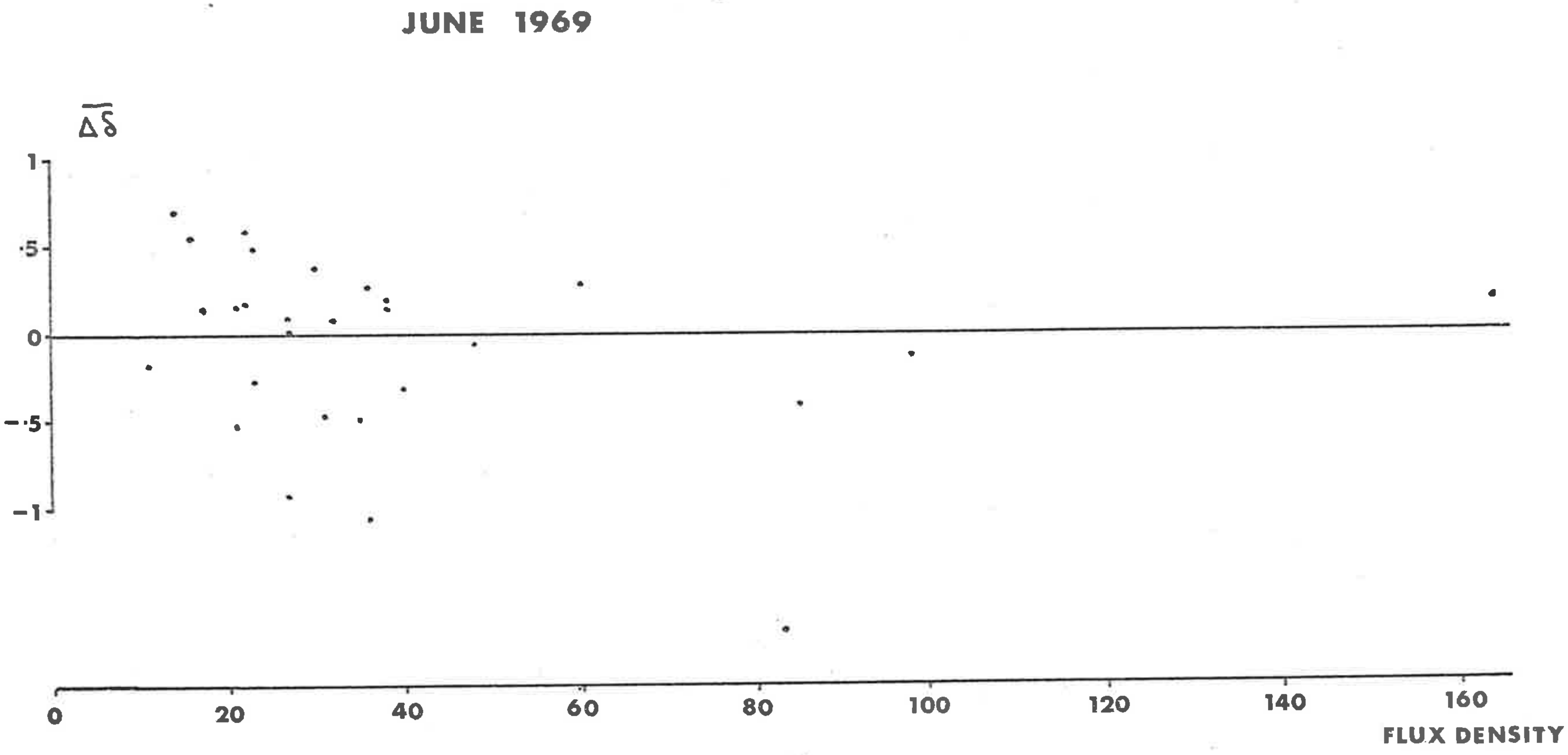

Figure 4.3 Values of $\overline{\Delta\delta}$ ('arc) plotted against flux density (in flux units) at 80 MHz

to a drift of a few seconds per day was much larger than the deviation of the main sidereal clock and its significance was not fully appreciated during the observing session with the result that the accuracy of the sidereal times written on the charts was reduced. To constantly maintain a completely accurate time would have been beyond the capabilities of the author and other persons responsible for recording some of the data because as mentioned before the observing schedules were very full, especially during June 1969 and 1970. The spread of the September/October 1968 values is seen, from Figure 4.2, to be slightly less than those of the other observations. During this observing session accurate times were maintained and the scatter of points about the line representing the collimation error is believed to be a statistical effect.

Returning to Figure 4.1, the plots of $\overline{\Delta\delta}$ against declination, we notice two effects, one being the general displacement of the points to the north and the other a trend in $\overline{\Delta\delta}$ causing the higher declination sources to appear at more southerly positions. The displacement did not appear during June 1969 and was only slightly apparent during February 1969. It could be explained by the presence of a N-S gradient in the ionosphere whose effect was reduced during June 1969. To test this idea the variation in critical frequency, f_oF_2, needed to produce a source displacement of 1' arc was calculated, using an expression derived by Komesaroff (1960) for the refraction caused by a wedge or gradient.

Although the equation strictly applies to sources at transit it was expected to give a good approximation. It is based on the assumption that we know the profile of the ionosphere above and below the F-region peak. The critical frequency (squared) can therefore be directly related to the total content, the derivative of which is proportional to the refraction. Taking a bi-parabolic model of the ionosphere as shown in Figure 4.4, the refraction in radians is given by

$$\alpha = \frac{(y_m + y^1{}_m)\ k}{3(r_m + y^1{}_m)\ f^2} \ \frac{d(f_o{}^2)}{d\phi} ,$$

where f is the observing frequency and f_o the critical frequency of the ionosphere; y_m and $y^1{}_m$ are the semi-thicknesses of the ionosphere below and above the peak; r_m is the distance from the earth's centre to the height of maximum density; ϕ is the latitude, and k is a constant ∿1 increasing slowly with zenith angle. Putting y_m = 120 km

$y^1{}_m$ = 410 km

and r_m = 6370 km

then at 80 MHz, $\frac{d(f_o{}^2)}{d\phi}$ = 67.8 MHz^2 rad^{-1} or 1.18 MHz^2 deg^{-1} for a N-S refraction of 1' arc. The average values of $d(f_o{}^2)$ were calculated for Canberra to Brisbane ($d\phi = 7.8^0$), and Brisbane to Townsville ($d\phi = 8.2^0$). A large gradient existed from Canberra to Brisbane but leveled out on nearing the equator. Between Brisbane and Townsville, during September and October 1968, $d(f_o{}^2)$ was ∿10 MHz^2, a value of the correct magnitude to account for the observed displacement of the source positions in declination. The critical frequency data from Brisbane and Townsville

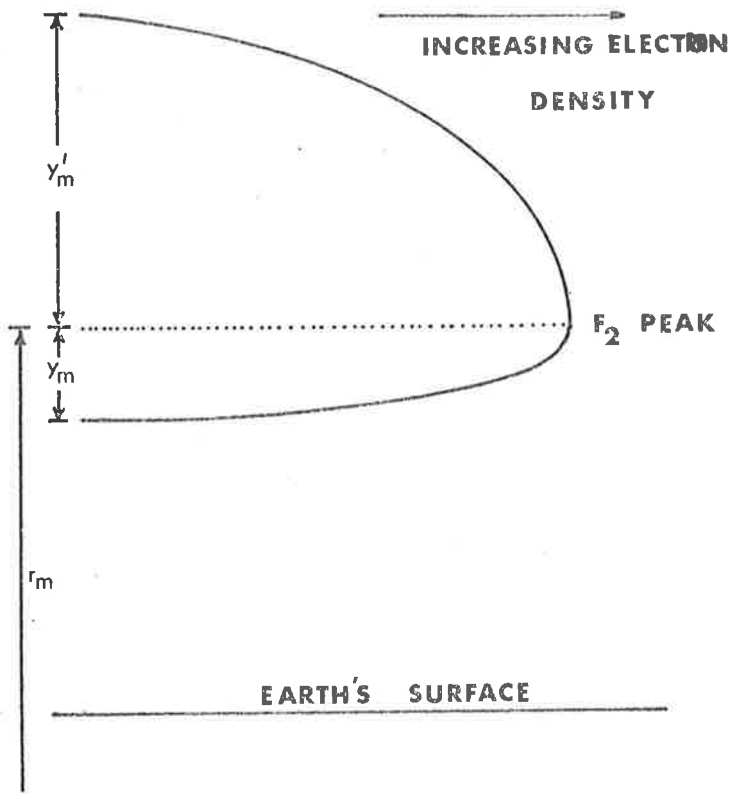
INCREASING ELECTRON
DENSITY
y_m'
F_2 PEAK
y_m
r_m
EARTH'S SURFACE

Figure 4.4 Bi-parabolic ionospheric profile with maximum density at a distance r_m above the centre of the earth

were used because the region of ionosphere through which the radio sources were observed was close to the line joining these two stations. Good agreement, however, was not found during the two winter observing sessions. From the monthly mean values of the critical frequency, f_oF_2, during June 1970 the expected refraction was calculated to be $\sim 0.2'$ arc which does not agree with the observed values. However, one correlation was observed, in that the ionogram data indicated that the expected average refraction during June 1969 would have been less than during June 1970 by a factor ~ 5. This effect was observed, as seen in Figure 4.1.

The nature of the second effect, the downward trends on all plots of $\overline{\Delta\delta}$ against declination, suggests that spherical refraction may be predominant at low elevation angles. Again adopting an equation from Komesaroff (1960), we have an expression for the spherical refraction

$$\alpha = - \frac{(y_m + y^1{}_m)}{3\,r_m} \left[\frac{f_o}{f}\right]^2 \sec^2(k)\,\tan(k),$$

where k is the inclination of the ray path to the vertical at the peak of the ionosphere, and is approximately equal to the zenith angle of the observations at our frequency. The remaining parameters have the same meaning and also the same values as previously, and for $f_o \sim 7.5$ MHz we have $\alpha = 0.85 \sec^2(k)\tan(k)$. Values of α are tabulated in Table 4.1 against values of k, with the corresponding declination assuming the observations were made at zero hour-angle. The trend in these values is

Declination		Spherical Refraction
k ($^{\circ}$)	δ ($^{\circ}$)	α (' arc)
0	-30	0.00
10	-20	0.15
20	-10	0.35
30	0	0.65
40	10	1.22
50	20	2.46
60	30	5.88

(At 80 MHz $k \simeq \delta$)

Table 4.1

greater than the observed variation, indicating that the effective ionospheric thickness might have been over estimated. Also the formula is valid only for moderate zenith angles ($< 45^\circ$) and the calculated spherical refraction for $k > 45^\circ$ may be in error. However, the exercise has demonstrated that the trend in the data was due to spherical ionospheric refraction.

The plots of $\overline{\Delta h}$ against declination in Figure 4.2 also show a trend, but this was believed to arise from a collimation error due to the misalignment of the radioheliograph aerials. This misalignment has been carefully measured by C.S.I.R.O. surveyors and on each of the plots a line has been drawn representing the error. The values of $\overline{\Delta h}$ in all cases appear randomly scattered about this line. Therefore the average source positions in hour-angle (or right ascension) appear to be unaffected, within the limits of accuracy, by the declination.

The usefulness of the data consisting of single samples, $\Delta\delta$ and Δh (rather than the mean values of each source, $\overline{\Delta\delta}$ and $\overline{\Delta h}$), was restricted as a set of random samples because of the large scatter of $\overline{\Delta\delta}$ and $\overline{\Delta h}$ as seen in Figures 4.1 and 4.2, and also because of the unequal number of single samples contributing to these means. In other words the data were biased by the number of contributions from each source or declination position, and this would be reflected in the results of any attempt to detect minor trends in the data when plotting, say, $\Delta\delta$ against local time or hour-angle. Such minor trends would be, for example, sunrise and sunset effects. The minimum detectable trend would be ∿1' or greater corresponding to the scatter of points in Figures 4.1 and 4.2. Even if this were not the case we would need to remove the northerly displacements and the spherical refraction effects from the $\Delta\delta$ values, and the instrumental effect from the Δh values, before proceeding with further analysis. Data from June 1969 and June 1970 were the most likely choices for investigating small trends, because the number of contributions from each source was reasonably constant (∿ 20 - 25). However, only about 25 sources from each session fell into this category, thus limiting the declination and local time coverage. Ideally we would need to group the data into, for example, declination ranges to study the local time variation of $\Delta\delta$ and Δh, but not enough sources were observed to allow this type of approach.

Another approach to extracting information from the June 1969 and 1970 data was to study the variations of the rms widths, $\Delta\delta$ rms and Δh rms, of the distributions for each source rather than their mean values, $\overline{\Delta\delta}$ and $\overline{\Delta h}$. In Figures 4.5(a) and 4.5(b) the rms widths of the declination and hour-angle distributions of each source have been plotted against declination for the two observing sessions. A significant increase in $\Delta\delta$ rms with declination is observed for both years, whereas the Δh rms values show only a slight increase. This has been attributed to the effect of large scale disturbances in the ionosphere. Since these disturbances travel in an approximately N-S direction (Heisler, 1963), their main effect is on the declination of the sources, rather than the hour angle. For larger declinations we observe through a thicker region of ionosphere and thus find a greater degree of refraction in both the declination and hour-angle directions. The increase in the Δh rms values with declination is not very clear and apparently was masked by the errors in the Δh values, discussed earlier, which would have generally increased all Δh rms values in a random fashion. From Figures 4.5(a) and 4.5(b) we see that this is the case, the values of Δh rms are equal to or greater than the $\Delta\delta$ rms values rather than being less as would be expected from predominantly N-S refraction. It is interesting to note that the average value of $\Delta\delta$ rms during 1969 was only 0.6 of the average for 1970, the effect being clearly apparent on inspection of Figures 4.5(a) and 4.5(b). This difference was probably due to the ionosphere being more disturbed during 1970 and, since the state of the ionosphere is known to reflect the activity of the sun, this is in agreement with the increase in solar activity and activity in the interplanetary medium during this period. The averages of the Δh rms values were approximately equal although the errors may have affected these in such a way that the differences would not be detectable.

It was also interesting to examine the diurnal variations of $\Delta\delta$ rms and Δh rms. For each observing session the random samples (i.e. the $\Delta\delta$ and Δh values) were combined and divided into two-hourly local time

Figure 4.5 (a)

Variation with declination of the spread in the declination position measurements for each source.

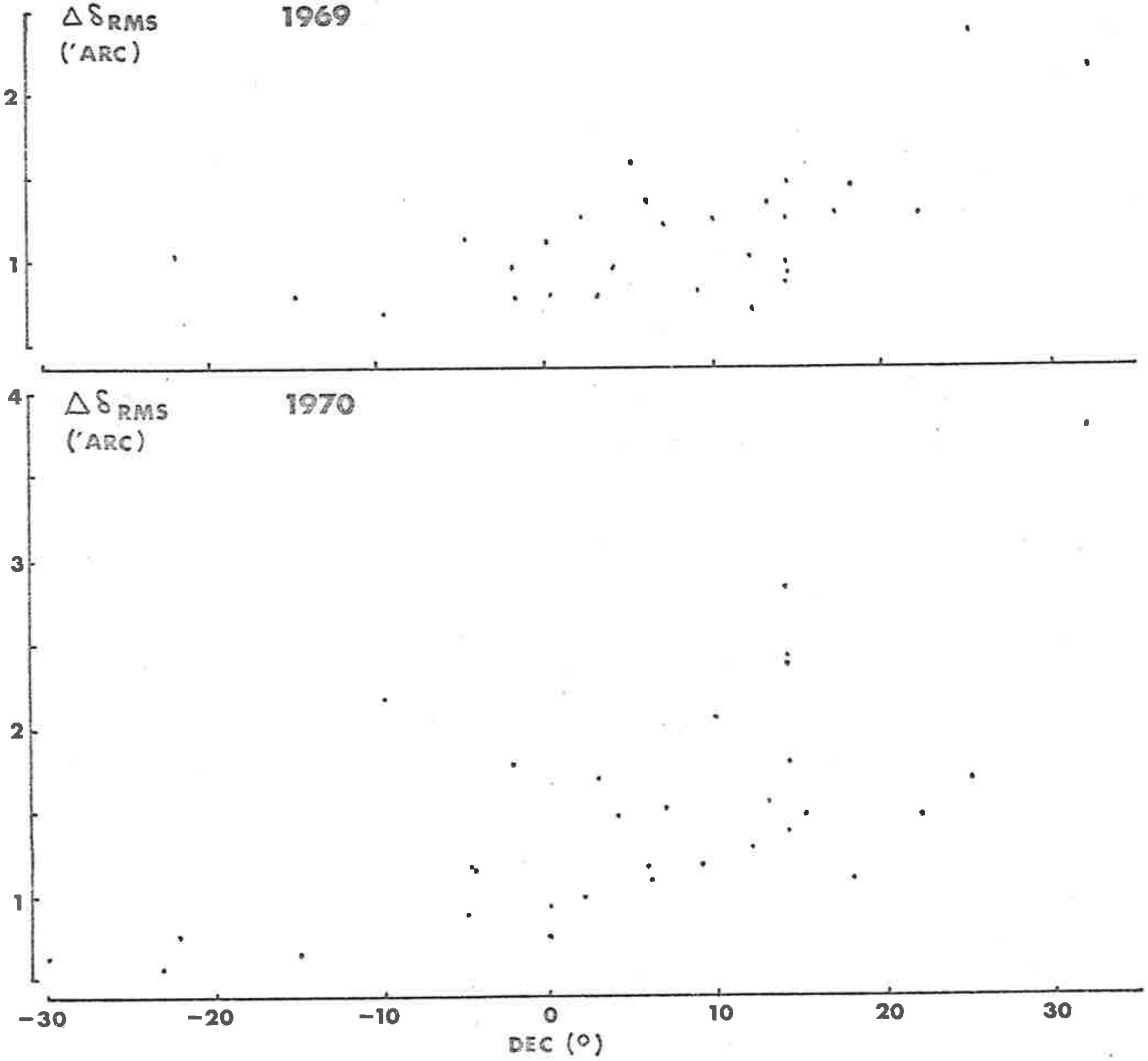

Figure 4.5 (b)

Variation with declination of the spread in hour angle position measurements for each source.

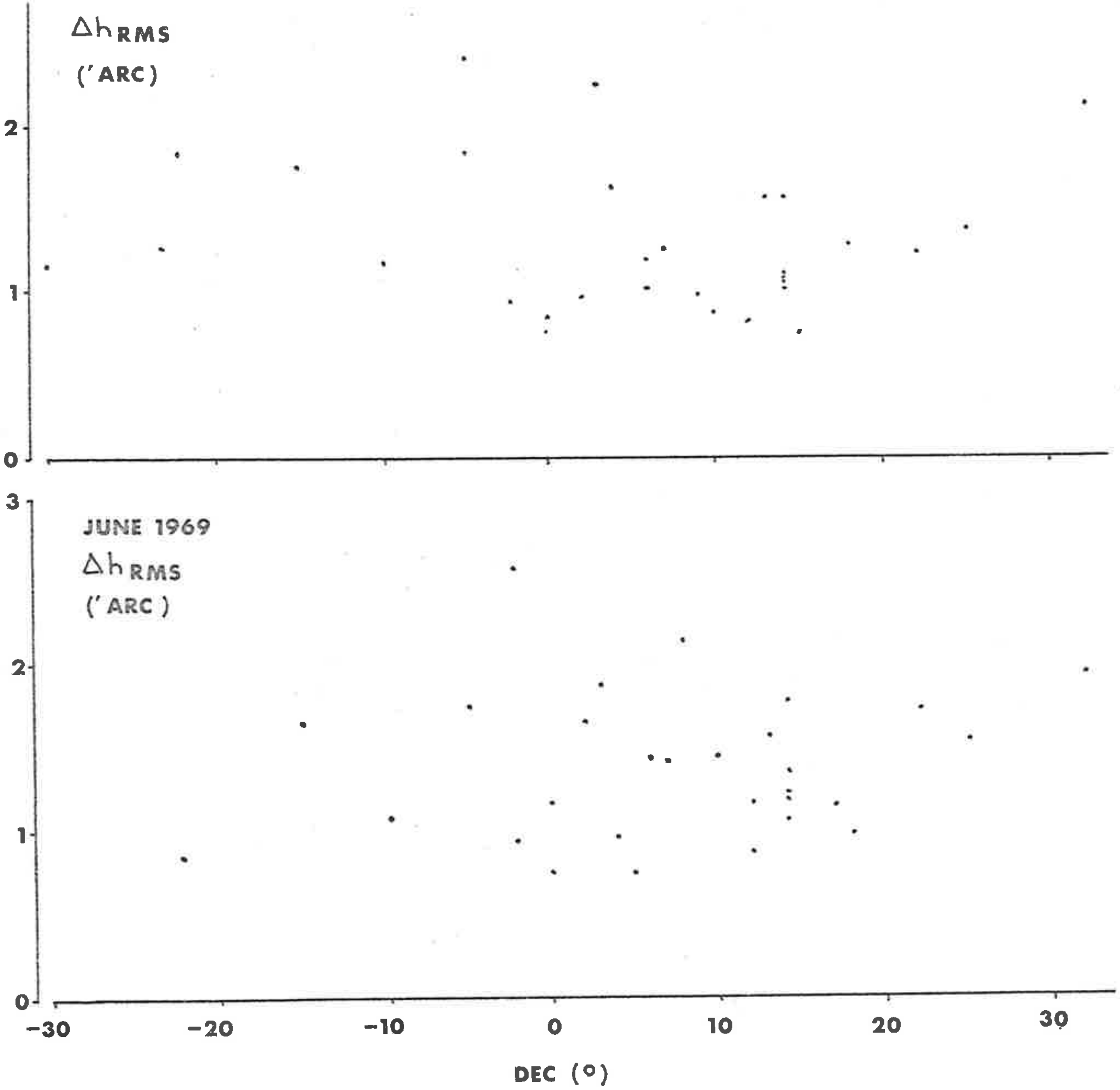

groups. One source could contribute to two or (rarely) three adjacent groups. The rms deviations of the resultant distributions were plotted against local time, as shown in Figure 4.6. This figure, then, represents the degree of random changes in the source positions as a function of local time. It is evident that large peaks occur in the daytime during the winter months only. The detailed variations shown in Figure 4.6 must be treated with caution since they were probably affected by selection effects related to the source position differences mentioned earlier. For instance the large peak at 0900 arises largely from observations of the source 0134 + 32 (elevation $\sim 30^{\circ}$). It was observed during the morning following sunrise when increasing ionisation might have caused enhanced refraction. Also the low elevation would have increased the effect. The summer data indicate mainly a nighttime increase in random source movement whereas the equinox data show only a slight midday peak. The ideal approach would be to examine the fluctuations at constant declinations, but our data were far too limited to allow such an analysis to be attempted successfully. In Figure 4.7 are plotted the diurnal variations of the rms deviations of the hour-angle values. The trends although still evident are not as clear in these diagrams, indicating less variation than the declination values. In both cases however, the winter variations were greatest during the day. The summer variations, although in general smaller than those in winter, were greatest during the night.

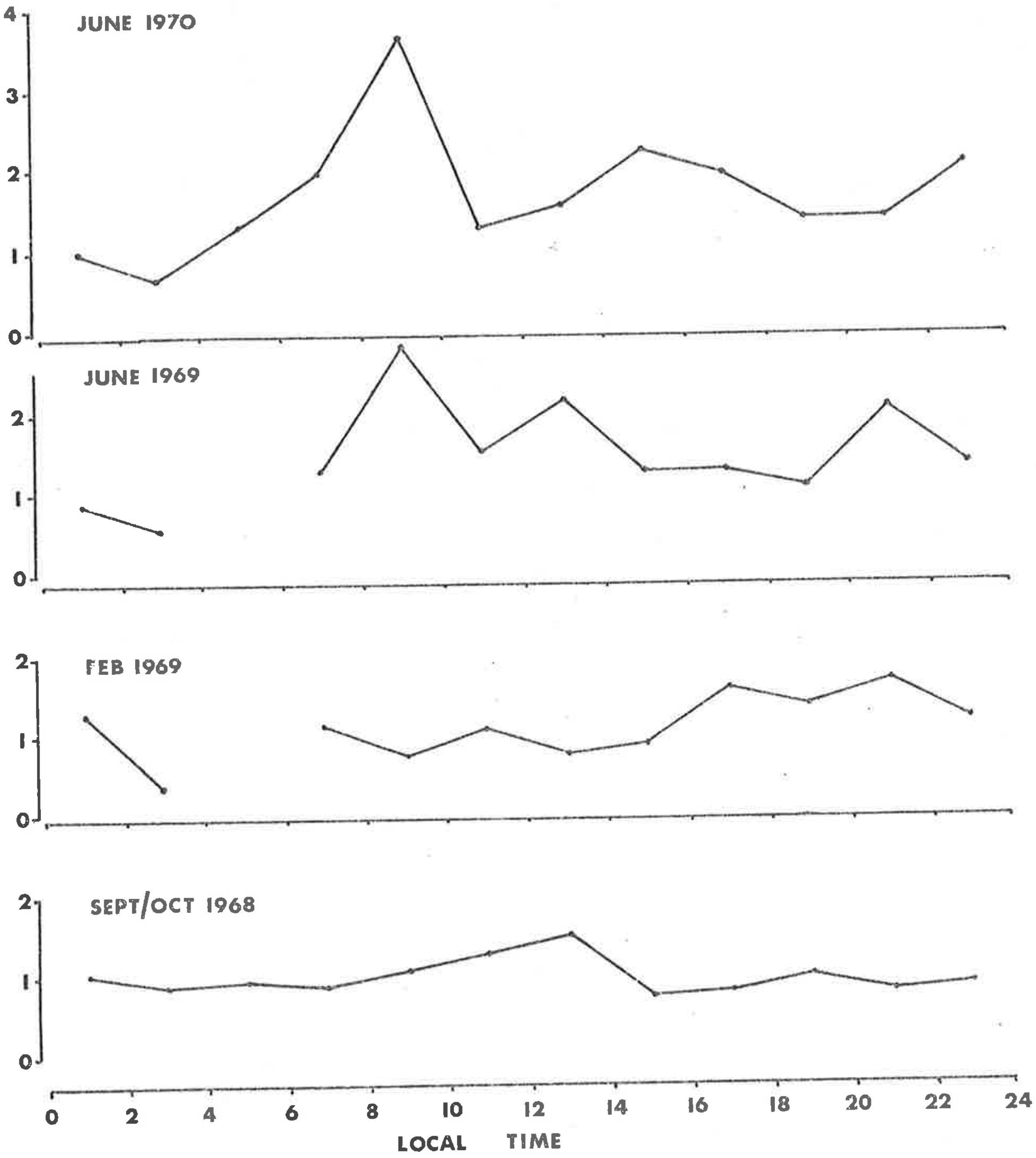

Figure 4.6 Plot of $\Delta\delta$ rms ('arc) against local time (in two-hourly groups)

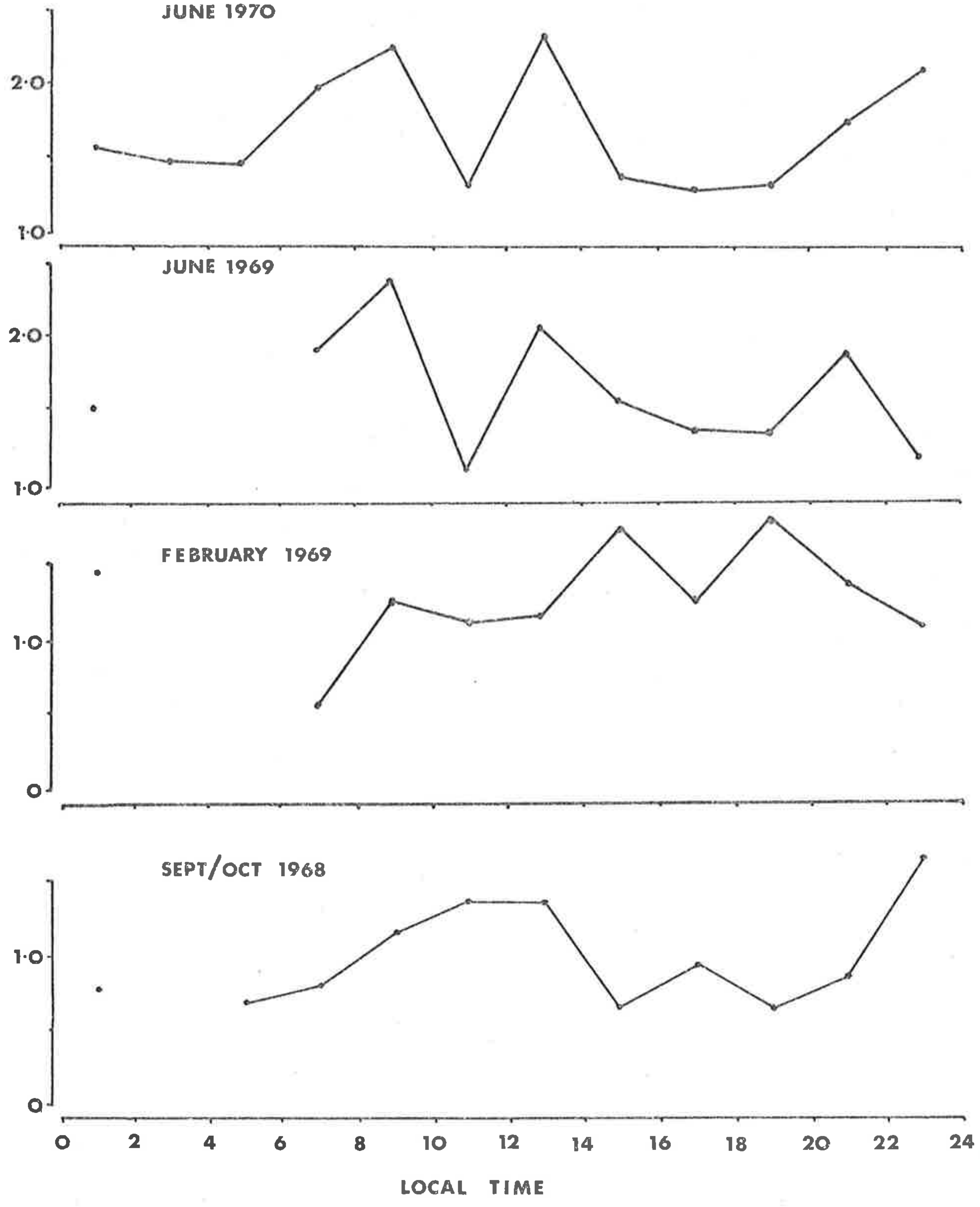

Figure 4.7 Plot of Δh rms ('arc) against local time (in two-hourly groups)

The records consisting of long series of consecutive drift scans provided position measurements of sources usually at intervals of about 2 min. Most of the data were daytime observations of the Crab Nebula and 3C123 during June 1969 and 1970, although three other sources were observed at night on a few occasions during June 1969. In February 1969, 9 sources were observed on various days providing a total of 24 series of scans, 8 of which were taken at night. Except for 3 records from May 1968 the remainder of the data came from 10 observations in September and October 1968.

From each set of scans the rms deviations of the source declination and hour angle, $\Delta\delta_{rms}$ and Δh_{rms}, were calculated. The observations are summarised in Table 4.2 which lists the source, the rms deviations, the average local time and the number of scans per record. In addition, the predominant direction of motion is indicated, and if a source showed any tendency to regular motion an appropriate comment is made.

On examination of the rms deviations distinct seasonal and diurnal variations are apparent, agreeing with the variations found in the statistical data. These effects will be discussed in more detail in Section 3. The data was also examined by plotting the two-dimensional motion of the sources for each series of scans. Figure 4.8(a) is a typical N-S orientated pattern based on scans made approximately every 2 min. Other examples of two-dimensional patterns are presented in

Source	Date	No. Scans	Local Time	$\Delta\delta_{rms}$	Δh_{rms}	Predominant Direction+	Half-periods* (min)
0531+21	680528	48	15.0	1.50	2.00	NE-SW	
1416+06	680525	37	0.1	.50	.40		
1226+02	680526	20	21.9	.30	.45	NE-SW	
0531+21	680925	21	7.4	1.75	2.34		
	28	10	6.7	.71	.32	N-S	
	30	4	7.4	.51	.57		
	681002	5	5.0	.26	1.51		
	4	7	5.7	.27	.11		
	5	7	5.5	.17	.07		
1648+05	681006	9	16.8	.26	.28		
	7	21	17.1	.43	.28		
	8	29	17.2	.97	.64		
	9	17	16.8	.37	.37		
0134+32	690131	56	17.4	1.70	1.18		
0433+29	690131	33	21.5	2.17	2.78	NE-SW	20,42
	690202	32	19.2	.73	1.49	NW-SE	
0531+21	690130	44	20.5	1.52	1.35		
	690131	20	23.4	1.87	1.43		
	690202	33	22.7	1.24	1.85	NW-SE	20,25
	4	11	20.4	1.01	.85		
0624-05	690201	12	18.1	1.97	1.24	SW-NE	18
0850+14	690130	33	22.8	1.74	1.79	SW-NE	
0915-11	690130	4	0.4	.19	.27		
1648+05	690131	21	9.7	.50	.44	NW-SE	
	690201	14	9.2	.16	.19		
	2	37	9.9	.65	.63		
	3	22	9.1	1.76	.66	N-S	
	5	14	9.1	1.22	.45	N-S	
	6	15	9.3	.68	.31	N-S	
	7	11	8.6	.48	.28		
2012+23	690201	42	13.7	1.20	2.37		
	4	4	13.1	1.05	1.21		
	5	10	10.7	.88	.38	N-S	
	9	13	10.5	1.09	.75	N-S	
211-17	690202	24	13.0	.32	.26		
	3	30	13.5	.35	.61	E-W	
	9	9	13.5	.35	.55	NW-SE	

Table 4.2

Source	Date	No. Scans	Local Time	$\Delta\delta_{rms}$	Δh_{rms}	Predominant Direction+	Half-periods* (min)
0433+29	690531	7	13.3	1.79	1.65		
	690601	16	10.2	6.28	1.92	N-S	16
	2	5	12.1	3.07	.89		
	3	5	11.8	.54	.57		
	4	19	11.2	7.25	1.56	N-S	14
	5	12	11.3	3.53	1.07	N-S	14,14
	6	26	12.5	3.43	1.08	N-S	7,9,13,8
	7	10	11.9	1.67	.76	N-S	
	8	30	11.2	4.68	2.19	N-S	12,15,9
	9	21	11.4	1.34	2.62	E-W	
	10	28	12.4	7.85	2.77	N-S	10,14,16
	11	23	12.2	5.41	1.77	N-S	20
	14	10	12.3	2.50	1.04	N-S	
	15	13	11.1	4.63	.94	N-S	
	16	20	10.4	4.48	1.34	N-S	8
	17	32	11.4	5.51	2.44	N-S	10
	18	8	11.2	5.37	1.44	N-S	12
	19	4	11.8	1.81	.26		
	20	4	11.0	.81	.69		
	22	14	11.9	4.41	.84	N-S	
	23	10	11.5	3.53	2.09	N-S	13
	24	25	11.2	6.44	.80	N-S	10,12
0531+21	690531	36	15.6	5.12	1.32	N-S	10,12,15
	690601	43	13.3	2.71	1.30	N-S	8,13,15
	2	37	12.4	4.13	1.62	NW-SE	9,10,8,15
	4	38	13.9	5.43	1.21	N-S	15,10,18
	6	26	11.0	5.00	1.66	N-S	
	8	38	13.1	3.02	1.23	N-S	10,20,15
	9	11	14.2	3.11	.94	N-S	
	9	23	12.8	1.32	2.47	E-W	
	10	18	13.4	5.20	1.03	N-S	15,10,12
	11	19	10.8	3.95	1.31	N-S	12,5
	19	20	10.6	4.69	1.57	N-S	16,10,10
1226+02	690607	21	20.7	2.42	1.18	NE-SW	12
1514+07	690612	23	22.3	1.43	.74		
1648+05	690530	13	.7	1.26	.52		
	690603	15	.5	.78	.44		
	10	25	.4	1.56	1.07		

Table 4.2 (cont)

Source	Date	No. Scans	Local Time	$\Delta\delta_{rms}$	Δh_{rms}	Predominant Direction +	Half-periods* (min)
0433+29	700530	6	12.9	7.77	1.85	N-S	
	700601	11	12.8	.86	.53		
	2	5	12.1	4.79	1.83	N-S	14
	3	9	11.8	2.40	1.00	N-S	
	4	10	12.4	1.35	.72		
	5	13	12.2	3.15	1.01	N-S	
	6	8	13.3	2.23	.56		
	7	19	11.9	2.68	1.06	N-S	
	8	14	11.6	3.21	.95	N-S	
	9	11	11.7	7.82	1.53	N-S	10
	10	15	11.5	2.41	.95	N-S	11
	11	10	11.8	5.17	1.14	N-S	14
	12	13	11.5	5.01	1.27	N-S	
	13	7	11.4	1.55	2.16		
	15	5	11.5	5.12	1.40		
	17	9	11.4	3.91	1.64	N-S	
	20	10	11.5	1.64	.80	N-S	
	21	19	10.7	3.47	1.02	N-S	18,10
0531+21	700530	13	12.2	7.15	3.20	NW-SE	10,10
	31	14	11.4	4.97	3.76	NW-SE	10
	700601	19	11.9	2.37	1.29	NW-SE	10,13
	2	14	11.5	1.81	1.67	NW-SE	8
	3	15	11.2	7.34	3.55	N-S	10
	5	16	11.3	4.21	1.47	N-S	8,9,9
	6	7	11.0	2.36	.96	N-S	8
	7	14	10.8	4.44	1.70	N-S	9
	8	16	10.9	4.25	1.36	N-S	13
	9	15	11.0	6.76	2.27	N-S	10
	10	14	10.8	1.18	.80		
	11	14	11.1	3.74	1.87	N-S	
	12	15	10.8	6.70	2.87	N-S	15
	19	7	10.9	1.39	2.35	NE-SW	
	20	13	10.6	2.73	.79	N-S	12
	21	20	11.6	2.46	1.09	N-S	7,7

* Indicates the half-period of sections of the pattern which appear regular.

+ Where no predominant direction is indicated the pattern was random.

Table 4.2 (cont)

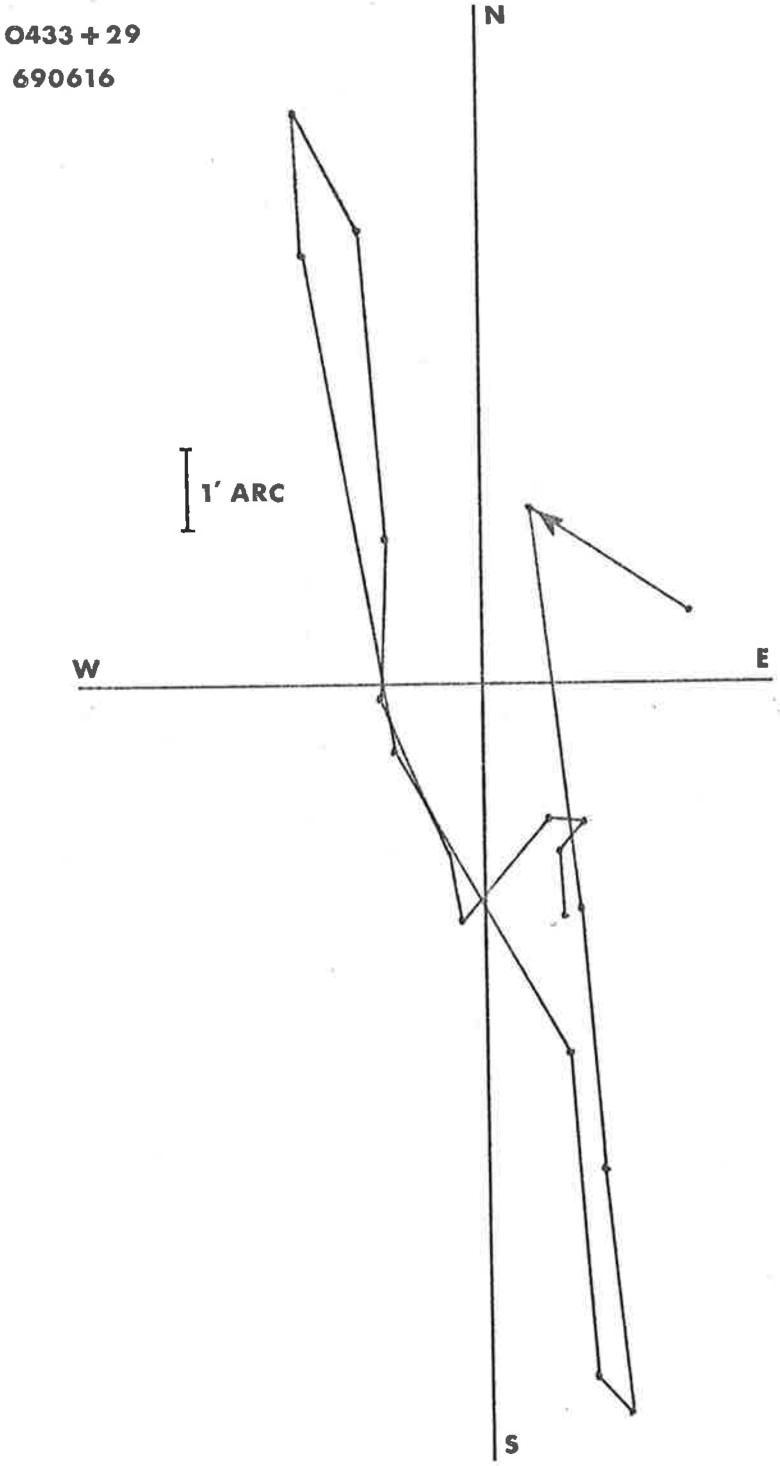

Figure 4.8 (a) Two-dimensional source movement derived from 2 minute samples

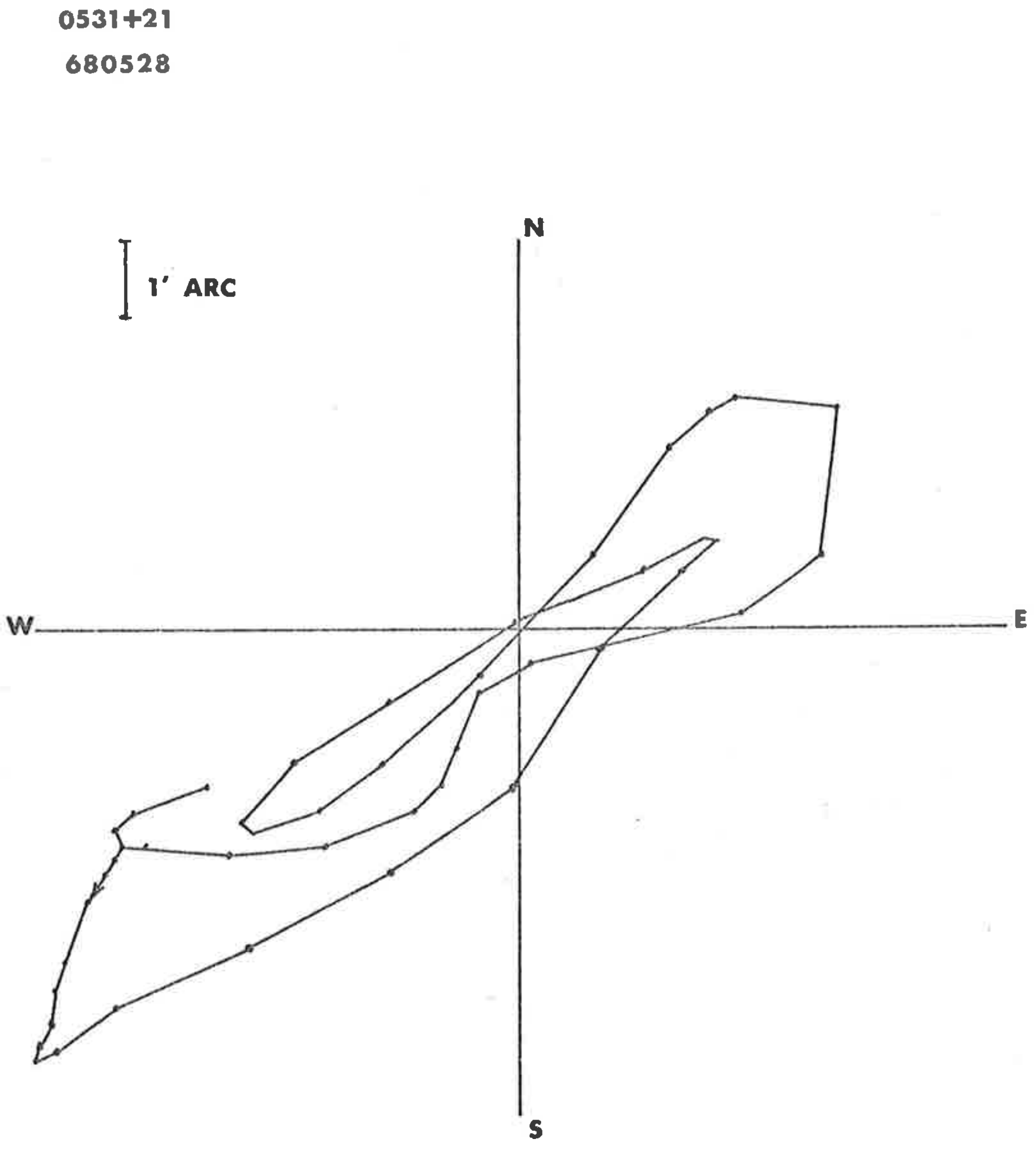

Figure 4.8 (b) Two-dimensional source movement derived from approximately one minute samples.

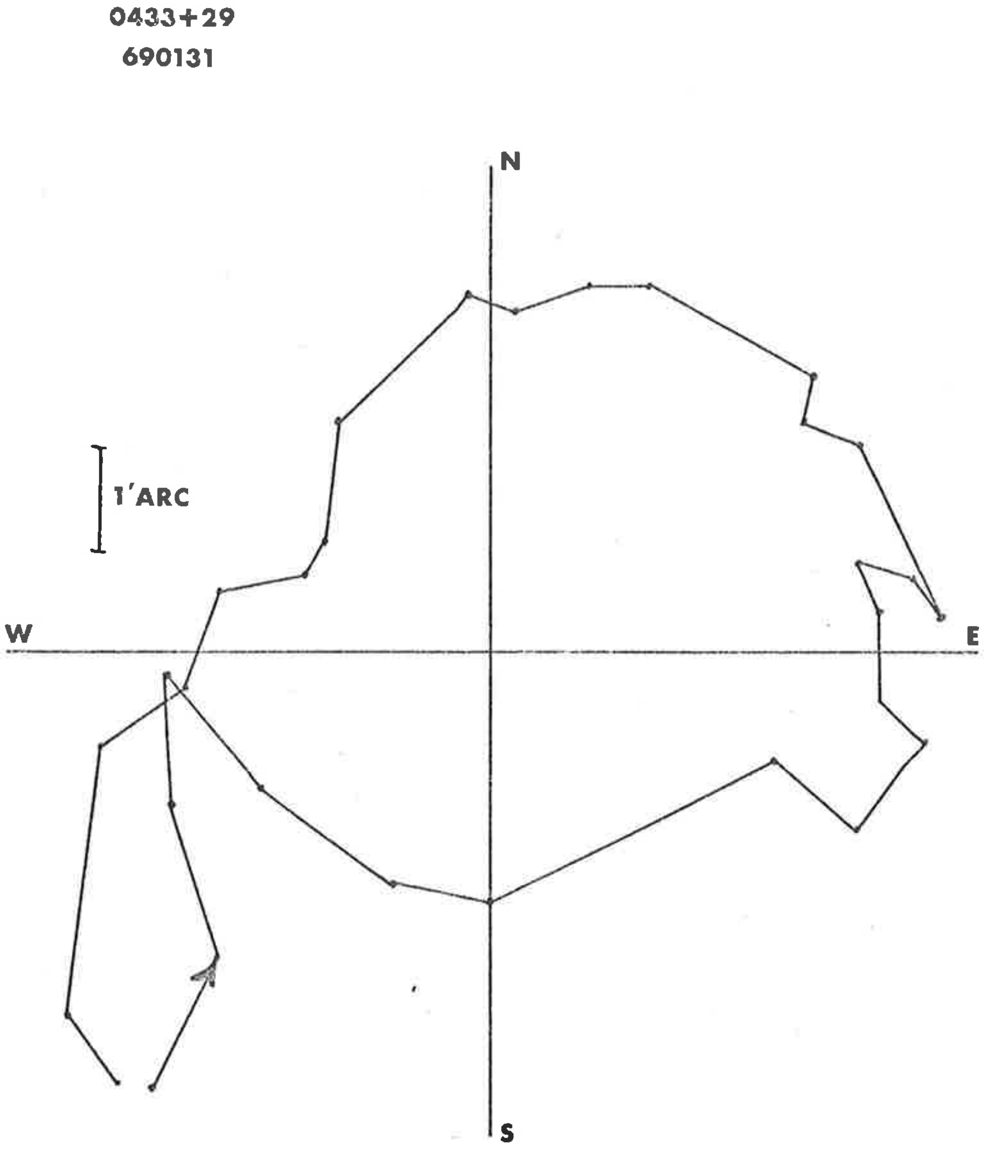

Figure 4.8 (c) Two-dimensional source movement showing a very regular pattern

Appendix I. Most of the data showing large variations indicated a predominantly N-S movement which was implied by the ratio $\Delta\delta$ rms:Δh rms. Sometimes however the directions were well away from N-S, and on several occasions even E-W motions were observed. Titheridge (1969) has remarked that waves with different velocities and directions propagate in the ionosphere at all times. Also Munro (1950) has noticed that sometimes abrupt changes occur in the direction of motion of large scale ionospheric irregularities. From our own data the azimuth of the observations bore no relation to the direction of the predominant refraction and we conclude that these observations were probably caused by phenomena such as those mentioned by Munro and Titheridge. A large number of plots showed a rough periodicity ∿20 min, and on occasion very regular patterns of motion, examples of which are shown in Figures 4.8(b) and 4.8(c). The nature of the movements of the sources, and also the diurnal and seasonal variations, suggest the refraction was due mainly to travelling ionospheric disturbances (TID's) which will be discussed in Section 4.2. The statistical data discussed previously suffered from a selection effect reducing the maximum magnitude of the measured refraction. This arose because the sources, from which interplanetary scintillation were recorded, were not followed from beam to beam when extremes of refraction were present, and a limit of about ± 5' arc was thus imposed on the declination values. On the other hand, when recording a series of drift scans care was taken to track the source through its complete excursion, revealing an upper limit of about 15' arc in declination. From the rate and magnitude of the refraction, conclusions may be drawn about the properties of the irregularities causing the source displacements. Smaller variations in the position may be attributed to refraction and scintillation of field aligned irregularities in the ionosphere and also to errors in the reading of the charts.

4.2 Travelling Ionospheric Disturbances

Before we begin relating in detail the observed refraction to the structure of the ionosphere, a description of the properties of travelling ionospheric disturbances (TID's) will be given. Recalling Chapter 1, where a survey of publications which were specifically concerned with ionospheric refraction in radio astronomy was presented, many authors found that the observed steady wedge refraction could be explained in terms of local gradients within the ionosphere. However, an irregular and rapid form of wedge refraction, which did not produce the same smooth diurnal variation, also existed. This form which was observed to have a period of about 20 min. and was suggested to be the result of TID's is typical of our observations.

Basically three types of irregularities may exist in the ionosphere. In order of increasing size there are field aligned irregularities, TID's and very large scale disturbances (Georges, 1968) which have horizontal wavelengths of ∿1000 km and occur during magnetic storms.

LIBRARY UNIVERSITY OF ADELAIDE

One of the pioneers in the study of TID's was Munro, at Sydney, N.S.W. The analysis of 9 year's virtual height records using fixed frequency pulsed sounders at a number of different sites has been published (Munro, 1958). These observations indicated the presence of fluctuations which were most common during the day and caused variations ∿10% in the electron content at the peak of the ionosphere. The deduced directional information suggested the disturbances travelled to the NE in winter and SE in summer. Nighttime irregularities were sometimes observed with directions NW in winter and SW in summer. Speeds of about 130 m sec^{-1} were estimated. Heisler (1958, 1963) using swept frequency ionosondes showed the disturbances were very common in winter during the day with a northerly motion and speed of about 160 m sec^{-1}. Titheridge working in New Zealand has extensively studied the properties of TID's for a number of years (Titheridge, 1968a, 1968b, 1969 and 1971) using both low altitude moving satellites and geo-stationary satellites. In general, satellite information is more useful than ionosonde data which is confined to the ionosphere below the F-region peak. However, the use of both enables the height of the disturbances to be measured (Titheridge, 1969). Other work in the field, for example backscatter measurements (Tveten, 1961) and incoherent scatter-sounder records (Thome, 1964), suggest the presence of disturbances in the ionosphere similar to those found by Titheridge.

The following discussion of TID's will therefore be based mainly on the works of Titheridge because his results are most easily compared with our data and his diurnal and seasonal coverage is greater than other authors. The total electron content of the ionosphere is constantly changing by amounts ranging up to 10% or more. This is caused by irregularities, or more correctly wavemotions in the ionosphere, having a wide variation in size, velocity and direction of motion. In general the fluctuations are more common at high latitudes (> 40°S), diminishing rapidly towards the equator. Also they are most common during the daytime in winter. The irregularities are not field aligned and have a vertical thickness of 0.4 of their horizontal extent. They appear as waves or ripples in the ionosphere with fronts extending over ∿1000 km. Their observed periods show a sharp lower limit of 15 min, although other authors have found disturbances with periods down to 3 min (Reddi and Rao, 1971) using phase-path techniques.

Titheridge has been able to distinguish several classes of irregularities which appear to have in some respects distinctly different properites. In general, they can be divided equally into either periodic types where the ionosphere shows a wave-like structure, or non-periodic when only an isolated increase or decrease is observed in the total electron content.

The periodic disturbances have sizes typically between 40-160 km, with periods of about 60 min down to 15 min. Their occurrence is twice as common during the summer and winter as compared with the equinoxes. In addition, Titheridge observed twice as many events at 42°S than at 34°S suggesting a strong latitudinal dependence. A slight decrease in the number observed over two years was believed to reflect the increasing sunspot number when the ionosphere became more disturbed.

Semi-diurnal variations peaking around noon and midnight are observed, with the daytime irregularities more frequent in winter and at higher latitudes, and the nighttime irregularities more frequent in summer and slightly more common at lower latitudes. The change in total content of the ionosphere is roughly proportional to the period (or size) of the fluctuation.

Non-periodic or isolated disturbances displayed a similar dependence to the periodic type except the number observed at 34°S peaked in winter only, and those observed at 42°S occurred most frequently during summer. This is a manifestation of the diurnal variation showing less irregularities during summer nights at 34°S, and during winter days at 42°S, compared with the periodic variety. The isolated irregularities may either be increases or decreases in total electron content. Negative disturbances show a tendency to occur near 0700, and may be localised decreases in the rapid production of ionosation just after sunrise.

A type of large ionospheric disturbance confined mainly to the topside ionosphere was also discovered. It occurred between 10 a.m. - 1 p.m. on about half the summer nights and rarely in winter. The disturbance was strongest at latitudes north of 40°S, moving NW with a velocity $\sim$140 m $\sec^{-1}$. The duration of the disturbance was 15-100 min with no preferred value. Associated increases in total content of $\sim$30% and sometimes up to 80% were observed, and since it was mainly a topside effect there must have been large local changes in density by a factor of 2 or more. Unlike the other irregularities which occur at all ionospheric heights this variety displayed a much stronger solar cycle dependence, but with an increase in the number of occurrences with sunspot number.

4.3 Comparison with Results

From the results we have tabulated in Table 4.1, from the drift scan analysis, we immediately notice a correlation with the TID's discussed above. First, as mentioned earlier the movement was predominantly N-S, or more accurately the source movement followed a preferred direction agreeing with a wave motion passing across the line of sight in a N-S direction. Secondly, large movements of the sources were most common during daytime in winter. Refraction of a lesser degree was observed during the summer (February 1969) being slightly greater at night. No large refraction was observed during the equinox period (September/October 1968), although the data were recorded close to 0600 and 1700 local times corresponding to minima in the diurnal variation of occurrence of TID's. These effects were supported by the variation of $\Delta\delta_{rms}$ and Δh_{rms} with local time shown in Figures 4.6 and 4.7. These figures indicate an occurrence of strongly refracting irregularities during the daytime in winter, in agreement with Titheridge's observations.

The pattern traced by the source showed varying degrees of regularity and in general the predominant period associated with such cases was about 20 min. Also a source displacement of 15-20' arc appeared to be an upper limit to the refraction. This was of interest because it allowed limits to be placed on the electron density gradient and the size of the irregularity responsible, as we shall now describe.

Assume a perturbation in the total content having a Gaussian cross-section represented by $N = N_o \exp\left(-\frac{x^2}{2x_o^2}\right)$, where N is total content along a line of sight, N_o is the maximum value of the perturbation, x is the horizontal distance and x_o the half width (at $e^{-\frac{1}{2}}$) of the disturbance. The angle of refraction is given by the following equation,

$$\alpha = \frac{e^2}{\varepsilon_o\, m\, \omega^2} \cdot \frac{dN}{dx} \text{ radians}$$

where $\frac{e^2}{\varepsilon_o\, m\, \omega^2} = 7.95 \times 10^{-13}$ (MKS) at 80 MHz. Taking the maximum value of $\frac{dN}{dx}$ we find a corresponding maximum value for the refraction,

$$\alpha_{max} = 7.95 \times 10^{-13} \quad \frac{No}{x_o}\, e^{-\frac{1}{2}} \text{ radians.}$$

Substituting the observed value 20' arc for the maximum refraction we find that,

$$\frac{No}{x_o} = 1.2 \times 10^4 \text{ electrons cm}^{-2}/\text{cm}.$$

If the velocity of the travelling disturbance was 140 m $\sec^{-1}$, a typical value, then since the period of motion was ∿20 min the maximum displacement of the source would be observed after 5 min or after the irregularity had travelled a distance, $x_o = 4.2 \times 10^6$ cm = 42 km. The value of the total electron content required to produce the observed refraction can now be calculated giving, $N_o = 5 \times 10^{10}$ electrons cm^{-2}. A diagram illustrating this disturbance is shown in Figure 4.9. The electron content of the ionosphere at noon during winter is typically $\sim 10^{13}$ electrons cm^{-2}, so that a change in total content of 0.5% would be caused by an irregularity 84 km in size, sufficient to produce the observed refraction. At a greater velocity we would require a larger irregularity and a correspondingly larger change in total content. The irregularity we have considered was representative of typical large disturbances in the ionosphere observed at a latitude of about 30°S. Unless the velocity was much greater than the value used in the example the changes in total electron content were small compared with those observed by Titheridge at a more southerly latitude. This suggests that the magnitude of the TID's decreases rapidly towards the equator which agrees with the strong latitude dependence found by Titheridge.

A three dimensional ray tracing technique was used to simulate the

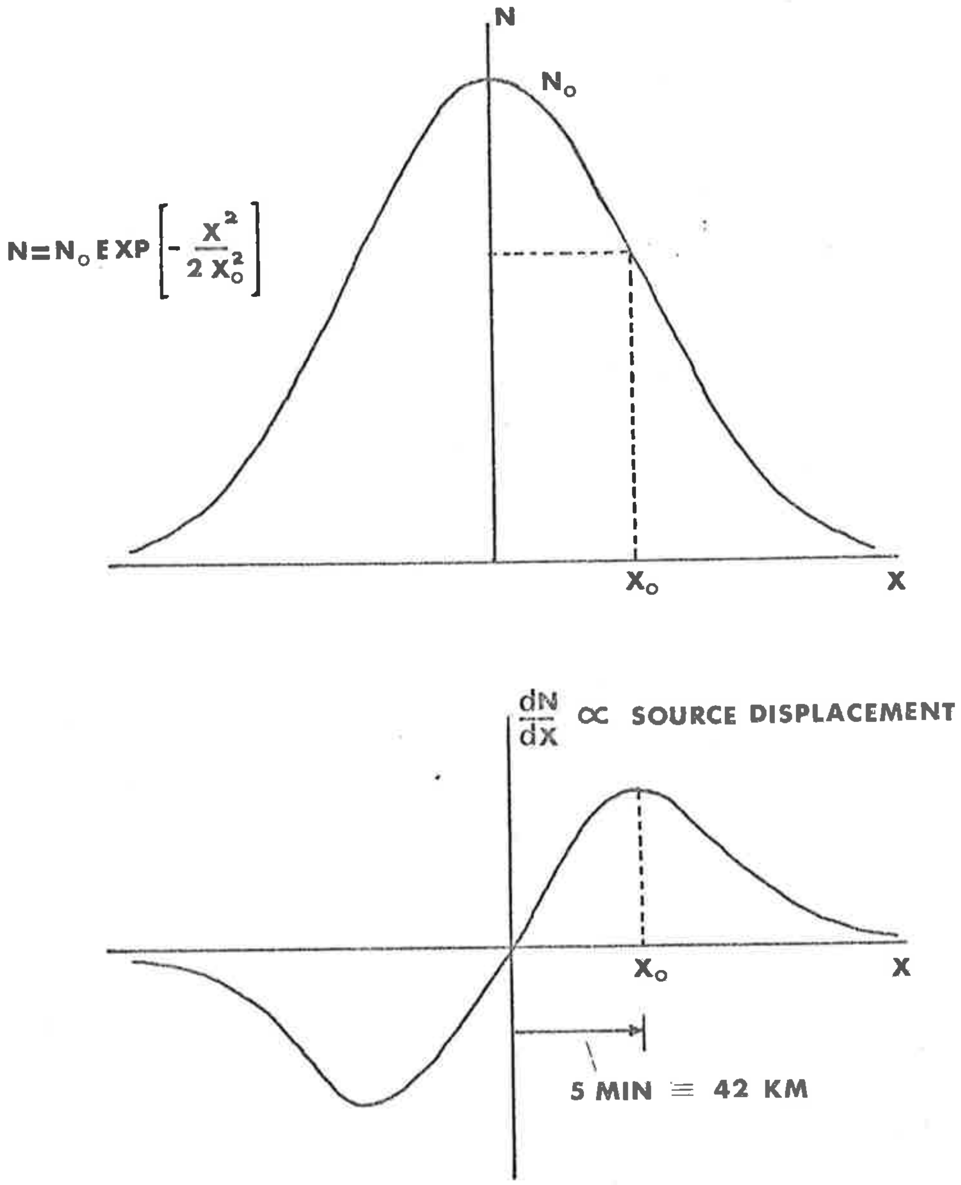

Figure 4.9 An idealized Gaussian shaped TID showing corresponding maximum source displacement

effects of a moving ionospheric dusturbance on the position of a radio source. For simplicity a parabolic ionosphere was used with a thickness of 200 km and a maximum density of 10^{11}electrons cm^{-3}. Deviations in the ray path were computed as the ray passed through different cross-sections of a three-dimensional Gaussian perturbation of width 100 km, length 200 km, depth 60 km and maximum density 10^{12} electrons cm^{-3}. The patterns followed by these deviations were similar to sections of the more regular observed patterns, suggesting that the disturbances in the ionosphere in these cases were also very regular. A computed pattern is shown in Figure 4.10.

4.4 Conclusions

Discussed in Section 1.5 were some of the attempts to correct position measurements of radio source surveys for ionospheric refraction. However, only moderate success has been achieved due to the existence of a rapidly varying component which at times has a magnitude greater than the steady wedge component caused by the slowly varying gradients in the electron density of the ionosphere. From appropriately placed ionosondes it is possible to estimate approximately these average gradients and thus allow for the steady and slowly varying components of refraction (the spherical and wedge refraction). The values derived from the ionosonde data are usually averaged over about one month to remove the random component. This component however is seen to have a magnitude of the same order as the steady wedge

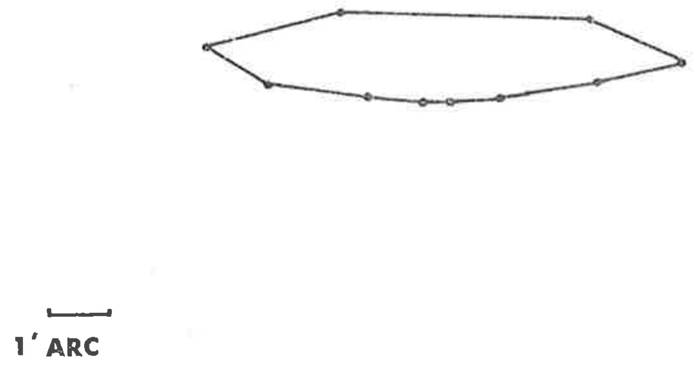

Figure 4.10 Computed source movement based on a theoretical model of a TID.

refraction and therefore constitutes a major problem when accurate position measurements at metre wavelengths are required. The degree of refraction scales as λ^2, where λ is the observing wavelength, and obviously high frequency position measurements will not be affected to the same extent as those at lower frequencies. For instance we observed the fluctuations at 80 MHz to be ∿15' arc (maximum), so that at 160 MHz we would expect variations of only 4' arc. However, at 40 MHz the magnitude would be $\sim 1^{\circ}$.

The spherical and steady wedge components can be estimated from a knowledge of the ionospheric parameters through ionosonde data. However, it appears impossible to correct, in practice, the effect of the rapid variations due to TID's. The only solution is to avoid taking accurate position measurements at the times when disturbances occur most frequently, that is during the daytime in winter. This, of course, is not always convenient; for example, the C.S.I.R.O. radioheliograph is normally used to observe sources of radiation on the sun and is naturally confined to daytime use. When integrating these data over a period of time the refraction would tend to broaden the image of such sources. In an early paper concerning movements of sources of radiation on the sun, Wild, Sheridan and Neylan (1959) reported a periodic movement ∿20 min and attributed the phenomenon to the effect of TID's in the ionosphere.

Surveys of radio sources at metre wavelengths such as those by Mills, Slee and Hill (1958, 1960, 1961) at 80 MHz (MSH survey), Bennett (1962) at 178 MHz (revised 3C survey) and Gower, Scott and Wills (1967) at 178 MHz (4C survey) would also have suffered significantly from refraction effects and consequently some disagreement is found between the different position determinations of the same radio sources.

At Culgoora the refraction was observed to have an upper limit of ∿15' arc which indicated only small changes in the total electron content of the ionosphere were observed compared to the changes seen by Titheridge at a more southerly latitude. We therefore conclude that the latitude at which observations are taken is an important consideration as well as the local time and the season. From the work of Titheridge TID's do not appear to have a large solar cycle dependence and variations from year to year would not be expected.

CHAPTER 5

SOME ASPECTS OF INTERPLANETARY SCINTILLATION

5.1 Introduction

Interplanetary scintillation of small diameter radio sources is the result of phase deviations imposed on the wavefront of the radiation after passing through irregularities in the solar wind. These irregularities move outwards from the sun causing the diffraction pattern to sweep across the observer situated on the Earth, with a velocity equal to the projected velocity of the solar wind at the point of maximum scattering. Usually the observer measures the variations in intensity of the received signal and if only a single aerial is used the subsequent analysis is based on the assumption that the spatial characteristics of the pattern remain unchanged over the duration of the observation. Such is the case with the observations we have made at Culgoora and Parkes, N.S.W. From the recorded data it is possible to compute the scintillation index, the power spectrum, the auto-correlation function and the intensity probability distribution. However, only limited information about the interplanetary medium may be gained unambiguously from this type of data, particularly if recorded at a single frequency. For instance the phase deviation ϕ_o cannot be calculated and the detailed structure of the irregularities such as the projected velocity, size and anisotropy remain unknown. In fact only large structures within the medium may be analysed in any detail and even then supplementary data from both heliocentric and Earth-bound spacecraft are usually required to consolidate conclusions. Interplanetary scintillation from a single station is, however, very useful for investigating the angular structure of small diameter radio sources and is found to be a very sensitive measuring device in this respect.

It is well known that interplanetary scintillation constantly exhibits minor day to day variations, but on occasion large increases in the scintillation indices of some sources are observed. If the indices of a number of sources scattered uniformly over the celestial sphere are constantly monitored they are usually found to vary in a regular manner suggesting that, at times, disturbances progressively move past the lines of sight to these sources. Recent studies of this phenomenon have revealed that the sudden increases in scintillation are due to corotating streams and plasma blast waves emanating from active regions on the sun (e.g. Dennison and Wiseman, 1968; Burnell, 1969; Wiseman and Dennison, 1972). In addition movements of sector boundaries have been detected in this way (Wiseman and Dennison, 1972; Houminer, 1972). Analysis of the June, 1970 data by Wiseman (1972) revealed three large scale structures within the interplanetary medium at the time of observation. Therefore we propose to discuss these observations in terms of the changes and features of the power spectra and intensity probability distributions and generally discuss angular diameter estimations from the Culgoora data. This approach has been adopted because the observed signal from a radio source depends on both the intrinsic source structure and the properties of the scattering medium. During June, 1970 different scattering regimes existed as the enhanced plasma streams moved around the sun. Some power spectra exhibited changes in width as the scattering became dominated by the plasma enhancements when they swept past the Earth.

The next observations to be discussed concern three frequency data obtained during three days in January, 1968 at Parkes, N.S.W. Records at two or more frequencies allow the nature of the scattering process to be determined. That is, from the correlation of signals at different frequencies it is possible to say whether the process was due either to weak scattering when $\phi_o < 1$ or strong scattering when $\phi_o > 1$. Unfortunately during this period very little scintillation was found on the sources observed, although one unusual change in the scintillation index of 1938-15 was noticed. This event, which may have been related to an outburst of plasma from the sun, will be discussed in detail in Section 5.4.

In the following Section 5.5, we return again to data obtained at Culgoora, but recorded during May, 1968. The procedure adopted for the analysis is of interest here because we obtain, after making certain assumptions, the cross-section of the two-dimensional power spectrum.

Lovelace et al. (1970) was the first to use this approach to interplanetary scintillation analysis and we will discuss in detail the method and its applicability at our observing frequency.

Before discussing any of the observed phenomena we will devote a section to the methods of power spectral analysis and the procedure used in analysing our own data. We analyse a time-dependent signal to obtain a temporal power spectrum which is the projection of the two-dimensional power spectrum on to a plane parallel to the direction of motion of the irregularities. Also we assume the signal constitutes a second-order stationary random process and that temporal averages are equivalent to spatial averages. Physically this means that the characteristics of the diffraction pattern moving across the observer remain unchanged with time, implying that the irregularities within the diffracting medium maintain a constant distribution and there exists no dispersion or random variations in their velocity.

5.2 Digital Spectral Analysis

Since the data recorded at Parkes were analysed using the discrete Fourier transform as described in detail by Blackman and Tukey (1958), and the Culgoora data were analysed by the relatively new fast Fourier transform (e.g. Cooley et al., 1970), it is worth drawing a parallel between the old and new methods and discussing some of the practical aspects of power spectral analysis.

5.2.1 The Old Method of Analysis

We shall consider a real stationary time series of N samples and length NΔt, where Δt is the increment between samples. Under the old method of power spectral analysis the first step is to estimate the auto-covariance function (ACVF). This is achieved by calculating a series of mean lagged products to a maximum lag, M, which is usually chosen to be $\leqslant$ 10% of N, the length of the data, to maintain statistical stability. The first point of the ACVF is the variance of the time series. By dividing the function by the variance, or in other words by normalising the function to unity at zero lag, we have the auto-correlation function (ACF). The width of these functions specifies the predominant scale or wavelength within the time series. From the auto-covariance function the power spectrum is computed by a cosine Fourier transform which is appropriate in this case where the functions concerned are even. The spacing of the spectral estimates, or elementary frequency bands, is $\frac{1}{2M\Delta t}$, the reciprocal of the full width of the ACVF.

5.2.2 The Nyquist Frequency and Aliasing

In both methods of analysis estimates can be calculated only to the Nyquist frequency f_N, which is one half the sampling rate of the data and in this case is $\frac{1}{2\Delta t}$. If power exists beyond f_N, then during analysis it becomes folded across this frequency into the main spectrum. During an experiment one must therefore ensure that the sampling rate is adequate for the signal being recorded otherwise the results may be rendered useless by a large amount of power being aliased into the spectrum. The frequencies at which the aliases occur are defined by the equation $f = 2nf_N \pm f_o$, where n is an integer and f_o the frequency lying outside the Nyquist frequency, f_N. The principle aliases occur in the range $- f_N \leqslant f \leqslant f_N$, although other aliased frequencies falling outside this range are again folded back into the spectrum, but with reduced power. It is therefore obvious that a very strong component of the signal outside the Nyquist frequency could produce a number of spurious peaks of varying heights within the main spectrum.

5.2.3 The Shape of the Spectral Estimates

Since the series we have considered is finite in length the elementary frequency bands consist of not single lines but averages over neighbouring frequencies centred about these lines. The envelope of the adjacent frequencies in this case is given by $\frac{\sin (2\pi fM\Delta t)}{2\pi fM\Delta t}$, the first zeros of which occur at $\frac{1}{2M\Delta t}$ from either side of the centre. Therefore, there exists a certain amount of overlap between adjacent bands which have a spacing of $\frac{1}{2M\Delta t}$. Because the $\frac{\sin x}{x}$ function has relatively large sidelobes, significant leakage will result from the overlap of the elementary frequency bands and if the spectrum varies rapidly with frequency this leakage may dominate and distort the spectrum. This effect may be reduced if we can replace the function with one having smaller sidelobes. The envelope of the frequencies centred around an elementary frequency band is defined by the Fourier transform of the function with which the ACVF is multiplied. This function is called the 'lag window' and so far in our example it has been simply a square function. If, however, the ACVF was multiplied by a triangular function the shape of the elementary frequency bands would be given by $\left(\frac{\sin\ (\pi f M\Delta t)}{\pi f M\Delta t}\right)^2$, as shown in Figure 5.1. Obviously the sidelobes of this spectral estimate are significantly reduced compared to the case when no lag window was used, thus reducing leakage but simultaneously increasing the equivalent widths of the bands by nearly a factor of 2 and hence increasing their stability. Also the first zeros occur at $\frac{1}{M\Delta t}$, and to obtain almost independent estimates the power spectrum values at intervals of $\frac{1}{M\Delta t}$ must be taken. Blackman and Tukey (1958) define this, rather than $\frac{1}{2M\Delta t}$, as the resolution of the spectrum. A window of the type just described is called a Bartlett window. The Hamming and Hanning window are two others which are commonly used having a similar effect on the leakage and stability as the Bartlett window. One must, however, be cautious in using these windows because a function with small initial sidelobes may still have significant sidelobes at a large interval from the central frequency and hence the leakage problem would still exist. In practice there is no best function for this purpose and one form may remove leakage at long range by having sidelobes which taper off quickly, (e.g. the Hanning window), and another form may remove leakage at short range by having small initial sidelobes with less taper (e.g. the Hamming window). Another equivalent method of applying the window is to

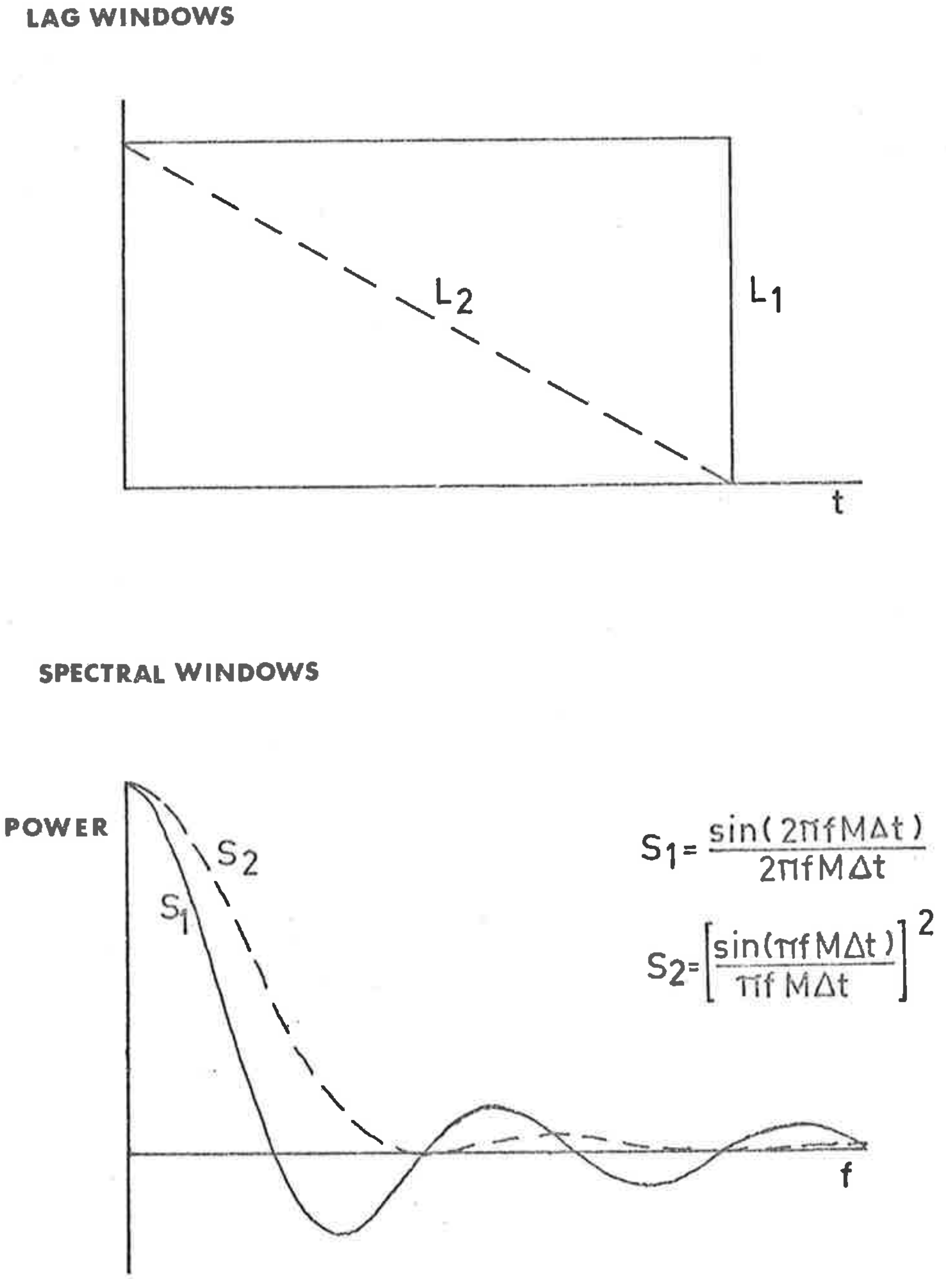

Figure 5.1 Lag windows and corresponding spectral windows

convolve the power spectrum generated without a lag window, called the 'raw power spectrum', with the Fourier transform of the lag window called the corresponding 'spectral window'. We can therefore improve the raw spectrum by the use of a lag or spectral window which has the effect of reducing leakage between estimates and also increasing their stability.

5.2.4 The Fast Fourier Transform

The fast Fourier transform (FFT) which we will now discuss actually evolved near the beginning of the century but an algorithm was not developed until 1965, by Cooley and Tukey. Perhaps the reason for this was that large computations involving Fourier transforms were not envisaged until the advent of large computers in the last decade. However, the procedure has opened up new avenues in data analysis particularly where large numbers of Fourier transformations are involved. The number of arithmetic operations required to perform a FFT is given by NN_F, where N is the number of points in the series and N_F the sum of its factors. Thus if $N = 2^K$, where K is an integer, then the computational effort is given by $2N\log_2 N$. The old method of calculating the discrete Fourier transform required N^2 operations and obviously if N is large then an enormous time saving is achieved by using the FFT. For instance, taking N = 1024 the time factor involved is about 50. Since the paper by Cooley and Tukey (1965) numerous algorithms have been developed, in particular the mixed radix algorithm written by Singleton (1969), which was used for the analysis of the Culgoora interplanetary scintillation data. This algorithm efficiently operates on factors other than 2 enabling a wider range of sample numbers instead of being restricted to 2^K.

To estimate the power spectrum and auto-covariance function of a series using the FFT, the real and imaginary Fourier coefficients of the time series are computed directly, instead of calculating mean lagged products as before. The square of the modulus of these values then gives the elementary power spectrum estimates. Another application of the FFT then computes the ACVF. It is quite remarkable that the ACVF derived in this way, via the power spectrum, is obtained with much less computing effort than if it were calculated directly from mean lagged products.

5.2.5 The Shape of the Spectral Estimates

Again we must correct the elementary spectral estimates for leakage but in this case, without correction, they have the shape of $\left(\frac{\sin\,(\pi f N \Delta t)}{\pi f N \Delta t}\right)^2$. Corrections must therefore be applied to the Fourier coefficients by convolving them with a spectral window, or by multiplying the data with the corresponding 'data window', in a way wimilar to the multiplication of the ACVF by a lag window. The windows used in the FFT case are the same as those mentioned in connection with the old method of analysis and described by Blackman and Tukey (1958). Linear modification of spectral estimates is the term applied to the procedure we have just described, whereas quadratic modification is applied to the previous procedure. Sloane (1969) has given details of the differences between the two methods by comparing the expectation values and variances of the spectral estimates in each case.

As well as being much faster, the FFT method opens up a variety of approaches to spectral analysis depending on the nature of the original data and the type of spectrum expected. For instance, the resolution of the spectrum and the shape of the estimates via the old method was determined basically by the maximum lag chosen for the auto-covariance function. On processing a series using the FFT method various shapes of spectral estimates may be achieved. If we transform the N points directly and compute the elementary spectral estimates, p_i, $(i = 1, 2 \ldots N,)$ it is found that (for Gaussian data) the variance $\mathrm{var}(p_i) = p_i^2$. Therefore this form of spectrum is very unstable but the spacing of estimates is only $\frac{1}{N\Delta t}$, whereas the spacing obtained from the old method was $\frac{1}{2M\Delta t}$. To obtain equivalent stability the widths of the estimates in both cases must be roughly the same and we must average the elementary estimates of the unstable spectrum over about $\frac{N}{2M}$ adjacent frequency bands. However, the shape of this estimate would be almost square if $\frac{N}{2M} \sim 5$, while the shape of the other type of estimate is given by $\frac{\sin(2\pi f M\Delta t)}{2\pi f M\Delta t}$, or by a similar form after correcting for leakage. Figure 5.2 illustrates the different shapes of estimates for the different methods of analysis. One can actually obtain the required

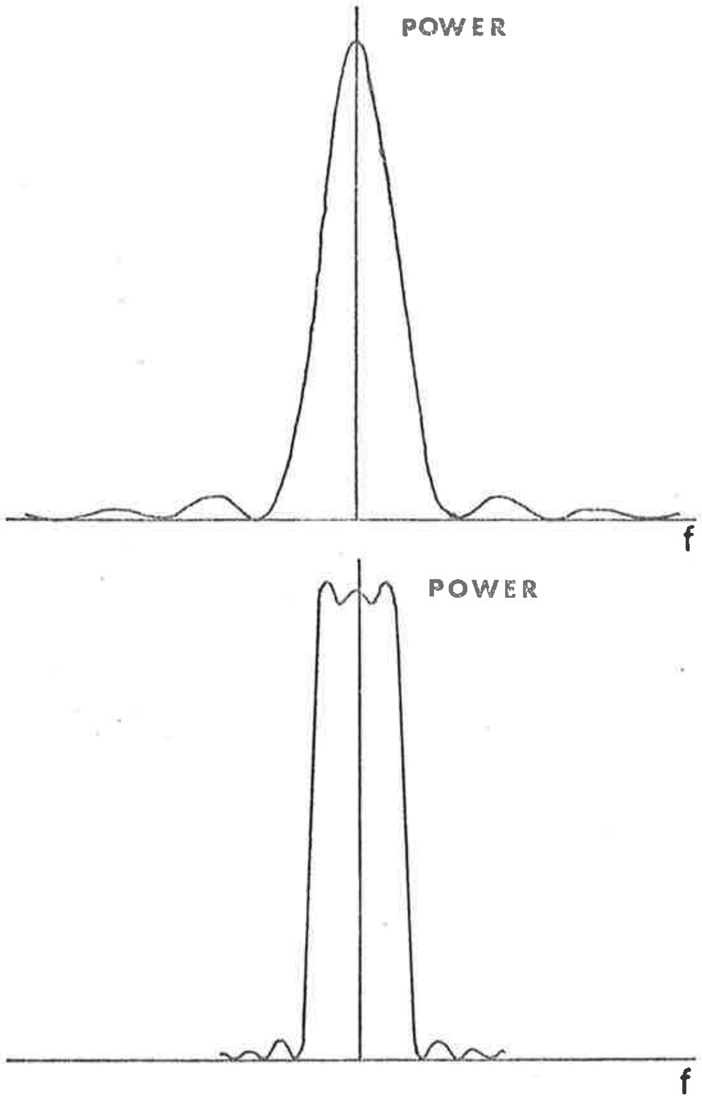

Figure 5.2 Two spectral windows derived by different procedures

width from the onset by dividing the data into (say) K equal sections each of length 2M, computing the power spectrum of each and averaging the K results. This also gives the required stability, although the shape of the estimates are of the form $\left(\frac{\sin(2\pi fM\Delta t)}{2\pi fM\Delta t}\right)^2$ rather than approximately square as mentioned before. By splitting up long arrays in this way it is possible to compute the power spectrum of a series with indefinite length utilising a very small amount of computer storage. Other possibilities immediately come to mind, for instance, the data may be split into K sections of length L and the power spectrum of each calculated. Then J adjacent frequency bands of the mean power spectrum are averaged. The selection of the method of analysis and the final form of the spectral estimates is based partially on computing convenience and partially on the type of data involved.

5.2.6 Filtering

Filtering of spectra becomes extremely simple when computing power spectra via the FFT and is achieved simply, by setting the unwanted frequency bands to zero. The remarkable aspect of this procedure is its simplicity, and the fact that there exist none of the problems which are associated with the old method of analysis. To filter the power spectrum using the old method the data must be convolved with a function whose spectrum represents the filter being applied to the power spectrum. However, because of the finite length of the data function the filter tends to oscillate or 'ring', thus affecting frequencies adjacent to the filtered section as shown in Figure 5.3. A filter which is the easiest to apply and the most economical to use is achieved by taking a running mean over the data. The shape of this filter is of the form $(\frac{\sin x}{x})^2$ which is a large departure from the approximately square filter achieved when using the FFT method of analysis. By using a tapered function instead of the running mean sidelobes of the filter can be reduced but the convolution becomes more complex. The best result is achieved by convolving a $\frac{\sin x}{x}$ function with the data to produce a square filter with slight ringing depending on the total width of the function. When only low frequencies are removed using a narrow high pass filter, a significant amount of data is wasted because it must be convolved with a very wide function.

If data is required in the filtered form the appropriate real and imaginary Fourier coefficients are set to zero and a reverse transform is applied. Unfortunately this is equivalent to a circular convolution of the data with a $\frac{\sin x}{x}$ function, and the end sections become contaminated by each other. This can be overcome by appending zeros to the beginning and end of the data until the number of points has doubled. A similar effect is found when computing the ACF.

We spoke of the restriction imposed on FFT transformations by the requirement that the number of points must be a product of factors. If the data is not the correct length it is acceptable to append zeros to the

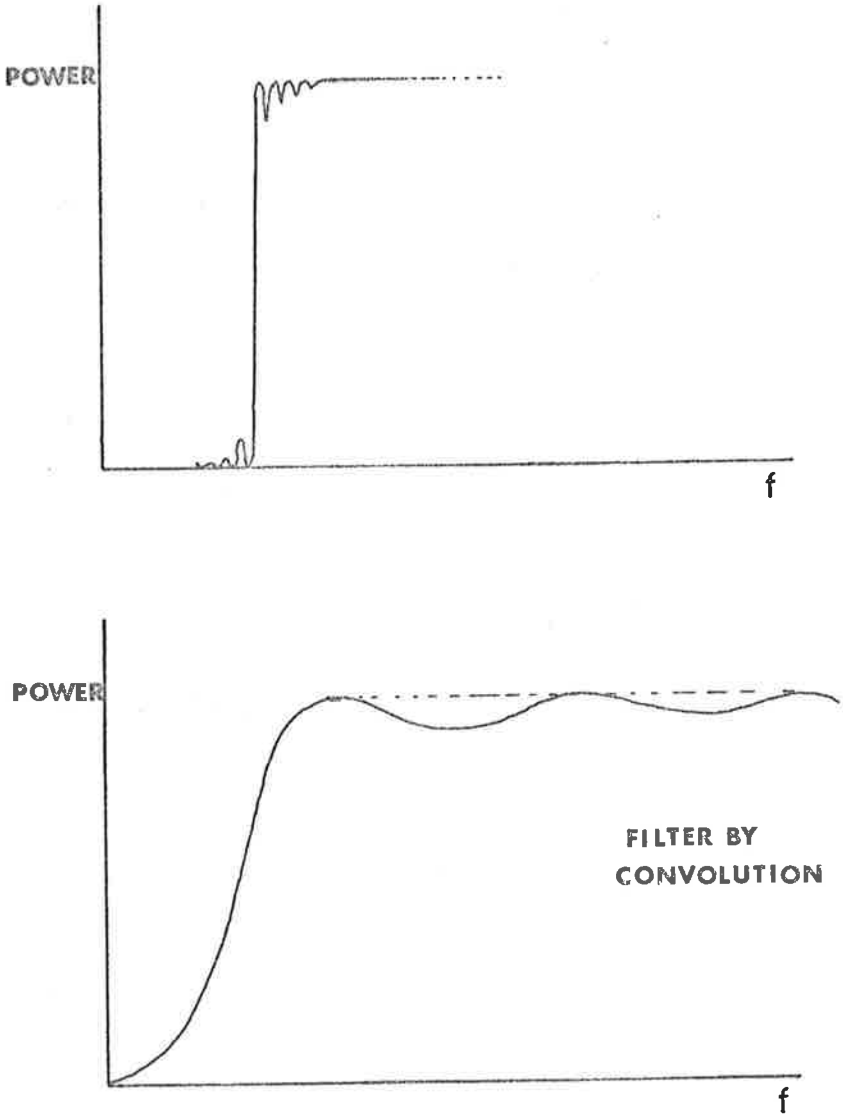

Figure 5.3 Filtered power spectra

end until the correct length is achieved. Although this does not change the width of the elementary power spectral estimates it does increase the number of estimates between 0 and f_N the Nyquist frequency. Hence, the zero values of the elementary frequency bands may no longer lie at the centres of these functions. If a stable estimate is calculated by averaging adjacent elementary estimates, then in this case the resultant frequency band may initially fall off more rapidly than the form computed without appending zeros and also the ripple would be less as illustrated in Figure 5.4.

5.2.7 Further Aspects of Linear Modification

It is of interest to look in more detail at the effect of different data windows used in conjunction with the FFT method of power spectral analysis. If the signal consists of a stationary random process with a (theoretical) Gaussian power spectrum, then the result of computing the squared modulus of the Fourier coefficients will be an approximation to the theoretical power spectrum. Buckley (private communication) has investigated the effects of the different windows, finding that at some stage leakage becomes predominant in all cases and causes the spectrum to deviate from the theoretical curve. The worst case occurs with no data window at all when the spectrum begins to deviate at a power level about two decades below the main peak. The best results are obtained using the Bartlett and Hanning windows which allow the spectrum to follow the theoretical curve for about five decades. The tails on the

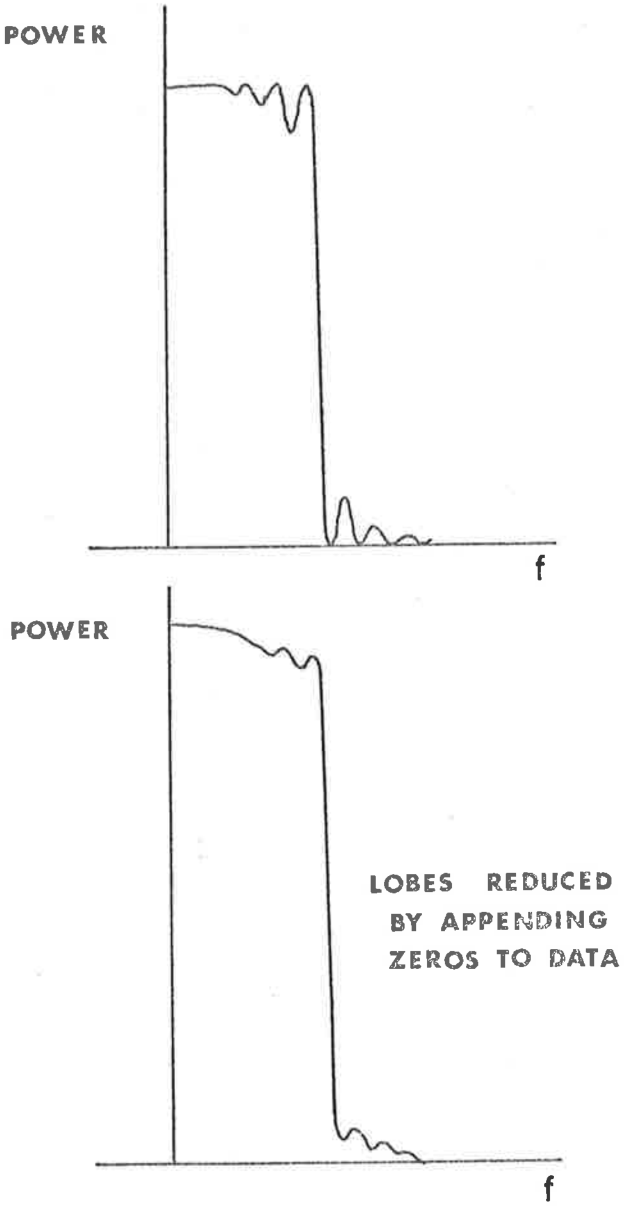

Figure 5.4 Two spectral windows illustrating the effect of appending zeros to the data

spectra, produced by the different data windows, settle down to constant power-law variations with frequency. For instance the absence of a data window produces a tail varying as f^{-2}, and the Bartlett and Hanning windows respectively produce tails varying as f^{-4} and f^{-6}. If the spectrum of the data fell off more rapidly than a Gaussian the deviations of the calculated power spectra would occur at higher power levels. Buckley also found that the second point of the computed power spectrum usually possessed a spurious component due to leakage through its sidelobe of the zero frequency value which depended on the mean value of the data.

5.2.8 The Auto-covariance Functions

The auto-covariance function is the Fourier transform of the power spectrum and therefore should be discussed in some detail. There is a difference between the ACVF derived from meaned lagged products and the function derived by the FFT method. This difference, however, is not large provided the length of data is much greater than the correlation length; a condition which is usually met. The difference occurs because the result via the FFT is equivalent to a constant length circular summation of products, whereas with the result using the old method the length of the summation decreases with increasing lag. It is in fact possible to force the two forms to be equivalent by appending N zeros to the N data points before processing with the FFT. This of course doubles the number of frequency bands.

5.2.9 Analysis of Scintillation

We are now in a position to discuss in detail the methods which were used to analyse the data recorded during June, 1970 at Culgoora. From the appropriate square-law detector[1] of the radioheliograph the signal was fed into an analogue to digital convertor and then written on to magnetic tape at the rate of 32 samples sec^{-1}. A time constant of 0.05 sec was used. Each block on the tape consisted of about 2815 data samples and began with an identifier containing the block number. The total time taken to record the data and an inter-record gap was 90 sec.

A computer programme was developed in conjunction with M. Wiseman for the purpose of decoding and analysing the scintillation data to obtain the power spectrum, autocorrelation function and intensity probability distribution. Each record, or block of information, was read by the computer and analysed before continuing with the next record. The sample values were represented by four digits, the first defining a factor of either 1, 8 or 64 which, when multiplied by the number represented by the remaining three digits gave the recorded value.

Before each tape was analysed the corresponding pen recordings of the scintillation were closely examined, noting blocks or parts of blocks containing bad data due to solar activity or other interference. During processing these records were bypassed or the bad points removed. Lightning spikes often contaminated the data and because of their rapid rise were easily detected during analysis by searching for sudden increases in the signal level. The spikes were removed and replaced by interpolation between existing data on either side.

---

[1] See Section 2.4 for a description of the recording procedure and the method of selecting the correct square-law detector output.

With a sampling rate of 32 samples $\sec^{-1}$, and an RC time constant of 0.05 sec, it was found that power from 50 Hz hum approximately equal to the scintillation power was aliased into the spectrum appearing as a large peak at 13.5 Hz. The sampling rate was in fact higher than necessary since the scintillation spectral widths were ∿1 Hz whereas the Nyquist frequency was 16 Hz. Therefore to reduce computing time every fourth point of the data was selected bringing the Nyquist frequency down to 4 Hz which was still in excess of the spectral widths. Selecting one quarter of the data in this way would have introduced other aliases. Therefore prior to this process the data sampled at 32 samples $\sec^{-1}$ were filtered by convolving with an 8 point running mean, thus decreasing and removing power at frequencies greater than 4 Hz. This convolution with a square function of width $\frac{7}{32}$ sec was equivalent to multiplying the power spectrum by a function given by $\left(\frac{\operatorname{Sin}\,(\pi f\frac{7}{32})}{\pi f\frac{7}{32}}\right)^2$, which has the first zero at $\frac{32}{7} = 4.6$ Hz. The magnitude of the sidelobes of this function fall off at the rate of f^{-2} and the only significant power aliased into the spectrum was between 4 and 9 Hz as shown in Figure 5.5; also the effect of the 50 Hz hum was practically eliminated. After the power spectrum was calculated the estimates were corrected to allow for the effect of the filter.

The number of points in the modified data at this stage was one quarter or less than in the original block. It was considered most useful to compute all the power spectra with equal resolution enabling them to be integrated simply, to gain better statistical stability in the spectral estimates. To achieve this, 768 samples were chosen for processing. If the data were shorter than the required length zeros were appended to make up the correct number.

Since data values are real quantities and the fast Fourier algorithm (Singleton, 1969) was designed to accept complex series, the choice was either to place all the data values in the real array and set the imaginary array to zero, or to divide the data into two equal parts placing them into the real and imaginary arrays respectively. This second method was used since it reduced the execution time of the Fourier transform by a factor of two. However, the result was not in the final form after applying the FFT and one further step was necessary to obtain the real and imaginary Fourier coefficients of each of the two halves of the original array. By computing the square of the modulus of the two sets of coefficients and adding them frequency by frequency

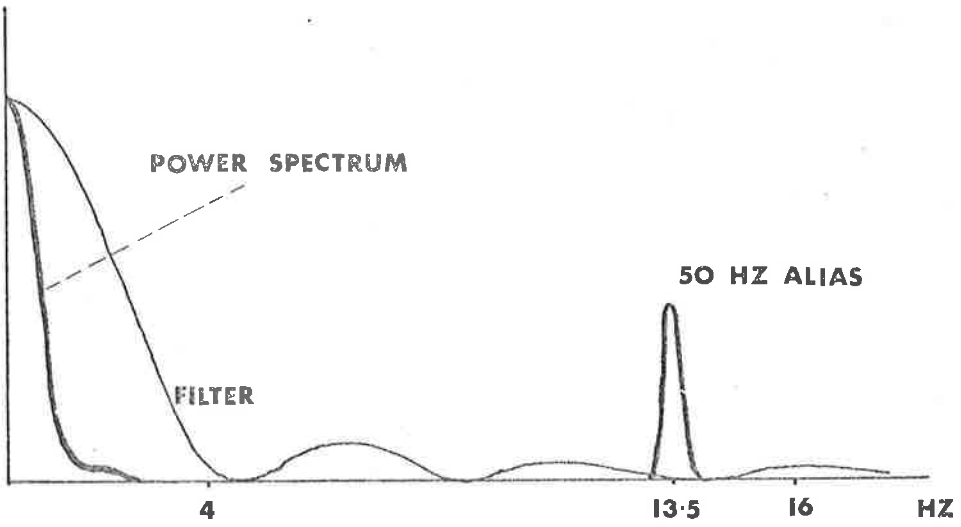

Figure 5.5 A typical power spectrum showing the effect of the running mean in reducing frequencies beyond 4 Hz

the final power spectrum was obtained.

Most of the data tended to drift with periods ∿20 sec or greater and the first five points of the power spectrum ($\lesssim$ 0.09 Hz) were ignored. To obtain better stability in the final estimates the elementary estimates were averaged in groups of four to produce the power spectrum in the final form.

The auto-covariance function was calculated by applying the FFT to the filtered (but not averaged) power spectrum. Also the original data were required in the filtered form to calculate the intensity probability distribution and its skewness. The two sets of Fourier coefficients were filtered in a similar manner to the power spectrum and were then combined into two arrays which were transformed in reverse to obtain the original data in a filtered form.

The unsmoothed version of each power spectrum up to the Nyquist frequency was written on to magnetic tape for further analysis which will be discussed in Section 5.3. It was found that different data windows had little effect on the shapes of the power spectra which often tended to develop tails at about 2-3 decades below the main peak. This suggested that all the spectra tended to fall off at a faster rate than a Gaussian spectrum. The tail, however, was not a nuisance in any way because it usually began at frequencies $\gtrsim$ 1 Hz. A noise spike also occurred at this frequency due to beam-phasing pulses of the radioheliograph occurring at one second intervals. Therefore the shape of the spectrum was affected at frequencies near 1 Hz, and details of the spectra were usually calculated using the section below ∿0.6 Hz, thus avoiding both the spurious 1 Hz peak and the leakage tail.

5.3 Interplanetary Scintillation at 80 MHz

5.3.1 General Considerations

From the large amount of data recorded at Culgoora many aspects of interplanetary scintillation might be investigated. The main aim of the observing sessions has been the study of variations in scintillation indices of selected sources over a period of 20-25 days, allowing the mapping of large structures within the interplanetary medium (Wiseman, 1972). Further investigation yields estimates of intrinsic source sizes and a better understanding of the distribution of irregularities causing the scattering. It is with this latter aspect that the author has been concerned, and in this section we discuss attempts to extract this type of information from the data recorded at Culgoora during June, 1970. Simultaneously included will be comments on the limitations of the data and some suggested improvements.

Examination of power spectra generated in the manner described in Section 5.2 reveal the presence of extraneous peaks which consistently appear at varying heights within the spectrum causing at times some doubt as to its true shape. It is believed these are aliases of the harmonics of the prominent 1 Hz peak mentioned previously and which was caused by the beam-tracking pulses. On strong sources such as 1226 + 02 (3C273), they are visible on the scintillation record as a series of spikes occurring every second and for cases when the scintillation was weak they produced significant peaks in the power spectra. Other switching pulses within the radioheliograph possibly had effects on the records, producing minor peaks at other frequencies in the power spectrum. The degree to which the signal was affected by pulses depended directly on the total power of the received signal. Thus a strongly scintillating but weak source would produce a 'cleaner' power spectrum than a stronger source. Also, the galactic contribution to the signal must be considered since it is included in the total power received by the radioheliograph. There was, therefore, a definite instrumental effect which could not be avoided, which was a product of the actual design of the system. Furthermore, being a total-power system the signal tended to drift due to both instrumental and ionospheric scintillation effects. In making these remarks about the radioheliograph it must be remembered that we are referring to very low signal levels in comparison to the signal levels from the sun, at which the instrument normally operates. These comments therefore are not designed to degrade the system, but are to point out the limitations when used for this type of work.

The drift in the signals produced large peaks at low frequency in most of the power spectra and the frequencies up to 0.1 Hz were therefore ignored. Unfortunately at 80 MHz the widths of the scintillation power spectra, except under unusual conditions, were 0.3 - 0.4 Hz (at e^{-1}) and the filter therefore removed 20-25% of the estimates making the calculation of spectral widths somewhat inaccurate.

Another problem encountered was associated with the statistical stability of the spectral estimates. Because of limited recording times for each source the stability of these estimates was, at the best, only five times better than for a single block. This entailed an average over 25 blocks or 36 min of data. Records of this length, from a single observation, were taken only on rare occasions and in the main the spectra consisted of averages over 4-10 blocks each of length 90 sec. Most of the spectra were therefore not very stable. Other authors working at higher frequencies (e.g. Cohen et al., 1967) have recorded data for about 5 min and successfully obtained angular diameter information. Their scintillation rate was, however, much faster than our rate because they were observing through smaller scale structure closer to the sun.

Data from other Culgoora observing sessions were even more limited and it was therefore decided to investigate angular diameter measurements using only the records from June, 1970.

5.3.2 The Power Spectrum

The process of obtaining widths (or square-root second moments) f_2, of the power spectra involved several steps. First, the single block spectra derived from observations both on-source and off-source were averaged for each observation of a source on each day. The averaged noise or off-source spectra were then subtracted from the averaged on-source spectra, leaving the spectra corresponding to scintillation alone. Each scintillation spectrum, which was an average over all records of an observation, was examined for statistical stability and either discarded or retained for further processing. Since the rms deviations of the spectral estimates are proportional to the values of the stimates, logarithms of the estimates were calculated. In this form they have a constant rms deviation and models may be fitted simply to the points. A log-Gaussian model was chosen and fitted by the method of least squares to a range of points within the power spectrum, delineated by the low frequency filter and the higher frequency noise peaks. On very few occasions were the spectra suitable to more than 0.5 Hz and usually the maximum useful limit was 0.35 - 0.4 Hz. Examples of spectra and their corresponding Gaussian models are shown in Figure 5.6. The width of the Gaussian model was then taken as the width of the actual spectrum. To obtain angular diameter information from these widths the approach adopted by Cohen et al., (1967) which assumes a circular Gaussian source. This places an upper limit on the diameter ψ, according to the relation $\psi \leqslant \frac{u}{1.2\pi f_2 z}$ radians, where u is

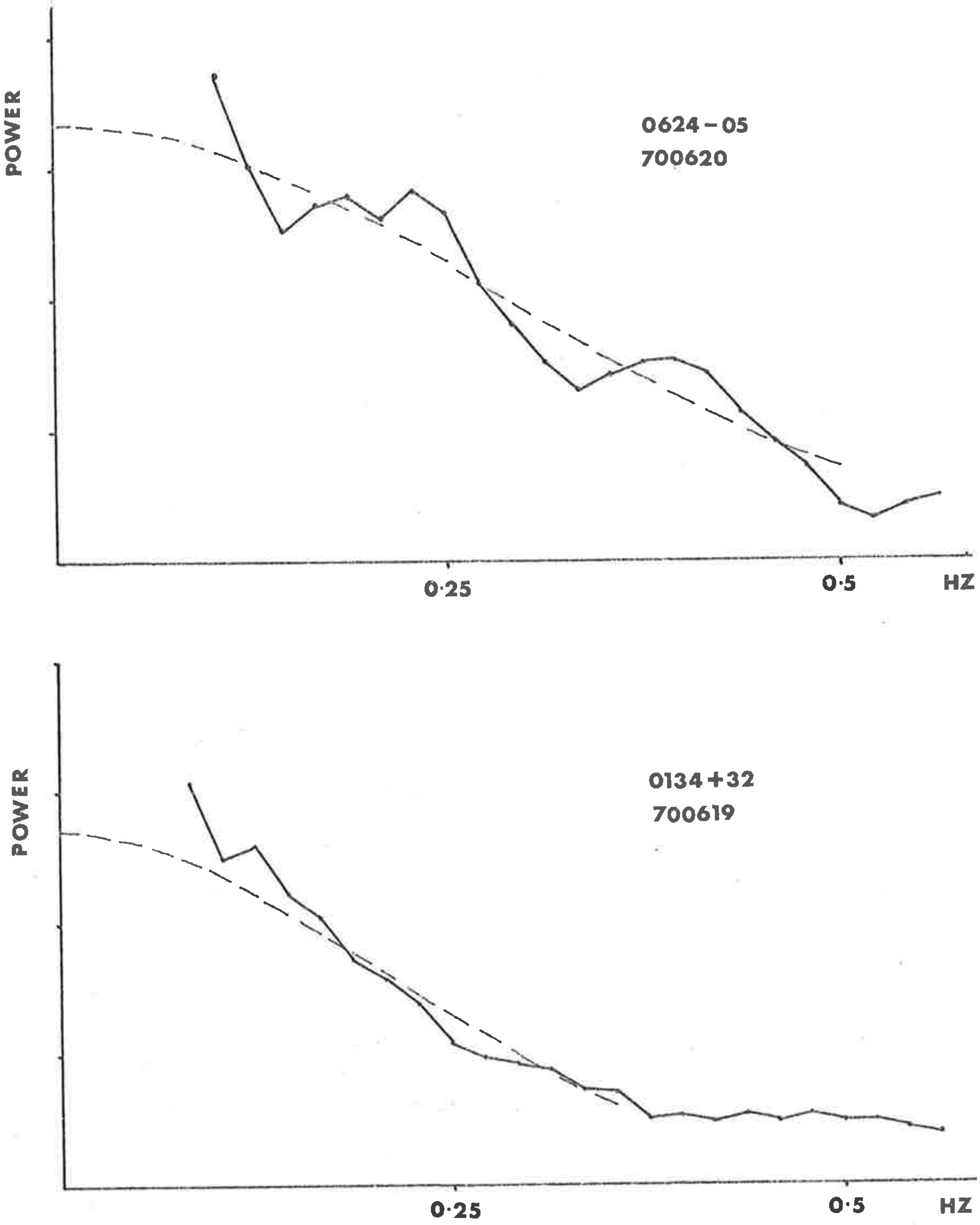

Figure 5.6 Examples of power spectra and the corresponding Gaussian curves

the velocity of the diffraction pattern across the observer and z is the distance from the diffracting screen.

It was found that f_2 varied considerably during the observing session due to the motion of three plasma streams shown in Figure 5.7. (Wiseman, 1972). The changes in f_2 roughly correlated with the changes in the nature of the scattering as the streams swept past the Earth. This meant that the velocity u was unknown, and in addition z varied considerably rather than being equal to the distance from the Earth along the line of sight to its closest approach to the sun. Conditions therefore varied from normal scattering in the undisturbed medium, to scattering by a stream in which the earth was often embedded. Under these circumstances of such a disturbed medium the data appeared unsuitable for angular diameter measurements and calculated estimates varied from ∿0.3" arc to ∿1.0" arc (depending on the values taken for u and z) for sources whose angular diameters were known to be less than 0.1 - 0.3" arc (Cohen et al., 1967; Little and Hewish, 1968). Thus almost all estimates of ψ were apparently a factor of 2 or 3 too large. Table 5.1 lists values of the calculated diameters for two sources without taking into account the possible positions of the scattering regions. A distance of 1 A.U. and a velocity of 350 km $\sec^{-1}$ were used in the calculation. If the streams were taken into account as dominant regions of scattering we would expect u to increase rather than decrease and z would generally decrease creating even larger values of ψ. On

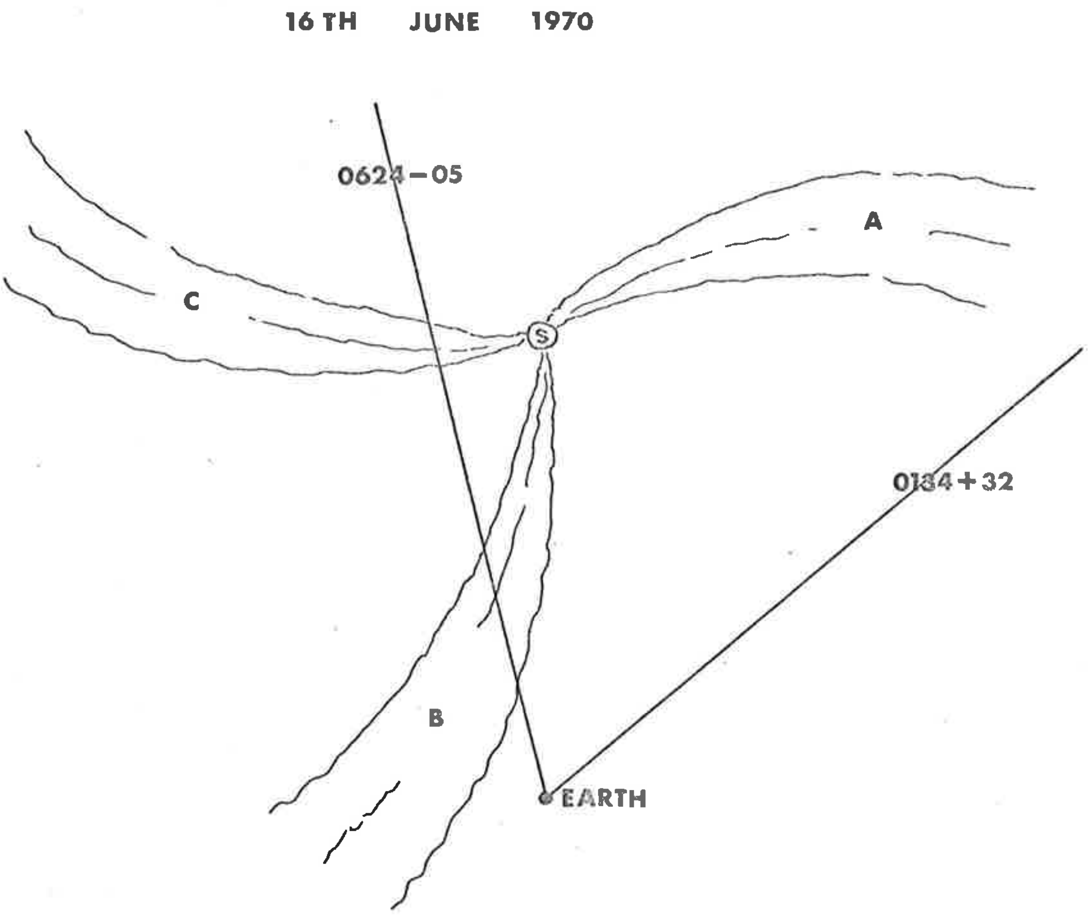
16 TH JUNE 1970
0624-05
A
C
S
0134+32
B
EARTH

Figure 5.7 Stream positions during 1970 showing the lines of sight from 0624-05 and 0134+32 projected onto the ecliptic plane.

	0134+32				0624-05			
	f_2 (Hz)	m	ψ (" arc)	Stream Movement	f_2 (Hz)	m	ψ (" arc)	Stream Movement
May 30								
31					.61	.24	.30	↑
June 1	.37	.56	.70	C				
2	.39	.50	.67	↓	.33	.30	.55	
3								
4								
5	.38	.50	.68		.38	.22	.47	
6	.37	.34	.70		.30	.24	.60	
7	.41	.32	.63		.46	.28	.39	
8	.44	.91	.59	+ A	.24	.23	.75	+ A
9	.23	.46	1.13		.28	.24	.64	
10	.24	.36	1.08		.32	.31	.56	↑
11	.35	.42	.74		.26	.34	.69	
12	.35	.29	.74		.27	.18	.67	
13	.36	.59	.72		.22	.24	.82	
14	.41	.45	.63	↓	.34	.23	.53	
15	.33	.36	.79		.34	.19	.53	
16	.22	.57	1.18					
17	.25	.35	1.04	+ B	.98	1.02	.18	+ B ↑
18	.35	.45	.74		.31	.32	.58	
19	.29	.27	.90		.21	.19	.86	
20	.40	.22	.65		.27	.27	.67	
21	.58	.61	.45	↓				C

f_2: half-width (to e^{-1}) of averaged scintillation power spectra
m^2: scintillation index
ψ : source diameter (" arc)
Stream movement (of corotating streams crossing line of sight)
+: Earth immersed in stream
→ : stream moving away from Earth (see Figure 5.7 for positions of streams A, B and C during 16th June, 1970)

Table 5.1

examination of all previous power spectra from Culgoora observations, similar spectral widths f_2 have been obtained. We therefore question the validity of the expression for ψ at our frequency of 80 MHz. The formula is based on a thin, weakly scattering screen and we propose that at 80 MHz the thin screen assumption is no longer valid leading to erroneous values for the angular diameter estimates.

We conclude that, apart from the possible breakdown of the formula, under the conditions of an active interplanetary medium the values of f_2 could be unreliable (since u and z may vary) giving misleading results for ψ. The coverage of sources during our observations was not very satisfactory since for the one month's data analysed only 6 scintillating sources were suitably situated for angular structure determinations in the range $\sim\pm 60^{\circ}$ from the sun. The angular diameter formula is not valid when the earth is contained within the scattering region as was the case for the remaining scintillating sources. The detailed shape of the power spectra remains open to question because of the detrimental effects mentioned previously. Other authors have observed power law tails on their spectra (Lovelace et al., 1970), but in our case such tails if present are contaminated by the 1 Hz peak.

5.3.3 The Intensity Probability Distribution

Close examination of probability distributions of the scintillation from radio sources might be expected to yield some information about angular diameters of sources. For instance very strong scintillation of a small diameter source would produce a skewed distribution whereas the distribution of scintillation from a nearby source of greater angular diameter would not be skewed to the same extent even though the same phase deviations would have been imposed on the wavefront. This is caused by the smearing effect of the larger diameter of the source. The scintillation in such a case is the sum of the signals from all parts of the source, with the result that the observed scintillation is blurred, and by the central limit thereom the probability distribution tends towards a Gaussian shape. No sources were suitable (that is, sufficiently close to the sun) for investigating this approach and the statistical stability of the distributions in most cases was not sufficient.

The results of these investigations of the power spectra and intensity probability distributions have demonstrated that the interplanetary scintillation data in the form recorded at Culgoora was not in general suitable for detailed analysis although the results suggest a breakdown of the formula used for estimating angular structure. The instrumental effects cannot be overcome but long records ($\sim$30 min) would provide better statistics. Also records of this length taken while the interplanetary medium was stable should allow better estimates of the source diameters provided the question concerning the validity of the formula for ψ could be resolved.

5.4 Observations at Parkes

5.4.1 Analysis of Data

As described in Section 2.6 simultaneous observations at 150, 600 and 1410 MHz were made at Parkes, N.S.W. during January 19th to 21st, 1968. The number of different sources observed during the three days was 56 but possible interplanetary scintillation occurred on only 14 of these. However, after detailed analysis no significant scintillation occurred on any of the sources except 1938-15 which scintillated at 600 MHz on all three days and possibly at 150 MHz on the 20th. This latter effect may have been due partially to solar activity increasing the background noise during the observation because the sun was active at this frequency on the following day. However, we shall assume that the increase was genuine and we shall attempt to explain the cause of the event on this basis.

The information was recorded on paper charts and when scintillation appeared to be present records of 4-8 min, both on and off the source, were punched on paper tape at 6 samples sec^{-1}. The digital data were analysed using the method described by Blackman and Tukey (1958). In most cases the signal drifted significantly necessitating the use of a high-pass filter. This was achieved by convolving the data with a $\frac{\sin x}{x}$ function having a spacing of 100 data points or 8.2 sec between the first zeros, and a total length of 16.4 seconds. This removed low frequency power up to ∿0.1 Hz. The autocorrelation function was calculated to a lag of 30 points and the corresponding spacing of the power spectral estimates was 0.098 Hz.

From the charts the intensity probability distributions were estimated using a method described by Orhaug (1965). The method involved selecting a section of scintillation and dividing the intensity variation into a series of equally spaced levels. The number of cross-overs encountered at each level was counted and a plot of these numbers against the arbitrary intensity levels represented the probability distribution for the selected section of data. The widths of the distributions represented the rms deviation of the recorded signals. By subtracting the off-source distribution from that of the on-source signal the rms deviation of the scintillation was found which, when divided by the source height, gave the scintillation index.

5.4.2 Results and Interpretation

Usually interplanetary scintillation at two or more frequencies provides useful information about the nature of the scattering within the medium from the degree of correlation between the observed signals. Under conditions of weak scattering and when the observer is situated beyond the Fresnel distance of the irregularities, the scales of the patterns over the ground are the same. The scintillation index m, is proportional to the observing wavelength, λ, and the radio of indices at two wavelengths is equal to the ratio of the wavelengths, $m \propto \lambda$.

Within the Fresnel zone, however, $m \propto \lambda^2$ thus allowing limits to be placed on the distance from the scattering region by comparing the ratio of indices to the ratio of the wavelengths. If the scattering were strong in both cases the indices would be near unity. However, if conditions allowed strong scattering at only the low frequency while the high frequency signal exhibited weak scattering, the ratio of the indices would deviate from the λ or λ^2 dependences and it would then be possible to estimate the distance from the sun at which multiple scattering began to dominate.

The cross-correlation of signals at different frequencies may also yield information about the nature of the scattering region. If at the higher frequency the observer was in the Fresnel zone while remaining in the Fraunhofer or far-zone at the lower frequency, the scales of the two diffraction patterns would be different and correlation between signals reduced. In general, if the scattering were weak the upper limit for good correlation between scintillation observed at frequencies f and $f + \Delta f$ is given by the relation (Budden, 1965) $\frac{\Delta f}{f} \sim \frac{2\pi a^2}{\lambda z}$, where a represents the irregularity scale, λ the radio wavelength and z the distance from the scattering region. Under conditions of strong scattering the correlation depends also on the phase deviation ϕ_o and we have (Salpeter, 1967) $\frac{\Delta f}{f} \sim \frac{2\pi a^2}{z\lambda\phi_o{}^2}$. Therefore, let us estimate whether a correlation would be expected between scintillation at 150 MHz and 600 MHz and between 600 MHz and 1410 MHz, by inserting into the weak scattering relation the following values for the parameters,

$a = 100$ km

$\lambda = 200$ cm (for the first pair of frequencies)

$z = 1$ A.U. $= 1.5 \times 10^8$ km.

The numerical value of the expression is 0.22 but $\frac{\Delta f}{f}$ has a value of 3 indicating that little correlation would be observed in this case. Evaluating the expression for the other pair of frequencies, taking $\lambda = 50$ cm, we obtain a value 0.84. However $\frac{\Delta f}{f} = 1.35$ and only slight correlation would be expected. If the scattering were strong $\phi_o > 1$, the differences would be even greater. Hence little information could be gained by cross-correlating signals at our observing frequencies because the change from weak to strong scattering would not be detectable at such low correlation values.

With the frequencies used, however, the possibility of observing scintillation simultaneously at three or even two of these frequencies would be remote because either the source would be too far from the sun for the high frequency, and we would be observing well within the Fresnel region before amplitude variations had developed, or too close to the sun for the low frequency when the intrinsic source size has the effect of blurring the scintillation until it becomes unobservable.

Under the conditions of the interplanetary medium during the 19th to the 21st January, 1968 significant scintillation was observed on only one source, 1938-15 and only at one frequency, 600 MHz. This suggests that the interplanetary medium was very quiet during this period particularly since sources were observed at solar elongations ranging from ∿8° to 90° and we obtained only extremely weak scintillation in most cases. Some of the sources had angular diameters large enough to prevent the scintillation being observed above the background noise, thus partially accounting for the lack of data. The scintillation index for 1938-15 on the three days was about 0.2 at 600 MHz. On the second day, the 20th January, the 150 MHz signal appeared to be scintillating although the increase was small and may have been partially due to an increase in the background noise mentioned previously. The index calculated for this occasion was $\leqslant 0.1$. Figure 5.8 shows the sun and 1938-15 projected onto the celestial sphere. Also illustrated in the figure is the position of a recurrent active region on the sun, McMath plage 9153, which may have been related to the observed change in scintillation. The region was situated on the western limb of the sun at N25-30° on 20-21st January and a class 2N flare was reported at 0115 UT on 20th.

To explain an increase in the scintillation index at 150 MHz without changing the signal at 600 MHz we require a decrease in the size of irregularities to an extent that the scintillation at 150 MHz was no

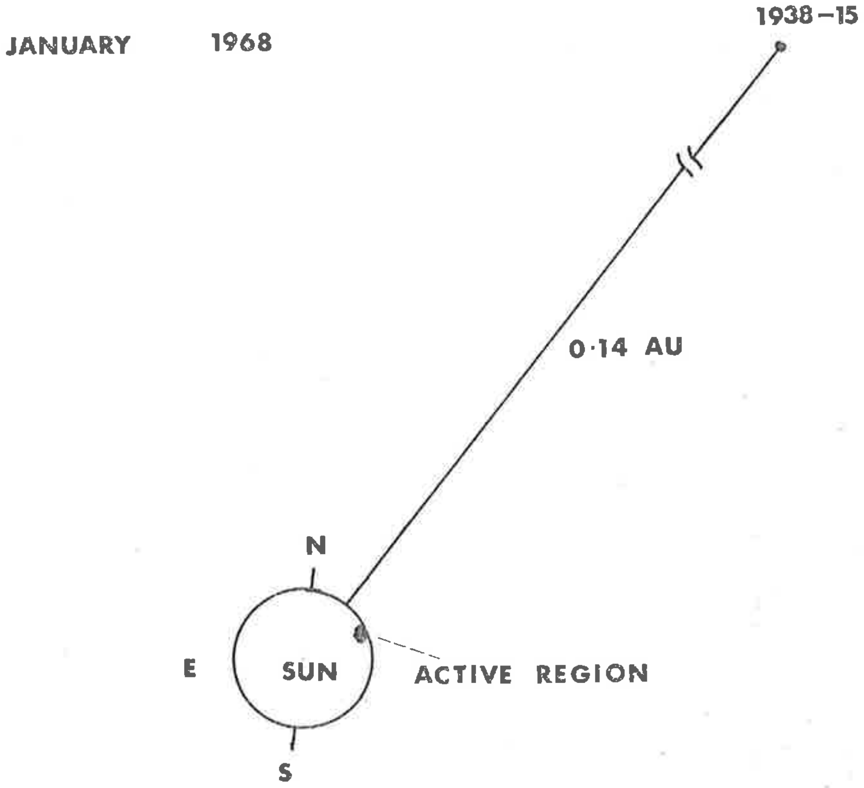
JANUARY 1968
1938–15
0·14 AU
N
E
SUN
ACTIVE REGION
S

Figure 5.8 Positions of 1938-15 and the sun during January 1968. A region of activity possibly related to the observations is marked on the solar disk.

longer blurred by the angular size effect. In addition, the variation in the electron density of the irregularities must remain unchanged thus causing no effect on the higher frequency signal, which we assume was not affected by the angular size of the source. This explanation is offered to account for the observations which could have resulted from a genuine change in the structure of the interplanetary medium near the line of sight to 1938-15. However, we state again that the 150 MHz observations were at times contaminated by solar activity especially during January 21st. The true explanation of the event therefore remains open to question.

5.5 Bessellian Power Spectral Analysis

5.5.1 Introduction

Observations of interplanetary scintillation at a single site yields only the temporal auto-correlation function, $\rho(t)$, of the received signal which depends on both the spatial structure and velocities of the irregularities within the diffracting medium. Hence, a change in width of $\rho(t)$ may be due to a change in velocity or a change in scale or a combination of both. Lovelace et al. (1970) pointed out that under certain conditions the observed power spectrum might develop a modulation from which the velocity of the drifting pattern (and hence the solar wind) could be determined. More recently Rufenach (1971) has applied the same approach to ionospheric scintillations and to some interplanetary scintillation data.

5.5.2 Theoretical Considerations

Consider the case of a thin, weakly scattering medium situated at a distance z from the observer. The two-dimensional intensity power spectrum of the received signal of wavelength λ can be approximated (Budden 1965; Salpeter, 1967) by

$$P_I\ (q_x, q_y) = 4\ P_\phi\ (q_x, q_y)\ \sin^2\left\{ \frac{\lambda z}{4\pi} q^2 \right\},$$

where q_x and q_y are spatial frequencies, $q^2 = q_x{}^2 + q_y{}^2$ and P_ϕ is the phase function of the wave on emerging from the diffracting layer. Therefore P_I is simply P_ϕ modulated by a $\sin^2$ term. The number of minima (or zeros) depends on the values of λ and z. For example, for a given form of P_ϕ and increase in λ or z causes the zeros to move to higher frequencies. Considering the limiting cases of either $z << z_o$, where $z_o = \frac{2\pi a^2}{\lambda}$ is the Fresnel distance of the scattering region containing irregularities of predominant scale a, and $z >> z_o$, then in the former case $P_I \simeq P_\phi\ (\frac{\lambda z}{4\pi}\ q^2)^2$ and no modulation is observed, whilst in the latter case the $\sin^2$ term oscillates rapidly and can be replaced by its mean value of ½ so that $P_I \propto P_\phi$ and again the modulation is not observed. For the intermediate case when $z \lessdot z_o$, P_I is modulated by a function whose argument is given by $\left(\frac{q}{q_F}\right)^2$, where $q_F = \sqrt{\frac{2\pi}{\lambda z}}$ is defined as the Fresnel filtering frequency. The modulation is observed only when the distance z from the scattering region is less than the Fresnel distance.

The spatial power spectrum $P(q_x, q_y)$ is related via a two-dimensional Fourier transform to the spatial auto-correlation function, $R(r_x, r_y)$. If the scintillation were monitored using three or more spaced antennas R could be observed directly. In the case of recordings taken using a single antenna this is, of course, not possible. In this case if the irregularities possessed a unique velocity u, $\rho(t)$ the temporal one-dimensional auto-correlation function would be stationary with respect to time and would represent a cross-section, $\rho(r = ut)$ of the two-dimensional auto-correlation function, where $r^2 = r_x{}^2 + r_y{}^2$, in the direction of motion of the irregularities. If we now assume R and hence P to be approximately circularly symmetric, implying near isotropic scattering in the interplanetary medium (a reasonable approximation since the elongation of the irregularities has been measured to be $\sim 2:1$ or less (Dennison and Hewish, 1967)), then P and R can be expressed as functions of single variables q and r, and in particular $\rho(r) \equiv R(r)$. The relation between P and ρ is given by the Bessel transform

$$P(q) = \frac{1}{2\pi} \int_0^\infty J_o\ (qr)\ \rho(r)\ r\ dr.$$

Since $r = ut$ and q is related to the temporal frequency by the relation $q = \frac{2\pi f}{u}$, then $P\ (f) = \frac{1}{2\pi} \int_0^\infty J_o\ (2\pi ft)\ \rho(t)\ t\ dt$. The normal method of spectral analysis involves a one-dimensional Fourier transform of $\rho(t)$ to obtain a temporal power spectrum $P'(f)$ where

$$P'(f) = \int_{-\infty}^{\infty} P(q_x = \frac{2\pi f}{u}, q_y)\ dy.$$

This is the projection of the two-dimensional power spectrum onto the vertical plane along the x-axis, here representing the direction of motion of the diffraction pattern. The integration has the effect of 'filling in' the modulation produced by the $\sin^2$ term. We therefore have under very specialised conditions a means of obtaining the two-dimensional power spectrum from the one-dimensional auto-correlation function received at a single site.

The minima occur when $q^2\frac{\lambda z}{4\pi} = n\pi$ ($n = 0, 1, 2\ldots$), that is when $f = \frac{u}{\sqrt{\lambda z}}\sqrt{n}$, and if z the distance to the scattering region is known then the projected velocity u of the irregularities can be estimated.

A more realistic case is for an extended medium of thickness L (Salpeter, 1967) in which case the observed intensity power spectrum is given by

$$P_I(q) = 2P_\phi(q)\left\{1 - \left(\frac{4\pi}{L\lambda q^2}\right)\sin\left(\frac{L\lambda}{4\pi}q^2\right)\cos 2\left(\frac{z\lambda}{4\pi}q^2\right)\right\},$$

which obviously does not have minima extending down to zero. When $L \ll z_o$ this equation reduces to the thin screen approximation discussed above, but if $L > z_o$ then the oscillations rapidly die out as q^2 approaches $\frac{4\pi}{L\lambda}$.

We now propose to examine the dependence of the theoretical spectra on the parameters of the screen. To illustrate the effect of varying the distance z and thickness L of the screen, spectra at 80 MHz have been computed and are shown in Figure 5.9. As the screen is approached the minima move to higher frequencies and become more difficult to observe. As the thickness is increased the minima become smeared out at lower frequencies. The effect of the shape of the phase function P_ϕ is also evident. It can be seen from Figure 5.9 that the rapid fall-off of the Gaussian form of P_ϕ, compared to the power law form, diminishes the visibility of the fringes. In both cases an irregularity scale of 200 km was used because at 80 MHz the weak scattering condition is applicable only at solar elongations > 30° where the scale would be of this order. The exact value of the scale was not important for the above illustration, and a reduction in the value would decrease the slopes of the computed spectra. Also from Figure 5.9 we notice that under ideal conditions of constant irregularity scale and velocity only three minima at the most are visible at 80 MHz. If the variation of the projected velocity along the line of sight and the effects of velocity dispersion had been included in the calculation we would expect the visibility to be even less. We shall now consider these two effects.

To asses the first effect, which is purely geometrical, we assumed the scattering was very weak and divided the medium into a series of thin screens ($L << z_o$) along the line of sight. The theoretical power spectrum of each screen was calculated. These were then added with a weighting factor proportional to the scattering power of the medium (r^{-4}, where r is the distance from the sun). A Gaussian phase function

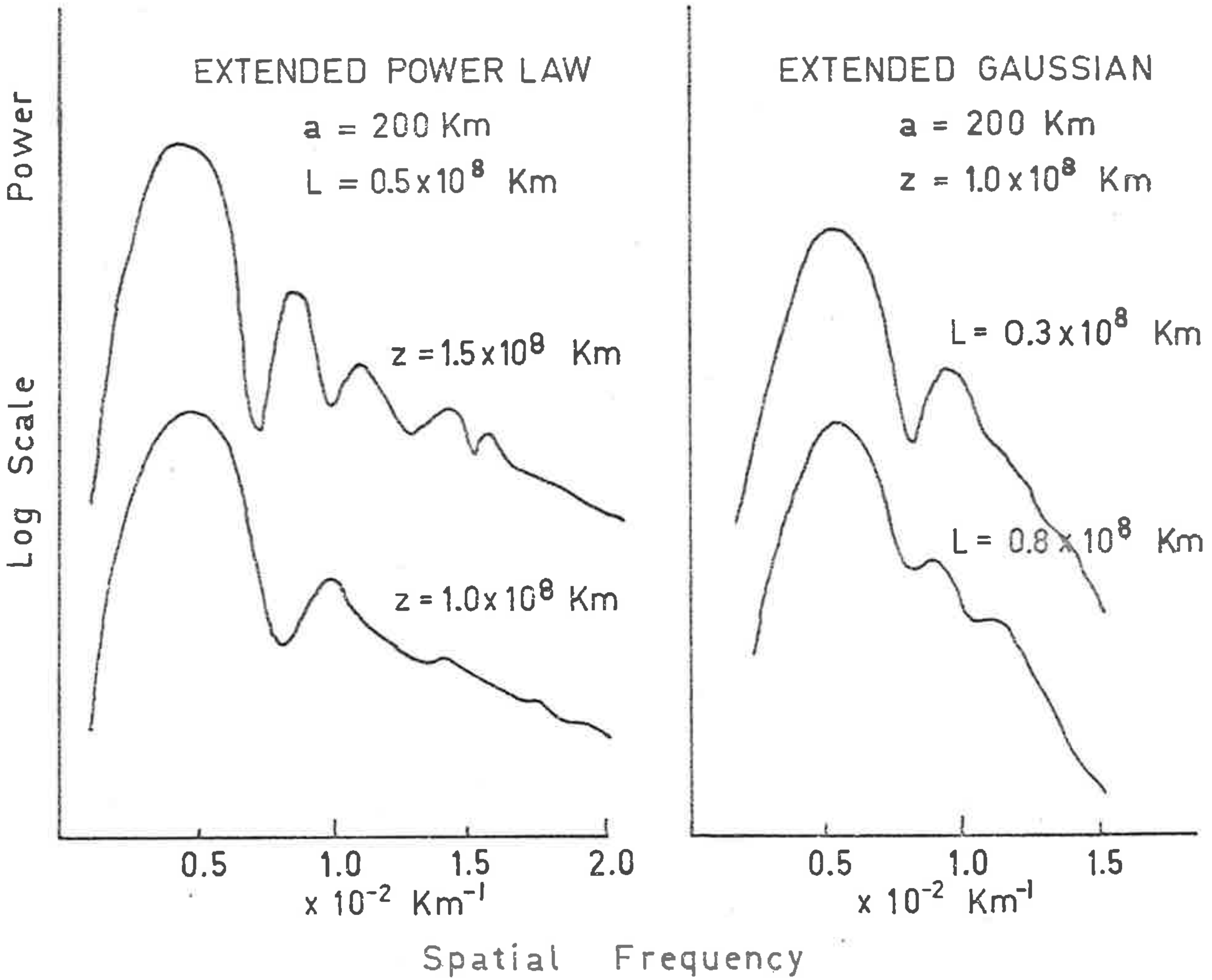

Figure 5.9 Theoretical spectra illustrating the effects of changes in Z and L. The models are based on an extended scattering region using a power law phase function in the left hand diagram and a Gaussian phase function in the right.

was used having a width dependent on the scale a, of the irregularities. Values for a were taken from Readhead (1972) and vary from ∿20 km at r = 0.1 A.U. to ∿220 km at r = 1 A.U. The results are shown in Figure 5.10 from which it is apparent that the modulation is blurred rapidly for elongations $\gtrsim 35^{\circ}$. This rapid onset of blurring is the result of both the geometrical velocity effect and also the increase in scale which steepens the spectra. It is also clear from Figure 5.10 that at larger elongations the reduction of the apparent (integrated) velocity causes the minima to move to higher spatial frequencies. Because the weak scattering conditions are violated at 80 MHz for elongations > 30°, we have calculated the spectra for a wavelength of 10 cm (3 GHz). To adjust to another (longer) wavelength say λ_1, the spatial frequency scale must be multiplied by $\sqrt{\frac{10}{\lambda_1}}$, where λ_1 is expressed in cm.

The second effect which might blur the fringes is the presence of a range of velocities at a fixed distance z. This effect is shown in Figure 5.11 (solid line), where a random velocity field of 350 ± 25 km $\sec^{-1}$ has been introduced. The power spectra using the thin screen approximation were calculated for velocities at 1 km $\sec^{-1}$ intervals and then averaged. An irregularity scale of 200 km and a distance of 1 A.U. were used as well as a Gaussian phase function. The broken curve in Figure 5.11 illustrates the effect of resolution on the fine structure of the power spectrum when only one velocity component is present (350 km $\sec^{-1}$). All the minima should theoretically extend to zero but points

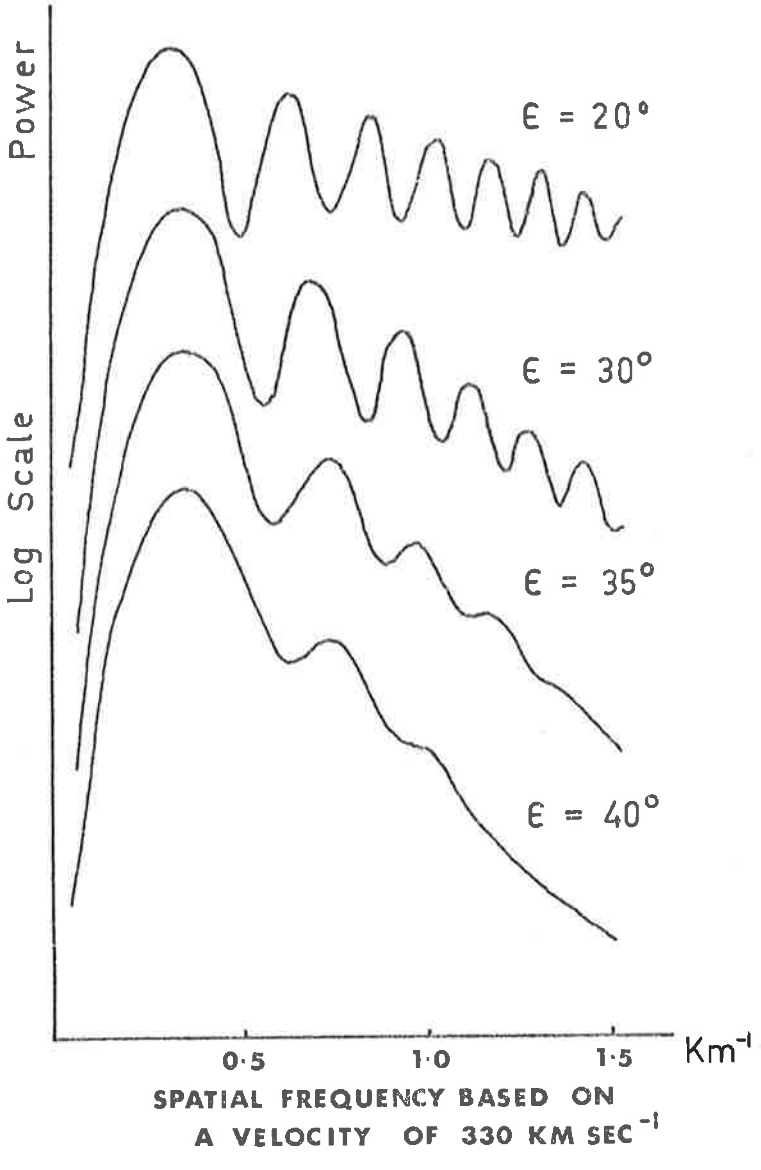

Figure 5.10 Theoretical spectra showing the geometrical effects on the visibility of the fringes. The frequency scale corresponds to an observing wavelength of 10 cm.

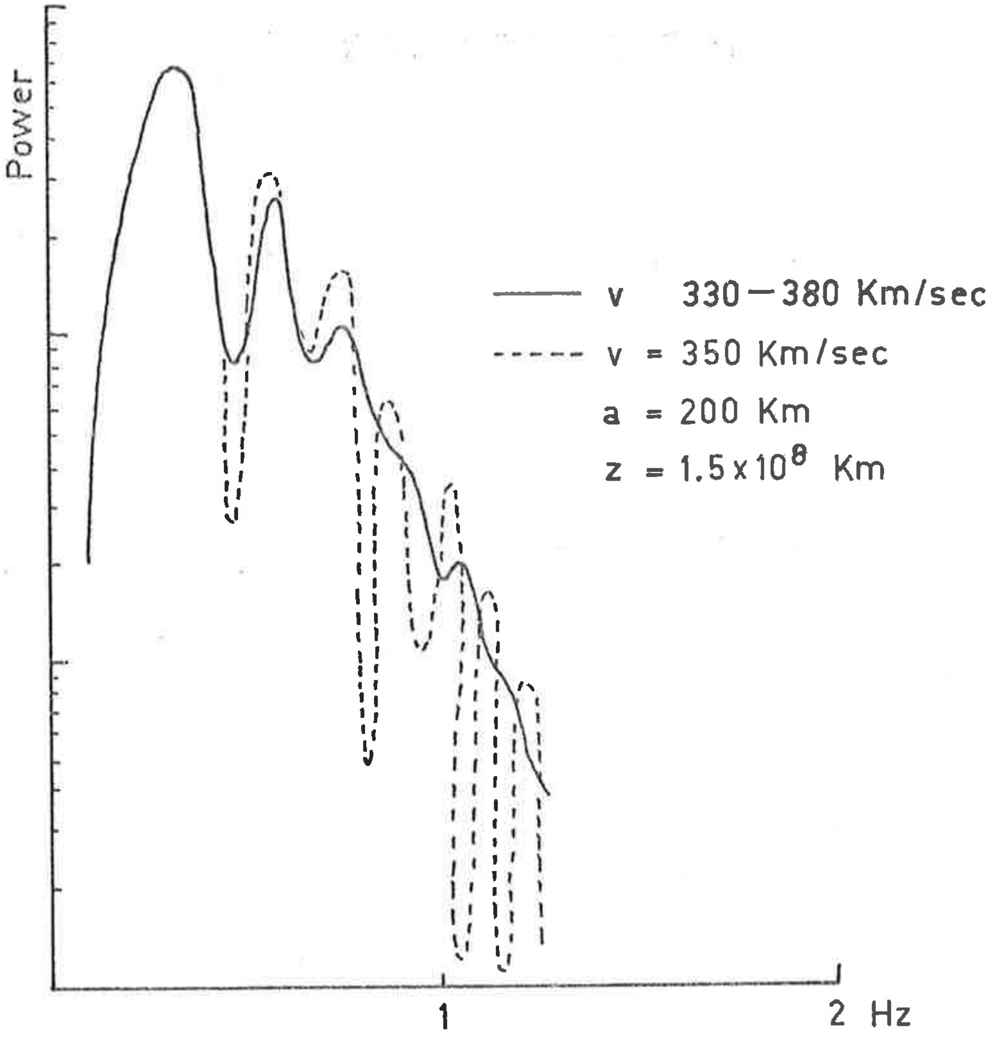

Figure 5.11 Theoretical spectra illustrating the effects of a random velocity field and (the dotted line) resolution

were plotted at frequency intervals equal to the intervals used in estimating the Bessel power spectra of the Culgoora data. It is seen that the depth of the minima are affected and after ∿1.3 Hz they are no longer resolved. The solid line was also drawn through points separated by the same interval and therefore is subjected to smoothing by the finite resolution as well as to smoothing by the random velocity field.

In summarising the theoretical investigation it appears that under normal conditions it is unlikely that minima in either the Fourier or Bessel transforms would be observed at 80 MHz. If the strict assumptions of weak isotropic scattering are relaxed we expect even less chance of observing fringes. The requirement for weak scattering limits the observations to elongations greater than ∿30°. This introduces a geometrical velocity effect and an increase in effective irregularity scale which steepens the spectra making minima less visible. Also, of course, the screen cannot be considered as thin at these elongations. With all these factors in mind we can say conclusively that under normal conditions the minima would be blurred completely. The one-dimensional power spectra derived from the real data rarely showed any indication of a low frequency dip, suggesting that the blurring is actually complete as predicted and only under special circumstances would positive results be obtained.

It is of interest to consider the results of Lovelace at al. (1970)

in the light of our present investigation. Records of 3 min duration at 430 MHz were analysed and the Fourier and Bessel transforms showed interpretable minima on two occasions. At the small elongations of 12° and 22.5° there would be very little line of sight smearing of the fringes as seen in Figure 5.10. Velocity dispersion has been observed to persist out to elongations of ∿8° (Ekers and Little, 1971) and therefore would not have affected, to a great extent, the scintillation observed by Lovelace et al. At higher frequencies (∿1 GHz) this effect may be a problem, and fringes in the spectra of observations made close to the sun (< 8°) could be blurred. Observing frequencies near 500 MHz therefore appear to be the best choice if this method of analysis is to be employed.

5.5.3 Analysis of Culgoora Data

Over the past three years a large amount of scintillation data has been collected from observations using the radioheliograph at Culgoora. No intensity spectra were observed to show dips at low frequencies except during 28th May, 1968 (Dennison and Wiseman, 1968) on the source 0134 + 32. This was interpreted as evidence for the proximity of the scattering region which was, in fact, the leading edge of a corotating plasma stream passing across the earth. The proximity of the region brought the earth into the Fresnel scattering region so that there was a possibility of observing fringes in the Bessel Transform or if they were deep enough, in the normal Fourier transform. The overall width of the stream was estimated at $\sim$0.5 A.U. but on examination of Earth-satellite data the stream was found to be subdivided into three narrower plasma enhancements and it was the first of these which created the required conditions. On the following day when the earth became embedded in the stream the scintillation index was greater but no low frequency dips were observed.

Other attempts have been made to estimate the screen parameters from these data by fitting a theoretical projected spectrum to the observed Fourier power spectrum (Golley, 1971). However, only approximate values could be obtained in this way because the variance of the spectral estimates allowed a wide range for the derived screen parameters. A typical Fourier power spectrum is shown in Figure 5.13 where it can be seen that only the first low frequency dip is clearly visible. The form of this spectrum allowed the screen to be placed approximately at a distance of 0.1 A.U. from the Earth.

In order to improve the resolution of the minima an attempt was made to compute the Bessel transform of the data. Whereas Lovelace et al. (1970) used the normal Bessel transform (or rather its prewhitened form), it proved more convenient from the point of view of computational simplicity to use a sec (Θ) transform of P_F, the Fourier power spectrum, given by

$$P(f) = - \frac{d}{df} \int_0^{\frac{\pi}{2}} P_F \ (f \sec \Theta) \ d\Theta.$$

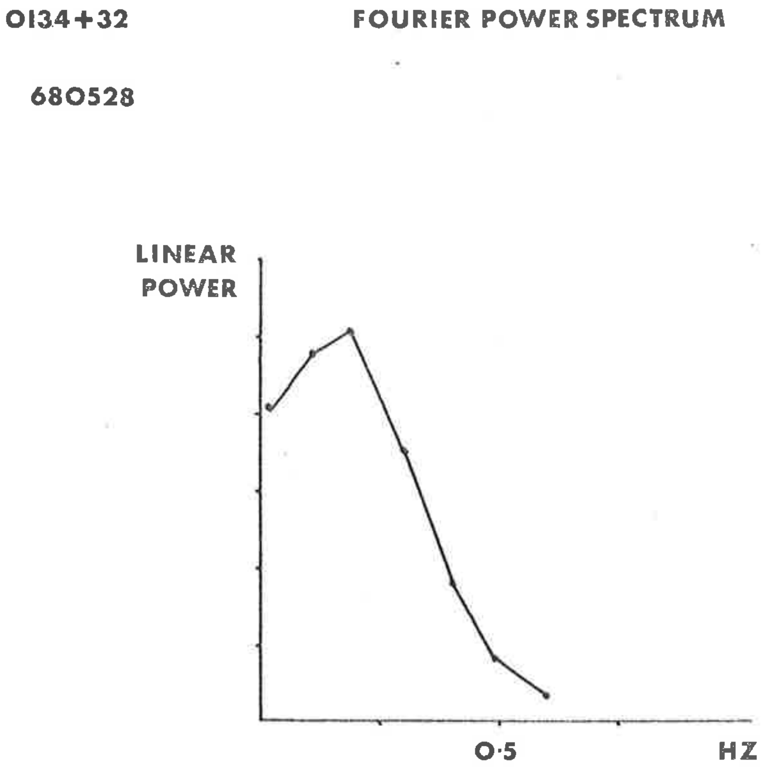

Figure 5.13 Fourier power spectrum of scintillation of 0134+32.

The sec Θ transform, P(f), has been shown to be equivalent to the Bessel transform by Buckley (private communication). Several records of 0134 + 32 were analysed in this manner and although low frequency dips were found in the Fourier spectra of these data, a significant increase in resolution using the sec Θ transform was found only in the case of one record when a $\sqrt{n}$ dependent series of minima was revealed. This is shown in Figure 5.12 where, apart from the low frequency dip ($n = 0$), three or possibly four minima can be seen. After ∿1.4 Hz the spectrum becomes statistically unstable. Taking the distance of the screen $z = 0.1$ A.U., a velocity of 315 km $\sec^{-1}$ was derived in agreement with spacecraft measurements at that time. The minima in the spectra were not as pronounced as those in the spectra derived by Lovelace et al., probably due to the shape of the irregularities in the stream. Evidence for this conclusion came from Golley (1971), who when fitting the theoretical projected spectra to the actual spectrum found that an irregularity scale of 500 km was required suggesting a more elongated structure within the stream compared to the normal scale in the interplanetary medium of ∿250 km. The velocity derived by Golley was 330 km $\sec^{-1}$ in close agreement with the Bessel transform results.

Recent detailed analysis of scintillation data obtained during June 1969 has revealed spectra with even more pronounced dips at low frequencies than the 0134 + 32 (1968) spectra (Wiseman, 1972). These observations have also been associated with the proximity of a corotating

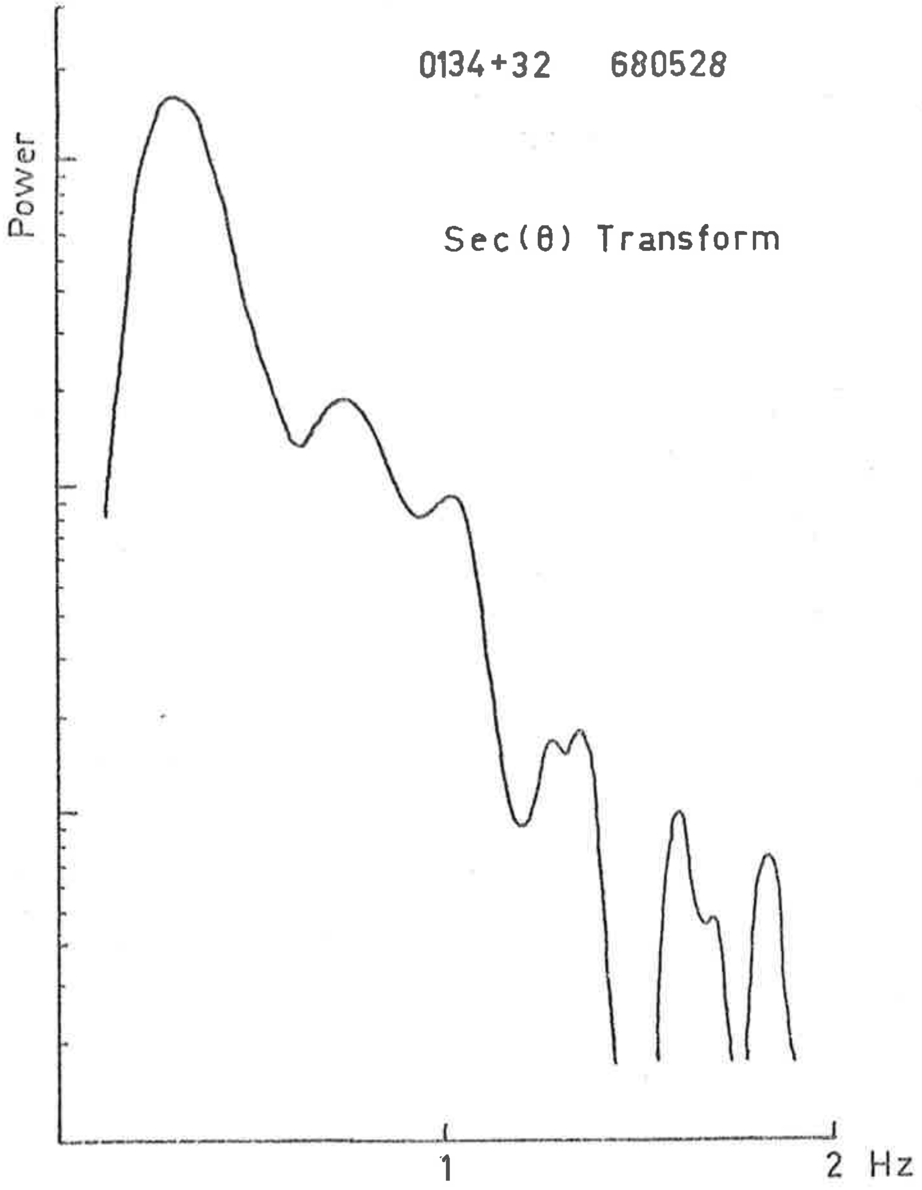

Figure 5.12 Sec(θ) transform of data from observations of 0134+32. Four minima are apparent before spectrum becomes unstable

stream to the earth. However, the spectra were not brought to the notice of the author in time for their inclusion in this dissertation.

CHAPTER 6

THE ADELAIDE PROJECT

6.1 Introduction

In the previous chapter we briefly discussed the limitations of interplanetary scintillation for obtaining detailed information about the interplanetary medium. For instance, the main restriction concerned the measurement of parameters such as the size, velocity and direction of motion of the irregularities within the diffraction pattern observed at the Earth. This restriction arose because most interplanetary scintillation is recorded at only a single site thus being unable to provide estimates for these parameters. In situ measurements via spacecraft provide another means of investigating the properties of the interplanetary medium by determining the magnetic field structure and the proton (and more recently electron) densities. However, these measurements are related to very large-scale structures within the medium whereas interplanetary scintillation yields information on a much smaller scale (10 - 250 km). Also, spacecraft are confined to the ecliptic plane and to a distance of about 1 A.U. from the sun. This does not apply to observations of interplanetary scintillation thus allowing investigations at all heliocentric distances and latitudes. To establish the previously mentioned parameters and hence gain a better understanding of the scattering processes occurring in the medium we must observe interplanetary scintillation not at one receiving site but at three or more spaced sites.

Previous work of this nature (Dennison and Hewish, 1967) has been based largely on observations of the source 0134 + 32 (or 3C48) and has given information on these parameters to within 0.35 A.U. of the sun. Observations of other sources are therefore needed to obtain a greater coverage of the scattering medium and it was proposed to set up a project near Adelaide as a development of this previous work. The author's part in this project was mainly constructional, but valuable practical experience in the design and construction of a radio-astronomy array and receiving equipment was gained.

6.2 Specifications

6.2.1 The Spacing of the Sites

In designing a spaced receiver array the first consideration is the spacing between the receiving sites. Information about the velocity and scale of the diffraction pattern is obtained from the correlation and time delays between scintillation records at the three sites. The techniques of correlation analysis are described by Briggs (1968a, 1968b). As the spacing increases between the receiving sites the time delay increases and the correlation between signals decreases. Since the shape of the auto-correlation function of interplanetary scintillation is almost Gaussian both too high and too low values for the correlation must be avoided if accurate results are to be obtained.

The optimum spacing is therefore the distance when the auto-correlation function has fallen to about one half. Previous work in the region 0.35 - 1.0 A.U. from the sun has shown that for the observed diffraction pattern the scale L (to e^{-1}) $\sim$100 - 200 km and the velocity V $\sim$300 - 500 km sec^{-1}. Figure 6.1 shows the expected correlation values and time delays between scintillation observed at sites separated by distances up to 200 km. The optimum spacing would be about 100 km yielding correlation values in the range 0.35 - 0.75 and time delays of 0.2 - 0.3 sec.

The location of the main recording station or base-station was at the Buckland Park field station already in use for ionospheric work and situated about 38 km north of Adelaide. Sites for the two other stations were near Burra and Kadina as shown in Figure 6.2.

6.2.2 The Choice of Frequencies

The nature of the scattering process plays an important role in the choice of a suitable observing frequency. For example when ϕ_o, the rms phase deviation is less than one radian, the observed parameters of the diffraction pattern can be related in a simple way to the parameters of the medium. However, when $\phi_o > 1$ multiple scattering occurs and the relation becomes more complicated, involving the magnitude of the phase deviation ϕ_o. Both ϕ_o and the scintillation index are inversely proportional to the frequency and decrease with radial distance from the

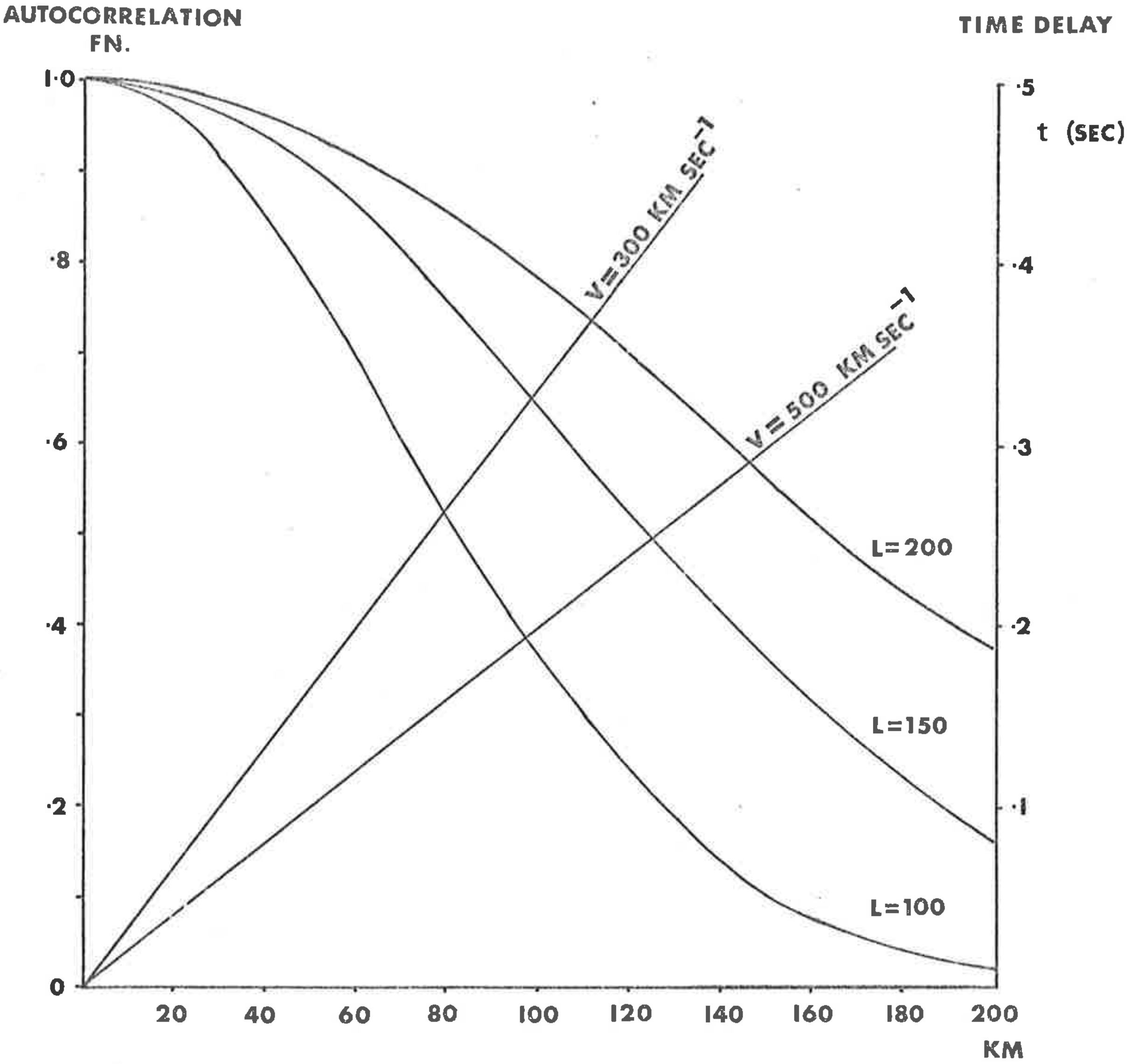

Figure 6.1 Autocorrelation functions and time delays for distances up to 200 km.

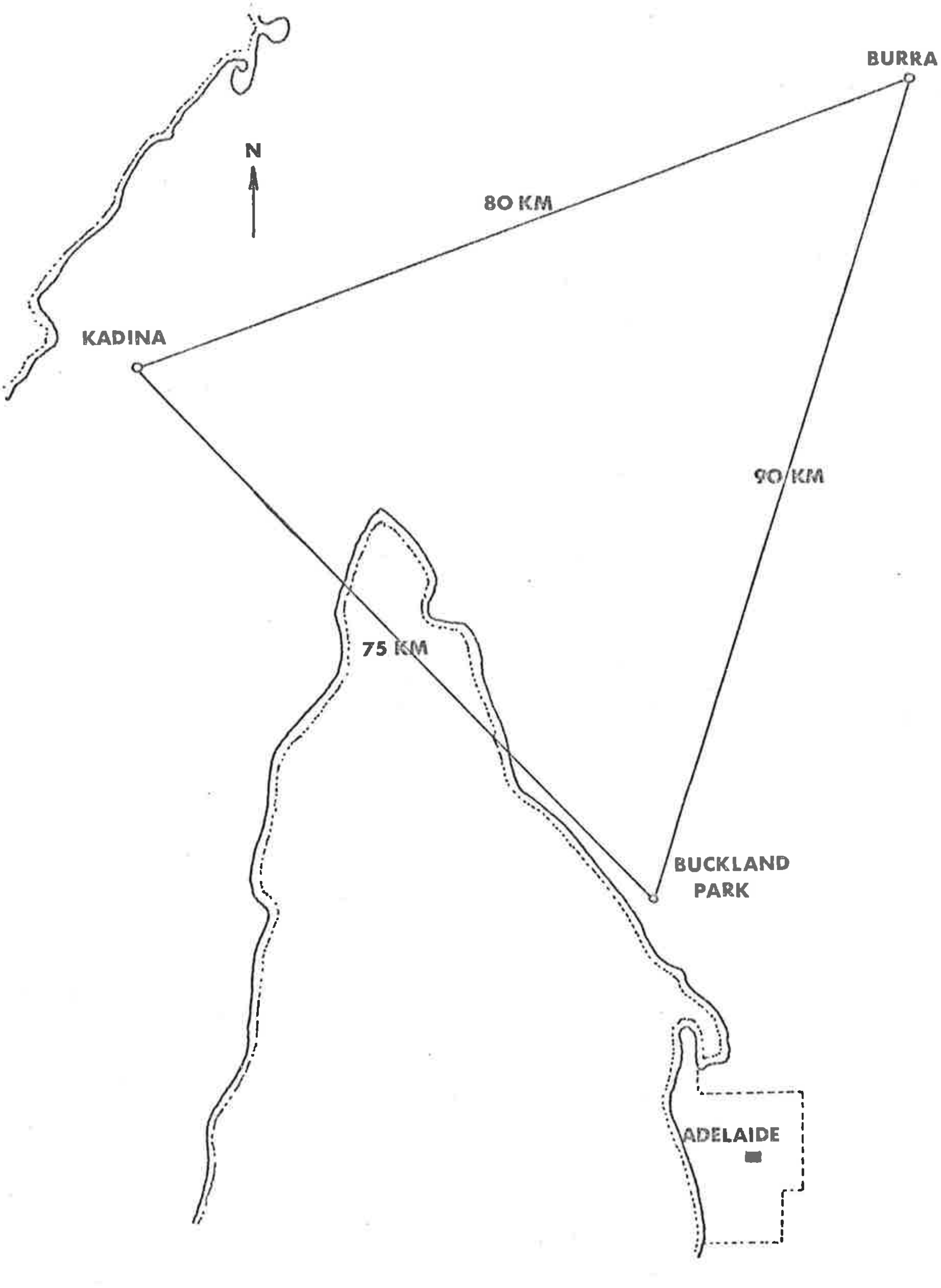
BURRA
N
80 KM
KADINA
90 KM
75 KM
BUCKLAND
PARK
ADELAIDE

Figure 6.2 The receiving sites

sun. Thus at 80 MHz it has been shown that strong scattering occurs at distances $\lesssim$ 0.3 A.U. (Hewish and Symonds, 1969) so that to investigate regions closer to the sun, under weak scattering conditions, a higher frequency would be needed. At a much higher frequency of $\sim$1 GHz the observations would be restricted to only a small region close to the sun due to the reduction of scintillation further out. Therefore metre wavelengths appeared to be the most useful for investigations at heliocentric distances $\sim$0.1 - 1.0 A.U. Two frequencies were actually chosen in the range 100 - 300 MHz with the object of observing both signals simultaneously. Observation at two frequencies not only enables a wider coverage of the interplanetary medium but also provides a more complete description of the scattering process. For example, the heliocentric distance at which the scattering changes from being weak to being strong can in principle be established from the ratio of the scintillation indices and also from the correlation between the two signals. At some particular distance the scattering would be weak at the high frequency and strong at the lower frequency and the predominant scales of the diffraction patterns would be respectively a and $\frac{\sqrt{2}}{\phi_o}a$, where a is the scale of the irregularities in the interplanetary medium and ϕ_o is the rms phase deviation. From the ratio of the scales it would therefore be possible to estimate the rms phase deviation ϕ_o.

To ensure freedom from interference the final choice of frequencies was made in consultation with the Postmaster-General's

Department and the frequencies allocated were 111.5 MHz and 235.9 MHz with bandwidths of 1 MHz and 2 MHz respectively.

6.2.3 Collecting Area and Noise Considerations

At metre wavelengths it is possible by careful design of the receiving equipment to ensure that the main contribution to the system noise comes from the galactic background. At 111.5 MHz the background temperature is $\sim 500^\circ$K increasing to 4000°K at the Galactic centre (Kraus, 1966). At 235.9 MHz the corresponding temperatures are $\sim 100^\circ$K and $\sim 1000^\circ$K. Since the sources to be observed lie well away from the galactic centre, and assuming the receiver noise contribution is $\sim 300^\circ$K, we may then assume typical system noise temperatures, T_{sys}, of 800°K and 500°K at 111.5 and 235.9 MHz respectively.

We now wish to calculate the antenna collecting area required to record at least two or three of the strongest scintillating sources. Based on 80 MHz observations at Culgoora, Table 6.1 lists the strongest scintillating sources available and it is seen that four of these have fluxes greater than 50 flux units (50×10^{-26} Wm^{-2} Hz^{-1}) at 111.5 MHz.

For a phase switching receiver the minimum detectable noise temperature ΔT, when the signal to noise ratio N = 1, is given by (Kraus, 1966),

$$\Delta T = \frac{2T_{sys}}{\sqrt{\beta\tau}},$$

Source (Parkes Catalogue No.)	Flux Units $S_{111.5}$
1226+02	90
1416+06	90
0624-05	85
1309-22	50
2313+03	40
1938-15	35
0758+14	30

Table 6.1

where τ is the recording time constant and β the bandwidth of the receiver. The antenna temperature T_A, produced by a source of flux S is given by,

$$T_A = \frac{SA}{2k},$$

where k is Boltzmann's constant and the factor 2 is due to the fact that only one component of polarisation is recorded. Combining the above two equations we find that the collecting area required to produce a signal to noise ratio N, where $N = \frac{T_A}{\Delta T}$, is given,

$$A = \frac{4\ k\ NT_{sys}}{S\sqrt{\beta\tau}}.$$

Substituting values into this equation we find for a receiving frequency of 111.5 MHz with a system temperature $T_{sys} = 800^{\circ}K$, bandwidth $\beta = 1$ MHz and time constant $\tau = 0.1$ sec, the required collecting area to record a 50 flux unit source with a signal to noise ratio of 5:1 is $\sim$1400 m^2. At 235.9 MHz a slightly smaller collecting area is required for the same source.

6.3 The Antenna Design

To obtain the required collecting area which is nearly half that of the 210 ft radio-telescope at Parkes, N.S.W. (physical collecting area $\sim$3600 m^2), the only possibility in view of limited finances was to build a transit-type instrument. E-W corner reflectors were chosen in preference to flat reflector screens, to reduce the beam-width in the N-S direction. Within each reflector two dipole arrays were constructed, one at each observing frequency.

Corner reflectors containing dipole active elements have been studied in detail by Cottony and Wilson (1958) and Wilson and Cottony (1960). The parameters for the final design of the corner reflectors were obtained from these empirical studies and were chosen for a minimum N-S sidelobe response with maximum gain. The final design, illustrated in Figure 6.3, had a 'corner' angle $\Theta = 85^{\circ}$, width of sides $W = 12$ ft $\simeq 3\lambda$ at 235.9 MHz, and dipole distances from the apex $S = 0.33\lambda$ and 0.4λ at 111.5 MHz and 235.9 MHz respectively. The length of the corner reflectors was chosen to be 250 m giving a physical collecting area of about 1400 m^2. Since 1969 eight such antennas have been constructed, two at each of the outstations and four at the base-station, Buckland Park. The separation between adjacent corner reflectors was equal to 3λ at 111.5 MHz. In Figure 6.4 the arrays at Buckland Park are shown. The spacing between the wires of the reflector screens was $\lesssim \frac{\lambda}{20}$ at the highest frequency to obtain reasonably efficient reflection with a front-to-back ratio $\gtrsim$ 20 dB (Wilson and Cottony, 1960). Full-wave dipoles were used whose high impedance allowed groups of 10 - 12 to be fed in parallel through open-wire feeders with characteristic impedances of 300Ω. This was achieved by constructing an open-wire feeder along the total length of the aerial and isolating each group of 10-12 dipoles by $\frac{\lambda}{4}$ shorts at each end of the group. The feeder and the connected dipoles can be plainly seen in the photograph. To achieve equal path lengths to

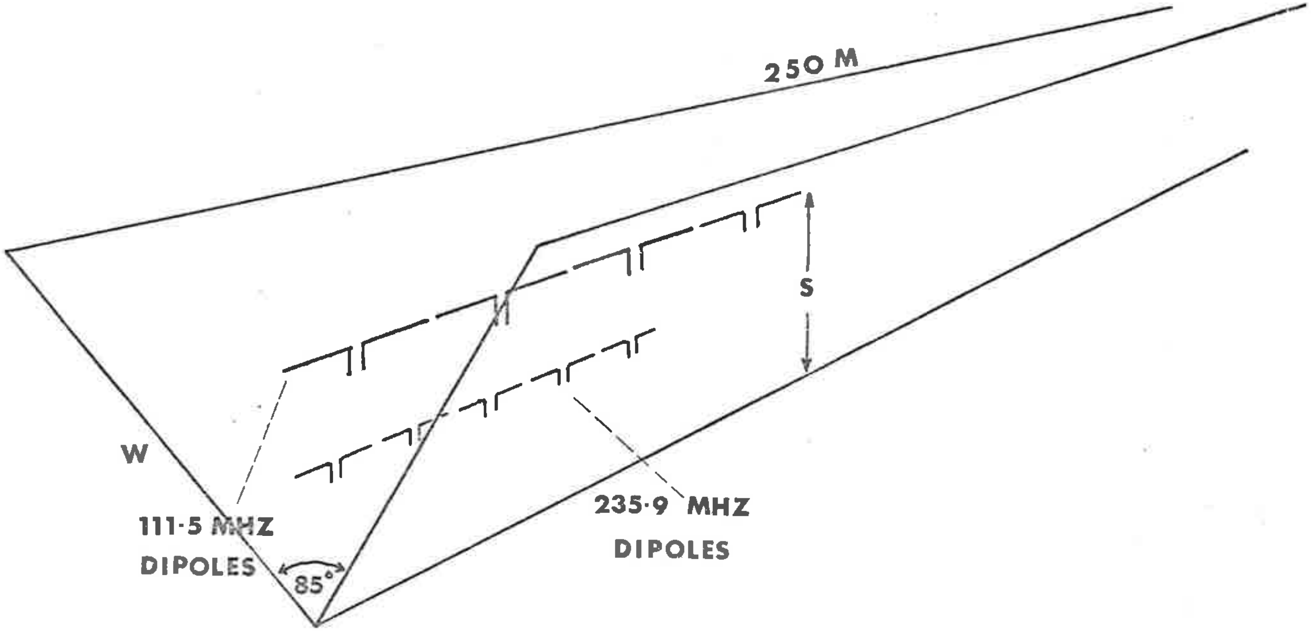
250 M
S
W
111·5 MHZ
DIPOLES
85°
235·9 MHZ
DIPOLES

Figure 6.3 The corner reflector antenna

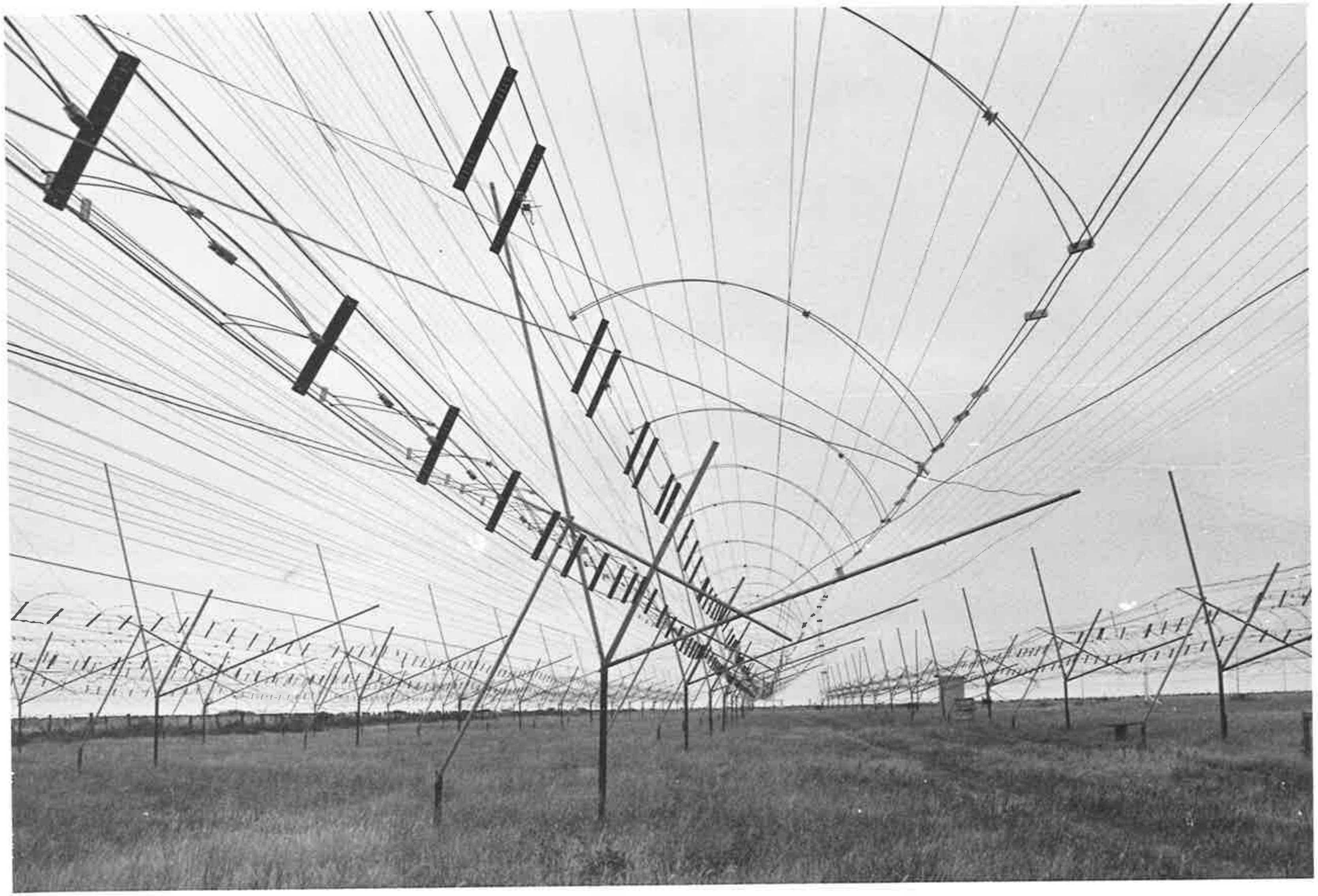

Figure 6.4 The aerial arrays at Buckland Park

the receiver from each part of the corner reflector a 'Christmas tree' feed system was used as illustrated in Figure 6.5.

The impedance of each group of 10 or 12 dipoles was measured using a VHF bridge and matched to another 300Ω open-line feeder using a $\frac{\lambda}{4}$ shorted stub transformer. Before transformation the impedance measured was typically (70 + j70)Ω, the large reactance being due to the interaction between the two different frequency arrays. Stub matching reduced the bandwidth of the arrays but measurements indicated that the standing-wave ratio remained < 2 over a 1% bandwidth around each of the observing frequencies and this was within the required specifications. Finally, the feeders were connected by 'baluns' (balanced to unbalanced transformers) to two coaxial cables taking the signal from each half of the corner reflector to the receiver.

As seen in Figure 6.5 each corner reflector was operated as an interferometer, one half being phase-switched against the other to remove the galactic contribution to the signal (Ryle, 1952). A typical transit record of a radio source is shown in Figure 6.6. The beamwidth (to half power) in declination of each corner reflector was $\sim 40^{\circ}$. Since the project was designed for the study of interplanetary scintillation, most of the sources for observation would lie in the declination range $\pm 20^{\circ}$, around the ecliptic. Therefore the corner reflectors were constructed such that the beam pointed towards 0° in declination and the 40°

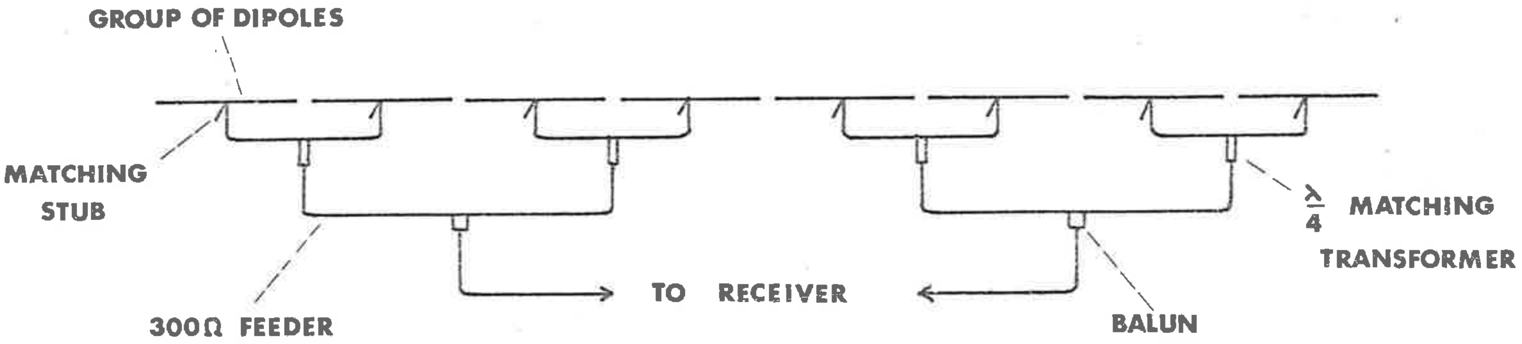
GROUP OF DIPOLES
MATCHING STUB
$\frac{\lambda}{4}$ MATCHING TRANSFORMER
TO RECEIVER
300Ω FEEDER
BALUN

Figure 6.5 Schematic representation of the feed system for the 111.5 MHz dipoles. The same principle is used at 235.9 MHz

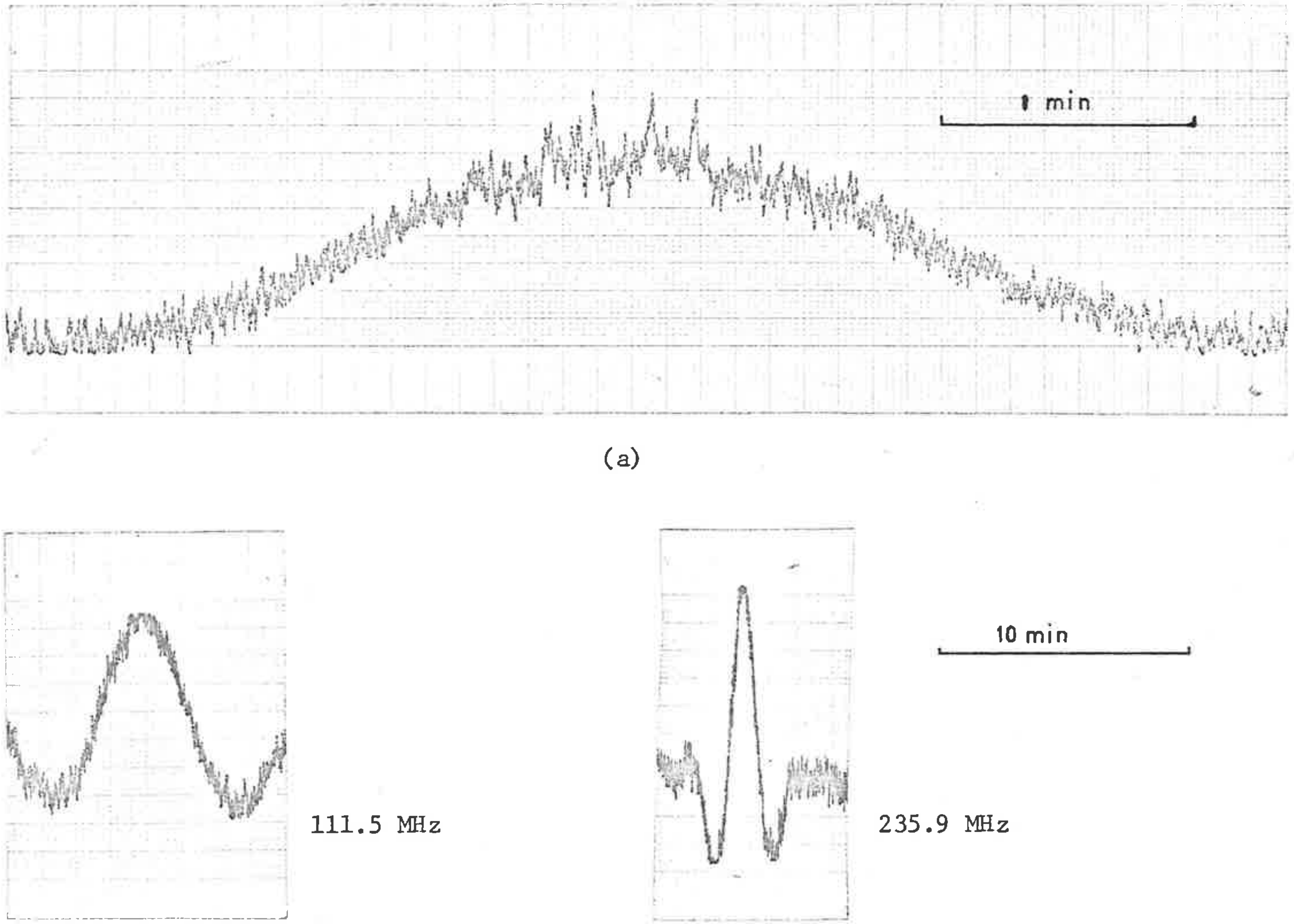

(a)

(b)

Figure 6.6 (a) Record of scintillation on 0624-05 at 111.5 MHz
(b) Source transits showing the shape of the polar diagrams

beamwidth allowed observations of sources 20° on either side. However when the four aerials at Buckland Park were combined responses at every 20° in declination were obtained (at 111.5 MHz), each response having a full width at half power of $\sim 5^\circ$. By combining the aerials in different phase relationships it was possible to move the beams in declination over the 40° envelope of a single corner reflector. A phasing device based on the use of the 'hybrid ring' (Smith 1961) was constructed to enable four beam positions in declination to be available for simultaneous recording. A Schematic diagram of the phasing device used at 111.5 MHz is shown in Figure 6.7, and in Figure 6.8 are illustrated the resulting beam patterns. As mentioned above, responses occur every 20° and the beams labelled '1' in the figure are the result of connecting the four corner reflectors in phase. Beams numbered '2' are produced by progressively introducing path differences of $\frac{\lambda}{4}$ into the feed lines of adjacent aerials. The remaining beams '3' and '4' result from introducing progressive path differences of $\frac{\lambda}{2}$ and $\frac{3\lambda}{4}$ respectively. All the beams illustrated are contained in the declination response of the main lobe (40° full width at half power) of the individual corner reflectors. The same principle was used in constructing phasing devices at the higher frequency.

To enable simultaneous observation of a source at all three stations it was necessary to build the arrays at each of the outstations slightly offset from the E-W direction. This offset depended on the

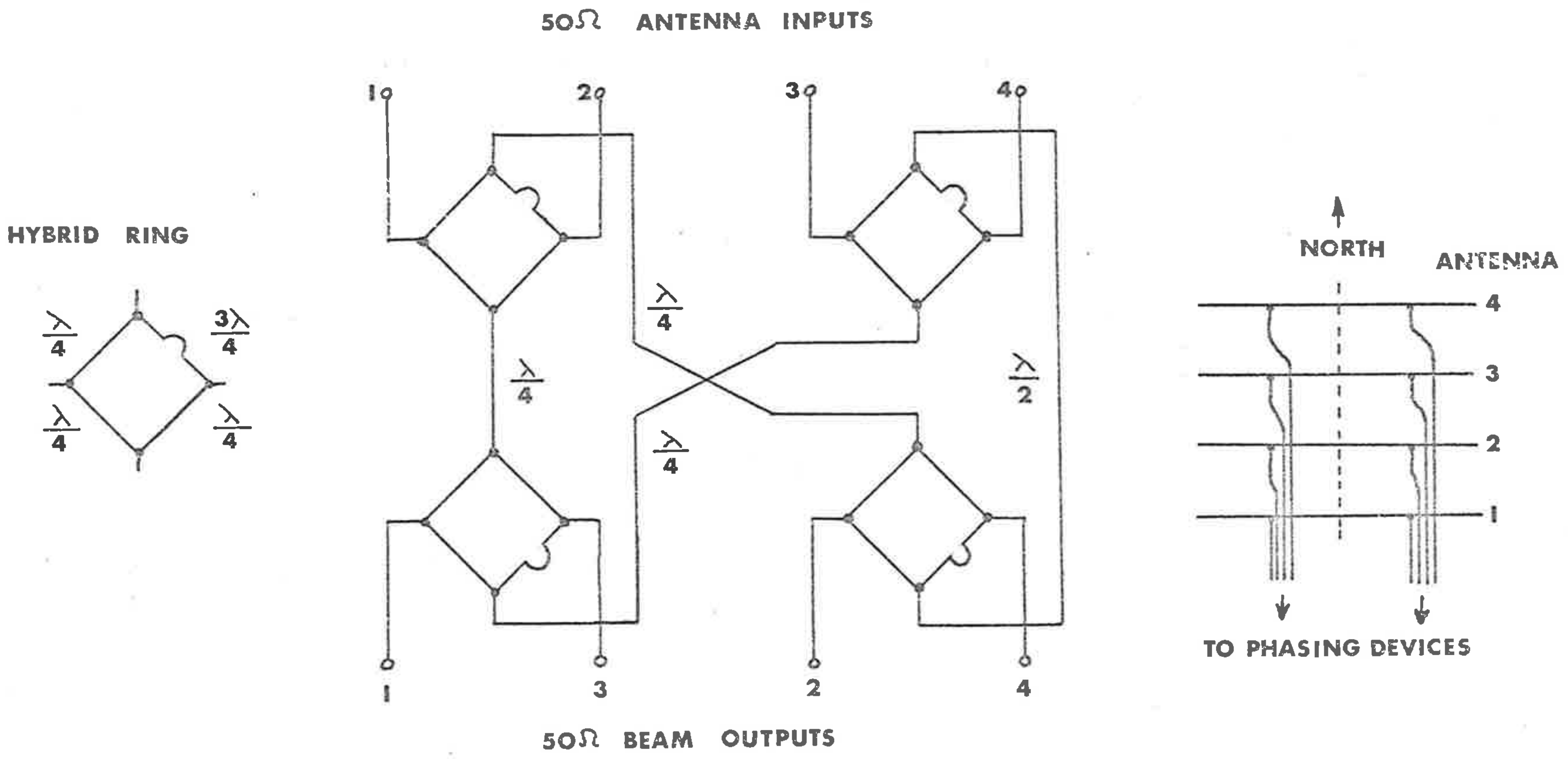
50Ω ANTENNA INPUTS
1
2
3
4
HYBRID RING
λ/4
3λ/4
λ/4
λ/4
λ/4
λ/4
λ/2
λ/4
1
3
2
4
50Ω BEAM OUTPUTS
NORTH
ANTENNA
4
3
2
1
TO PHASING DEVICES

Figure 6.7 The phasing device

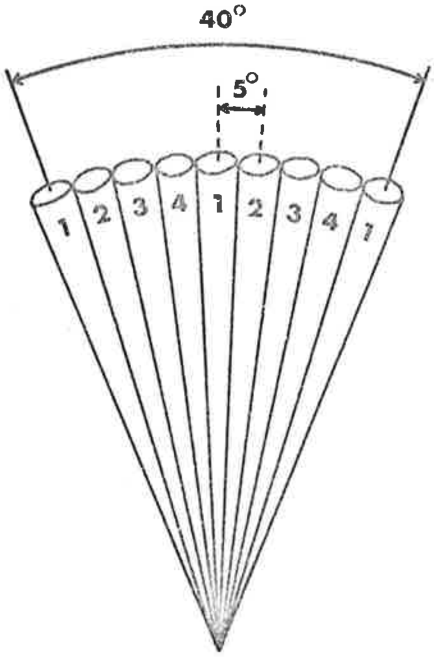
40°
5°
1
2
3
4
1
2
3
4
1

Figure 6.8 Beam configuration in declination at 111.5 MHz from the phasing devices

longitude difference to the base station.

6.4 The Receivers

As mentioned in the previous section a phase-switched receiving system was chosen in order to avoid the galactic contribution to the final receiver output. The principle of the phase-switched receiver is well known and illustrated in Figure 6.9. The signals from the East and West halves of the antenna arrays are combined at the input to the receiver by a hybrid to give independent in-phase and out-of-phase signals. These combined signals are then alternately connected to the converter using diode switches operating at 385 Hz. A signal received from a radio source gives rise to a square-wave component at the output of the detector. By reversing the phase of this square wave in the demodulator operating synchronously with the phase switch, a DC output is obtained which is proportional to the flux of the radio source. Uncorrelated galactic noise does not contribute to the output.

Much assistance in the receiver development was received from the Department of Electrical Engineering at Sydney University. In particular the synchronous demodulator, which constitutes the most important part of the receiver, followed closely a design of the Sydney group (Frater, 1965). A feature of the demodulator is the provision for integrating synchronously before demodulation which produces a dynamic range practically independent of the amount of noise present at the input.

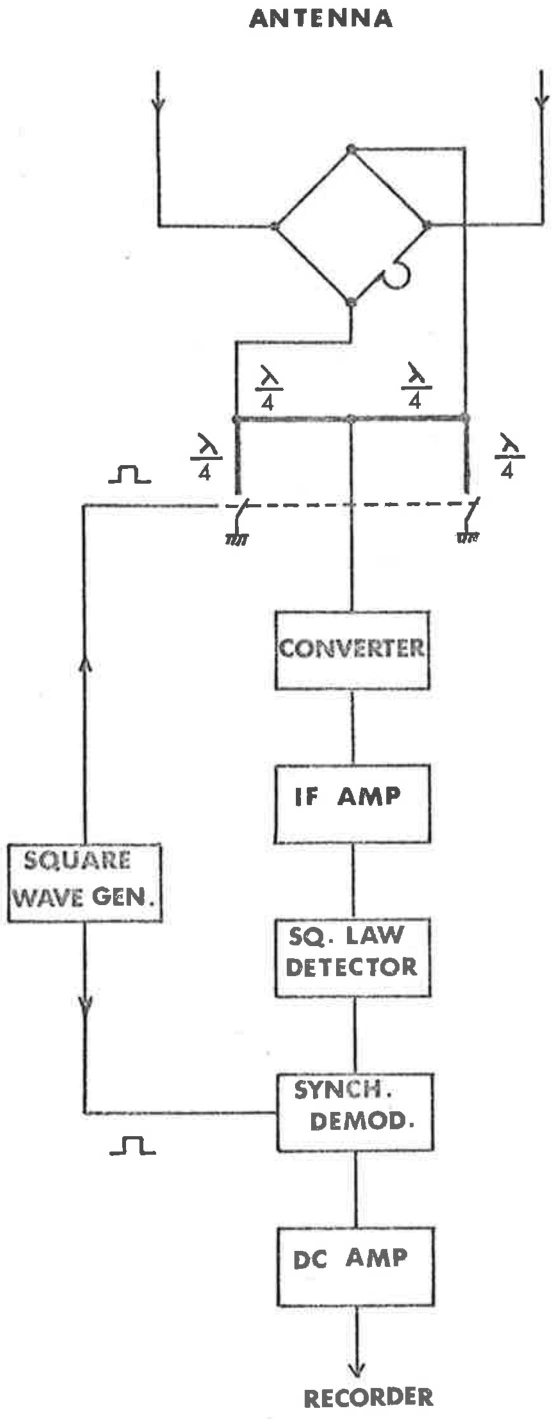
ANTENNA
λ/4
λ/4
λ/4
λ/4
CONVERTER
IF AMP
SQ. LAW DETECTOR
SYNCH. DEMOD.
DC AMP
RECORDER
SQUARE WAVE GEN.

Figure 6.9 Block representation of the phase switched receivers

The operation of the individual sections of the receiver will be described only briefly here and the circuits are included in Appendix II. The converter section as illustrated in the block diagram consisted of a moderately low-noise preamplifier (noise temperature $\sim 1000^{\circ}$K at 111.5 MHz), crystal local oscillator and mixer all built into a single brass box paying careful attention to shielding and RF bypassing of the DC supply lines. At 111.5 MHz, the frequency of 81.5 MHz from the crystal oscillator was injected directly, whilst at 235.9 MHz it was necessary to triple the frequency of a 68.63 MHz crystal oscillator to obtain the required 205.9 MHz signal. The gain of the converter was 20 dB with bandwidths of 10 and 5 MHz at the low and high frequencies respectively. The intermediate frequency amplifier having a gain of 65 dB, consisted of three stagger-tuned cascode pairs with the damping on each stage being adjusted to give an overall flat response centred on 30 MHz with the required 3 dB bandwidth of 1 or 2 MHz at the two frequencies.

The operation of the phase switch made use of a principle which has successfully been applied at frequencies in the GHz range (Landecker and Wielebinsky, 1970). Diodes are used to alternately short and open one end of a $\frac{\lambda}{4}$ length of coaxial cable, the other being connected to the signal path as shown in Figure 6.9. In the original design gold-bonded germanium diodes (OA47) were used resulting in a rejection of about 30 dB of non-correlated input signals. As a future development it is possible that PIN diodes may be used to achieve a higher rejection particularly useful at the higher observing frequency. The square wave generator used to control the phase switch and synchronous integrator/demodulator was a multi-vibrator with the output frequency carefully set away from harmonics of the 50 Hz power supply line.

To achieve the required low-noise characteristics mentioned earlier in the chapter and also to overcome the cable loss to the receivers, preamplifiers were installed at the feed points for each half of each corner reflector. The preamplifiers used germanium transistors GM290 in a simple cascode-pair arrangement and resulted in noise temperatures of $\sim 500^{\circ}$K and $\sim 700^{\circ}$K at 111.5 MHz and 235.9 MHz respectively. The higher frequency figure does not meet the specification laid down earlier and at the time of writing development is taking place to reduce this figure to $\sim 300^{\circ}$K by using more recently developed transistors. The overall gain of the preamplifiers after allowing for attenuation by the cables was about 10 dB which was sufficient to make them the determining factor in the overall receiver noise figure.

In the final receiver design automatic gain control was not included but a dynamic range of ~ 30 dB was achieved and was sufficient for the type of observations. A switched attenuator, ranging from 3 to 33 dB in 3 dB steps, was also included in the input to the intermediate frequency amplifier. The final DC output level was raised to about 2 volts, required by the pen recorders, with a single operational amplifier. A photograph of the receiver is shown in Figure 6.10, and the converter and IF amplifier are shown separately in Figure 6.11.

6.5 Progress and Future Development

At the time of writing, observations have been carried out at the low frequency (111.5 MHz) and tests are being carried out at the high frequency (235.9 MHz). Also radio links are being installed between Buckland Park and the outstations to transmit the signals back from the two outstations allowing simultaneous recording of the three signals.

As well as studying the solar wind via the parameters of the intensity diffraction pattern it is also hoped that the project will develop to a stage where phase information might be obtained by operating pairs of stations as long-baseline interferometers. Fluctuations in the interference fringe positions will give a measure of the phase difference $\Delta\phi$ between each pair, at a sampling rate determined by the fringe frequency as a radio source moves across the lobes of the interferometer. For a separation of 100 km and an observing frequency $\sim$200 MHz this sampling interval would be about 0.2 sec. If the scale of the phase diffraction pattern is comparable with that of the intensity pattern, that is about 400 km between maxima in the pattern, the sampling rate should be sufficient to allow the phase fluctuations to be followed. The record would consist of an oscillating signal or fringe pattern as the

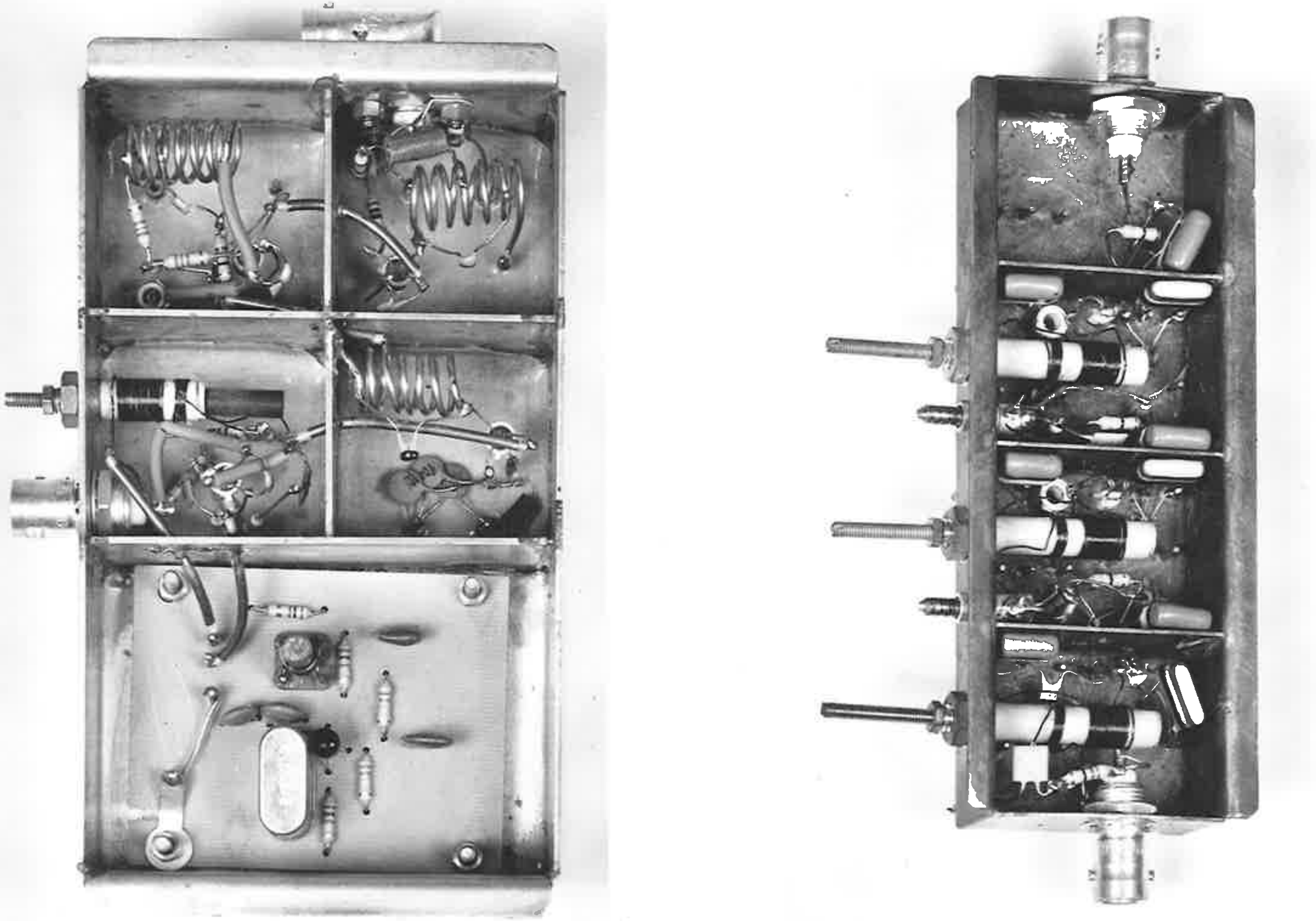

CONVERTER

I.F. AMPLIFER

Figure 6.11

source moved in and out of the interferometer lobes. By estimating the deviation of the recorded fringes from the known fringe positions a measure of $\Delta\phi$ is obtained. From this information the parameters of the phase diffraction pattern may be obtained. By recording both intensity and phase information simultaneously, the complex amplitude of the diffraction pattern moving across the array may be deduced. The auto-correlation function of this pattern is related directly to the auto-correlation function of the wave-front on emerging from the scattering region and remains unchanged with distance from the region. Also by comparing the scales of the amplitude and phase patterns it should be possible to deduce the extent to which the initial phase deviations have developed into amplitude deviations on moving away from the scattering region. Only limited work has been carried out on phase observations (Slee and Higgins, 1968), and it is therefore important to obtain a better knowledge of the phase variations to throw more light on to the actual nature of the scattering processes.

Obviously another use of the receiving sites operated in the long-baseline interferometer mode is the determination of angular structures of radio sources whose diameters are a few seconds of arc. This is apart from interplanetary scintillation estimates which yield diameter information ∿0.01 - 0.1" arc.

CHAPTER 7

CONCLUSIONS

In this chapter we endeavour to summarise our observations and results and in addition suggest future development of the work which has been described.

Chapter 3 was concerned with the first direct observations of the two-dimensional image of the Crab Nebula when broadened by the solar corona. The method of observation, using the C.S.I.R.O. radioheliograph, removed most of the uncertainties associated with previous observations carried out by other authors with interferometers and enabled a direct determination of the size, shape and orientation of the image. Values of the radial and tangential widths of the images were shown to agree well with previous estimates by other authors. The orientation of the image indicated no definite departure from the tangential direction, suggesting that during June of the three years (1969-71) the solar magnetic field remained radially oriented to the sun. On nearing the sun an increase in the axial ratio of the scattering ellipse was noted. The axial ratio of the observed scattered distribution was shown to be a true indication of the shape of the irregularities in the solar corona and it was thus inferred that the irregularities became more elongated in regions close to the sun ($< 9\ R_\odot$). It was suggested that the difference between the magnetic field and kinetic gas pressures may be responsible for this effect. Further observations at a somewhat higher frequency would allow clearer images to be obtained close to the sun since the degree of broadening would be reduced, and hence more reliable estimates of the size and orientation would be available. At present work by the C.S.I.R.O. staff is in progress to install facilities for recording at additional frequencies of 40 and 160 MHz. These extensions should allow the corona to be studied over a wider range of heliocentric distance since the degree of scattering varies as the wavelength squared. The higher frequency as mentioned above will be of particular interest, enabling more accurate estimates of the size, shape and orientation of the image close to the sun.

Models of brightness, distributions based on a Gaussian spectrum of scattering irregularities in the solar corona were computed and found to agree remarkably well with the observed distributions. These suggested that the actual spectrum of irregularities in the corona might also be Gaussian. However, spacecraft observations near the orbit of the Earth have found that the scale of the magnetic field irregularities follows a modified power law variation and it has been suggested that the irregularities in electron density might have a similar spatial power spectrum. One is tempted to extrapolate this form back to regions close to the sun giving intuitively a modified power law for irregularities in these regions. It was shown, assuming a thin scattering layer, that such a spectrum would not produce brightness distributions as we have observed although a rigorous treatment might prove otherwise, particularly if an extended scattering region was considered. Detailed theoretical work of this nature has yet to be published and our conclusion that the spectrum of the scattering irregularities is Gaussian remains open to question.

Several unusual image formations and sudden increases in the degree of angular broadening were described. The interplanetary medium was known to contain large-scale structure on most occasions. These structures consisted of corotating plasma streams and during one year a blast wave, all associated with active regions on the sun. However, in some cases the lines of sight to the Crab Nebula and 3C123 were well away from known structures in the medium assuming typical cone angles of $\sim 30^{\circ}$ for corotating streams. If the observed phenomena were actually related to changes in the medium we must propose that disturbances, particularly near the sun sometimes occupy cone angles in excess of 30° and that disturbances in the medium well away from the ecliptic plane must exist. Further studies of the interplanetary scintillation of a grid of radio sources situated well away from the ecliptic plane might allow a better understanding of the lateral extent of these corotating streams and plasma blast waves. Most observations so far have been carried out with a grid of sources which have not adequately covered high ecliptic latitudes at solar elongations $< \pm 90^{\circ}$. Therefore it is suggested that observations should be conducted near December rather than June. During this time a greater percentage of scintillating sources with larger ecliptic latitudes occupy solar elongations < ± 90°.

In Chapter 4 a study of ionospheric refraction was presented. It was noted that during the analysis of the angular broadening of the Crab Nebula and 3C123 the effect of ionospheric refraction was initially of major concern. Fortunately, however, no large refraction was noticed in the final analysis.

Reduction of the refraction data has yielded some interesting results. Trends noticed in the apparent source positions have been attributed to spherical refraction and to gradients increasing northward in the ionosphere. The variability of the source positions and two-dimensional plots of source movements derived from long series of scans were shown to agree with source movements predicted from the current knowledge of TID's. The extent of the refraction appeared to be < 15-20' arc mainly in a N-S direction, with pseudo-periods of up to ∿40 min.

Refraction in the ionosphere is of interest to all persons concerned with accurate position measurements of radio sources at metre wavelengths. The steady components, spherical refraction and refraction due to average gradients in the ionosphere, can be estimated from a knowledge of ionospheric parameters through appropriately placed ionosondes. To account for the irregular wedge refraction due to travelling ionospheric disturbances a much more detailed knowledge is required at the time and place of observation. Due to the somewhat irregular and rapidly varying nature of this type of refraction, it is impossible to directly account for it. Unfortunately on some occasions it constitutes the major component of refraction. The best approach is, if possible, to avoid the seasons and times of the day at which it is most common. Minima in their occurrence are found near 0600 and 1800 hr local time and during the equinoxes. The most extensive refraction occurs during the daytime in winter.

Chapter 5 was devoted to a discussion of three aspects of interplanetary scintillation. First an attempt was made to obtain angular structure information from scintillation recorded at Culgoora during June 1970. Single station observations yield this type of information only if the observed scintillation is caused by weak scattering and if the irregularities move across the line of sight with a unique velocity. Calculations using the spectral widths revealed diameters larger than expected by factors of 2-3. Since all the sources suffered from a similar effect it was thought that the assumptions on which the formula was based broke down when observing at 80 MHz. To retain the weak scattering condition, sources closer than about 30° from the sun were avoided during the analysis. Outside this range the scattering region becomes a thick layer and it is possible that this effect produced the errors. Investigation into the validity of the formula is therefore necessary to clarify the problem.

In addition, other effects on the scintillation were considered, the main effect being the introduction of pulses from the radioheliograph into the data. These produced peaks in the power spectra tending to restrict the usefulness of the data. The power spectra were also found to fall off very rapidly, thus introducing another detrimental effect during analysis. They tended to develop 'tails' at about 2-3 decades below the main peak. This was attributed to bad leakage between adjacent spectral estimates and perhaps future analyses might include prewhitening in an attempt to improve the spectra. As mentioned previously the C.S.I.R.O. staff are engaged in adding recording facilities for 40 and 160 MHz to the present 80 MHz system. Any observations of interplanetary scintillation which may be carried out in future will yield further information about the scattering regions by, for example, comparing indices at the three frequencies. However, it will not be possible to observe at these frequencies simultaneously.

Using the 210 ft radio-telescope at Parkes, N.S.W. during January 1968, an attempt was made to record interplanetary scintillation at 150, 600 and 1410 MHz. Since significant scintillation was observed on only one source and at one frequency, the medium was presumed to be very quiet during the three days of observations. It was shown theoretically that such widely spaced frequencies would not allow reliable estimates of the parameters of the medium even if more scintillation had been observed.

The final topic in Chapter 5, concerning interplanetary scintillation, was a discussion of the possibility of determining two-dimensional power spectra from observations at a single site, by using the Bessel transform. Theoretical considerations indicated that the appearance of a low frequency dip, and particularly the accompanying fringes, was extremely unlikely at 80 MHz. The conditions under which they would be observed might be found at higher frequencies (∿1 GHz) or when unusual events occurred in the interplanetary medium. One such event did occur during May 1968 when a corotating stream approached the earth providing conditions suitable for the observation of a low frequency dip in the Fourier power spectra and fringes in the Bessel power spectrum.

In the remaining chapter the construction of aerials and receivers for the study of interplanetary scintillation from three spaced sites was described. This system, situated in South Australia, will record the intensity signals at 111.5 and 235.9 MHz. From a three-station network it is possible to obtain detailed information about the irregularities in the interplanetary medium and by observing simultaneously at two frequencies additional information may be gained. The major step forward will be when the receiving and recording equipment is modified to enable both phase and intensity information to be recorded. Phase scintillation has been recorded only in one previous instance, so that this development will enable a better understanding of the scattering processes in the interplanetary medium.

This summary has listed the main points of interest encountered during the analysis of data recorded at Culgoora. Some arguments have been left open because of insufficient observations or theoretical work in the particular fields. Where possible suggestions have been included for future work carried out along similar lines.

BIBLIOGRAPHY

Allen, L.R., Anderson, B., Conway, R.G., Palmer, H.P., Reddish, V.C., and Rawson, B., 1962, Mon. Not. Roy. Ast. Soc., 124, 477.

Bakhareva, M.F., 1959, Radiotekh. Elektron., 4, 88.

Bennett, A.S., 1962, Mem. Roy. Ast. Soc., 68, 163.

Blackman, R.B., and Tukey, J.W., 1958, "The Measurement of Power Spectra from the Point of View of Communications Engineering". (Dover)

Blackwell, D.E., and Petford, A.D., 1966, Mon. Not. Roy. Ast. Soc., 131, 399.

Bliokh, P.V., Sinitsyn, V.G., and Fuks, I.M., 1969, Astr. Zh., 46, 348.

Bowen, E.G., and Minnett, H.C., 1963, Proc. IRE (Aust.), 24, 98.

Bramley, E.N., 1954, Proc. Roy. Soc. A, 225, 515.

Bramley, E.N., 1955, Proc. Inst. Elect. Eng., 102, Part III, 533.

Bramley, E.N., and Young, M., 1967, Proc. Inst. Elect. Eng., 114, 553.

Briggs, B.H., 1968a, J. Atmos. Terr. Phys., 30, 1777.

Briggs, B.H., 1968b, J. Atmos. Terr. Phys., 30, 1789.

Buckley, R., 1970, Aust. J. Phys., 24, 351.

Buckley, R., 1971, Planet. Space Sci., 19, 421.

Buckley, R., 1971, Aust. J. Phys., 24, 373.

Budden, K.G., 1965, J. Atmos. Terr. Phys., 27, 883.

Budden, K.G., and Uscinski, B.J., 1970, Proc. Roy. Soc. A, 316, 315.

Budden, K.G., and Uscinski, B.J., 1971, Proc. Roy. Soc. A, 321, 15.

Burnell, S.J., 1969, Nature, 224, 356.

Carovillano, R.L., and Siscoe, G.L., 1969, Solar Phys., 8, 401.

Chandrasekhar, S., 1952, Mon. Not. Roy. Ast. Soc., 112, 475.

Clarke, M.E., 1964, Ph.D. Thesis, University of Cambridge.

Cohen, M.H., 1965, Nature, 208, 277.

Cohen, M.H., Gundermann, E.J., Hardebeck, H.E., Harris, D.E., Salpeter, E.E., and Sharp, L.E., 1966, Science, 153, 745.

Cohen, M.H., and Gundermann, E.J., 1967, Astrophys. J., 148, L49.

Cohen, M.H., Gundermann, E.J., and Harris, D.E., 1967, Astrophys. J., 150, 767.

Cohen, M.H., Gundermann, E.J., Hardebeck, H.E., and Sharp, L.E., 1967, Astrophys. J., 147, 449.

Cohen, M.H., Gundermann, E.J., 1969, Astrophys. J., 155, 645.

Cooley, J.W., and Tukey, J.W., 1965, Mathematics of Computation, 19, 297.

Cooley, J.W., Lewis P.A.W., and Welch, P.D., 1970, J. Sound Vib., 12, 339.

Cottony, H.V., and Wilson, A.C., 1958, IRE Trans. Antennas Propag., 6, 366.

Croft, T.A., 1971, Radio Science, 6, 55.

Cronyn, W.M., 1970, Astrophys. J., 161, 755.

Dennison, P.A., and Hewish, A., 1967, Nature, 213, 343.

Dennison, P.A., and Wiseman, M., 1968, Proc. Astr. Soc. Aust., 1, 142.

Dennison, P.A., 1969, Planet. Space Sci., 17, 189.

Ekers, R.D., and Little, L.T., 1971, Astron. and Astrophys., 10, 310.

Erickson, W.C., 1964, Astrophys. J., 139, 1290.

Fejer, J.A., 1954, Proc. Roy. Soc. A, 220, 455.

Frater, R.H., 1965, Rev. Sci. Instr., 36, 634.

Georges, T.M., 1968, J. Atmos. Terr. Phys., 30, 735.

Golley, M.G., 1970, Ph.D. Thesis, University of Adelaide.

Golley, M.G., and Dennison, P.A., 1970, Planet. Space Sci., 18, 95.

Gorgolewski, S., and Hewish, A., 1960, Observatory, 80, 99.

Gower, J.F.R., Scott, P.F., and Wills, D., 1967, Mem. Roy. Ast. Soc., 71, 49.

Harries, J.R., Blesing, R.G., and Dennison, P.A., 1970, Proc. Astr. Soc. Aust., 1, 319.

Harris, D.E., and Hardebeck, E.G., 1969, Astrophys. J., 170, 115.

Heisler, L.H., 1958, Aust. J. Phys., 11, 79.

Heisler, L.H., 1963, J. Atmos. Terr. Phys., 25, 71.

Hewish, A., 1955, Proc. Roy. Soc. A, 228, 238.

Hewish, A., 1958, Mon. Not. Roy. Ast. Soc., 118, 534.

Hewish, A., and Wyndham, J.D., 1963, Mon. Not. Roy. Ast. Soc., 126, 469.

Hewish, A., Scott, P.F., and Wills, D., 1964, Nature, 203, 1214.

Hewish, A., Dennison, P.A., and Pilkington, J.D.H., 1966, Nature, 209, 1188.

Hewish, A., and Dennison, P.A., 1967, J. Geophys. Res., 72, 1977.

Hewish, A., and Symonds, M.D., 1969, Planet. Space Sci., 17, 313.

Hewish, A., 1971, Astrophys. J., 163, 645.

Hollweg, J.V., and Harrington, J.V., 1968, J. Geophys. Res., 73, 7221.

Hollweg, J.V., 1970, J. Geophys. Res., 75, 3715.

Hollweg, J.V., and Jokipii, J.R., 1971, Proc. Asilomar Solar Wind Conference.

Houminer, Z., 1971, Nature, 231, 165.

Högbom, J.A., 1960, Mon. Not. Roy. Ast. Soc., 120, 530.

Jaeger, J.C., and Westfold, K.C., 1950, Aust. J. Sci. Res., A3, 376.

Jokipii, J.R., and Coleman, P.J., 1968, J. Geophys. Res., 73, 5495.

Jokipii, J.R., and Hollweg, J.V., 1970, Astrophys. J., 160, 745.

Kerr, F.J., Shain, C.A., and Higgins, C.S., 1949, Nature, 163, 310.

Komesaroff, M.M., and Shain, C.A., 1959, Nature, 183, 1584.

Komesaroff, M.M., 1960, Aust. J. Phys., 13, 153.

Kraus, J.D., 1966, "Radioastronomy", (McGraw-Hill).

Landecker, T.L., and Wielebinsky, R., 1970, Proc. IREE (Aust.), 31, 73.

Lawrence, R.S., Little, C.G., and Chivers, H.J.A., 1964, Proc. IEEE, 52, 4.

Link, F., 1952, Bull. Cent. Ast. Inst. Czechoslovakia, 3, 6.

Little, L.T., Hewish, A., and Dennison, P.A., 1966, Planet. Space Sci., 14, 1221.

Little, L.T., and Hewish, A., 1966, Mon. Not. Roy. Ast. Soc., 134, 221.

Little, L.T., and Hewish, A., 1968, Mon. Not. Roy. Ast. Soc., 138, 393.

Little, L.T., 1968, Planet. Space Sci., 16, 749.

Little, L.T., 1971, Astron. and Astrophys., 10, 301.

Lovelace, R.V.E., Salpeter, E.E., Sharp, L.E., and Harris, D.E., 1970, Astrophys. J., 159, 1047.

Machin, K.E., and Smith, F.G., 1951, Nature, 168, 599.

Machin, K.E., and Smith, F.G., 1952, Nature, 170, 319.

Matheson, D.N., and Little, L.T., 1971, Nature, 234, 29.

Mercier, R.P., 1962, Proc. Camb. Phil. Soc., 58, 382.

Mills, B.Y., Slee, O.B., and Hill, E.R., 1958, Aust. J. Phys., 11, 360.

Mills, B.Y., Slee, O.B., and Hill, E.R., 1960, Aust. J. Phys., 13, 676.

Mills, B.Y., Slee, O.B., and Hill, E.R., 1961, Aust. J. Phys., 14, 497.

Munro, G.H., 1950, Proc. Roy. Soc. A, 202, 208.

Munro, G.H., and Heisler, L.H., 1956, Aust. J. Phys., 9, 359.

Munro, G.H., 1958, Aust. J. Phys., 11, 91.

Ness, N.F., Scearce, C.S., and Cantaro, S., 1966, J. Geophys. Res., 71, 3305.

Okoye, S.E., and Hewish, A., 1967, Mon. Not. Roy. Ast. Soc., 137, 287.

Orhaug, T.A., 1965, Chalmers tek. Högsk. Handl., Nr 299.

Parker, E.N., 1958, Astrophys. J., 128, 664.

Pneuman, G.W., 1966, Astrophys. J., 145, 242.

Ratcliffe, J.A., 1956, Rep. Progr. Phys., 19, 188.

Readhead, A.C.S., 1971, Mon. Not. Roy. Ast. Soc., 155, 185.

Reddi, C.R., and Rao, B.R., 1971, J. Atmos. Terr. Phys., 33, 251.

Rufenach, C.L., 1971, J. Atmos. Terr. Phys., 33, 1941.

Ryle, M., 1952, Proc. Roy. Soc. A, 211, 351.

Salpeter, E.E., 1967, Astrophys. J., 147, 433.

Sharp, L.E., and Harris, D.E., 1967, Nature, 213, 377.

Singleton, R.C., 1969, IEEE Trans. Audio and Electroacoustics, 17, 93.

Slee, O.B., 1959, Aust. J. Phys., 12, 134.

Slee, O.B., 1961, Mon. Not. Roy. Ast. Soc., 123, 223.

Slee, O.B., 1966, Planet. Space Sci., 14, 255.

Slee, O.B., and Higgins, C.S., 1968, Aust. J. Phys., 21, 341.

Sloane, E.A., 1969, IEEE Trans. Audio and Electroacoustics, 17, 133.

Smith, F.G., 1952a, Mon. Not. Roy. Ast. Soc., 112, 497.

Smith, F.G., 1952b, J. Atmos. Terr. Phys., 2, 350.

Smith, F.G., 1961, Inst. Elect. Eng., 108B, 201.

Thome, G., 1964, J. Geophys. Res., 69, 4047.

Titheridge, J.E., 1968a, J. Atmos. Terr. Phys., 30, 73.

Titheridge, J.E., 1968b, J. Geophys. Res., 73, 243.

Titheridge, J.E., 1969, J. Geophys. Res., 74, 1195.

Titheridge, J.E., 1971, J. Geophys. Res., 76, 6955.

Tveten, L.H., 1961, J. Res. Nat. Bur. Stand., 65D, 115.

Vitkevitch, V.V., 1955, Dokl. Akad. Nauk. U.S.S.R., 101, 429.

Vitkevitch, V.V., 1958, Astr. Zh., 35, 52.

Vitkevitch, V.V., 1958, Radiotekh. Electron., 3, 478.

Vitkevitch, V.V., and Kokurin, I.L., 1958, Radiotekh. Elektron, 3, 1373.

Vitkevitch, V.V., 1960, Astr. Zh., 37, 32.

Wild, J.P., Sheridan, K.V., and Neylan, A.A., 1959, Aust. J. Phys., 12, 369.

Wild, J.P., 1965, Proc. Roy. Soc. A, 286, 499.

Wild, J.P., 1967, Proc. IREE (Aust), 28, No. 9.

Wilson, A.C., and Cottony, H.V., 1960, IRE Trans. Antennas Propag., 8, 144.

Wiseman, M., and Dennison, P.A., 1972, Proc. Astr. Soc. Aust., In Press.

Wiseman, M., 1972, Ph.D. Thesis, University of Adelaide.

APPENDIX I

Some examples of two-dimensional source movements.

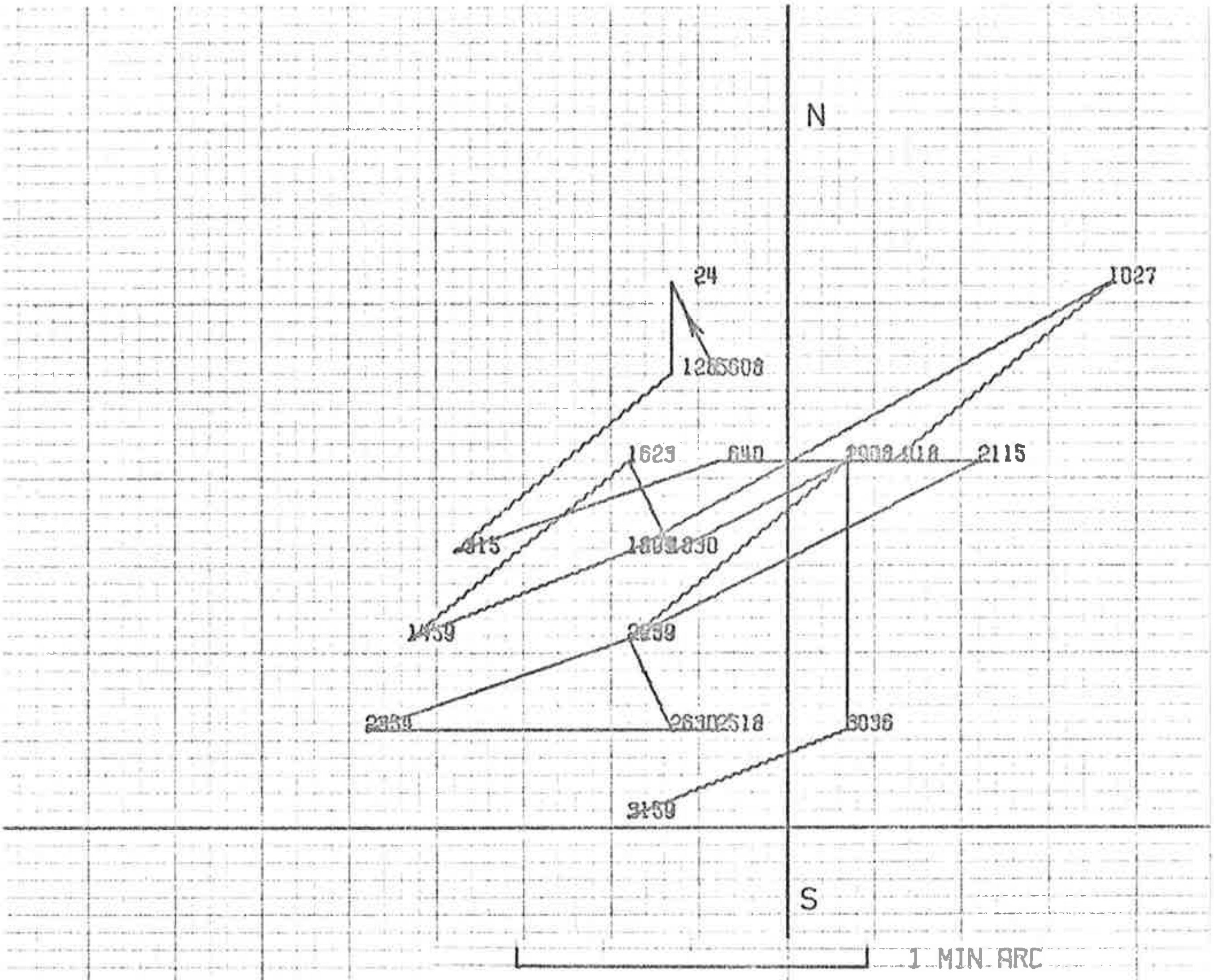

1226+02
680526

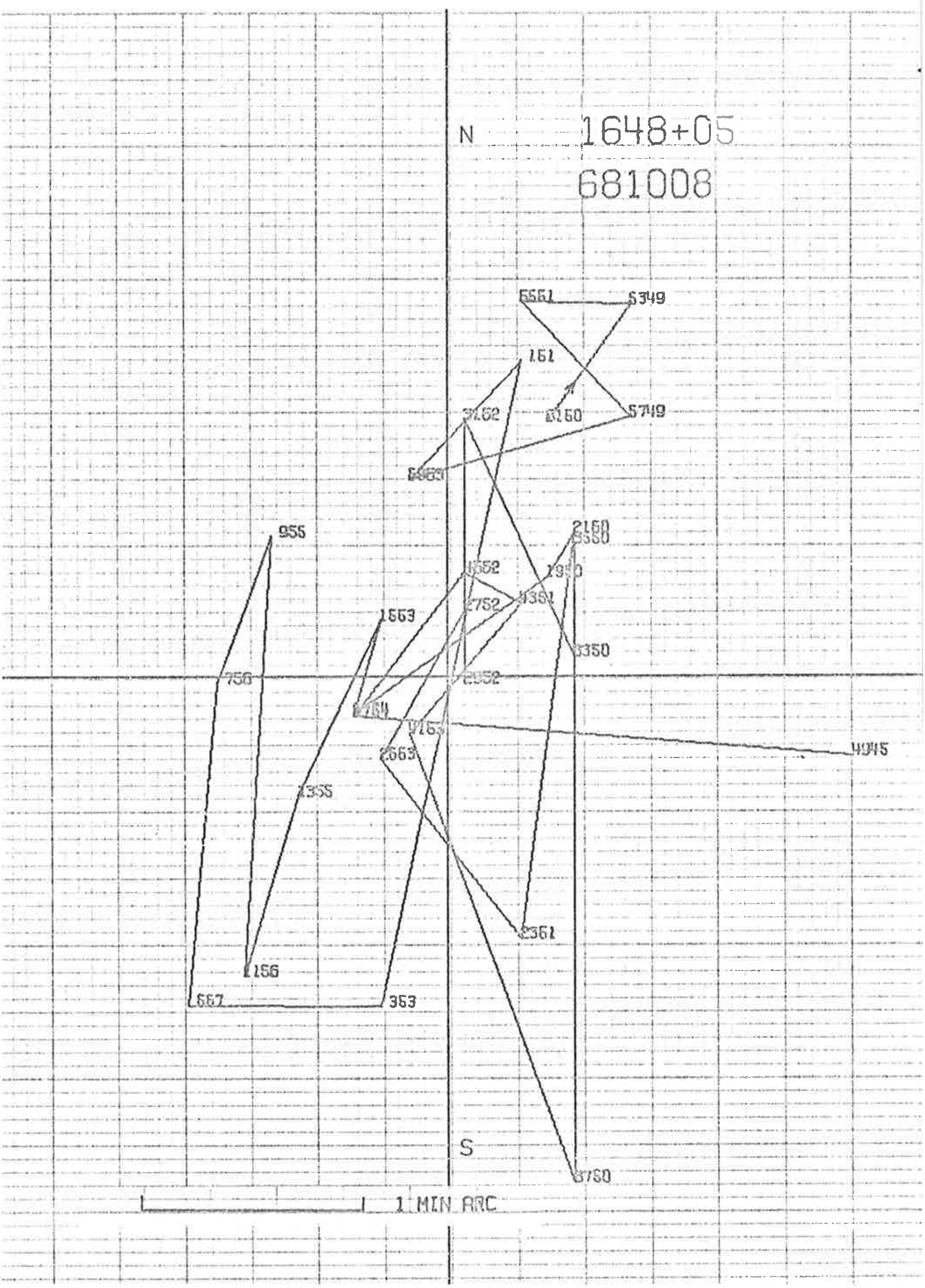
N
1648+05
681008
5561
5349
161
3162
0160
5749
6563
2150
3550
1950
1552
4351
2752
955
1563
3350
756
2052
0764
9163
4945
2663
1355
2361
1156
567
353
S
3760
1 MIN ARC

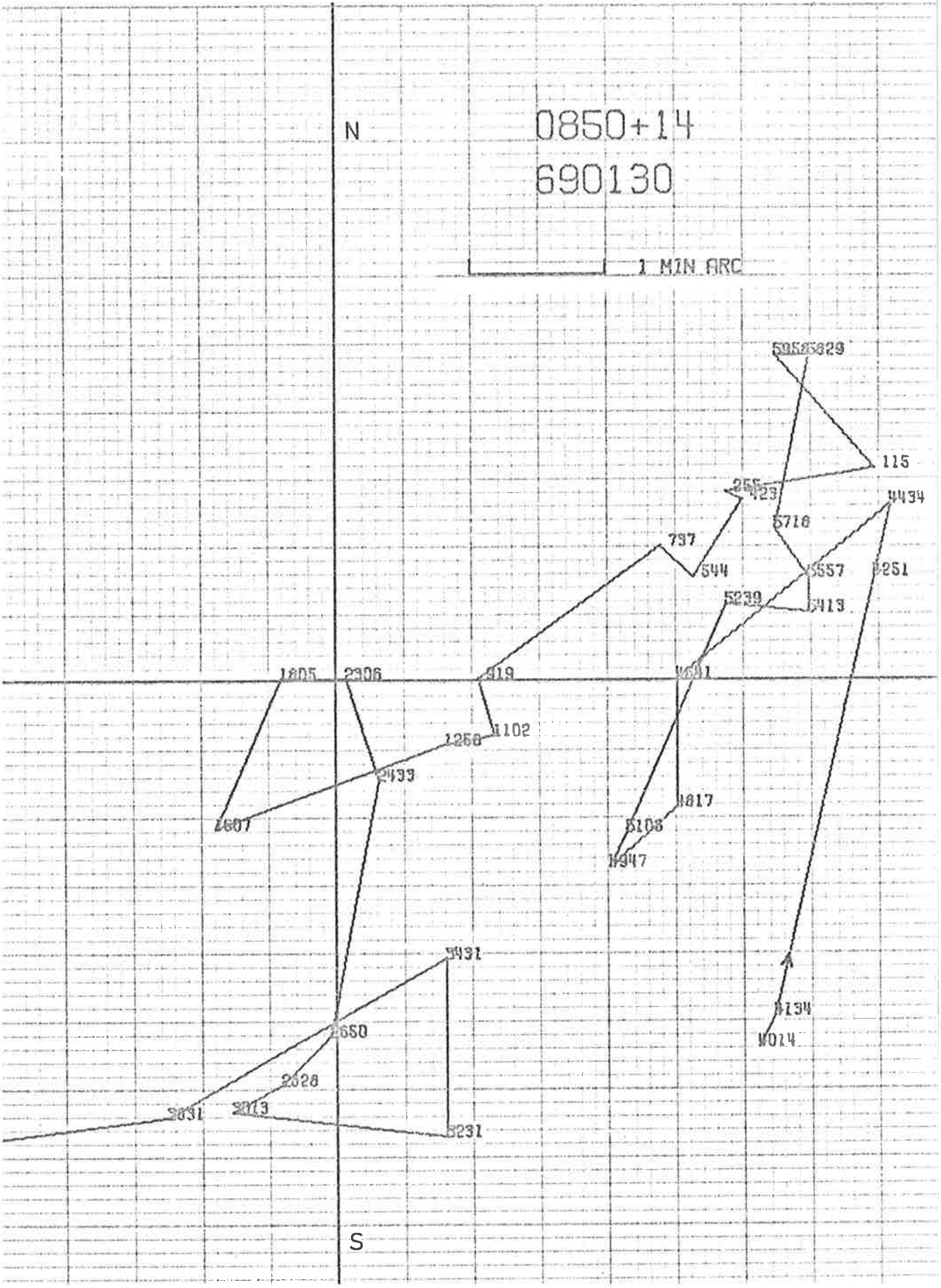
N
0850+14
690130
1 MIN ARC
59585829
115
255
423
4434
5718
737
544
5557
5251
5239
5413
1805
2306
919
4681
1258
1102
2433
4817
2607
5108
4947
5431
4134
4014
2650
2828
2831
2813
5231
S

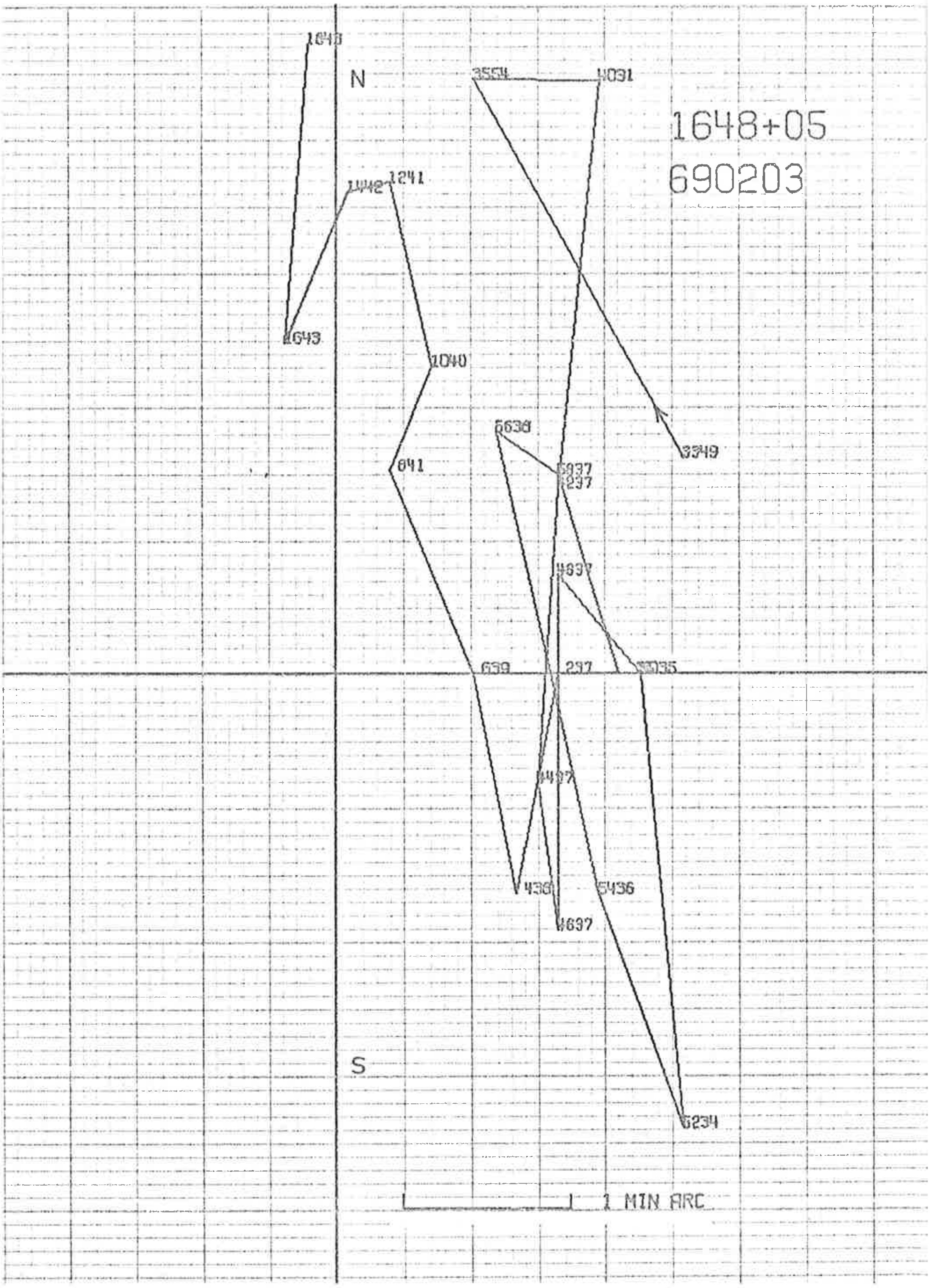
1648+05
690203
N
S
1640
1643
1442
1241
1040
841
639
3554
4031
3349
5638
5837
5237
4837
237
5035
4437
436
4637
5436
5234
1 MIN ARC

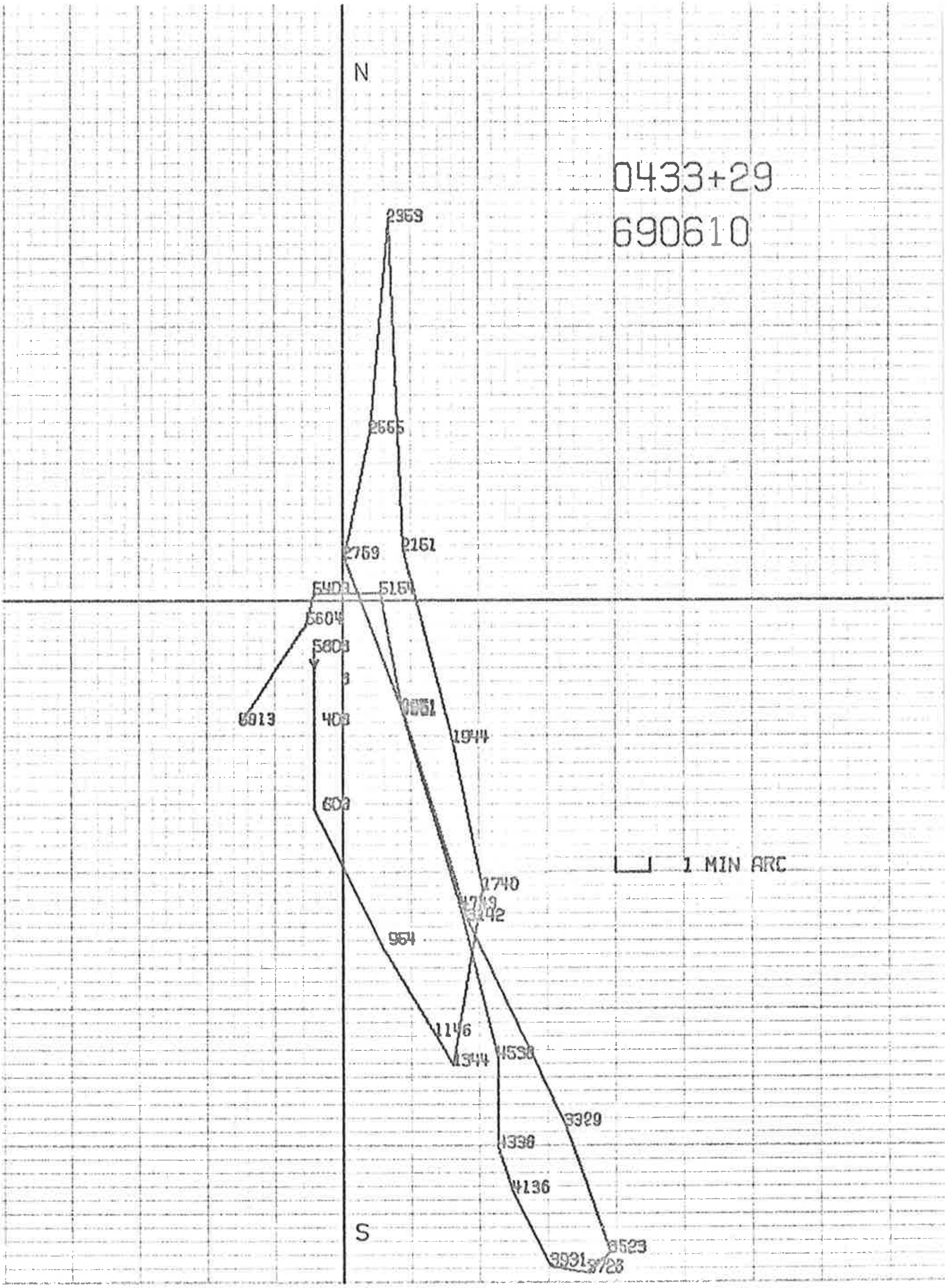
N
0433+29
690610
2969
2665
2769
2161
5403
5164
5604
5803
3
6013
409
0051
1944
603
1 MIN ARC
1740
4739
3342
964
1146
1344
4538
3329
4338
4136
S
3523
3931
3728

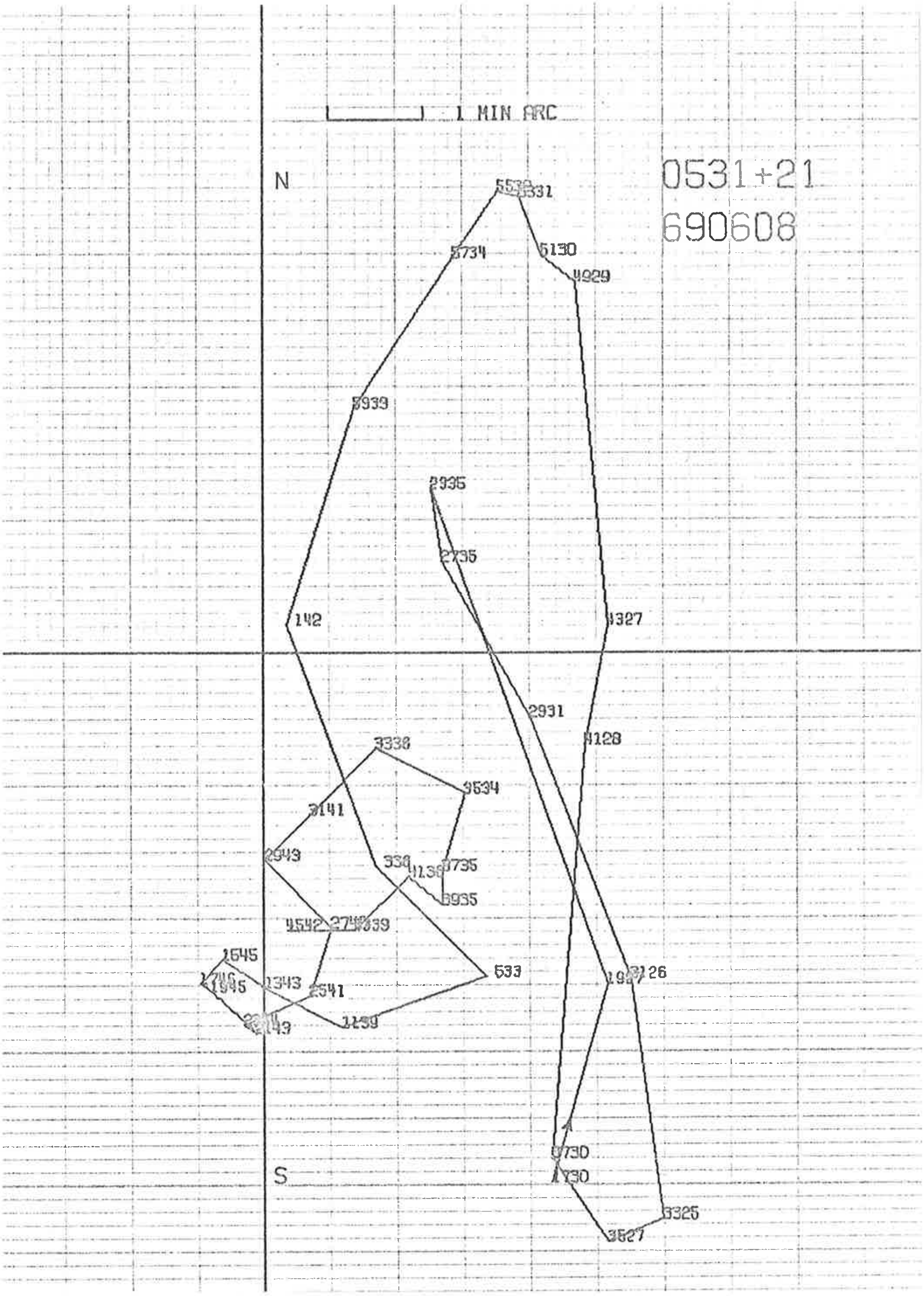
1 MIN ARC
0531+21
690608
N
S
5530
5331
5734
5130
4929
5939
2935
2735
142
4327
2931
4128
3330
3534
3141
2943
330
4138
3735
3935
4542
2740
4339
1645
1746
1945
1343
2541
633
2044
2143
1159
1927
3126
0730
1730
3325
3627

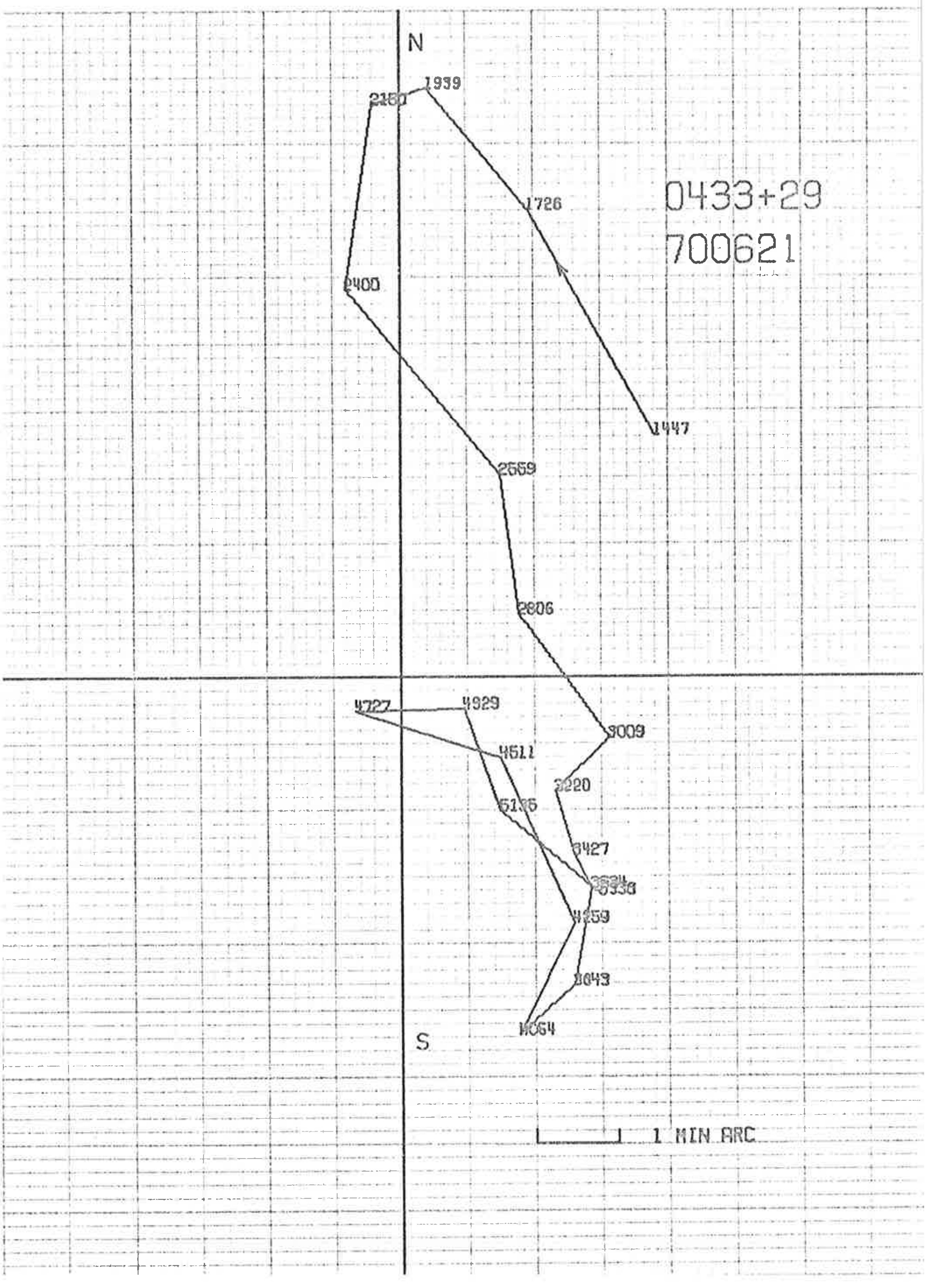
N
0433+29
700621
1939
2150
1726
2400
1447
2559
2806
3009
4727
4929
4511
3220
5136
3427
3634
5336
4259
3843
4064
S
1 MIN ARC

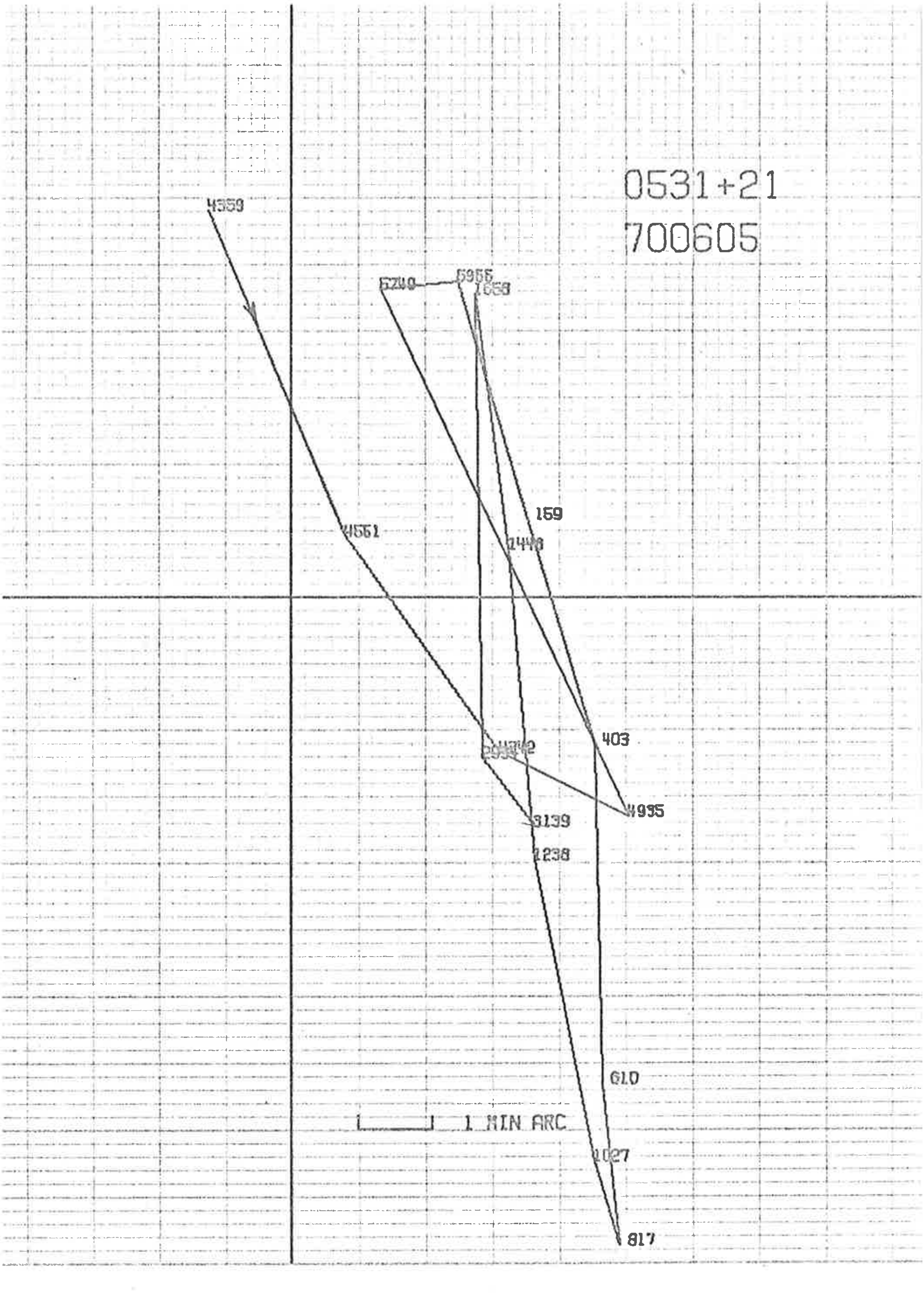
0531+21
700605
4359
6240
6966
1058
159
1448
4561
403
4742
2999
4995
3139
1238
610
1 MIN ARC
1027
817

APPENDIX II

Circuit diagrams of the receivers used on the Adelaide project.

Aerial Preamplifier

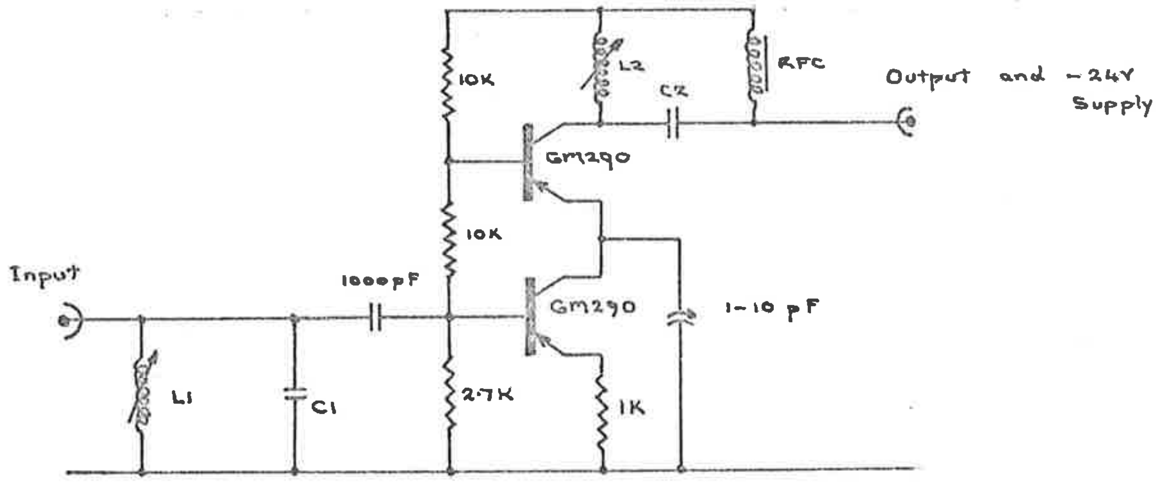
Input
L1
C1
1000pF
10K
10K
2.7K
GM290
GM290
1K
1-10 pF
L2
C2
RFC
Output and -24V Supply

	111·5 MHz	235·9 MHz
L1 :	8t Ferrite Slug	4t Ferrite Slug
L2 :	13t (22 SWG) Brass Slug	6t (22 SWG) Brass Slug
C1 :	3 pF	3pF
C2 :	5 pF	3pF

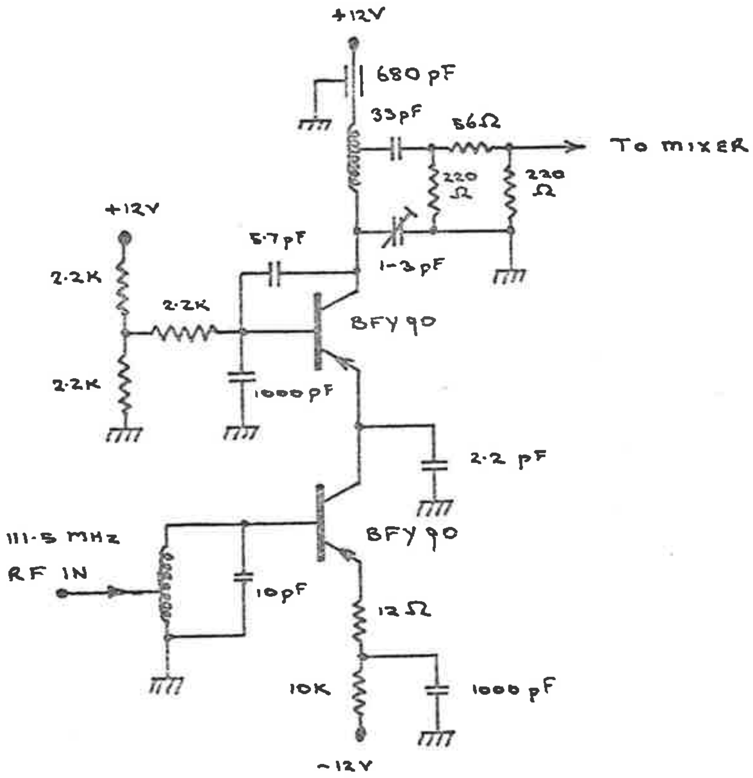
+12V
680 pF
33pF
56Ω
To mixer
220 Ω
220 Ω
1-3 pF
5·7 pF
+12V
2·2K
2·2K
2·2K
BFY 90
1000 pF
2·2 pF
111·5 MHz
RF IN
10pF
BFY 90
12 Ω
10K
1000 pF
-12V

Preamplifier

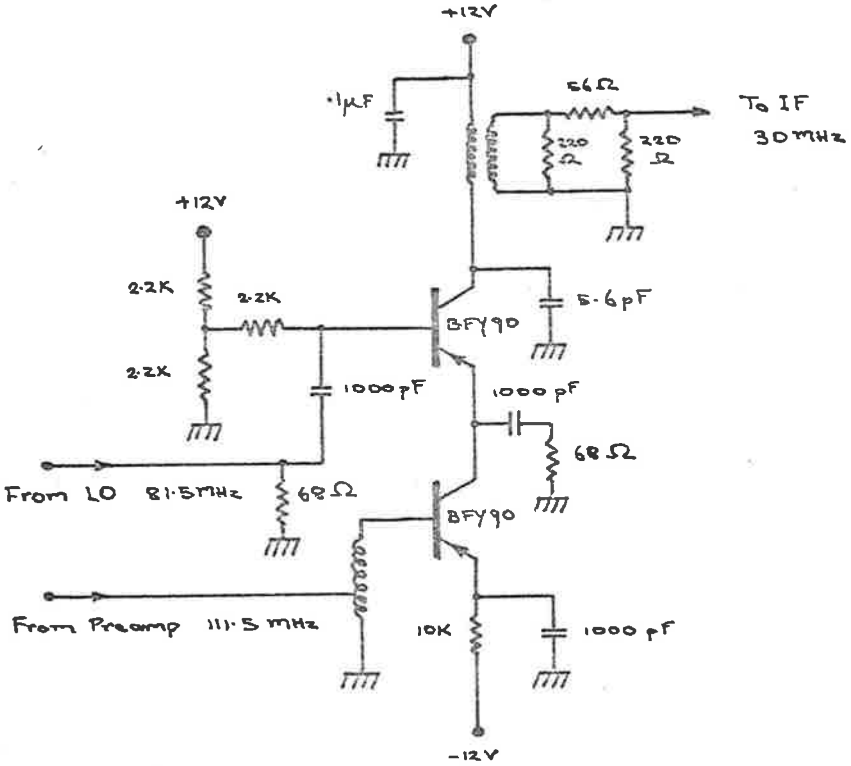
+12V
·1µF
56Ω
To IF
30MHz
220 Ω
220 Ω
+12V
2·2K
2·2K
2·2K
BFY90
5·6pF
1000pF
1000 pF
68Ω
From LO 81·5MHz
68Ω
BFY90
From Preamp 111·5 MHz
10K
1000 pF
-12V

mixer

Local Oscillator

PYE XL691

Converter Circuitry
(111·5 MHz)

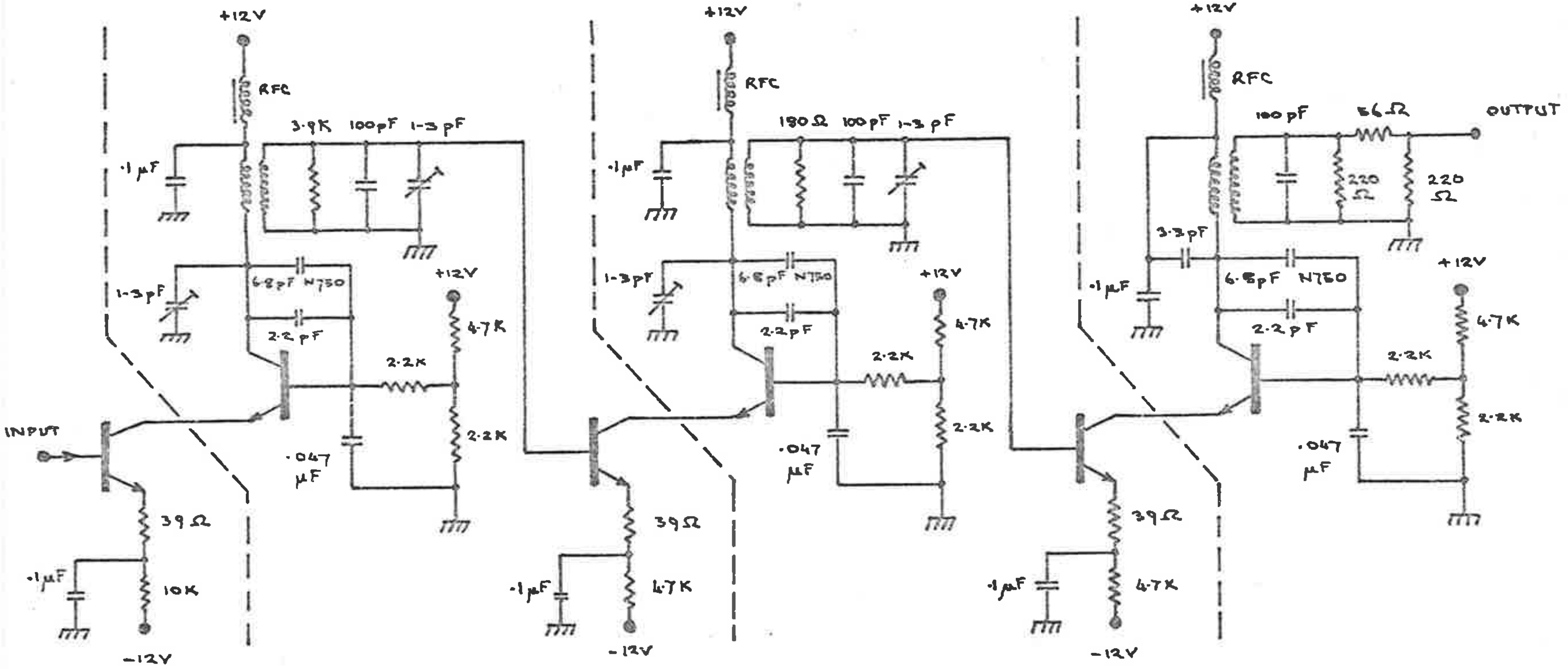
+12V
RFC
3.9K
100pF
1-3 pF
·1μF
1-3pF
6.8pF N750
2.2pF
+12V
4.7K
2.2K
2.2K
·047 μF
INPUT
39Ω
·1μF
10K
-12V
+12V
RFC
180Ω
100pF
1-3pF
·1μF
1-3pF
6.8pF N750
2.2pF
+12V
4.7K
2.2K
2.2K
·047 μF
39Ω
·1μF
4.7K
-12V
+12V
RFC
100pF
56Ω
OUTPUT
220 Ω
220 Ω
3.3pF
·1μF
6.8pF N750
2.2pF
+12V
4.7K
2.2K
2.2K
·047 μF
39Ω
·1μF
4.7K
-12V

All Tranzistors : BF 115

I.F. Amplifier

Frequency	30 MHz
Bandwidth	1 MHz
Gain	60 db

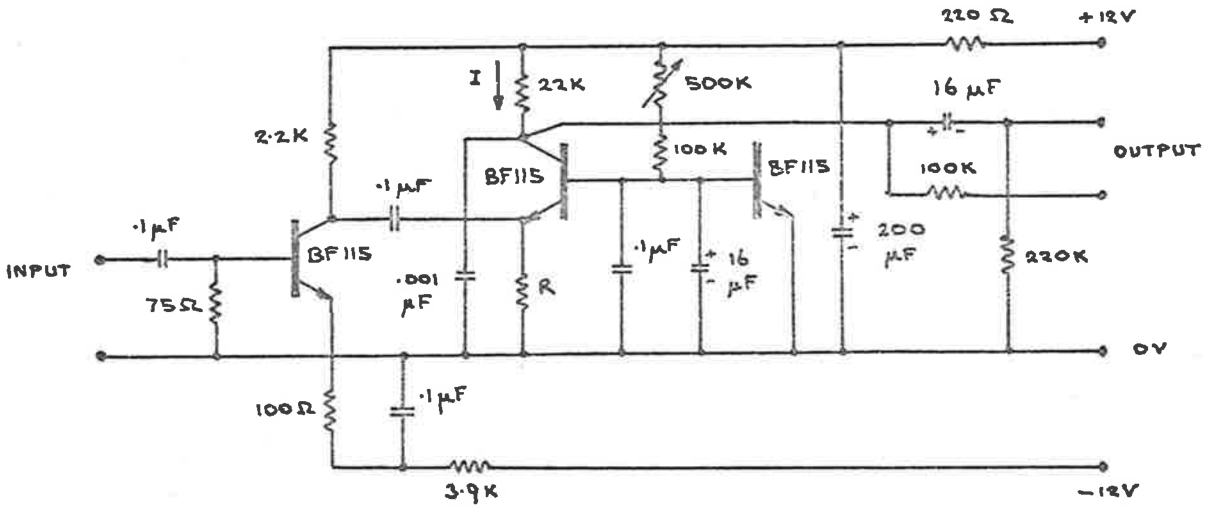
220 Ω
+12V
I
22K
500K
16 μF
OUTPUT
2·2K
100K
BF115
BF115
100K
·1 μF
·1 μF
INPUT
BF115
200 μF
220K
·001 μF
R
·1 μF
16 μF
75Ω
0V
100Ω
·1 μF
3·9K
−12V

Adjust I = 34 μA for R = 100 Ω

SQUARE LAW DETECTOR

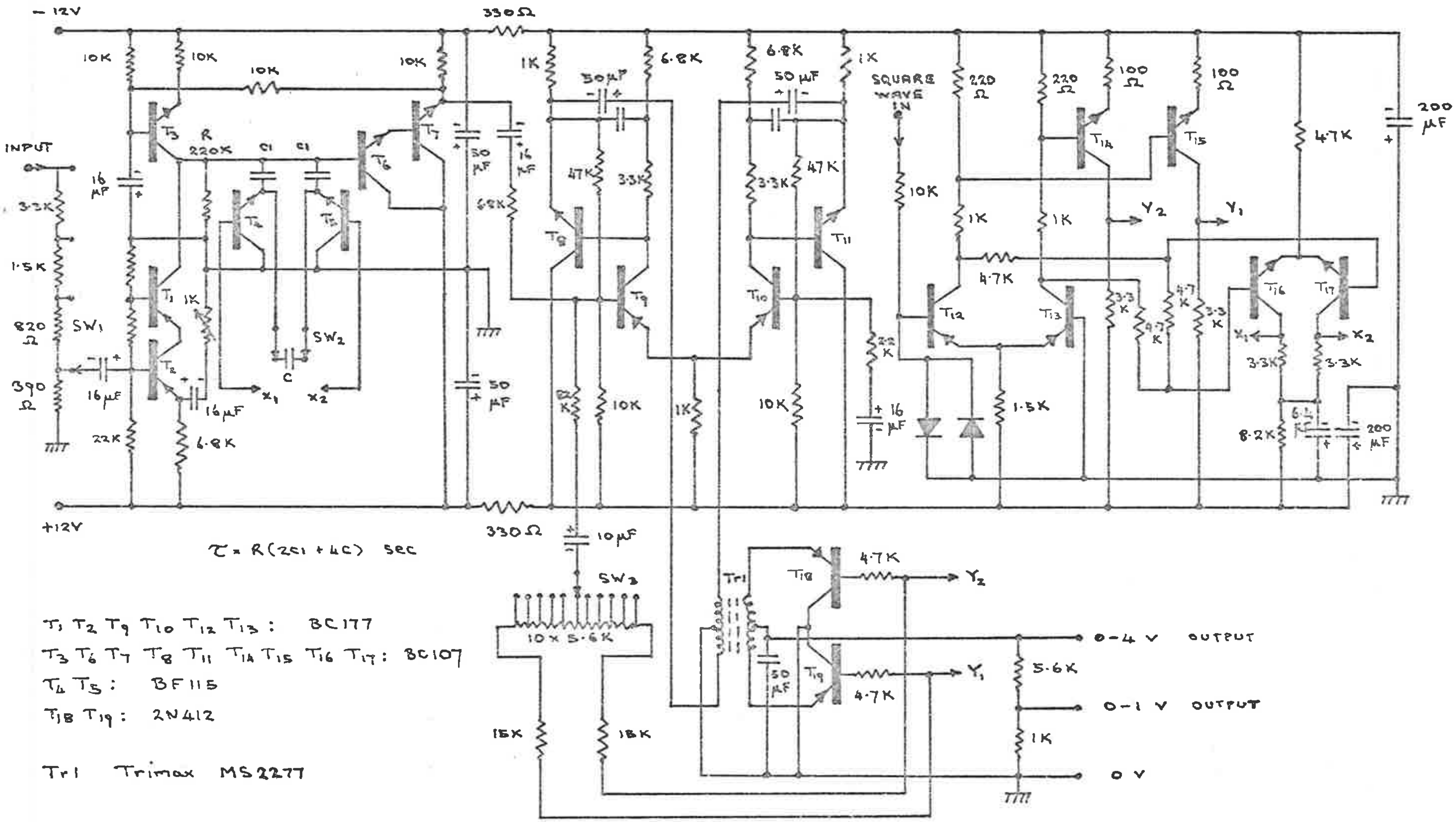

-12V
+12V
INPUT
330Ω
10K
10K
10K
10K
R
220K
C1
C1
C
1K
16 μF
50 μF
3.3K
1.5K
820 Ω
390 Ω
SW1
SW2
SW3
22K
6.8K
X1
X2
Y1
Y2
1K
6.8K
50μF
47K
3.3K
8.2K
10K
2.2K
10 μF
10 x 5.6K
15K
18K
SQUARE WAVE IN
220 Ω
100 Ω
4.7K
200 μF
6.2K
8.2K
1.5K
Tr1
T1
T2
T3
T4
T5
T6
T7
T8
T9
T10
T11
T12
T13
T14
T15
T16
T17
T18
T19
5.6K
0-4 V OUTPUT
0-1 V OUTPUT
0 V

$\tau = R(2C_1 + 4C)$ sec

T_1 T_2 T_9 T_{10} T_{12} T_{13} : BC177

T_3 T_6 T_7 T_8 T_{11} T_{14} T_{15} T_{16} T_{17} : BC107

T_4 T_5 : BF115

T_{18} T_{19} : 2N412

Tr1 Trimax MS2277

SYNCHRONOUS INTEGRATOR-DEMODULATOR

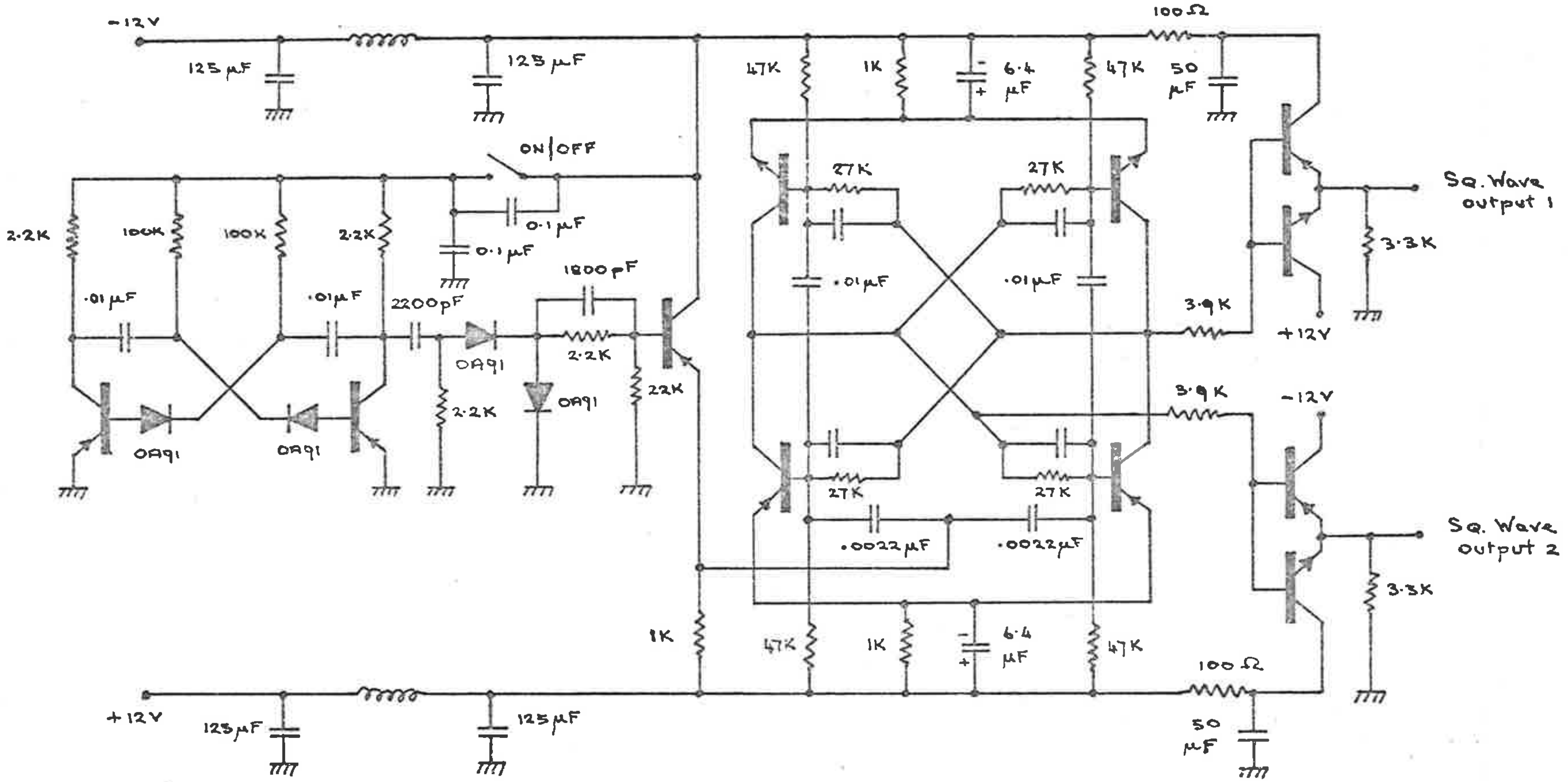
-12V
125 µF
125 µF
100Ω
47K
1K
6·4 µF
47K
50 µF
ON/OFF
2·2K
100K
100K
2·2K
0·1 µF
0·1 µF
·01 µF
·01 µF
2200pF
1800pF
OA91
2·2K
2·2K
OA91
22K
OA91
OA91
27K
27K
·01 µF
·01 µF
Sq. Wave output 1
3·3K
3·9K
+12V
3·9K
-12V
27K
27K
·0022 µF
·0022 µF
Sq. Wave output 2
3·3K
1K
47K
1K
6·4 µF
47K
100Ω
+12V
125 µF
125 µF
50 µF

Transistors: NPN BC107
PNP BC177

SQUARE WAVE GENERATOR

APPENDIX III

Reprint: "80 MHz Observations of the Coronal Broadening of the Crab Nebula" by J. R. Harries, R. G. Blesing and P. A. Dennison.

Harries, J. R., Blesing, R. G. & Dennison, P. A. (1970). 80 MHz observations of the coronal broadening of the Crab nebula. *Proceedings of the Astronomical Society of Australia, 1*(07), 319-320.

NOTE:
This publication is included in the print copy
of the thesis held in the University of Adelaide Library.

It is also available online to authorised users at:
http://dx.doi.org/10.1017/S1323358000012091